OUKA
The University of Osaka
Institutional Knowledge Archive

Title	Functional genetics with a hypomorphic CENP-C mutant reveals a regulatory system for chromosome congression
Author(s)	Miao, Jiahang
Citation	大阪大学, 2025, 博士論文
Version Type	VoR
URL	https://doi.org/10.18910/105272
rights	
Note	

The University of Osaka Institutional Knowledge Archive : OUKA

https://ir.library.osaka-u.ac.jp/

The University of Osaka

Functional genetics with a hypomorphic CENP-C mutant reveals a regulatory system for chromosome congression

機能的ゲノミックスクリーニングによる染色体整列機構の解明

JIAHANG MIAO

Graduate School of Frontier Biosciences

The University of Osaka

December 2025

Contents

Contents **1**

Abstract **5**

General Introduction **8**

1. Chromosome and Cell division **10**

2. Centromere and Kinetochore **13**

3. Kinetochore assembly **15**

3.1 Centromere Protein A (CENP-A), epigenetically defines the position of the centromere **15**

3.2 The Constitutive Centromere-Associated Network (CCAN), scaffold for kinetochore assembly **16**

3.3 The KMN network, linker between CCAN and microtubules **18**

4. Kinetochore-Microtubule attachment, a stepwise process **20**

5. Chromosome congression, a prerequisite for the subsequent mitotic events **22**

6. Microtubule dynamics critically influence stable kinetochore–microtubule attachment **24**

Key questions and purpose of this study **26**

Results **29**

Chapter 1. Functional genetics with CENP-C ∆M12BD mutant reveals a regulatory system for chromosome congression **29**

1. Characterization of K562 CENP-C ∆M12BD cells **29**

1.1 Generation of CENP-C ∆M12BD K562 cell line **29**

1.2 Mis12C-binding domain of CENP-C is dispensable for cell growth in human K562 cells **32**

1.3 CENP-C ∆M12BD reduces recruitment of KMN network during mitosis **33**

1.4 CENP-C ΔM12BD shows subtle mitotic defects like unaligned chromosomes and increased micronuclei **35**

2. CRISPR screening and validation in K562 CENP-C ΔM12BD cells **37**

2.1 A genome-wide CRISPR/Cas9 screening identified genes whose knockouts exhibit synthetic lethality with the CENP-C ΔM12BD mutation **37**

2.2 Individual knockout of candidate genes confirms synthetic lethality with the CENP-C ΔM12BD mutation **41**

2.3 *KIF18A* knockout with CENP-C ΔM12BD mutation shows strong mitotic defects accompanied with chromosome congression errors in human K562 cells **49**

2.4 CENP-C ΔM12BD cells are sensitive to the microtubule-destabilizing drug nocodazole **53**

3. Investigation of *KIF18A* knockout in human CENP-C ΔM12BD RPE-1 cells **55**

3.1 Generation of human CENP-C ΔM12BD RPE-1 cells **55**

3.2 *KIF18A* is essential for cell viability in CENP-C ΔM12BD RPE-1 cells **57**

3.3 Perturbation of Mis12C-CENP-C interactions leads to increase of *KIF18A*-KD sensitivity **59**

3.4 *KIF18A* knockout disturbs mitotic progression in CENP-C ΔM12BD RPE-1 cells **62**

3.5 Inhibition of SAC rescues lethality of CENP-C ΔM12BD RPE-1 cells after *KIF18A* knockout **64**

3.6 KIF18A C-terminal domain is important for KIF18A function in CENP-C ΔM12BD RPE-1 cells **65**

3.7 KIF18A microtubule plus-end localization is required for cell viability in CENP-C ΔM12BD RPE-1 cells **67**

3.8 Ndc80C or Aurora B reduction in CENP-C ΔM12BD RPE-1 cells does not cause mitotic defects after *KIF18A* knockdown **71**

3.9 Reduction of CENP-E at the kinetochore is a major cause for the *KIF18A*-KD sensitivity of CENP-C ΔM12BD RPE-1 cells **73**

3.10 CENP-E inhibition causes mitotic defect after *KIF18A* knockdown **82**

3.11 CENP-E levels were significantly reduced in cancer cell lines showing sensitivity to *KIF18A* knockdown **84**

4. A proposed model to demonstrate the correlation between KIF18A and CENP-E during mitosis **87**

5. Discussion **90**

5.1 *KIF18A*-KD reduced kinetochore localized CENP-E level **91**

5.2 Reduced CENP-E level in CENP-C ΔM12BD cells is not primarily due to CENP-E removal **93**

5.3 Aurora A inhibition rescued *KIF18A*-KD sensitivity in CENP-C ΔM12BD K562 and RPE-1 cells and HeLa cells **95**

5.4 Enhanced binding of Mis12C to CENP-C did not rescue *KIF18A*-KD sensitivity in HeLa cells **99**

5.5 KIF15 inhibition causes mitotic defects in CENP-C ΔM12BD K562 cells .. **101**

5.6 *SPAG5* knockdown dramatically increases micronuclei formation in CENP-C ΔM12BD K562 cells **104**

Chapter 2. Functional genetic screening reveals genes whose knockouts exhibit synthetic lethality with CENP-C ΔCC-motif mutation **106**

1. Generation of CENP-C ΔCC-motif K562 cell line **106**

2. CENP-C motif domain of CENP-C is dispensable for cell growth in human K562 cells **110**

3. CENP-C ΔCC-motif reduces recruitment of CENP-C and DSN1 during mitosis **111**

4. A genome-wide CRISPR/Cas9 screening identified genes that exhibit synthetic lethality with the CENP-C ΔCC-motif mutation **112**

5. Discussion **118**

Materials and Methods **119**

Key resources table **133**

Tables **141**

References **144**

Acknowledgements **156**

Achievements **157**

Abstract

All living organisms rely on a fundamental cellular process for growth and survival—cell division. This intricate process allows cells to duplicate themselves, faithfully transmit genetic information, and ensure the continuity of life across generations. A multitude of molecular machines and regulatory factors work in concert to accomplish this essential goal. Over the last century, despite rapid advancements in the biological field, our understanding of cell division still remains far from completion. While it may appear that key mechanisms have been uncovered, in reality, these insights represent only the tip of the iceberg. The cell division process resembles a complex web, with each component intricately interconnected. Focusing too narrowly on individual elements risks overlooking the broader network of interactions that govern cellular behavior. Therefore, it is critical to approach this field from a holistic, systems-level perspective. To see further, we must first stand higher. This principle forms the foundation of my PhD project: to explore and reveal the hidden mechanisms underlying the cell division process.

In human somatic cells, before entering the cell division process, several preparatory steps must be completed, including DNA replication and chromosome condensation. As the cell progresses into mitosis, the nuclear envelope first breaks down, followed by the formation of spindle microtubules. The spindle serves as an essential machinery that ensures each daughter cell inherits an exact copy of the chromosomes from the parent cell. A long-standing question in cell biology is how spindle microtubules accurately attach to chromosomes—an issue that researchers have grappled with for decades. Through the dedicated efforts of many scientists, it is now understood that a proteinaceous, layered structure forms a critical interface between the tips of microtubules and the chromosomes. This structure is known as the *kinetochore*, which is formed on the specific region of the chromosome called the *centromere*.

The kinetochore is a multi-protein complex that can be broadly divided into two functional groups. One group, known as the Constitutive Centromere-Associated Network (CCAN), remains anchored at the centromere throughout the entire cell cycle. The second group, referred to as the KMN network, interact with the CCAN and spindle microtubules during mitotic progression. CCAN is composed of 16 proteins, among

which Centromere Protein C (CENP-C) is thought to play a central role by bridging centromeric chromatin to the outer kinetochore via CENP-A and the KMN network, respectively. Although CENP-C was one of the first centromere proteins to be discovered in human cells, detailed insights into its functional mechanisms have only emerged over the past decade. CENP-C contains several functional domains. The N-terminal domain directly interacts with the Mis12 complex of the KMN network, while the C-terminal domain binds to the CENP-A nucleosome embedded in the centromeric chromatin.

Although CENP-C was expected to have a bridging function between centromeric chromatin and microtubules, previous research in my lab revealed that both the N-terminal and C-terminal domains of CENP-C are dispensable for cell viability and mitotic progression in chicken DT40 and human RPE-1 cells. This finding is unexpected and somewhat controversial, as these domains are highly conserved across species and are widely believed to be essential for CENP-C function. From a biological standpoint, the fact that these domains are conserved implies an underlying rationale, suggesting that there may be as-yet undiscovered functions associated with them. If so, what are these functions? Given the complexity of chromosome segregation, such roles might be masked under normal growth conditions, as the absence of these domains does not compromise cell proliferation.

To address this question, I utilized mutant human cells lacking CENP-C N-terminus or C-terminus and conducted a genome-wide CRISPR-Cas9 screen in these cells to uncover compensatory or previously hidden pathways. Through this approach, I identified *KIF18A* gene whose depletion shows synthetic lethality with deletion of the N-terminal domain of CENP-C in human RPE-1 cells. My further analysis revealed that CENP-E reduction in cells lacking CENP-C N-terminus is a major cause for the synthetic lethality of KIF18A depletion in human RPE-1 cells lacking CENP-C N-terminus. CENP-E is a motor protein, which has a critical function for chromosome congression in early prometaphase. My analysis of cells with KIF18A depletion suggests that KIF18A is also involved in chromosome congression via its control of microtubule dynamics. Therefore, based on my results, I propose that KIF18A and CENP-E work cooperatively to enable efficient chromosome congression during prometaphase, which is a critical prerequisite for successful cell division. I also

demonstrated that the reduction of CENP-E levels at mitotic kinetochores is one of the determinants of KIF18A dependency in certain cancer cell lines, nominating CENP-E as a potential biomarker for effective cancer therapy with KIF18A inhibition.

Taken together, although cells can tolerate the loss of either KIF18A or CENP-E individually with only mild mitotic defects, simultaneous loss of both proteins results in mitotic arrest. This synthetic lethality highlights a previously unrecognized interdependence between the CENP-C and KIF18A pathways in maintaining mitotic fidelity, representing the central conclusion of my PhD thesis. Furthermore, this study provided insights into parallel molecular mechanisms underlying chromosome congression and revealed sensitivities and biomarkers that may inform the development of future anti-KIF18A chemotherapeutic strategies. The following chapters describe in detail the experimental strategies, results, and interpretations that led to these findings.

General Introduction

Biology seeks to answer one fundamental question: **What is life?** The renowned Austrian physicist Erwin Schrödinger explored this question in his seminal book *What is Life? The Physical Aspect of the Living Cell* (Schrodinger et al., 1946). In this work, Schrödinger proposed that the phenomena of life can be explained through the principles of physics and chemistry. Notably, he suggested that the stability of genetic material is rooted in the structure of an "aperiodic crystal", a concept that would later align with the molecular structure of DNA. Schrödinger also introduced the concept of "negative entropy" (or *negentropy*) to explain how living organisms resist the natural tendency toward disorder. By absorbing energy from their environment, organisms sustain internal order—a principle manifested in metabolism, which involves the transformation of energy and the exchange of matter to maintain self-organization. Remarkably, this book was published in 1946, several years before Watson and Crick's discovery of the double-helix structure of DNA (Watson et al., 1953). Some people have even argued that *What is Life?* helped inspire this breakthrough, as it laid a theoretical foundation for molecular biology through its early articulation of the "genetic code."

Over time, the continuation of life has increasingly been interpreted as the perpetuation of genetic material. About three decades later, in 1976, British evolutionary theorist Richard Dawkins published the influential popular science book *The Selfish Gene* (Dawkins et al., 1976). Drawing on advances in biological research and his own theoretical insights, Dawkins argued that the fundamental nature of genes is inherently “selfish”. According to his view, genes are driven by a relentless imperative to survive and replicate, even if it means manipulating the behavior of the organisms that carry them. For example, when animals care for their offspring, this may appear altruistic at the individual level. However, because such behavior is governed by genes, it ultimately serves the purpose of ensuring their own replication. In this framework, all apparent acts of altruism in the biological world are in fact strategies deployed by selfish genes to perpetuate themselves. Genes are not concerned with the well-being of the organism per se; their sole "interest" lies in maximizing the number of copies of themselves made over time. As the carriers of the "genetic code," genes become the ultimate driving force behind reproduction,

adaptation, and evolution.

From this perspective, organisms, whether individuals or entire populations, are merely temporary vehicles for genes. It is the genes that are enduring, not the organisms they inhabit. Genes are not only the basic units of heredity but also the primary units of natural selection. Their intrinsic selfishness governs the biological activities and behaviors of living beings, all in service of faster and more efficient replication. To achieve this goal, genes will exploit any strategy necessary, provided it enhances their chances of being reliably passed on to future generations. In this way, genes ensure their own immortality, while the organisms that carry them are granted only a fleeting existence.

While this view may appear harsh—suggesting that we are all, in some sense, slaves to our genes—it powerfully captures the underlying logic of life: **the drive to persist.** Ultimately, life is not merely about the survival of the organism, but about the enduring legacy of the gene. The continuation of genes depends on the replication and division of living organisms, forming a mutually reinforcing relationship. Genes endow organisms with the ability to divide, while organisms utilize this function to grow, develop, and stably transmit the genes they carry to the next generation. Since the discovery of the vehicle for genetic material, people are struggling to understand how genes are inherited and passed from one generation to the next generation. In the following paragraphs, I will provide a detailed introduction of how genes are transmitted to the next generation.

1. Chromosome and Cell division

Genetic information is encoded in the linear sequence of nucleotides within DNA. Each DNA molecule is structured as a double helix, consisting of two complementary, antiparallel strands held together by hydrogen bonds between specific base pairs: guanine (G) with cytosine (C), and adenine (A) with thymine (T). The primary function of DNA is to carry genes. In eukaryotic cells, DNA is organized into chromosomes. Each chromosome contains a single, extraordinarily long linear DNA molecule, which is tightly folded and packaged with proteins into a more compact and manageable structure (Figure 1). From a functional perspective, chromosomes serve as the fundamental vehicles of genetic information.

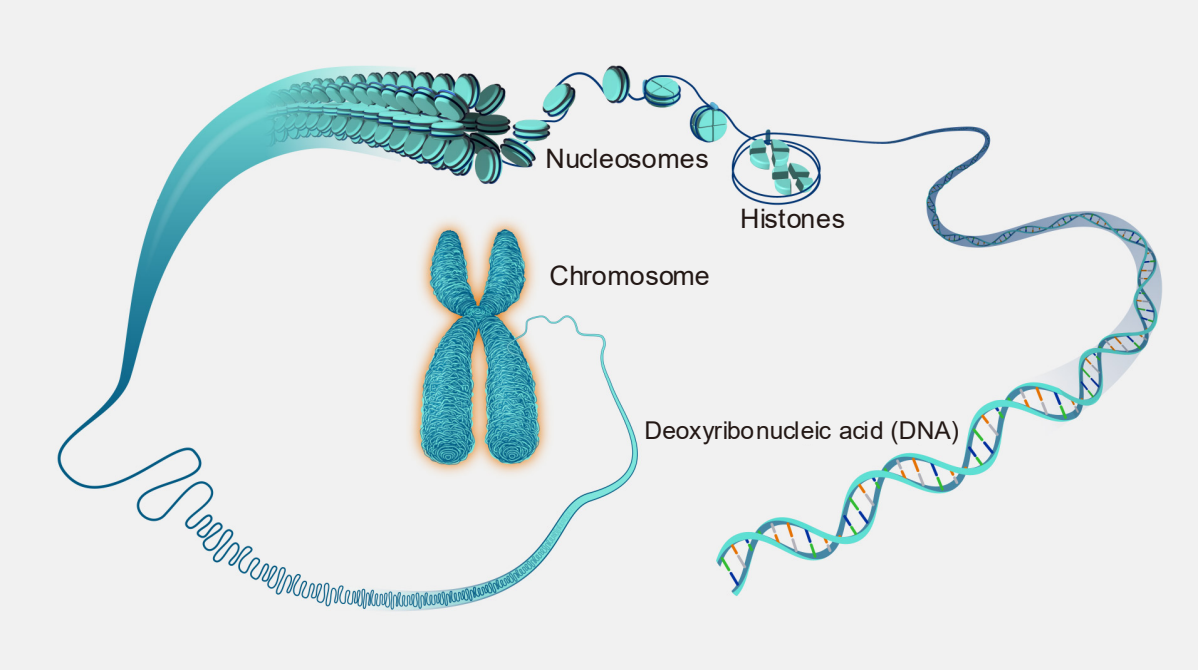


Figure 1. Chromosome consists of a single, enormously long linear DNA molecules along with the histones that fold and pack the fine DNA thread into a compact structure. Modified from https://www.genome.gov/genetics-glossary/Chromosome.

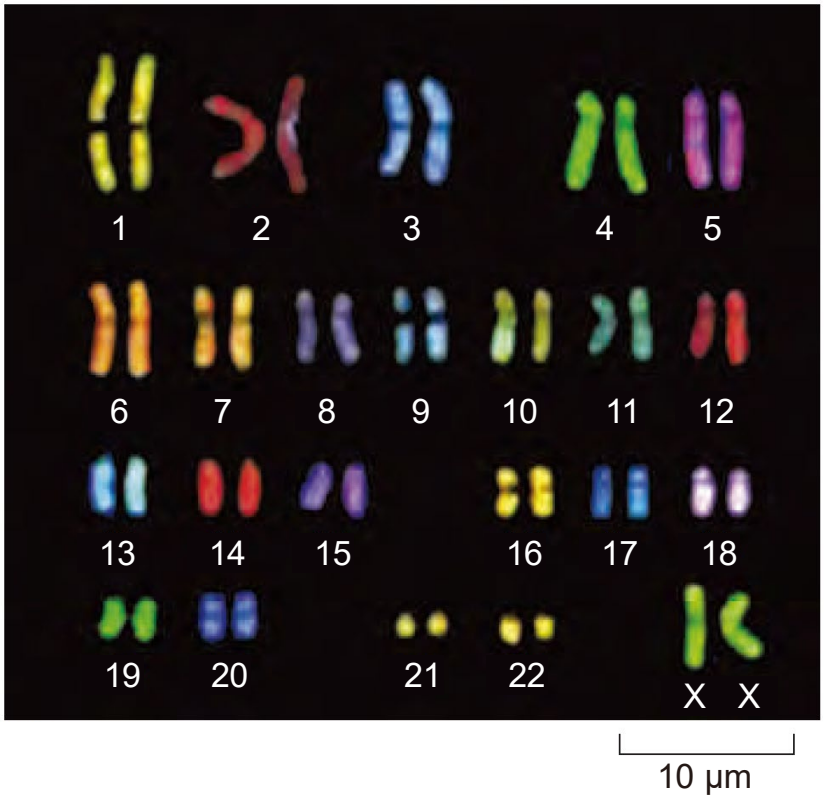


Figure 2. The complete set of human chromosomes. Adapted from McNeil et al., 2000.

Each human cell contains a total of 46 chromosomes—22 pairs common to both males and females, plus two sex chromosomes (X and Y in males, two Xs in females) (Figure 2). All of these chromosomes should be perfectly replicated and transmitted to the next generation with an event which is called cell division. Cell division is an extraordinarily complex process, involving thousands of genes and proteins that work together to achieve one critical goal: the flawless and accurate transmission of genetic material to the next generation without any errors (O'Connor et al., 2008). To prepare for cell division, cells must grow and approximately double their mass of proteins and organelles before duplicating their chromosomes and dividing. Chromosome duplication occurs during S phase (S for DNA synthesis), which requires about 10–12 hours in a typical mammalian cell. After S phase, chromosome segregation and cell division occur in M phase (M for mitosis), which requires much less time (around one hour in a mammalian cell). In addition to S and M phase, most

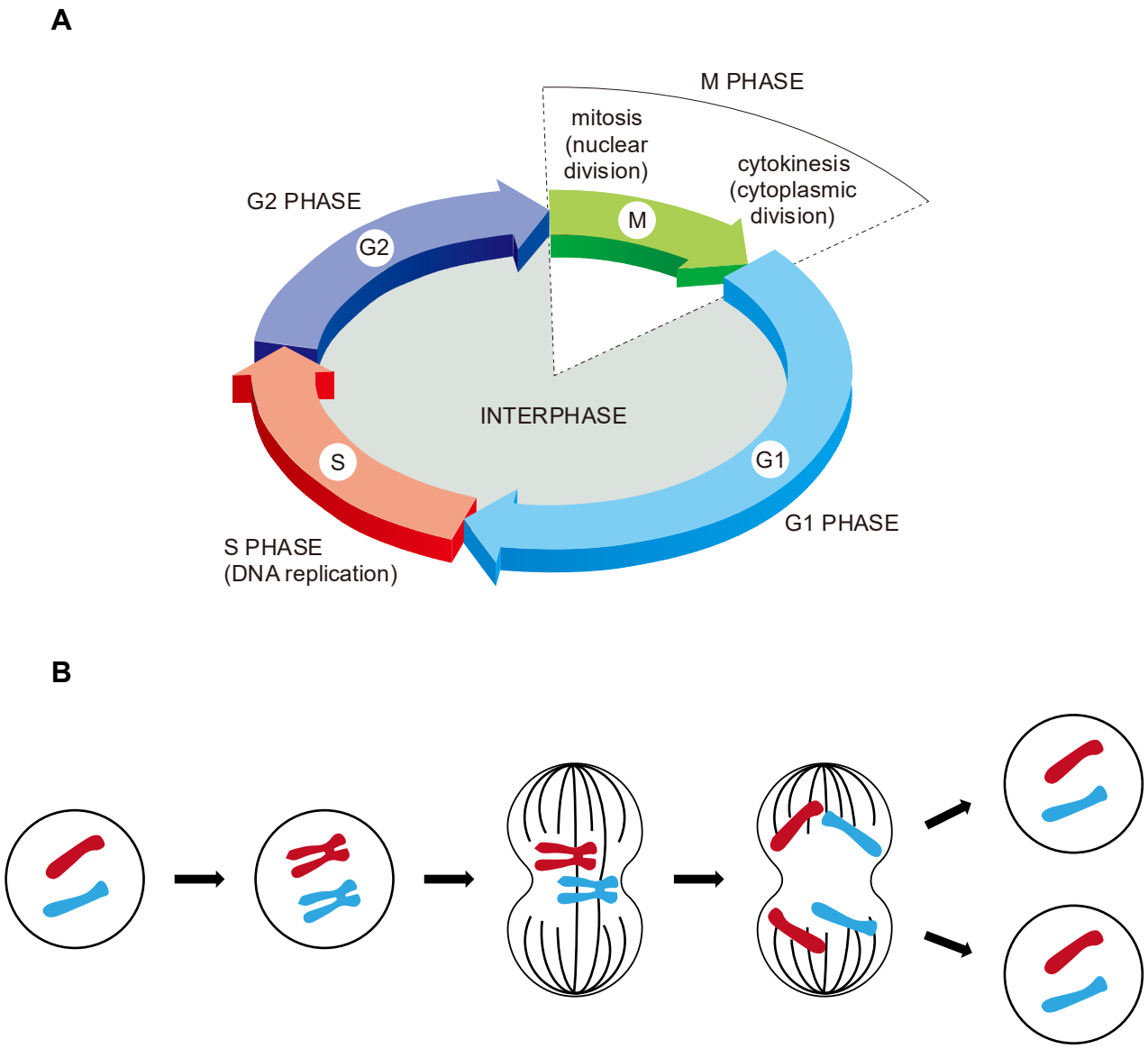


Figure 3. (A) The four phases of the cell cycle. Adapted from *Molecular Biology of the Cell*, Sixth Edition. (B) Diagram of the chromosome segregation in mitosis.

cell division cycles have gap phases: the G1 phase, which occurs between the M phase and the S phase, and the G2 phase, which lies between the S phase and M phase. Accordingly, the eukaryotic cell cycle is traditionally divided into four sequential phases: G1, S, G2, and M. The G1, S, and G2 phases together comprise interphase (Figure 3A). In a typical human cell proliferating in culture, interphase may occupy about 23 hours of a 24-hour cycle, with the remaining hour dedicated to the M phase

(Alberts et al., 2002). The two gap phases serve purposes beyond simply providing time for cell growth. They also allow the cell to monitor both internal and external conditions, ensuring that the environment is favorable and that all necessary preparations have been completed before the cell proceeds to the critical events of DNA replication (S phase) and mitosis. After DNA replication is completed during interphase, the cell enters mitosis. Each replicated chromosome, composed of two closely associated sister chromatids, attaches to spindle microtubules through specialized protein structures called kinetochores. The chromosomes then align at the spindle equator, positioned midway between the two spindle poles. At this stage, kinetochore microtubules connect each sister chromatid to opposite spindle poles. Next, the sister chromatids separate simultaneously, each becoming an individual daughter chromosome. These chromosomes are then pulled slowly toward the spindle pole to which they are attached. This movement is driven by two coordinated processes: the shortening of the kinetochore microtubules and the movement of the spindle poles away from each other—both of which contribute to the accurate segregation of chromosomes. Finally, the two sets of daughter chromosomes arrive at opposite spindle poles and begin to decondense. A new nuclear envelope forms around each set, completing the reformation of two distinct nuclei and marking the end of mitosis (Figure 3B).

2. Centromere and Kinetochore

During the mitosis, the key process for cells to ensure faithful chromosome segregation is based on the stable attachment of spindle microtubules with a chromosome. Spindle microtubules bind to a chromosome at a specific region which is called centromere. The centromere is a specialized genome region on which a large protein complex known as “kinetochore” assemble. Centromeres of humans and other primates are made of multiple copies of the conserved ~171–base pair (bp) a-satellite repeat that contains the histone H3 variant centromere protein A (CENP-A) (Earnshaw et al., 1985; Sullivan et al., 1994; Henikoff et al., 2001; Cleveland et al., 2003). And kinetochore forms a plaque on the surface of the centromere that directly binds to both the chromosomal DNA and the ends of spindle microtubules to mediate chromosome segregation (Figure 4).

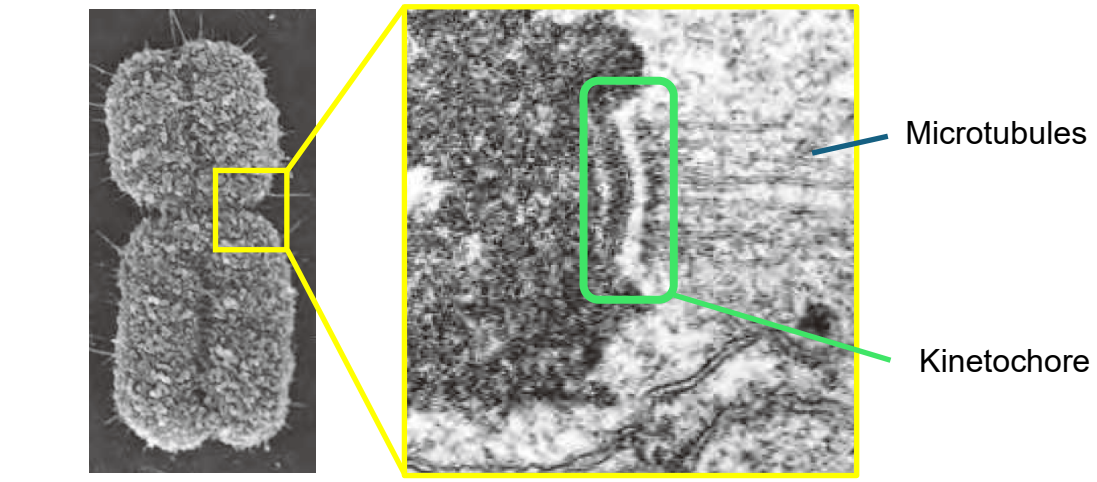


Figure 4. Kinetochore mediates attachment between microtubule and chromosome. Adapted from *Molecular Biology of the Cell*, Sixth Edition.

Kinetochore is a large protein complex composed of more than 100 distinct proteins (Bloom et al., 2010; Cheeseman et al., 2014; Nagpal et al., 2016). In metazoans, kinetochores consist of two major subcomplexes with distinct localization patterns and assembly dynamics. The inner kinetochore, also known as the Constitutive Centromere-Associated Network (CCAN), remains bound to centromeric DNA throughout the entire cell cycle (Hori et al., 2008; Cheeseman et al., 2008; Cheeseman et al., 2014; Musacchio et al., 2017). It functions as a structural platform for the recruitment of the outer kinetochore, which assembles fully only during mitosis (Musacchio et al., 2017; Sridhar et al., 2022). The outer kinetochore serves as the functional domain of the complex and is essential for the kinetochore's two key roles in chromosome segregation. First, it mediates the attachment to spindle microtubules, enabling chromosomes to move along microtubule surfaces and to track microtubule plus-ends. This interaction allows the mitotic spindle to align chromosomes at the cell equator and subsequently segregate them toward opposite spindle poles (Grishchuk et al., 2017). Second, the outer kinetochore monitors the fidelity of microtubule attachments. It serves as a signaling hub for the spindle assembly checkpoint (SAC), a surveillance mechanism that delays mitotic progression until all sister chromatids are properly attached to microtubules emanating from opposite spindle poles (Musacchio et al., 2015).

3. Kinetochore assembly

3.1 Centromere Protein A (CENP-A), epigenetically defines the position of the centromere

In most organisms, centromere identity is defined by epigenetic mechanisms. A key determinant of this identity is the centromere-specific histone H3 variant, CENP-A, which is essential for centromere function. Human CENP-A was first identified as an antigen in sera from scleroderma CREST patients (Moroi et al., 1980; Earnshaw et al., 1985). Structural analyses of the protein have revealed that the C-terminal histone-fold domain of CENP-A shares approximately 57% amino acid identity with canonical histone H3 and contains a unique RG loop in the histone-fold domain for kinetochore assembly. This structural configuration is critical for the proper incorporation and function of CENP-A (Sullivan et al., 1994; Black et al., 2008; Earnshaw et al., 2013; Ariyoshi et al., 2021).

Disruption of CENP-A, either through deletion or mislocalization caused by overexpression, results in defective chromosome segregation, highlighting its essential role in maintaining genome stability (Howman et al., 2000; Régnier et al., 2005; Black et al., 2008; Shrestha et al., 2017; Shrestha et al., 2021). Importantly,

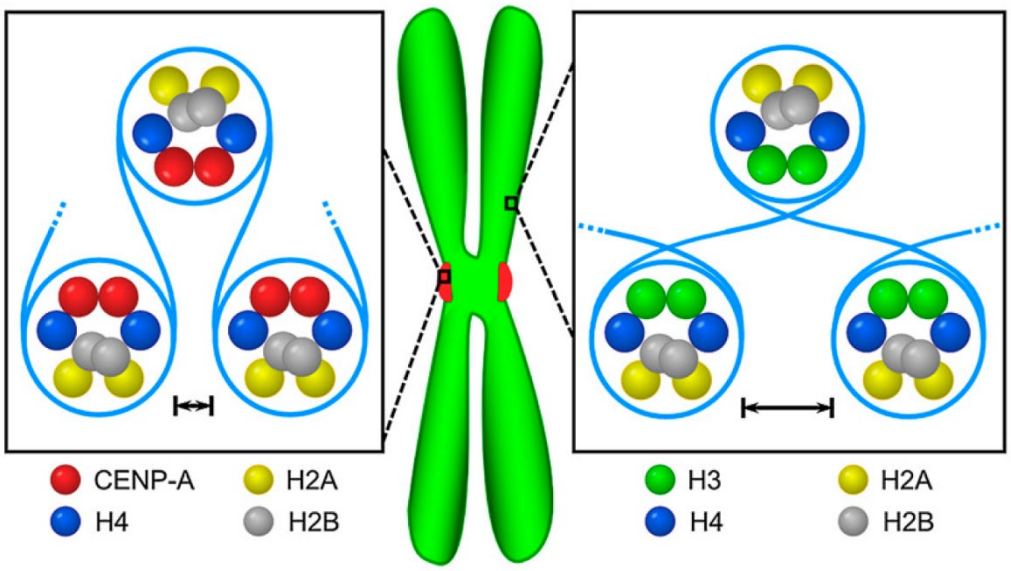


Figure 5. CENP-A is an essential histone H3 variant that epigenetically marks the centromeric region of chromosomes. Adapted from Panchenko et al., 2011.

CENP-A is loaded exclusively onto the active centromere of dicentric chromosomes, further supporting its role as an epigenetic marker (Warburton et al., 1997; Panchenko et al., 2011). In addition, functional centromeres can be artificially established at non-repetitive DNA locus using the LacO/LacI system (Hori et al., 2013). Through decades of scientists' study, people conclude that CENP-A is an essential histone H3 variant that epigenetically marks the centromeric region of chromosomes (Figure 5). After CENP-A define the centromere, CENP-A can interact with a network of other centromeric proteins, offering key insights into the mechanisms governing kinetochore assembly and faithful chromosome segregation.

3.2 The Constitutive Centromere-Associated Network (CCAN), scaffold for kinetochore assembly

Once CENP-A is deposited at a specific genome locus, a group of 16 chromatin-proximal proteins termed the constitutive centromere-associated network (CCAN) associated with centromeric chromatin to initiate the assembly of kinetochore (Gascoigne et al., 2011; Hara et al., 2017). CCAN consists of several subunits, including CENP-C, CENP-TWSX complex, CENP-LN complex, CENP-HIKM complex and CENP-OPQUR complex (Figure 6) (Hori et al., 2008; Hara et al., 2017; Yan et al., 2019; Tian et al., 2022). CENP-C directly interacts with the CENP-A nucleosome (Kato et al., 2013; Ariyoshi et al., 2021) and recruits the CENP-LN complex (Musacchio et al., 2017; McKinley et al., 2015; Yatskevich et al., 2022). Together, CENP-C and CENP-LN facilitate the recruitment of the CENP-HIKM complex. In turn, CENP-HIKM, in cooperation with CENP-LN, promotes the assembly of the CENP-TWSX and CENP-OPQUR complexes (McKinley et al., 2015; Pesenti et al., 2022; Yatskevich et al., 2022). The stable localization of these complexes on centromeric DNA is highly interdependent: the proper kinetochore localization of CENP-LN and CENP-HIKM is mutually dependent, and both are required for CENP-TWSX localization (McKinley et al., 2015). CENP-OPQUR is reported to be downstream in this assembly cascade and is not required for the localization of the other CCAN components (Yatskevich et al., 2022).

In addition to the DNA-binding capability of the CENP-A nucleosome itself,

several inner kinetochore components, including CENP-LN, CENP-HIKM, and CENP-TWSX—contain regions that directly associate with DNA (Yatskevich et al., 2022; Pesenti et al., 2022). Together, these inner kinetochore proteins form a multivalent DNA-binding platform that robustly anchors the kinetochore to chromosomes, enabling resistance against the mechanical forces exerted by the mitotic spindle. As previously noted, CENP-C and CENP-T serve as key connectors between the inner and outer kinetochore (Kim et al., 2015; Screpanti et al., 2011; Nishino et al., 2013; Petrovic et al., 2016). Both proteins possess N-terminal domains that are sufficient to recruit outer kinetochore proteins (Petrovic et al., 2016; Takenoshita et al., 2024).

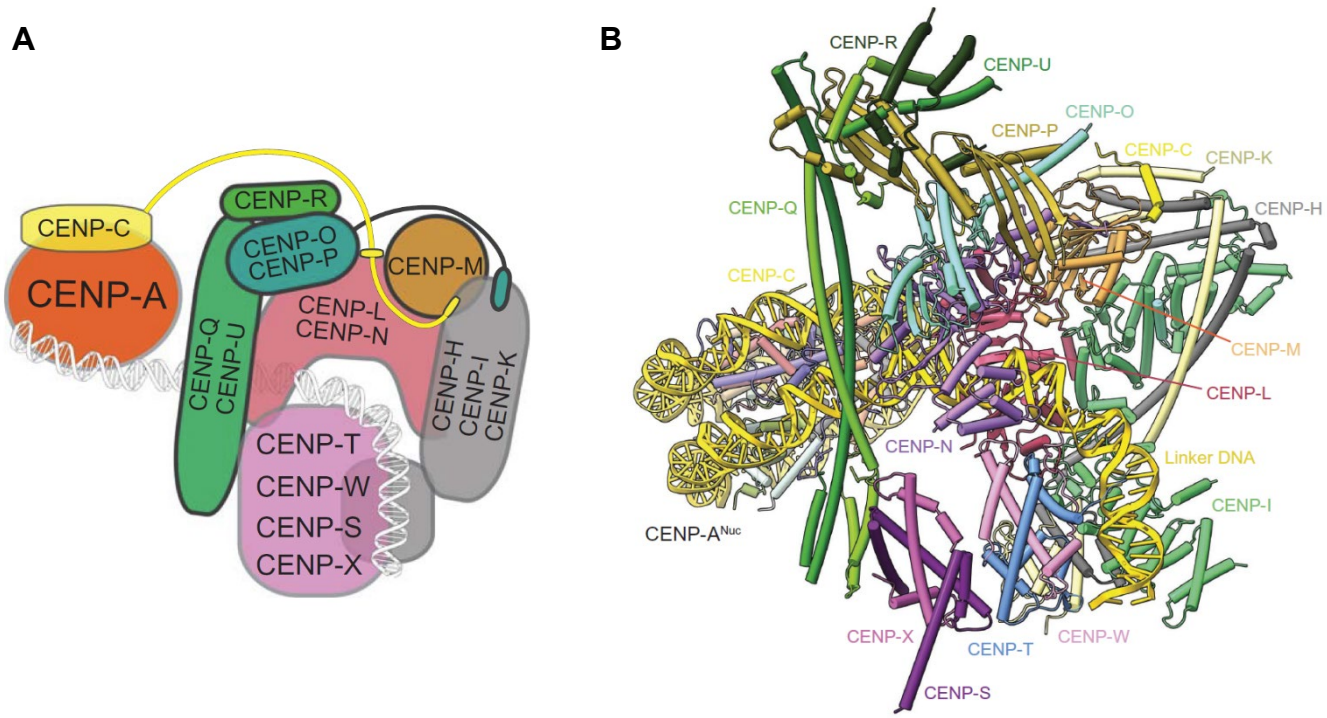


Figure 6. (A) Schematic model of CCAN-CENP-A complex. (B) Protein model of CCAN-CENP-A complex. Adapted from Yatskevich et al., 2022.

3.3 The KMN network, linker between CCAN and microtubules

As mentioned above, the CCAN complex is present at the centromere throughout the entire cell cycle (Okada et al., 2006; Foltz et al., 2006; Cheeseman et al., 2008; Musacchio et al., 2017), whereas in metazoans, the outer kinetochore is assembled at centromeres only during mitosis (Cheeseman et al., 2004; Hori et al., 2008; McKinley et al., 2016). The outer kinetochore is composed of the central and evolutionarily conserved ten-subunit KMN network, which comprises three subcomplexes: MIS12 complex (Mis12, Dsn1, Nsl1, Pmf1), NDC80 complex (Ndc80, Nuf2, Spc24, Spc25), and KNL1 complex (Knl1, ZWINT), along with auxiliary microtubule-associated components such as the SKA complex (Figure 7). Within this architecture, the rod-shaped MIS12 complex (MIS12C) serves as a central interaction hub, directly binding to the RWD (RING finger, WD repeat, DEAD-like helicase) domains of Spc24–Spc25 from NDC80 complex (NDC80C) and Knl1 from KNL1 complex (KNL1C), thereby coordinating the microtubule-binding module (NDC80C) and the KNL1 complex (KNL1C), which serves as the primary platform for SAC signaling, within the KMN network (Dimitrova et al., 2016; Petrovic et al., 2016; Petrovic et al., 2014; Yatskevich et al., 2024). MIS12C constitutes one of the primary linkages between the KMN network and the inner kinetochore. At the base of the MIS12C stalk, two distinct head domains engage with linear motifs of the inner kinetochore proteins CENP-C and CENP-T (Dimitrova et al., 2016; Petrovic et al., 2016; Yatskevich et al., 2024; Takenoshita et al., 2024; Hara et al., 2018). Crystallographic studies of both human and yeast MIS12C have revealed that the N-terminal 45 amino acids of CENP-C interact with the head domain formed by Mis12 and Pmf1 (MIS12C Head-1), whereas the head domain formed by Dsn1 and Nsl1 (MIS12C Head-2) is positioned laterally relative to MIS12C Head-1 (Dimitrova et al., 2016; Petrovic et al., 2016) (Figure 7A-C). CENP-T engages MIS12C in a binding mode that is mutually exclusive with CENP-C–MIS12C interaction, and this binding requires CDK1-mediated phosphorylation of CENP-T (Takenoshita et al., 2024).

The NDC80C is the primary and essential force-coupling component of the kinetochore in nearly all eukaryotic organisms (Powers et al., 2009). It features an approximately 50-nanometer-long coiled-coil stalk that separates the calponin homology (CH) microtubule-binding domains of Ndc80–Nuf2 at one end from the

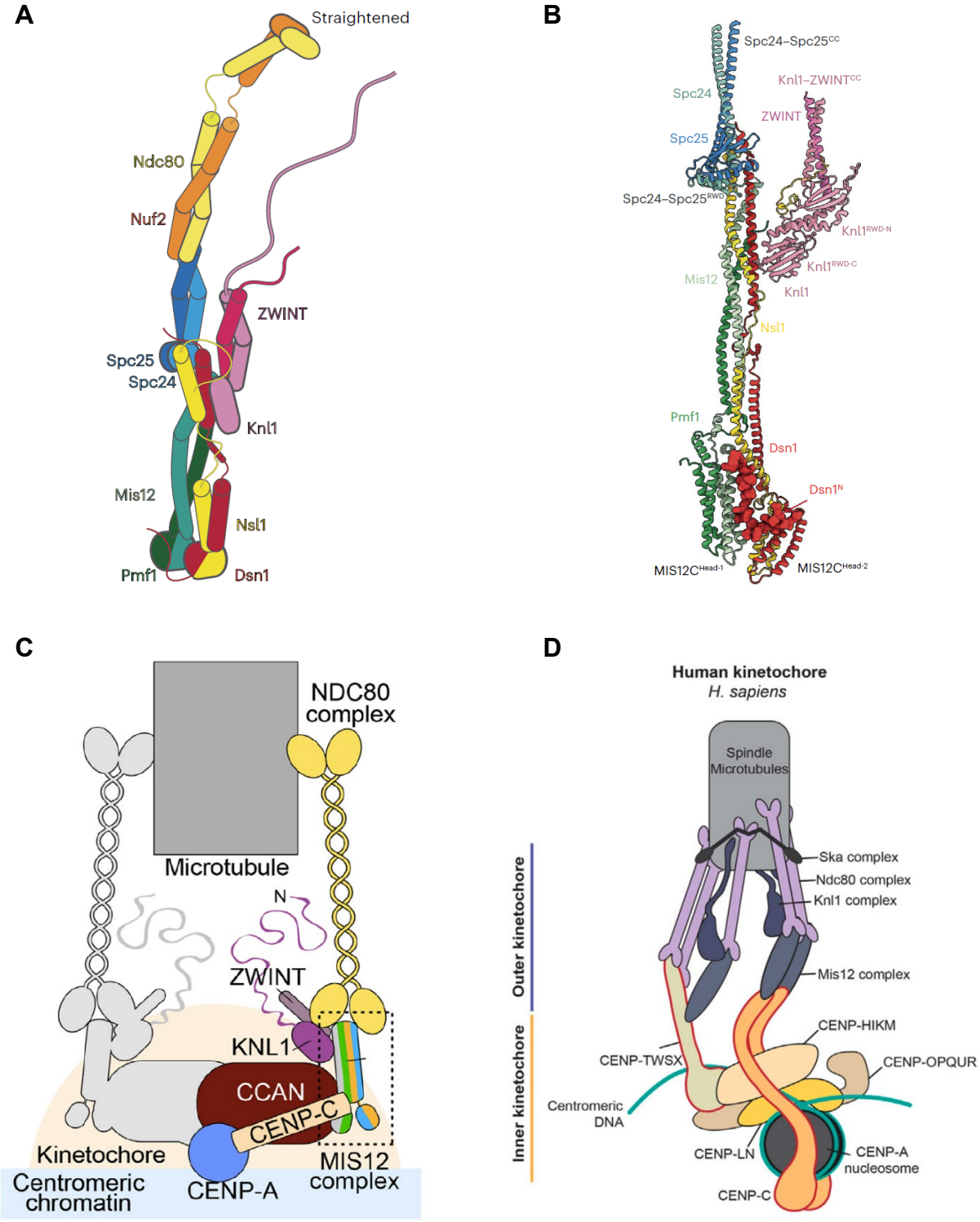


Figure 7. (A) Schematic model of KMN complex. (B) Protein model of KMN complex. Adapted from Yatskevich et al., 2024. (C) Schematic model of CENP-C-KMN network. Adapted from Petrovic et al., 2016. (D) Schematic model of CCAN-KMN network. Adapted from Sridhar et al., 2022.

Spc24–Spc25 domains that engage MIS12C at another end (Ciferri et al., 2008; DeLuca et al., 2006; Valverde et al., 2016). Multimerization of NDC80C enables it to bind and track both polymerizing and depolymerizing microtubules (Powers et al., 2009; Valverde et al., 2016), a function dependent on a conserved coiled-coil element known as the Ndc80 Loop, which interrupts the continuous Ndc80–Nuf2 coiled-coil (Maure et al., 2011; Polley et al., 2023). In addition to MIS12C-mediated recruitment, the CCAN component CENP-T can also recruit two copies of NDC80C independently via direct interactions with the Spc24–Spc25 RWD domains (Veld et al., 2016; Nishino et al., 2013) (Figure 7A-D).

Human Knl1 is a large protein comprising 2,342 amino acids and is predicted to be largely intrinsically disordered, and its only structured region resides at the carboxy terminus and includes an RWD domain and a predicted coiled-coil segment. The RWD domain of Knl1 is sufficient for its kinetochore localization (Petrovic et al., 2010; Yatskevich et al., 2024), while the coiled-coil region is necessary for recruiting its constitutive binding partner, ZWINT (Petrovic et al., 2010). Knl1 plays a pivotal role in SAC signaling through the recruitment of essential checkpoint proteins such as Bub1, BubR1, and Bub3 via multiple conserved motifs (Kiyomitsu et al., 2011; Shepperd et al., 2012). ZWINT also contributes to the recruitment of the ROD–Zwilch–ZW10 (RZZ) complex, which assembles the fibrous corona around unattached kinetochores and promotes checkpoint activation (Raisch et al., 2022). Moreover, the extreme N-terminal region of Knl1 exhibits microtubule-binding affinity, suggesting an additional role in stabilizing kinetochore–microtubule attachments (Roscioli et al., 2020; Yatskevich et al., 2024) (Figure 7A-D). Overall, KMN network functions as a linker to bridge the inner kinetochore CCAN with the microtubules (Figure 7D).

4. Kinetochore-Microtubule attachment, a stepwise process

The primary function of kinetochores is to mediate the capture of chromosomes by spindle microtubules during mitosis. This process involves two distinct modes of microtubule interaction: lateral and end-on attachments (Cheeseman et al., 2014; Monda et al., 2018). During lateral attachment, kinetochores are associated with the wall of microtubules and are translocated along the microtubule lattice. This movement

is facilitated by motor proteins, including the minus-end-directed Dynein and the plus-end-directed kinesin CENP-E (Monda et al., 2018; Maiato et al., 2017; Shrestha et al., 2013) (Figure 8A). These motor proteins facilitate the lateral attachment between chromosome and the wall of spindle microtubules during early prometaphase and contribute to subsequent chromosome movement. In addition, CENP-E can promote stabilization of end-on attachments to initiate chromosome congression (Vukušić et al.,

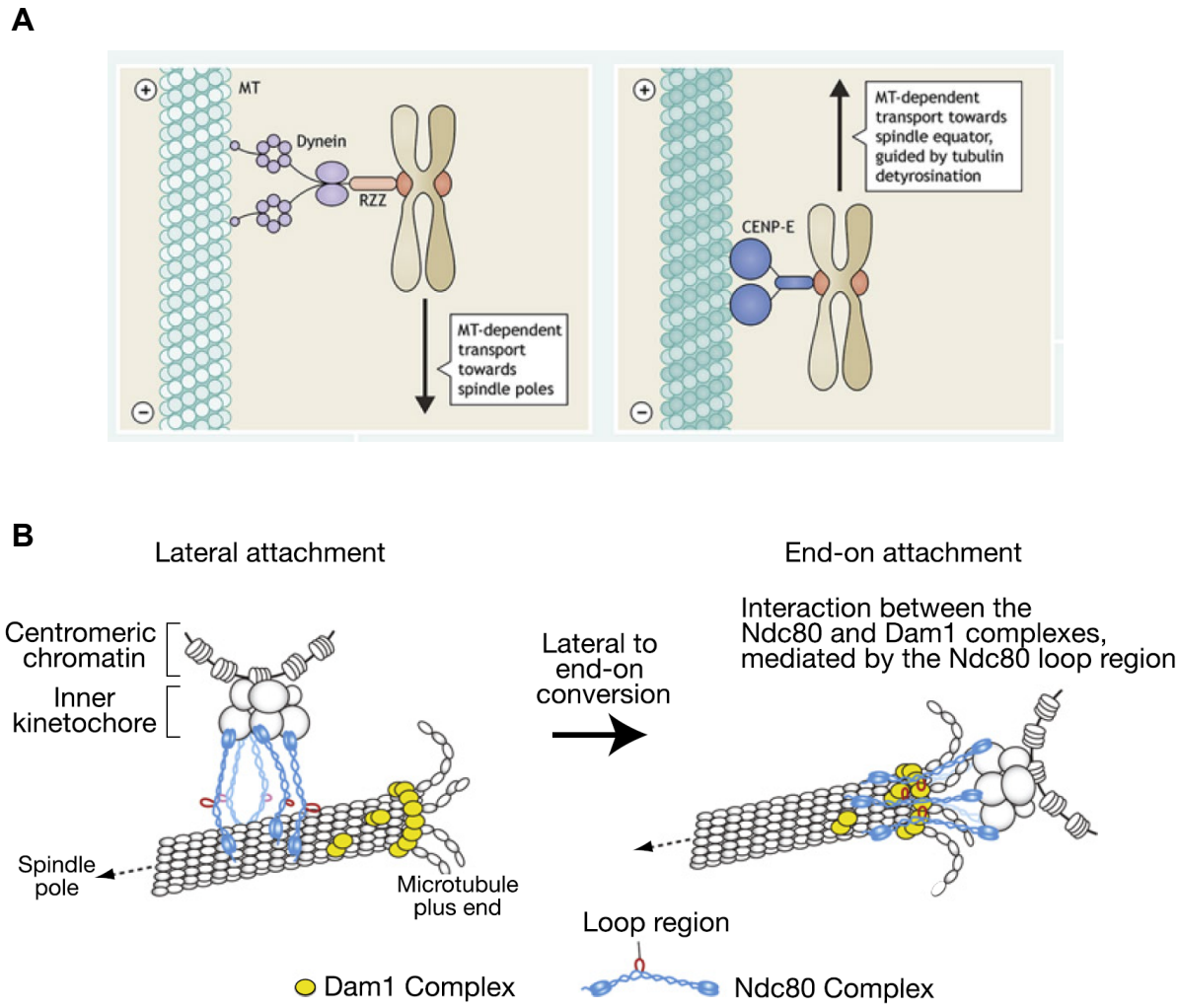


Figure 8. (A) Diagrams of motor-driven minus-end directed and plus-end directed kinetochore movement along the microtubule walls during early prometaphase. Adapted from Monda et al., 2018. (B) Schematic model of transition from kinetochore-microtubule lateral attachment to end-on attachment. Adapted from Maure et al., 2011.

2023).

Once kinetochores reach the plus ends of spindle microtubules, they establish a stable end-on attachment (Figure 8B). This configuration enables the kinetochore to harness dynamic microtubule forces—being pushed during polymerization and pulled during depolymerization (Monda et al., 2018; Joglekar et al., 2010; Zahm et al., 2024). End-on attachment is critical for the rapid and coordinated poleward movement of chromosomes during anaphase. In vitro reconstitution studies of kinetochore–microtubule interactions have been instrumental in elucidating how these attachments generate directional forces, thus advancing our understanding of the unique mechanical properties conferred by end-on binding (Regt et al., 2022; Shrestha et al., 2013; Monda et al., 2018).

5. Chromosome congression, a prerequisite for the subsequent mitotic events

Precisely at the onset of mitosis, following the breakdown of the nuclear envelope, all chromosomes begin to align at the spindle equator—the midpoint between the two spindle poles. This migratory process is known as chromosome congression. In mammalian cells, chromosome congression depends on the coordinated activity of both motor-dependent and motor-independent mechanisms, which are governed by the establishment of either lateral or end-on kinetochore–microtubule interactions. Consequently, any perturbation that disrupts microtubule dynamics or kinetochore functionality is likely to impair the congression of at least a subset of chromosomes during mitosis. More than 100 proteins have been reported to participate in chromosome congression (Maiato et al., 2017), including core kinetochore components and members of various motor protein families. Chromosome congression is regulated by a complex and highly coordinated network of these numerous factors that operate in parallel. For instance, during early prometaphase, the motor proteins Dynein and Centromere Protein E (CENP-E) mediate the lateral transport of peripheral chromosomes along microtubules—initially moving them toward the spindle poles and subsequently directing them toward the equator (Barisic et al., 2014; Shrestha et al., 2013; Vukusic et al., 2022) (Figure 9A). In addition, CENP-E can also directly promote microtubule chromosome end-on conversion and

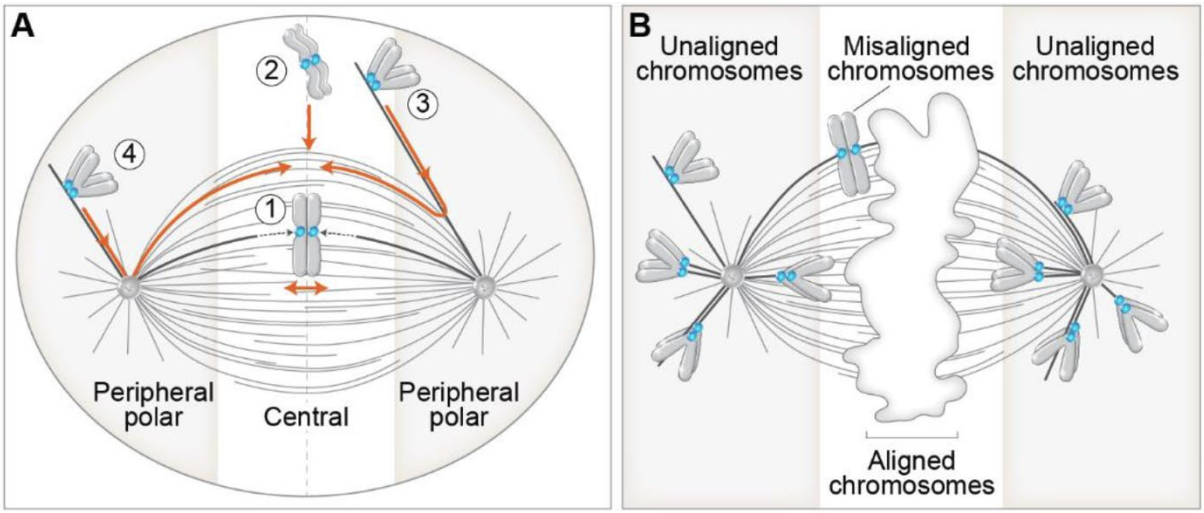


Figure 9. (A) Model of peripheral chromosome congression. Laterally attached peripheral chromosomes are transported along the microtubule wall, initially moving toward the spindle poles and subsequently congressing toward the spindle equator. (B) Both unaligned and misaligned chromosomes must be congressed to the spindle equator to ensure proper chromosome segregation during subsequent mitotic progression. Adapted from Vukusic et al., 2022.

biorientation, independently of its gliding activity (Vukušić et al., 2023).

In addition to these key components, a wide array of other proteins also contributes to chromosome congression. Some facilitate lateral kinetochore–microtubule attachments, while others function to stabilize spindle microtubules. Elucidating the precise roles of these proteins in chromosome congression remains a significant challenge for the field of mitotic research. Moreover, the architecture of the mitotic spindle itself, along with the forces it generates, plays a crucial role in promoting efficient chromosome congression. Importantly, the fidelity of this process is essential for preventing unstable or erroneous kinetochore–microtubule attachments and the resulting unaligned or misaligned chromosomes (Figure 9B). Such chromosomes are particularly vulnerable near the spindle poles, where elevated Aurora A kinase activity promotes phosphorylation of NDC80C (among other substrates), thereby reducing its microtubule-binding affinity and destabilizing attachments (Barisic et al., 2014; Ye et al., 2015).

6. Microtubule dynamics critically influence stable kinetochore–microtubule attachment

During mitosis, microtubules (MTs) assemble into a macromolecular structure known as the mitotic spindle, which ensures the accurate segregation of chromosomes into two daughter cells. Even subtle alterations in microtubule dynamics during spindle assembly can result in chromosome mis-segregation, chromosomal instability, and aneuploidy. Microtubules are highly dynamic polymers composed of α/β-tubulin dimers, and they undergo continuous phases of growth and shrinkage—a behavior termed dynamic instability (Burbank et al., 2006). This dynamic turnover of microtubules within the mitotic spindle is remarkably rapid. The regulation of microtubule dynamics is influenced by multiple factors, including the proximity of chromatin, the association with microtubule end-binding proteins, the spatial distribution of regulatory proteins, and the process of kinetochore capture. Numerous proteins modulate MT dynamics during both interphase and mitosis. Among these regulators, the Kinesin-8 family of motor proteins is evolutionarily conserved and has been shown to function both as plus-end-directed motors and as microtubule depolymerases (Gupta et al., 2006;

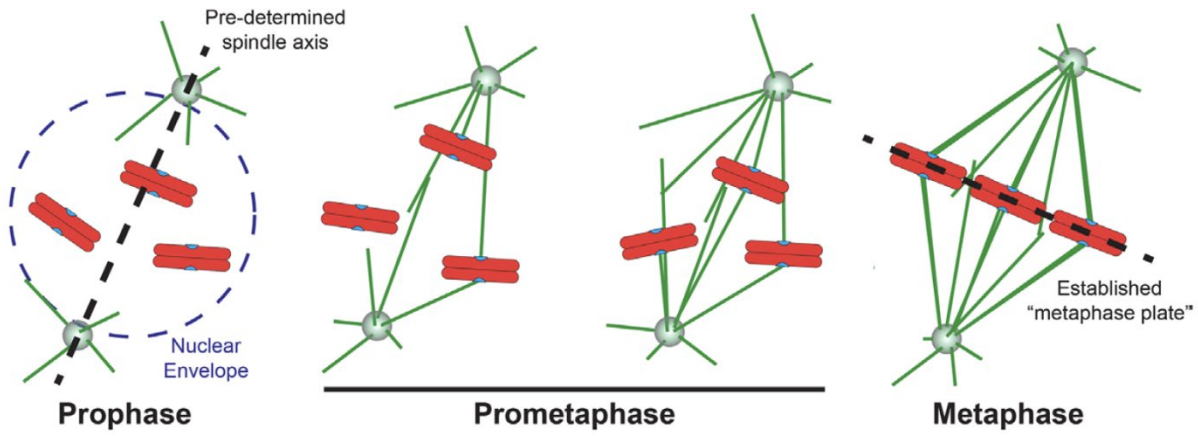


Figure 10. Fine-tuned microtubule dynamics is critical for accurate cell division. It not only facilitates efficient kinetochore–microtubule attachment during early prometaphase but also ensures the subsequent chromosome alignment. Adapted from Verma et al., 2022.

Stumpff et al., 2008; Mayr et al., 2007). Although KIF18A, a member of the Kinesin-8 family, was initially described as a microtubule depolymerase, subsequent studies indicate that it primarily suppresses microtubule growth by capping MT plus-ends (Du et al., 2010; Stumpff et al., 2008). Loss of Kinesin-8 function typically leads to abnormally long microtubules (Garcia et al., 2002; West et al., 2002; Mayr et al., 2007; Stumpff et al., 2008) and increased microtubule dynamics (Varga et al., 2006; Stumpff et al., 2008; Du et al., 2010). This, in turn, compromises the stability of kinetochore–microtubule attachments and disrupts proper chromosome alignment during mitosis (Mayr et al., 2007; Stumpff et al., 2008). The stability of microtubules is critical for accurate cell division. It does not only facilitate efficient kinetochore–microtubule attachment during early prometaphase but also ensures the subsequent stabilization of these attachments, which is essential for proper chromosome alignment and segregation (Figure 10).

Key questions and purpose of this study

The cell division process is a highly coordinated biological event that involves numerous molecular players and proceeds through a series of sequential, stepwise processes. Each phase is tightly regulated to ensure the fidelity of chromosome segregation and successful completion of mitosis. This leads me to an important consideration: since the cell must ensure that cell division proceeds in a stable and orderly manner, it raises the question of whether the cell has evolved multiple fail-safe mechanisms to safeguard this process. In other words, given the large number of proteins involved in mitosis, it is plausible that the cell employs redundant pathways as a form of molecular insurance to maintain the fidelity of division even when certain components are compromised. As I mentioned in the introduction section, the Constitutive Centromere-Associated Network (CCAN) is a key structural component of the kinetochore, playing a central role in establishing and maintaining stable kinetochore–microtubule attachments. In principle, each component of the CCAN should be essential for proper cell division, given its critical contribution to maintain chromosome segregation fidelity. However, unexpected experimental findings on one of the essential CCAN components—Centromere Protein C (CENP-C), suggested the existence of potential redundant pathways that may partially compensate for its functions in cell division.

CENP-C has multi-domains that mediate its various functions via interaction with various components within the kinetochore. The CENP-C binding proteins include CENP-A, the CCAN, and the KMN network (Przewloka et al., 2011; Screpanti et al., 2011; Dimitrova et al., 2016; Petrovic et al., 2016) (Figure 11A). In human cells, CENP-C associates with the CENP-A nucleosome via its central domain and the CENP-C motif (Kato et al., 2013; Watanabe et al., 2019). Additionally, the N-terminal domain of CENP-C mediates its interaction with the KMN network, linking the inner kinetochore to outer kinetochore components. Although these domains have long been considered critical for the functional activity of CENP-C within the kinetochore, my lab's previous study using CENP-C domain deletion mutant found that CENP-C-MIS12C interaction and CENP-C motif-CENP-A interaction are both dispensable for mitotic progression and cell viability in human, mouse, and chicken cells (Figure 11C and 11D) (Hara et al., 2018; Watanabe et al., 2019).

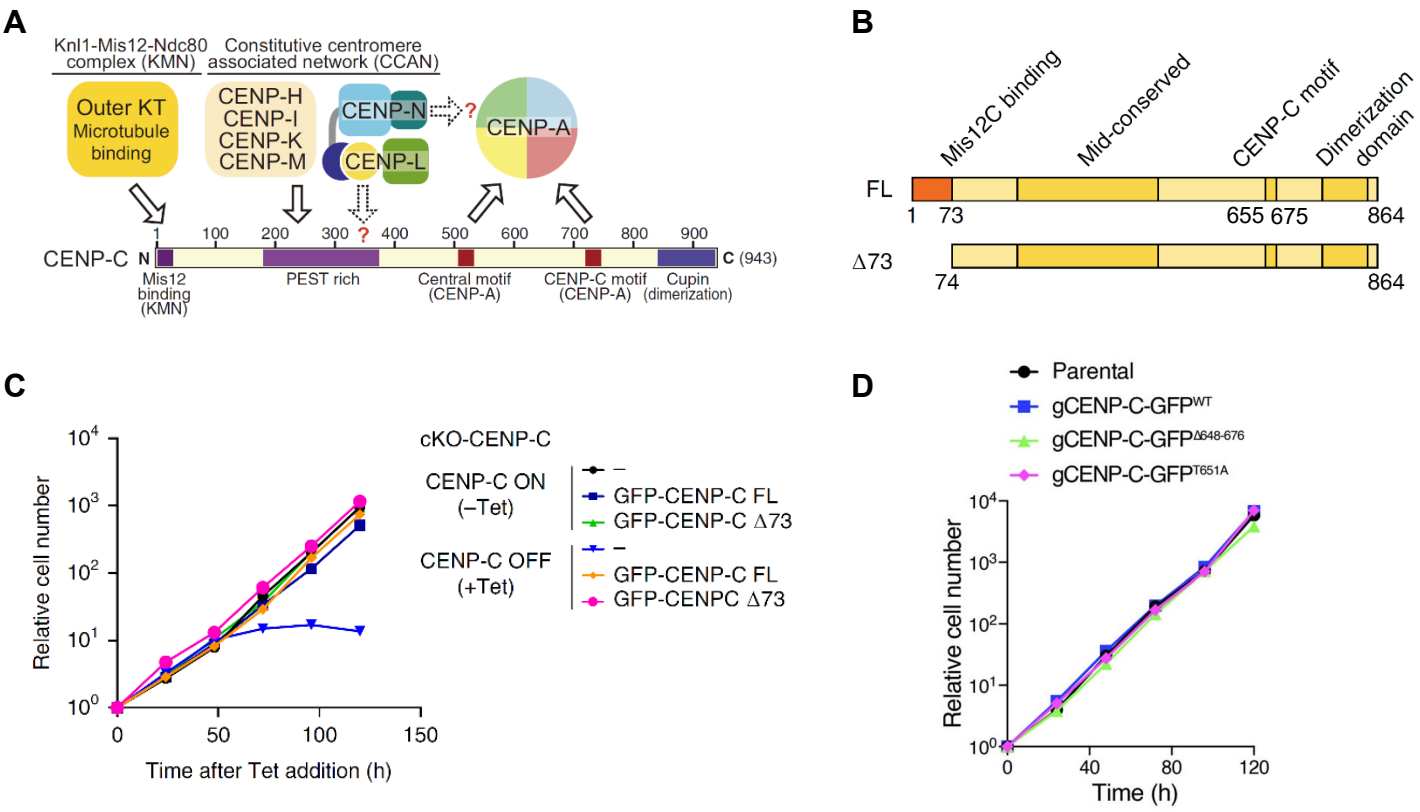


Figure 11. (A) Schematic model of human CENP-C protein, CENP-C binds to CENP-A, the CCAN, and the KMN network. Adapted from Pentakota et al., 2017. (B) Schematic model of chicken CENP-C protein. (C) Cell growth of CENP-C FL and CENP-C Δ73 in chicken DT40 cells. Adapted from Hara et al., 2018. (D) Cell growth of CENP-C WT and CENP-C Δ648-676 in chicken DT40 cells. Adapted from Watanabe et al., 2019.

In chicken DT40 cells, expression of a CENP-C mutant deleting the N-terminal domain can rescue the CENP-C knockout phenotype and cell growth is completely comparable with wild-type (WT) cells (Hara et al., 2018) (Figure 11C). This indicates that CENP-C-Mis12C interaction is dispensable for mitotic progression and cell viability in chicken cells. In addition, another work in my lab confirmed this result by using mouse MEF cells and human RPE-1 cells (Kong et al., 2024). My lab also demonstrated that deletion of CENP-C motif (CENP-A binding domain) is also dispensable for cell viability in chicken and human cells (Watanabe et al., 2019)

(Figure 11D).

All these results were unexpected, as the main function of CENP-C has long been considered to act as a linker within the kinetochore. However, my laboratory demonstrated that another linker protein, CENP-T, can compensate for this role (Hara et al., 2018; Takenoshita et al., 2024), providing an explanation for why cells lacking the CENP-C linker function remain viable. Notably, both the C-terminus and N-terminus of CENP-C are highly conserved among different species, suggesting that these domains may participate in other, as yet unidentified, kinetochore functions. Since these domains are dispensable for mitotic progression, it is plausible that other factors compensate for such hidden functions of CENP-C. If this is the case, what are these hidden functions, and which factors are involved? To address these questions, I utilized CENP-C mutants lacking either the N-terminus or C-terminus to identify factors whose depletion would cause synthetic lethality in the absence of these domains. The aim of this study is to identify such factors, as their characterization would provide new insights into the complex and redundant pathways that safeguard chromosome segregation.

Results

Chapter 1

Functional genetics with CENP-C ΔM12BD mutant reveals a regulatory system for chromosome congression

1. Characterization of K562 CENP-C ΔM12BD cells

1.1 Generation of CENP-C ΔM12BD K562 cell line

CENP-C N-terminal region binds to Mis12C (Mis12C-binding domain: M12BD; Figure 12) (Przewloka et al., 2011; Screpanti et al., 2011; Dimitrova et al., 2016; Petrovic et al., 2016; Hara et al., 2018). And my lab previously found that M12BD is dispensable for the proliferation in chicken DT40 cells, mice and human RPE-1 cells (Hara et al., 2018; Kong et al., 2024).

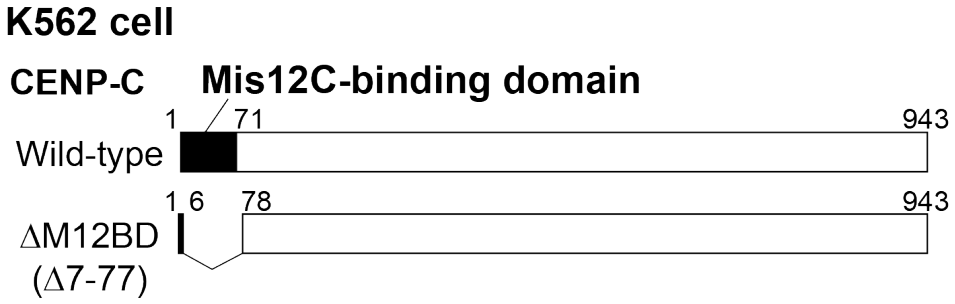
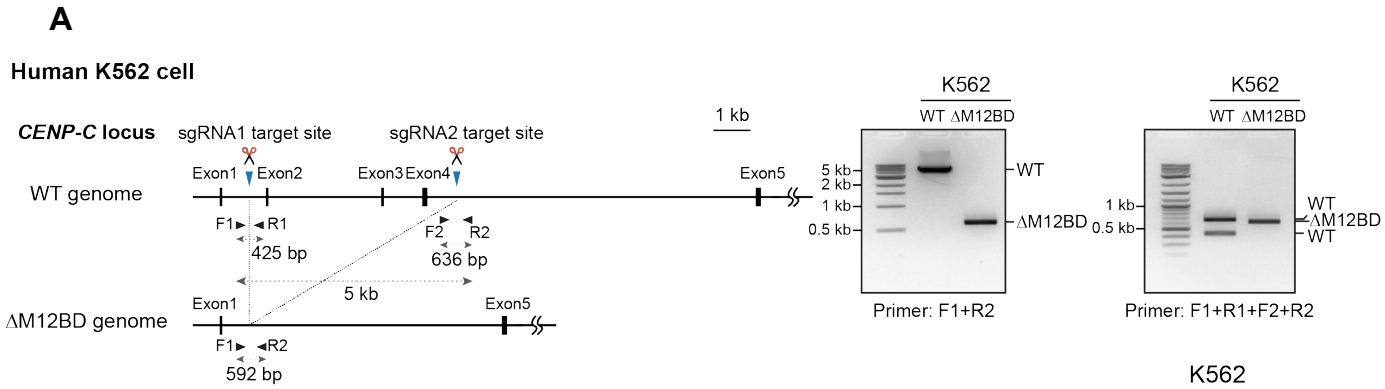
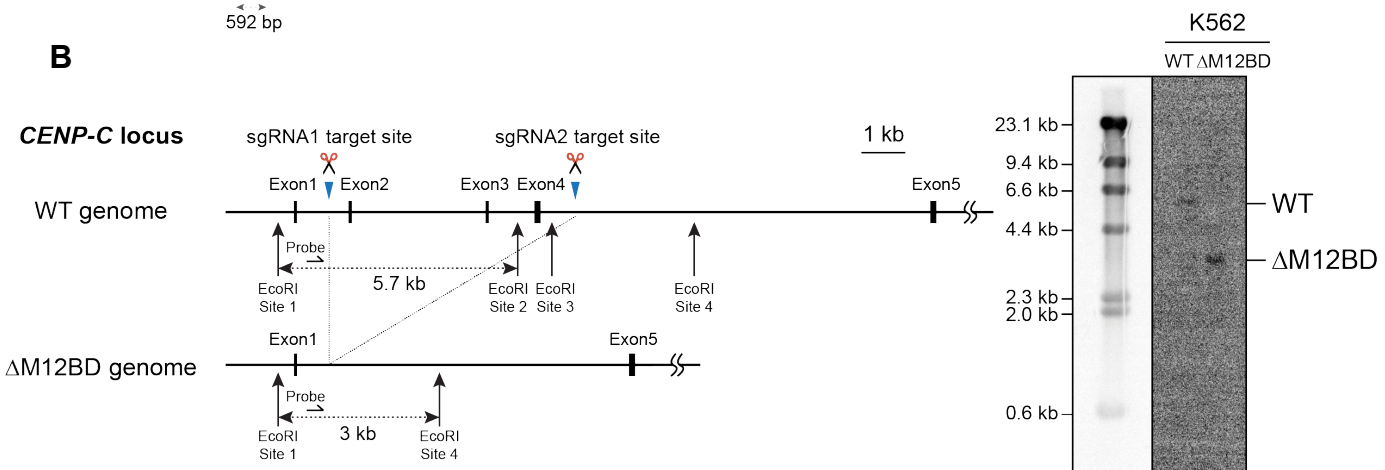
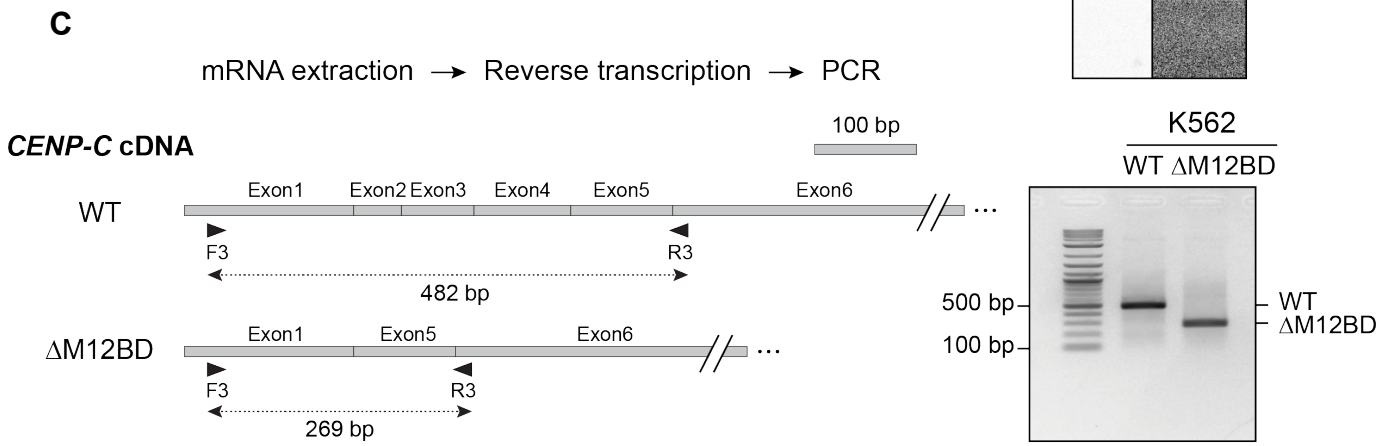


Figure 12. Schematic model of human CENP-C Wild-type and ΔM12BD.

I tried to identify genes that exhibit synthetic lethality with the CENP-C M12BD mutation by a genome-wide CRISPR screening. After that, I attempted to figure out why and how these genes can be related to the CENP-C pathway. As the CRISPR screening was well established by using human K562 cells (Wang et al., 2014; Su et al., 2025), I firstly generated mutant K562 cells deleting CENP-C M12BD (Figure 12).


A
Human K562 cell
CENP-C locus
sgRNA1 target site
sgRNA2 target site
WT genome
Exon1
Exon2
Exon3
Exon4
Exon5
F1
R1
F2
R2
425 bp
636 bp
5 kb
ΔM12BD genome
592 bp
1 kb
K562
WT ΔM12BD
5 kb
2 kb
1 kb
0.5 kb
WT
ΔM12BD
Primer: F1+R2
Primer: F1+R1+F2+R2


B
CENP-C locus
sgRNA1 target site
sgRNA2 target site
1 kb
WT genome
Probe
EcoRI Site 1
5.7 kb
EcoRI Site 2
EcoRI Site 3
EcoRI Site 4
ΔM12BD genome
3 kb
K562
WT ΔM12BD
23.1 kb
9.4 kb
6.6 kb
4.4 kb
2.3 kb
2.0 kb
0.6 kb
WT
ΔM12BD


C
mRNA extraction → Reverse transcription → PCR
CENP-C cDNA
100 bp
WT
Exon1
Exon2
Exon3
Exon4
Exon5
Exon6
F3
R3
482 bp
ΔM12BD
269 bp
K562
WT ΔM12BD
500 bp
100 bp
WT
ΔM12BD

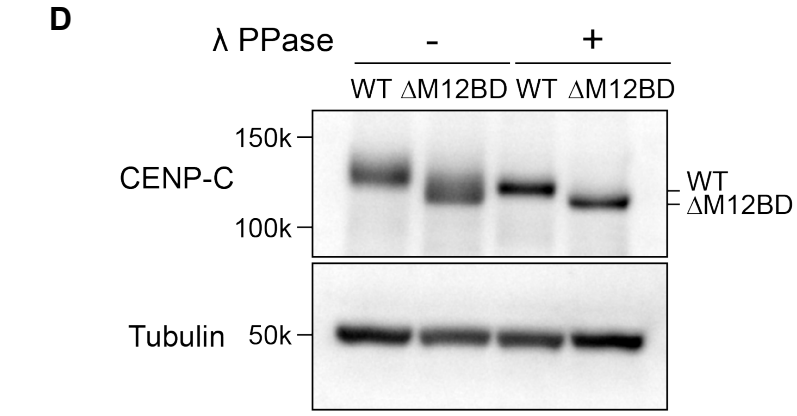

D
λ PPase
-
+
WT ΔM12BD WT ΔM12BD
150k
CENP-C
100k
WT
ΔM12BD
Tubulin
50k

Figure 13. Generation of K562 CENP-C ΔM12BD cells.

(A) Schematic representation of the exon 2-4 deletion from human CENP-C gene locus in K562 cells. Using the CRISPR-Cas9 system with two sgRNAs, the exon 2-4 is deleted to generate K562 CENP-C ΔM12BD cells. The position of sgRNAs and PCR primers for genotyping PCR are shown. The amplicon sizes are 425 bp (F1+R1) in K562 WT cells, 636 bp (F2+R2) in K562 WT cells, 592 bp (F1+R2) in K562 CENP-C ΔM12BD cells. Results of genotyping PCR with K562 WT and CENP-C ΔM12BD cells are shown.

(B) Design for Southern blot analysis to detect a deletion of the exon 2-4 at the CENP-C gene locus in K562 CENP-C ΔM12BD cells. EcoRI sites and the probe are shown. Purified genomic DNA from K562 WT or CENP-C ΔM12BD cells was digested with EcoRI and run on an agarose gel. The DNA fragments on the gel were transferred to the nylon membrane and hybridized with the indicated probe.

(C) RT-PCR to examine the expression and exon 2-4 deletion of mRNA for wildtype (WT) CENP-C and CENP-C ΔM12BD in K562 cells.

(D) Immunoblot analysis to detect WT CENP-C and CENP-C ΔM12BD in each cell line. α-tubulin was probed as a loading control. As CENP-C is highly phosphorylated, CENP-C band was smeared. To detect the CENP-C protein band, λPPase was used to dephosphorylate proteins.

Using the CRISPR/Cas9 based genome editing, I designed 2 gRNAs which target genomic sequence near exon2 and exon4 in human *CENP-C* gene locus in order to delete exons 2-4 from endogenous human *CENP-C* gene locus. *CENP-C* exon2-4 encodes aa 7-77 (Figure 12 and 13A), their deletion removed most part of the M12BD (CENP-C ΔM12BD; Figure 12 and 13A) (Screpanti et al., 2011; Petrovic et al., 2016) and I confirmed CENP-C M12BD deletion was successfully established in human K562 cells by checking with a genomic PCR, southern blot analysis, RT-PCR and immunoblot analysis (CENP-C ΔM12BD K562 cells; Figure 13B-13D).

For genomic PCR, I designed 4 primers (F1, R1, F2, R2) to check the

endogenous *CENP-C* allele. When I use a primer set of F1+R2, the PCR product size from the *CENP-C* WT allele is 5326 bp, and PCR product size from the *CENP-C* ΔM12BD allele is 592 bp. When I use primer sets for F1+R1+F2+R2, the PCR product sizes from *CENP-C* WT allele are 425 bp and 636 bp, meanwhile the PCR product size from *CENP-C* ΔM12BD allele is still 592 bp. I confirmed that CENP-C WT and CENP-C ΔM12BD both showed correct size of PCR band signal (Figure 13A).

For Southern blot analysis, EcoRI was used to digest genomic DNA, and I designed a 606 bp size probe to hybridize with digested DNA fragment. The hybridized signal can be detected by chemiluminescence. For *CENP-C* WT allele, the band size detected by the Southern blot is expected to be about 5.7 kb, and for *CENP-C* ΔM12BD allele, the band size is expected to be about 3 kb. I confirmed that CENP-C WT and CENP-C ΔM12BD both showed correct size of Southern blot band signal (Figure 13B).

For RT-PCR, mRNA of CENP-C WT and CENP-C ΔM12BD cells were extracted by the TRIzol Reagent. Using the isolated total RNA, *CENP-C* cDNA was reverse transcribed using SuperScript IV Reverse Transcriptase (Thermo Fisher Scientific), then cDNA was applied for PCR to examine the exon 2-4 deletion. The product size for the RT-PCR from CENP-C WT cells is 482 bp, and that of CENP-C ΔM12BD cells is 269 bp. I confirmed that CENP-C WT and CENP-C ΔM12BD both showed correct size of RT-PCR band signal (Figure 13C).

Human CENP-C is a highly phosphorylated protein. For immunoblot analysis to detect CENP-C WT and CENP-C ΔM12BD protein size, proteins in cell lysates were dephosphorylated by Lambda Protein Phosphatase in order to detect clear CENP-C signals. Expected immunoblot protein size of CENP-C WT is about 110 kDa, and smaller size of CENP-C protein band can be detected in CENP-C ΔM12BD by this immunoblot analysis. I confirmed that CENP-C WT and CENP-C ΔM12BD sample both showed correct size of immunoblot protein band signal (Figure 13D).

1.2 Mis12C-binding domain of CENP-C is dispensable for cell growth in human K562 cells

Consistent with the results of human CENP-C ΔM12BD RPE-1 cells (Kong et al., 2024),

CENP-C ΔM12BD K562 cells comparably grew like wild-type (WT) K562 cells (Figure 14), indicating that CENP-C M12BD is dispensable for cell growth in human K562 cells.

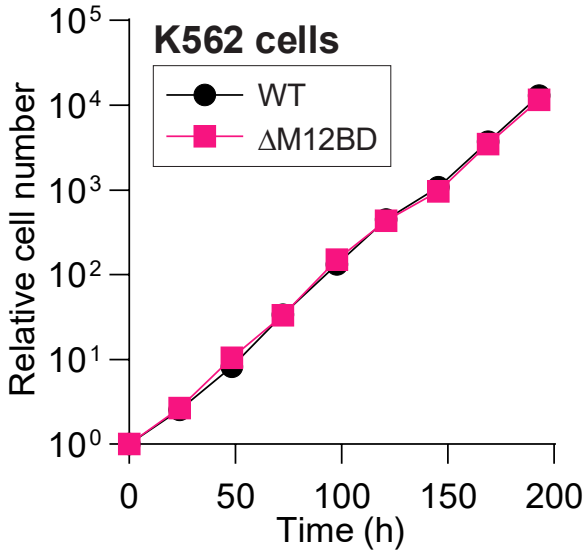


Figure 14. The growth curve of K562 WT or CENP-C ΔM12BD cells. The cell numbers were normalized to those at time 0 of each cell line.

1.3 CENP-C ΔM12BD reduces recruitment of KMN network during mitosis

I examined the levels of CCAN and KMN proteins on mitotic kinetochores in CENP-C ΔM12BD and CENP-C WT K562 cells. CENP-C and CENP-T levels at kinetochores in CENP-C ΔM12BD K562 cells were similar to those in CENP-C WT K562 cells (Figure 15). By contrast, DSN1 (a subunit of Mis12 complex), KNL1 (a subunit of KNL1 complex), and Hec1 (a subunit of Ndc80 complex) levels at kinetochores in CENP-C ΔM12BD K562 cells were significantly reduced in mitotic cells, compared with those in CENP-C WT K562 mitotic cells (Figure 15A-E). As observed in RPE-1 cells, these localization results in K562 cells were expected (Kong et al., 2024).

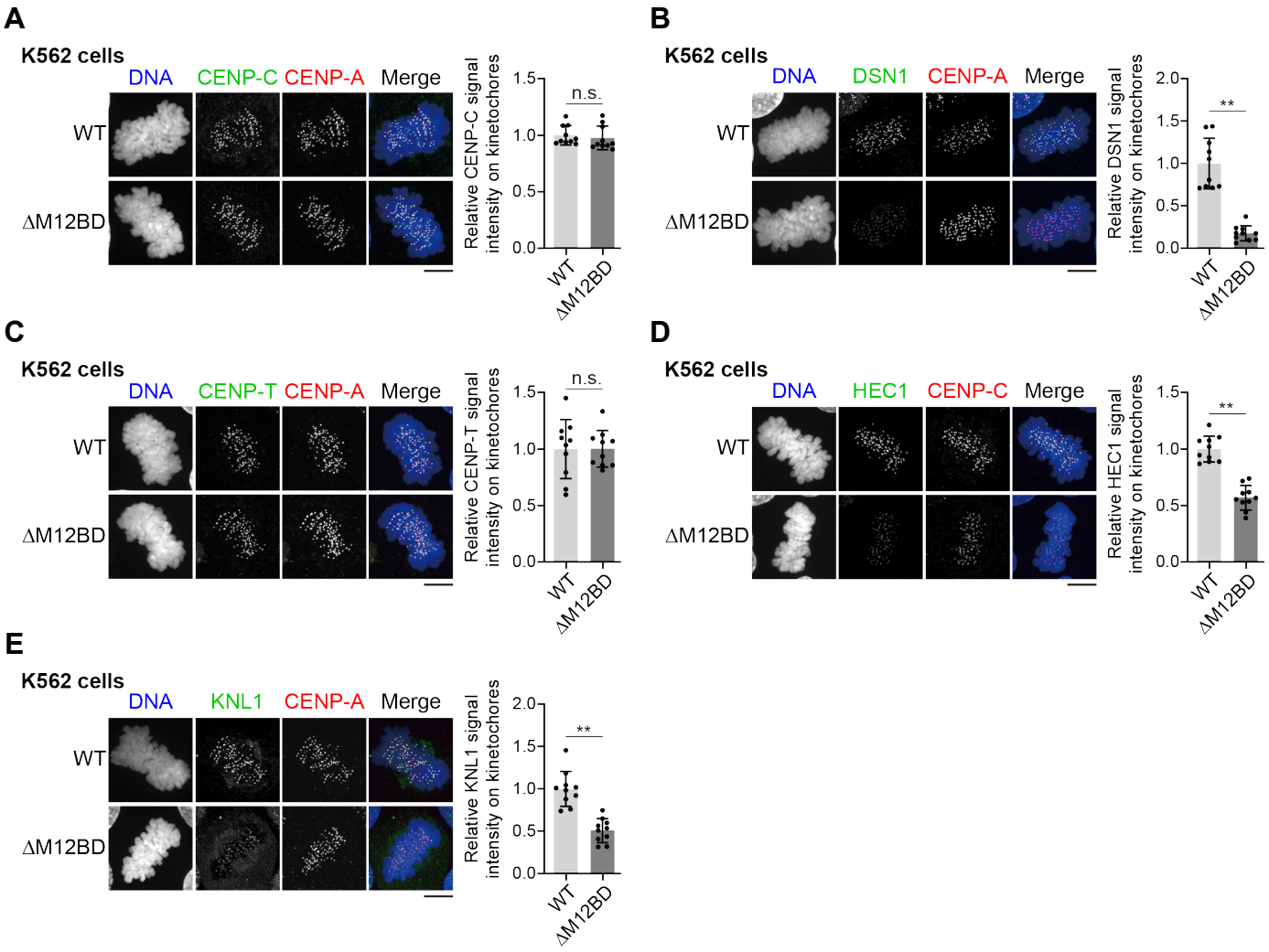


Figure 15. Immunofluorescence characterization of K562 CENP-C ΔM12BD cells. (A) CENP-C, (B) DSN1, (C) CENP-T, (D) HEC1 and (E) KNL1 localization in K562 WT or CENP-C ΔM12BD cells. Each protein was stained with an antibody against the target protein (green). CENP-A was stained as a kinetochore marker (red) except for HEC1 staining. For HEC1 staining, CENP-C was stained as a kinetochore marker (red). DNA was stained with DAPI (blue). Scale bar, 10 μm. Signal intensities of target protein on mitotic kinetochores were quantified (Mean and SD, two-tailed Student's t-test, K562 WT cells: n = 10 cells, K562 CENP-C ΔM12BD cells: n = 10 cells; n.s., non-significant; $^{**}p < 0.01$).

1.4 CENP-C ΔM12BD shows subtle mitotic defects like unaligned chromosomes and increased micronuclei

I examined mitotic progression of CENP-C ΔM12BD cells and observed that these cells show subtle mitotic defects with the following experiments. For the chromosome misalignment assay, I first treated CENP-C WT and ΔM12BD cells with 50 μM monastrol. Monastrol is a reversible Eg5 inhibitor (Kapoor et al., 2000). Function of Eg5 is to separate two spindle poles, and monastrol treated cells will be arrested in early prometaphase with a monopolar spindle. After monastrol treatment for 2 h, cells were then washed with fresh medium and released from monastrol. Then, MG132 was added into the cells and treated for 1 h before immunofluorescence fixation. MG132 is a proteasome inhibitor, during mitosis, treatment of this chemical can inhibit degradation of securin, then inactivate separase, as a result, cohesin cannot be cleaved, subsequently sister chromatid cannot be separated (Uhlmann et al., 1999;

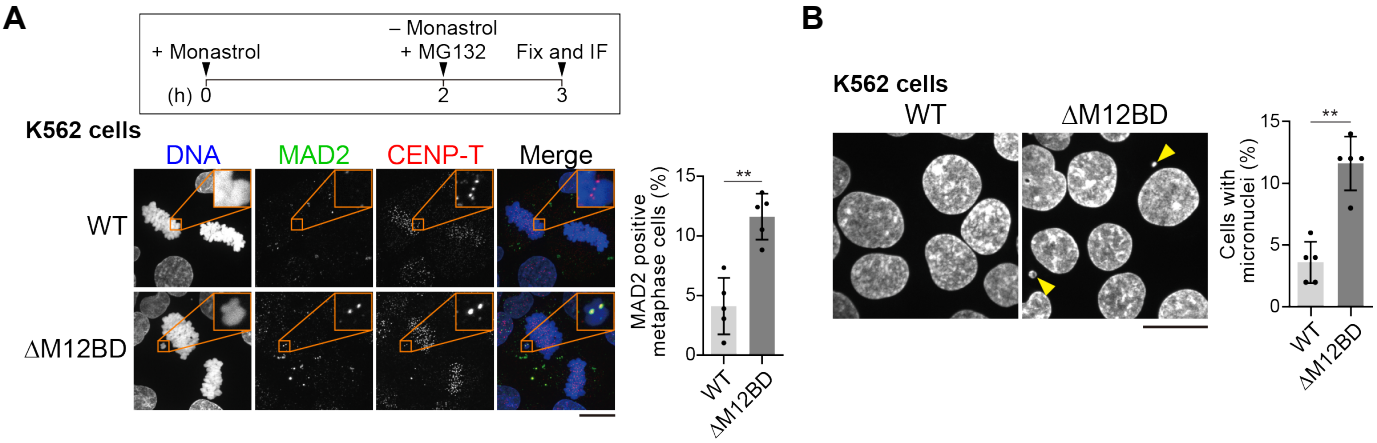


Figure 16. (A) MAD2 staining (green) in K562 WT or CENP-C ΔM12BD cells. Cells were treated with Monastrol for 2 h and after washout of Monastrol, cells were treated with MG132 to enrich mitotic cells. Cells with MAD2 positive chromosomes were counted (Mean and SEM, two-tailed Student's t-test, n = 5 experiments; $^{**}p < 0.01$). Scale bar, 20 μm. (B) Micronuclei observation in K562 WT or CENP-C ΔM12BD cells. Arrowheads show typical micronuclei. Cells with micronuclei were counted (Mean and SEM, two-tailed Student's t-test, n = 5 experiments; $^{**}p < 0.01$). Scale bar, 20 μm.

Kisselev et al., 2001; Waizenegger et al., 2002; Skoufias et al., 2007). Therefore, MG132 treatment arrests cells in metaphase. With this chromosome misalignment assay, I observed an increase of MAD2 positive cells in CENP-C ΔM12BD K562 cells (Figure 16A), MAD2 signal is a marker for detecting unattached kinetochore, this result indicates that CENP-C ΔM12BD cells do not exhibit stable kinetochore-microtubule interactions, compared to those in CENP-C WT cells.

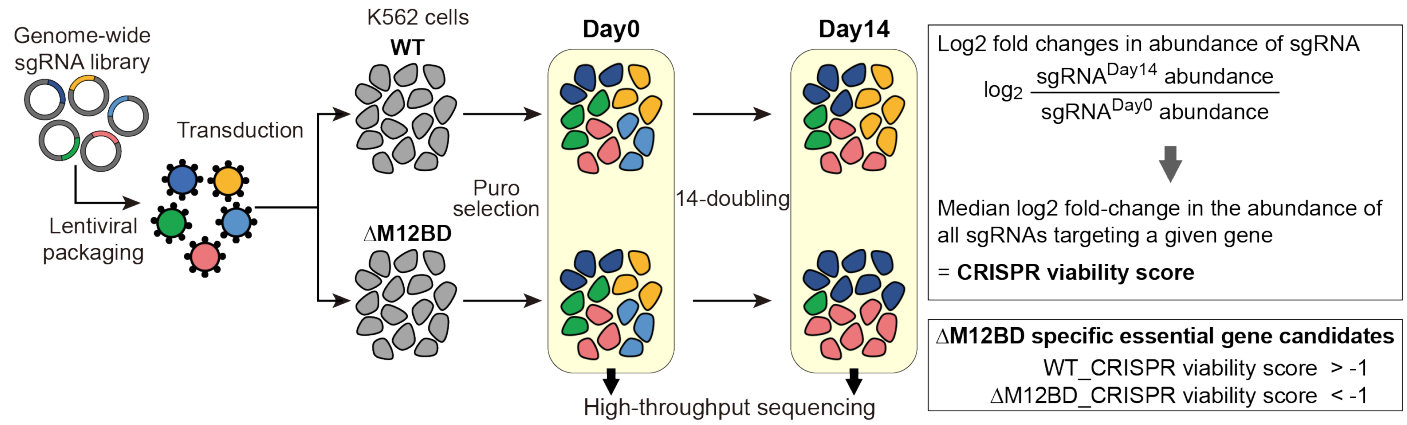
In addition, I also confirmed micronuclei formation was significantly increased in CENP-C ΔM12BD K562 cells (Figure 16B). These phenotypes are similar to those of CENP-C ΔM12BD RPE-1 cells (Kong et al., 2024). Importantly, as CENP-C ΔM12BD K562 cells grow comparably compared with wild-type K562 cells, thus this mutant cell line can be used for the further CRISPR screening analysis.

2. CRISPR screening and validation in K562 CENP-C ΔM12BD cells

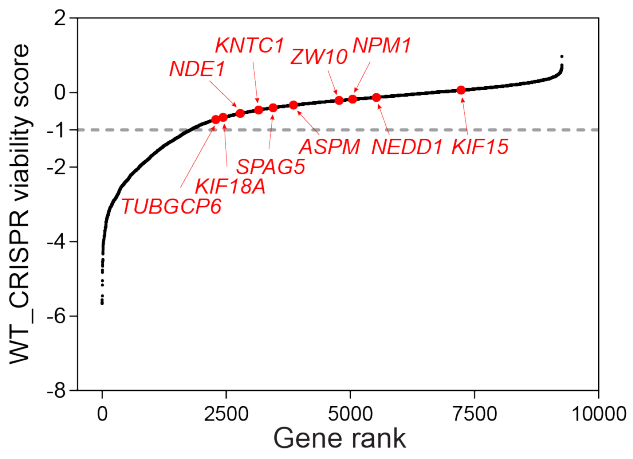
2.1 A genome-wide CRISPR/Cas9 screening identified genes whose knockouts exhibit synthetic lethality with the CENP-C ΔM12BD mutation

To identify hidden relationships within the CENP-C associated kinetochore network, we performed pooled genome-wide CRISPR/Cas9 screening in wild-type and CENP-C ΔM12BD K562 cells (Figure 17A), following previously described methods (Wang et al., 2014; Su et al., 2025). CENP-C WT or CENP-C ΔM12BD K562 cells were transduced with the lentivirus single guide RNA (sgRNA) knockout library targeting 18,663 genes and cultured for 14 population doublings (Figure 17A). Deep sequencing of the sgRNA representation allowed us to calculate a CRISPR viability score reflecting cell viability and proliferation change after sgRNA targeting for each gene (Figure 17A-

A



B



C

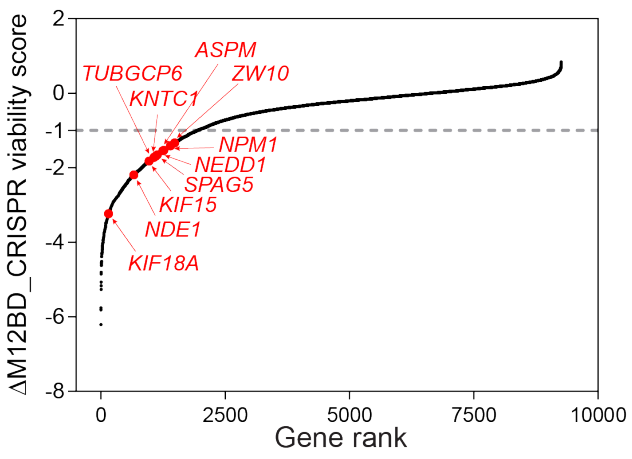


Figure 17. The CRISPR screening in K562 WT and CENP-C ΔM12BD cells.

(A) Schematic representation of the pooled CRISPR screening in K562 WT or CENP-C ΔM12BD cells. Using CRISPR viability scores, genes which are essential for cell growth in K562 CENP-C ΔM12BD cells but not in K562 WT cells were selected as candidates whose knockout showed synthetic lethality with CENP-C ΔM12BD.

(B) Distribution of CRISPR viability score of each gene in K562 WT cells. Gene with a median fold change (log2) > -1 was identified as a nonessential gene in K562 WT cells.

(C) Distribution of CRISPR viability score of each gene in K562 CENP-C ΔM12BD cells. Gene with a median fold change (log2) < -1 was identified as an essential gene in K562 CENP-C ΔM12BD cells.

17C). The CRISPR viability score was calculated by the log2 fold change in sgRNA abundance between Day 14 and Day 0. The negative viability score indicates that the knockout of the corresponding gene results in reduced cell viability, and the genes with scores less than –1 were defined as essential genes under a given growth condition.

Targeting of most genes resulted in similar overall fitness effects in wild-type or CENP-C ΔM12BD K562 cells (Figure 18A), with R^2 of 0.79 for K562 WT versus K562 CENP-C ΔM12BD cells (Figure 18A). However, a subset of gene knockouts displayed reduced viability scores in K562 CENP-C ΔM12BD cells compared to those in K562 WT cells (Figure 18A). This includes a total of 375 genes (Figure 18A; red dots). These 375 candidate genes were clarified as non-essential genes in K562 WT cells (Log2 fold change > –1) but essential in K562 CENP-C ΔM12BD cells (Log2 fold change < –1). Then these 375 candidate genes were preranked based on the magnitude of differences of log2 fold changes between K562 WT and CENP-C ΔM12BD cells, in descending order. Thereafter the preranked genes were analyzed with GSEA (Gene set enrichment analysis) version 4.2.3 (Broad Institute). Gene set enrichment analysis found that spindle pole, tubulin-binding, spindle, microtubule-binding, polymeric

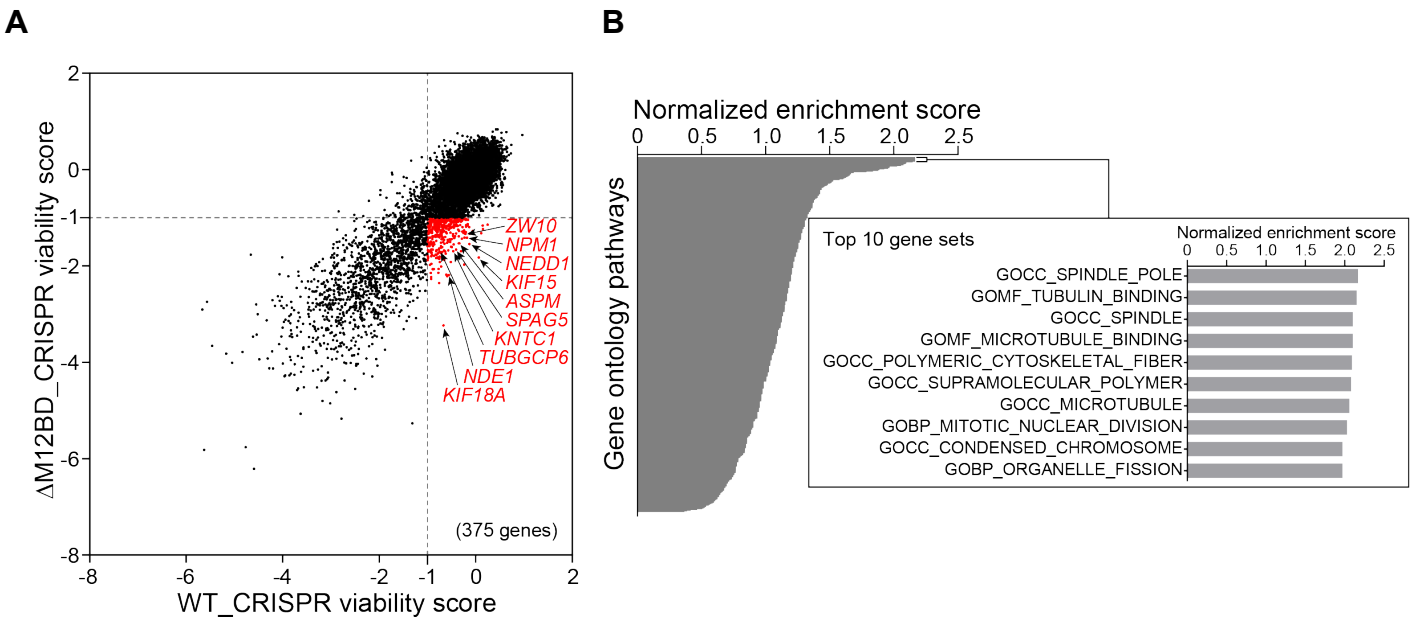


Figure 18. (A) Scatter plots showing the CRISPR viability score in K562 WT versus CENP-C ΔM12BD cell pools. Red dots are essential genes in K562 CENP-C ΔM12BD cells but not in K562 WT cells. (B) Gene set enrichment analysis (GSEA) for 375 candidate genes. The candidate genes were ranked by the magnitude of differences in CRISPR viability score between K562 WT and CENP-C ΔM12BD cells in descending order and applied to GSEA. The top 10 enriched gene sets were highlighted.

cytoskeletal fiber, supramolecular polymer, and microtubule-related gene sets were enriched amongst the depleted genes (Figure 18B). Several genes were commonly found in the leading edge gene list of top 6 enriched gene sets (Figures 18B, 19A-19F). Based on their relative viability scores in K562 WT and CENP-C ΔM12BD cells, I selected 10 genes for further validation: *KIF18A*, *KIF15*, *NDE1*, *NEDD1*, *SPAG5*, *NPM1*, *KNTC1*, *ASPM*, *ZW10*, and *TUBGCP6*.

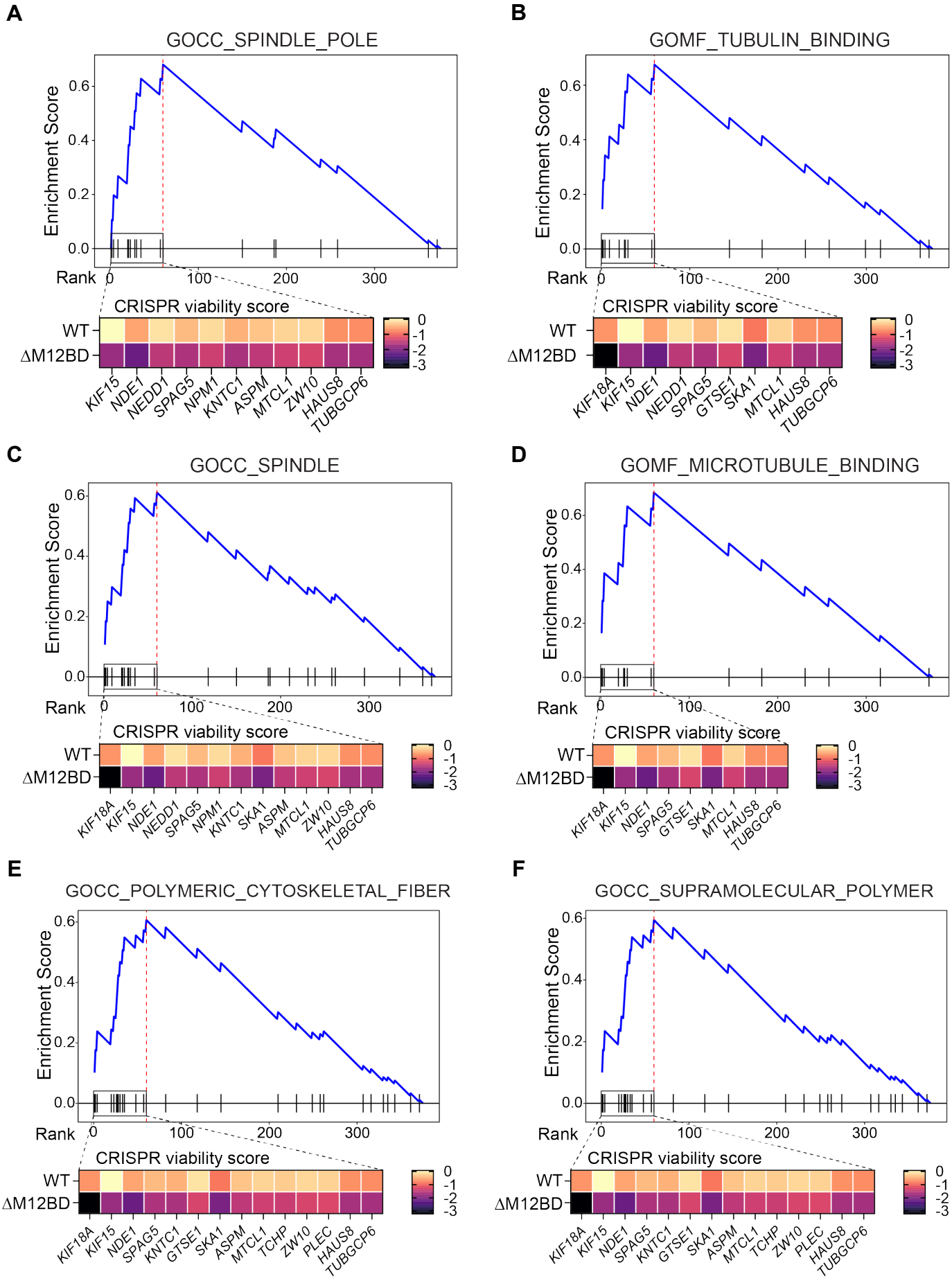

A
GOCC_SPINDLE_POLE
Enrichment Score
Rank
CRISPR viability score
WT
ΔM12BD
KIF15 NDE1 NEDD1 SPAG5 NPM1 KNTC1 ASPM MTCL1 ZW10 HAUS8 TUBGCP6
B
GOMF_TUBULIN_BINDING
KIF18A KIF15 NDE1 NEDD1 SPAG5 GTSE1 SKA1 MTCL1 HAUS8 TUBGCP6
C
GOCC_SPINDLE
KIF18A KIF15 NDE1 NEDD1 SPAG5 NPM1 KNTC1 SKA1 ASPM MTCL1 ZW10 HAUS8 TUBGCP6
D
GOMF_MICROTUBULE_BINDING
KIF18A KIF15 NDE1 SPAG5 GTSE1 SKA1 MTCL1 HAUS8 TUBGCP6
E
GOCC_POLYMERIC_CYTOSKELETAL_FIBER
KIF18A KIF15 NDE1 SPAG5 KNTC1 GTSE1 SKA1 ASPM MTCL1 TCHP ZW10 PLEC HAUS8 TUBGCP6
F
GOCC_SUPRAMOLECULAR_POLYMER
KIF18A KIF15 NDE1 SPAG5 KNTC1 GTSE1 SKA1 ASPM MTCL1 TCHP ZW10 PLEC HAUS8 TUBGCP6

Figure 19. (A) GSEA result of GOCC_SPINDLE_POLE gene set. The heat map indicates the CRISPR viability score of the leading edge genes of the preranking based on the magnitude of differences in CRISPR viability score between K562 WT and CENP-C ΔM12BD cells, in descending order.

(B) GSEA result of GOMF_TUBULIN_BINDING gene set. The heat map indicates the CRISPR viability score of the leading edge genes as in (A).

(C) GSEA result of GOCC_SPINDLE gene set. The heat map indicates the CRISPR viability score of the leading edge genes as in (A).

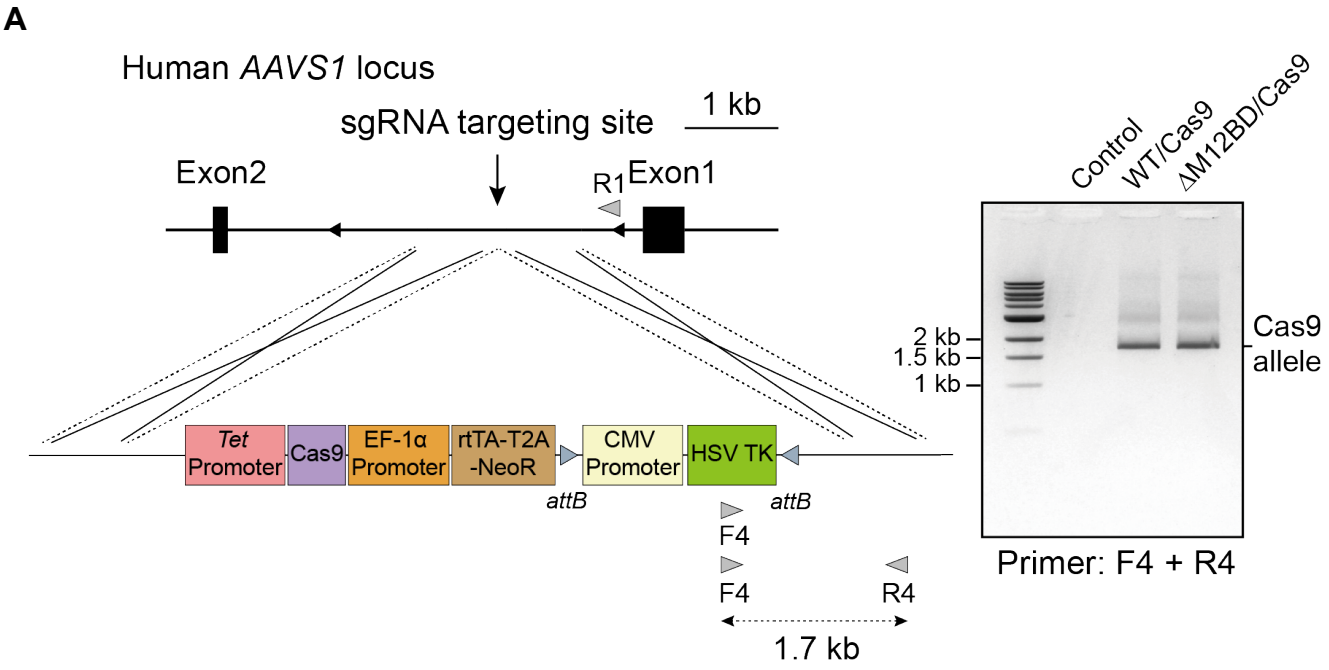
(D) GSEA result of GOMF_MICROTUBULE_BINDING gene set. The heat map indicates the CRISPR viability score of the leading edge genes as in (A).

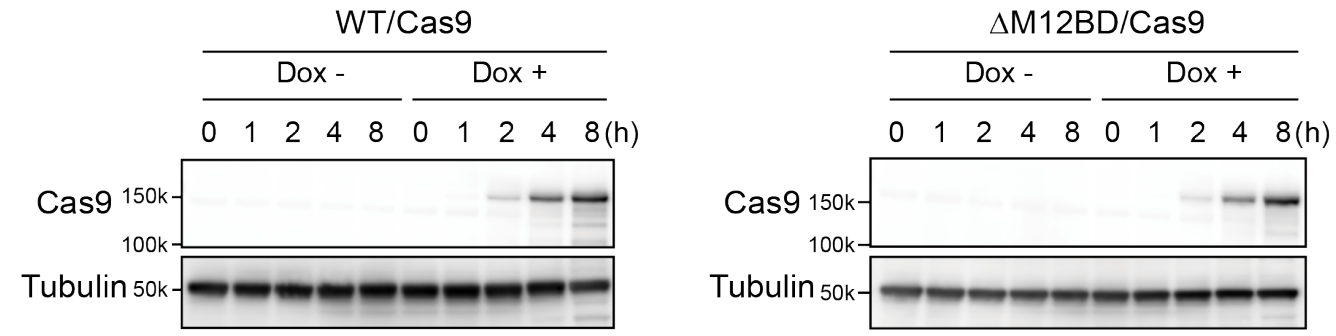
(E) GSEA result of GOCC_POLYMERIC_CYTOSKELETAL_FIBER gene set. The heat map indicates the CRISPR viability score of the leading edge genes as in (A).

(F) GSEA result of GOCC_SUPRAMOLECULAR_POLYMER gene set. The heat map indicates the CRISPR viability score of the leading edge genes as in (A).

2.2 Individual knockout of candidate genes confirms synthetic lethality with the CENP-C ΔM12BD mutation

To verify the CRISPR screening results, I conditionally knocked out each of the selected genes in K562 WT or CENP-C ΔM12BD cells. For these experiments, I established a Cas9 based conditional gene knockout system in CENP-C WT and CENP-C ΔM12BD cells. To achieve knockout experiments I firstly integrated a doxycycline (Dox)-inducible Cas9 cassette together with an exchange cassette which contains HSV TK flanked with two *attB* sequences into human *AAVS1* locus. Human *AAVS1* gene locus is a safe harbor for gene integration because it has an open chromatin structure and is transcription competent. Most importantly, there are no known adverse effects on cells resulting from the inserted DNA fragment of interest. After I established these doxycycline (Dox)-inducible Cas9 parental CENP-C WT and CENP-C ΔM12BD cell line, I applied genomic PCR to confirm this integration. Primer


A
Human AAVS1 locus
sgRNA targeting site
1 kb
Exon2
R1
Exon1
Tet Promoter
Cas9
EF-1α Promoter
rtTA-T2A -NeoR
CMV Promoter
HSV TK
attB
attB
F4
F4
R4
1.7 kb
Control
WT/Cas9
ΔM12BD/Cas9
2 kb
1.5 kb
1 kb
Cas9 allele
Primer: F4 + R4


B
WT/Cas9
Dox -
Dox +
0 1 2 4 8 0 1 2 4 8 (h)
Cas9 150k
100k
Tubulin 50k
C
ΔM12BD/Cas9
Dox -
Dox +
0 1 2 4 8 0 1 2 4 8 (h)
Cas9 150k
100k
Tubulin 50k

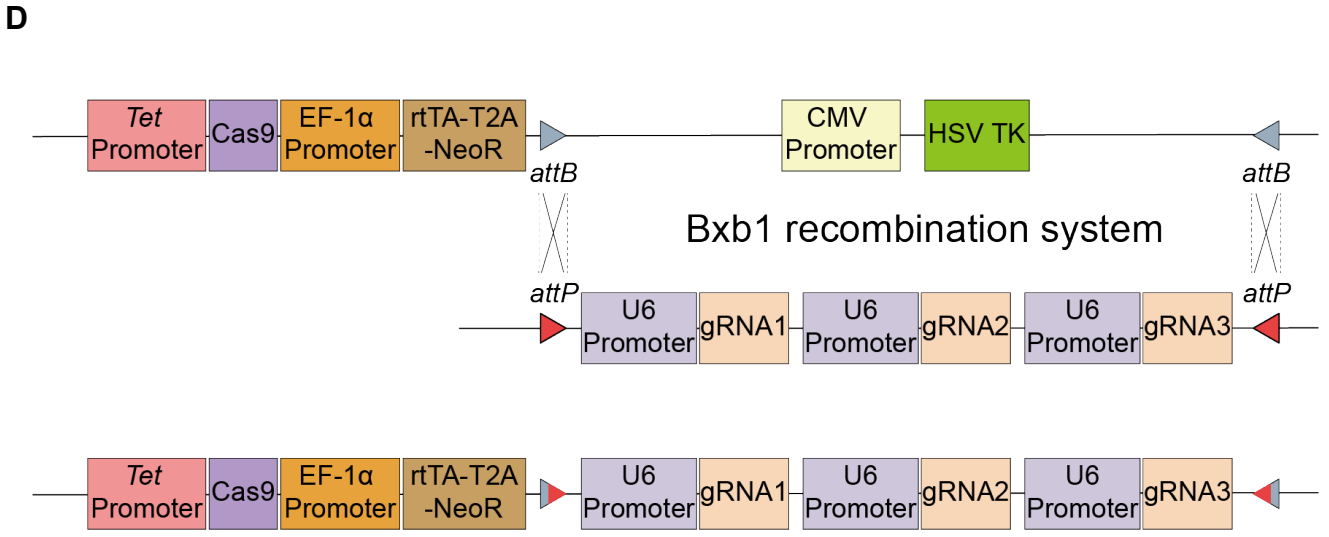

D
Tet Promoter
Cas9
EF-1α Promoter
rtTA-T2A -NeoR
CMV Promoter
HSV TK
attB
attB
Bxb1 recombination system
attP
attP
U6 Promoter
gRNA1
U6 Promoter
gRNA2
U6 Promoter
gRNA3
Tet Promoter
Cas9
EF-1α Promoter
rtTA-T2A -NeoR
U6 Promoter
gRNA1
U6 Promoter
gRNA2
U6 Promoter
gRNA3

Figure 20. Generation of CRISPR-based conditional knockout cell lines for genes identified by the CRISPR screening in K562 WT and CENP-C ΔM12BD cells.

(A) Schematic representation of the strategy to insert the Cas9 construct under the control of Tet-responsible (Tet On) promoter into human *AAVS1* locus in K562 WT or CENP-C ΔM12BD cells. Genotyping of PCR using indicated primers are also shown.

(B) Immunoblot analysis for conditional expression of Cas9 in K562 WT or CENP-C ΔM12BD cells after Dox addition.

(C) Strategy to insert sgRNAs for each target gene. As the Cas9 construct contains HSV TK flanked with two *attB* sequences, three U6 promoter-sgRNA sequences flanked by *attP* sequences can be inserted into this locus by *attB-attP* recombination with Bxb1 recombinase.

F4 was designed inside the integration sequence, primer R4 was designed outside the *AAVS1* homologous arm (Figure 20A), the PCR product size for an F4+R4 set is expected to be about 1.7 kb. WT/Cas9 and ΔM12BD/Cas9 show successful integration. Next, I applied an immunoblot analysis to check whether Cas9 protein can be induced after doxycycline addition or not. In both WT/Cas9 and ΔM12BD/Cas9 cells, Cas9 protein can be detected 2 h after the doxycycline addition (Figure 20B). All of these results indicate that this system works.

Then, three U6 promoter-sgRNA sequences flanked by *attP* sequences can be inserted into this locus by *attB-attP* recombination with Bxb1 recombinase (Figure 20C). For each knockout cell line, I designed 3 different sgRNAs which target different exons of the corresponding gene.

Knockout efficiency after doxycycline addition for each cell line was evaluated by measuring the mRNA expression levels of each gene (Figures 21A-21J). After doxycycline addition for 48 h, Real-Time quantitative PCR (rt-qPCR) was performed to check mRNA level of the target gene in each knockout cell line: *KIF18A*, *KIF15*,

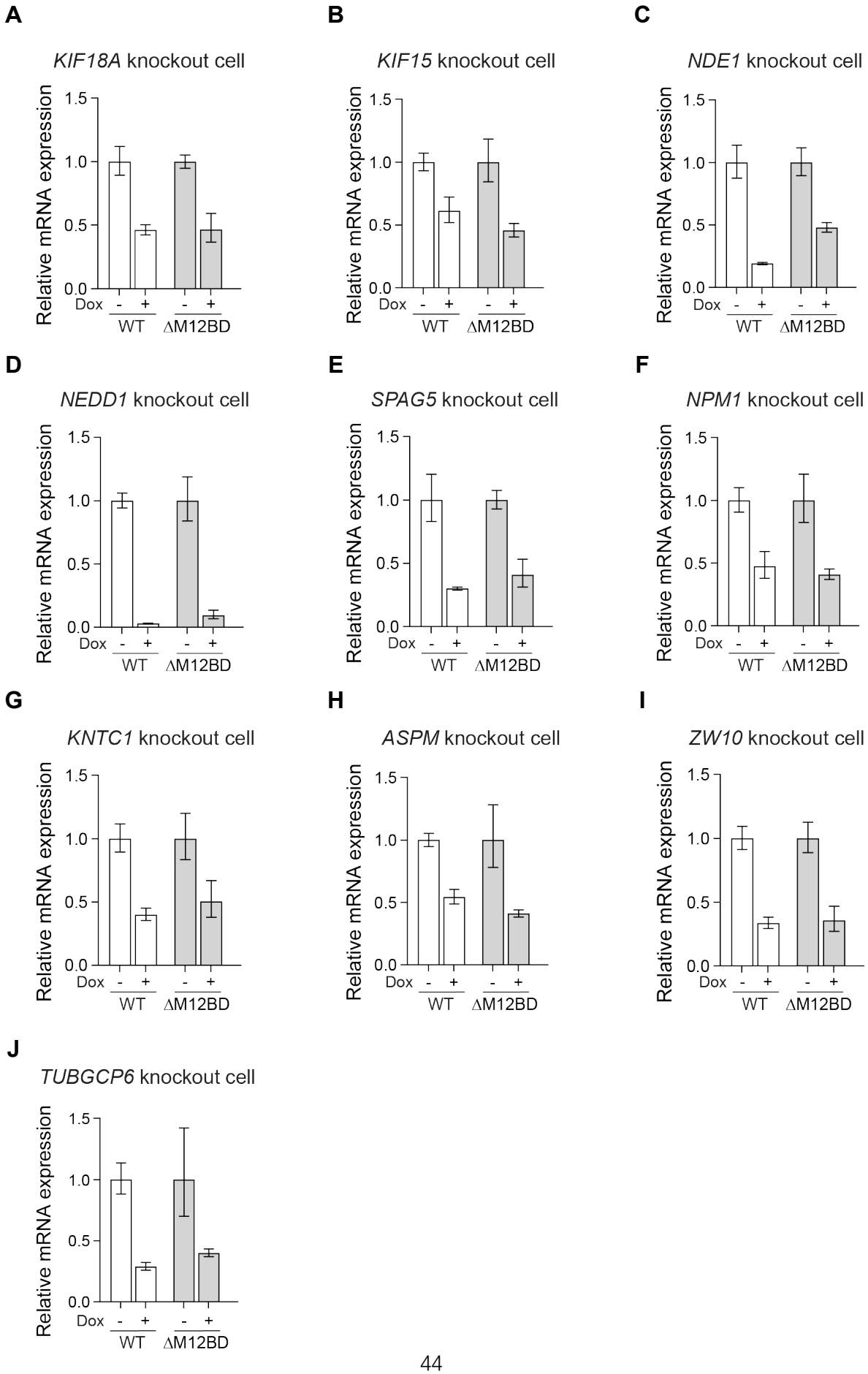

A
KIF18A knockout cell
B
KIF15 knockout cell
C
NDE1 knockout cell
D
NEDD1 knockout cell
E
SPAG5 knockout cell
F
NPM1 knockout cell
G
KNTC1 knockout cell
H
ASPM knockout cell
I
ZW10 knockout cell
J
TUBGCP6 knockout cell
Relative mRNA expression
1.5
1.0
0.5
0.0
Dox - + - +
WT
ΔM12BD

Figure 21. mRNA expression of (A) *KIF18A*, (B) *KIF15*, (C) *NDE1*, (D) *NEDD1*, (E) *SPAG5*, (F) *NPM1*, (G) *KNTC1*, (H) *ASPM*, (I) *ZW10* and (J) *TUBGCP6* in K562 WT and CENP-C ΔM12BD cells after Dox addition. Expression of all tested genes was reduced at 48 h after Dox addition. mRNA expression was calculated by QuantStudio Design & Analysis Software v1.5.1 using the RQ (Relative Quantitation) value, error bars indicate RQ minimum and maximum (each sample size: n = 3).

NDE1, NEDD1, *SPAG5*, *NPM1*, *KNTC1*, *ASPM*, *ZW10*, and *TUBGCP6*. In each knockout cell line, relative mRNA level of target gene was significantly reduced after the Dox addition, my conditional knockout system can successfully reduce expression of each target gene. In addition, I also performed immunoblot to check each target protein level in all of Tet-on Cas9 knockout cell lines after Dox addition. I confirmed that the level of tested proteins were reduced, except for those of KNTC1 and ASPM under the condition (Figure 22A-22J). Immunoblot showed the knockout efficiency for some proteins was not so good, this may be due to design of gRNAs. But by rt-qPCR experiments, mRNA expression reduction of all genes can be observed at 48 h after Dox addition (Figure 21).

As shown in Figure 23, knockout of either one of six genes (*KIF18A*, *KIF15*, *NDE1*, *NEDD1*, *SPAG5* or *NPM1*) significantly reduced viability in K562 CENP-C ΔM12BD cells relative to K562 WT cells at 4 days after Dox addition. *NEDD1* knockout substantially reduced the viability in K562 CENP-C ΔM12BD cells but also lowered viability in K562 WT cells (Figure 23). Although the knockout of two genes (*NDE1* and *NPM1*) reduced the viability of K562 CENP-C ΔM12BD cells compared to K562 WT cells, the changes were modest (Figure 23). The knockout of the remaining genes (*KNTC1*, *ASPM* or *ZW10*) did not show changes in viability in K562 WT or CENP-C ΔM12BD cells in this assay (Figure 23).

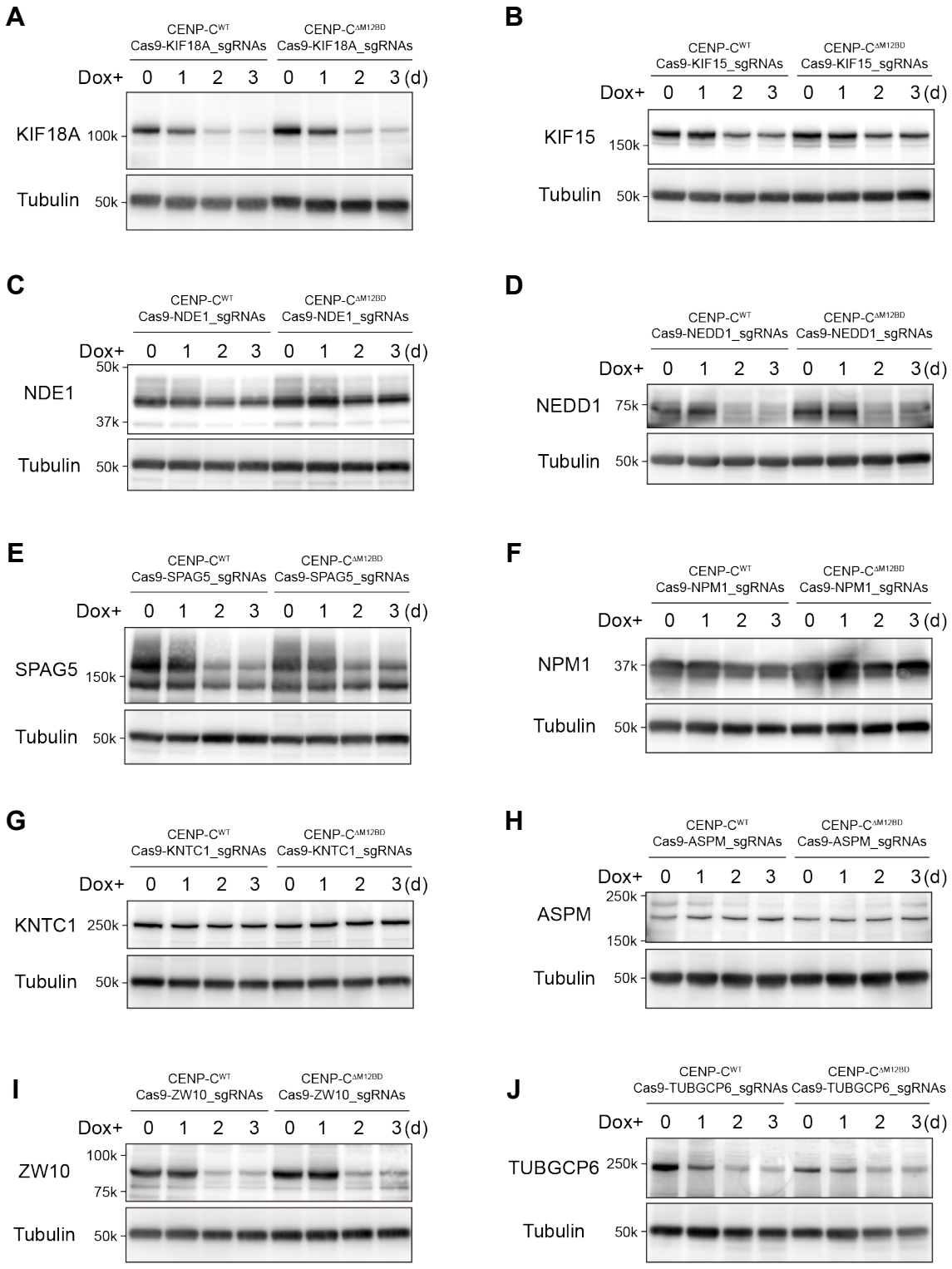


Figure 22. Protein expression of (A) KIF18A, (B) KIF15, (C) NDE1, (D) NEDD1, (E) SPAG5, (F) NPM1, (G) KNTC1, (H) ASPM, (I) ZW10 and (J) TUBGCP6 by immunoblot in K562 WT and CENP-C ΔM12BD cells after Dox addition. Expression of tested proteins were reduced after Dox addition except for KNTC1 and ASPM.

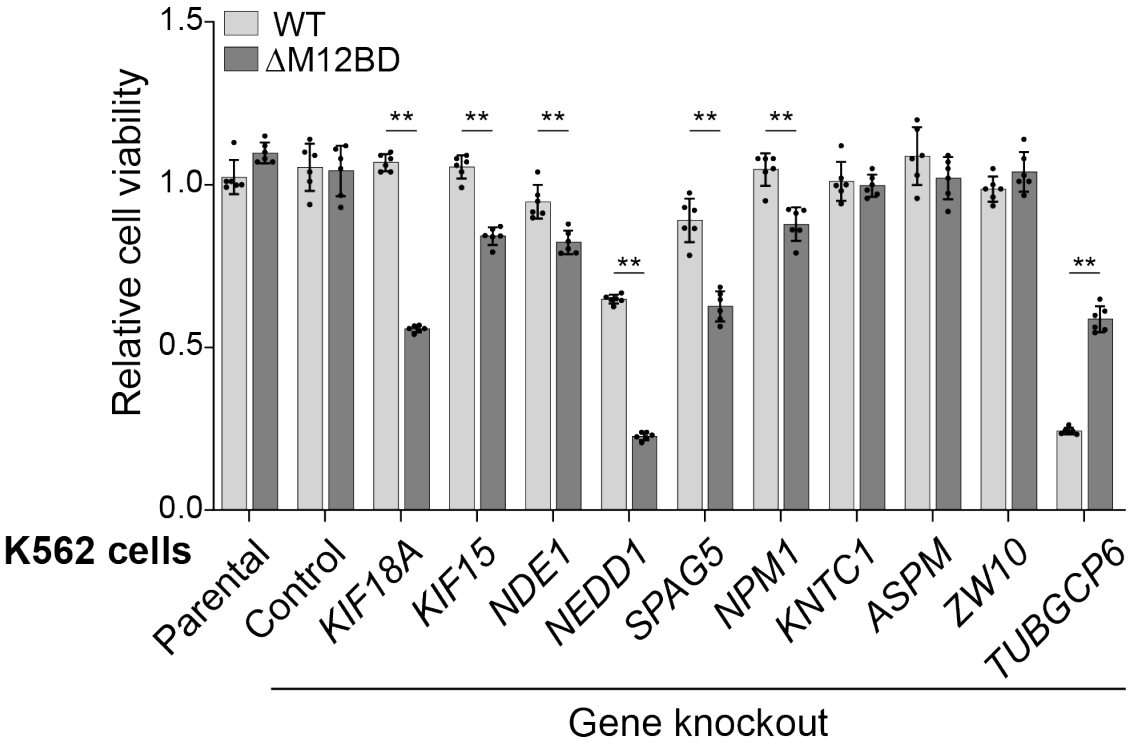
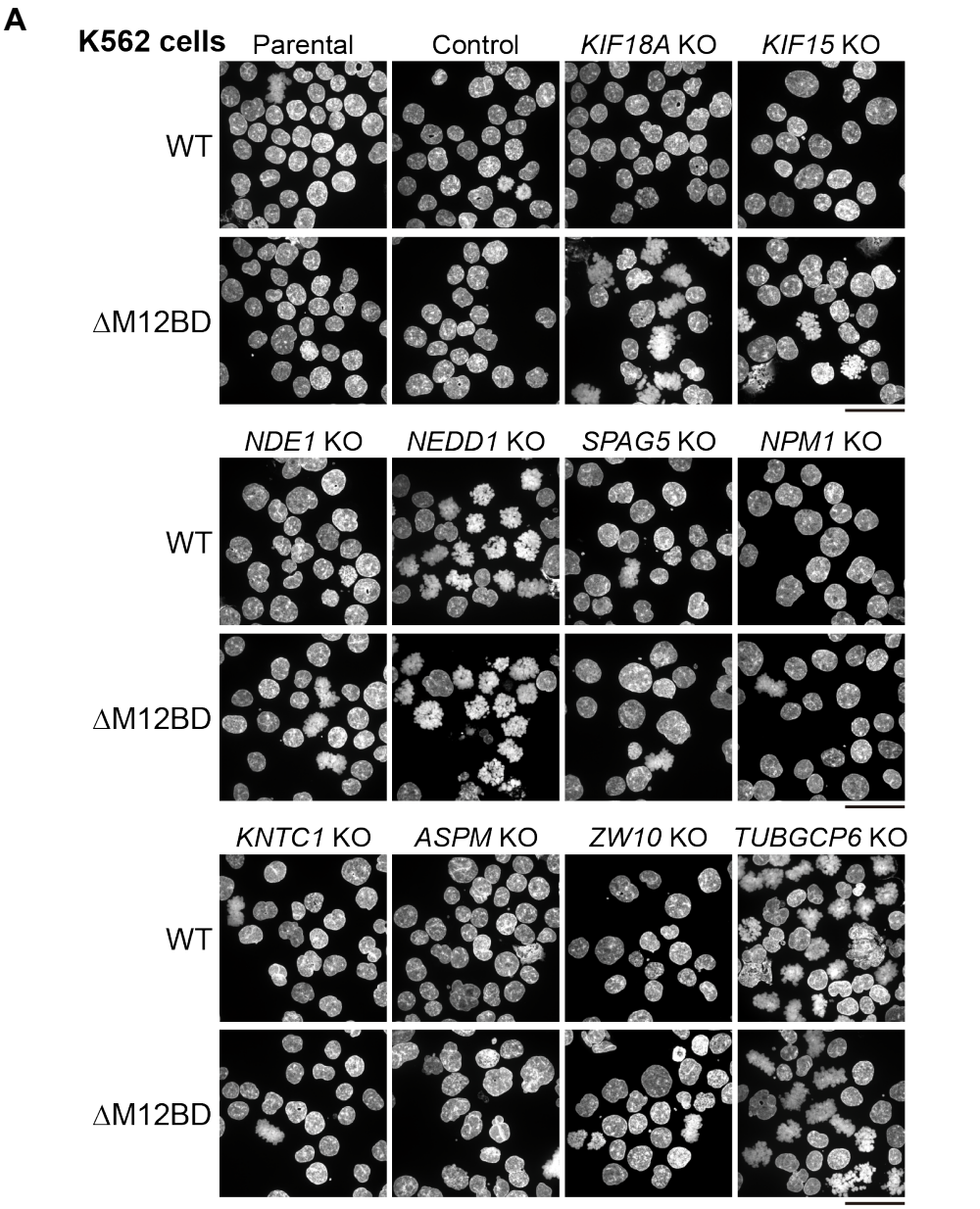


Figure 23. Cell viability of K562 WT or CENP-C ΔM12BD cells after knockout of indicated genes at 4 days after doxycycline (Dox) addition (Mean and SD, two-tailed Student's t-test, CENP-C WT cells: n = 6, CENP-C ΔM12BD cells: n = 6; $^{**}p < 0.01$).

Then I stained each knockout cell with DAPI to observe whether mitotic progression is defected or not upon knockout of the target gene. Detailed microscopic observation found that knockout of *KIF18A*, *KIF15*, *NDE1*, *NEDD1*, or *SPAG5* increased the mitotic cell population in K562 CENP-C ΔM12BD cells relative to K562 WT cells (Figures 24A and 24B). In addition, knockout of *KIF18A*, *KIF15*, *NEDD1*, *SPAG5*, *KNTC1*, *ASPM* or *TUBGCP6* increased cells with micronuclei in K562 CENP-C ΔM12BD cells more than in K562 WT cells (Figure 24B). These results confirm that my previous large-scale functional genetics analysis successfully isolated candidate genes whose knockouts exhibit synthetic mitotic defects in cells expressing the CENP-C ΔM12BD.


A
K562 cells
Parental
Control
KIF18A KO
KIF15 KO
WT
ΔM12BD
NDE1 KO
NEDD1 KO
SPAG5 KO
NPM1 KO
KNTC1 KO
ASPM KO
ZW10 KO
TUBGCP6 KO

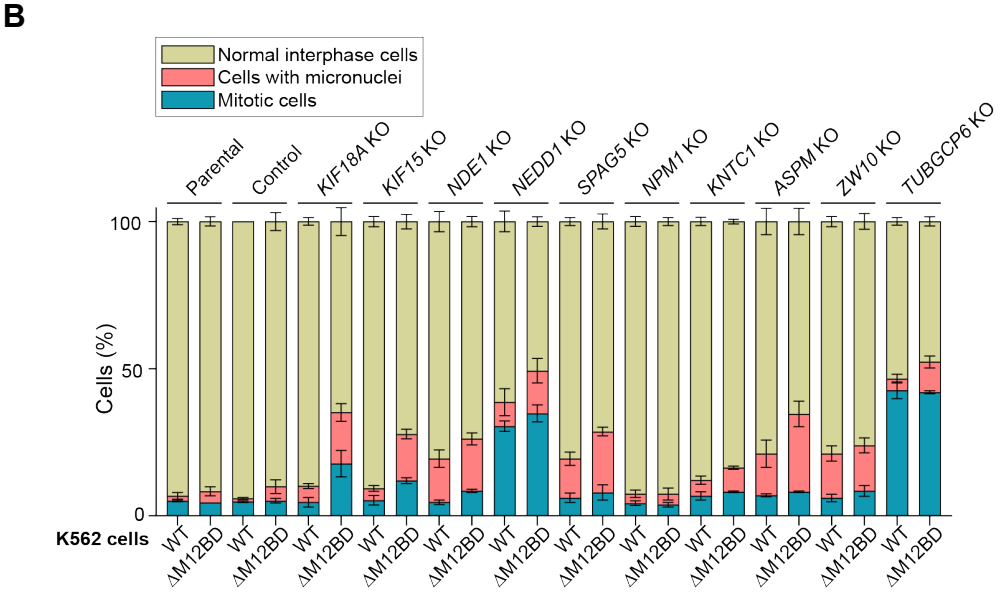

B
Normal interphase cells
Cells with micronuclei
Mitotic cells
Parental
Control
KIF18A KO
KIF15 KO
NDE1 KO
NEDD1 KO
SPAG5 KO
NPM1 KO
KNTC1 KO
ASPM KO
ZW10 KO
TUBGCP6 KO
Cells (%)
100
50
0
K562 cells
WT
ΔM12BD

Figure 24. (A) Representative images of DAPI-stained K562 WT or CENP-C ΔM12BD cells after knockout of indicated genes at 4 days. Scale bar, 50 μm. (B) Population of normal interphase cells, mitotic cells, and cells with micronuclei in K562 WT or CENP-C ΔM12BD cells after knockout of indicated genes at 4 days. Error bars indicated SEM. n = 3 independent experiments; 200 cells from each cell line were quantified in each experiment.

2.3 *KIF18A* knockout with CENP-C ΔM12BD mutation shows strong mitotic defects accompanied with chromosome congression errors in human K562 cells

Among isolated genes, *KIF18A* knockout shows clear synthetic lethality in CENP-C ΔM12BD K562 cells. *KIF18A* conditional knockout showed significant cell death even at 2 days after Dox addition (Figure 25A). Then, I examined phenotypes of these cells in depth to understand why *KIF18A* knockout causes lethality in CENP-C ΔM12BD K562 cells. First, I examined cell-cycle distribution of these cells after addition of Dox by flow cytometry analyses (FACS). Using wild-type K562 cells, I did not observe significant increase of the G2/M population after Dox addition, and cells are healthy after *KIF18A* knockout (Figure 25B). By contrast, the G2/M population was increased from 1 day after Dox addition, and it reached to ~35% at day 2 (Figure 25C). On day 3, I started to observe dead cells. This FACS profile suggested that clear mitotic arrest happened in CENP-C ΔM12BD K562 cells after *Kif18A* knockout. Then, I examined the time course of growth for CENP-C ΔM12BD K562 cells after *KIF18A* knockout (Figure 26A). Wild type K562 cells (WT/*KIF18A* ON) comparably grew with the cells after *KIF18A* knockout (WT/*KIF18A* OFF), which is also similar to CENP-C ΔM12BD K562 cells before *KIF18A* knockout (ΔM12BD/*KIF18A* ON, Figure 26A). However, inducible knockout of *KIF18A* stopped cell growth in CENP-C ΔM12BD K562 cells (ΔM12BD/*KIF18A* OFF) and cells finally died. The cell death appears to be due to the abnormal mitotic progression.

Then, I applied double thymidine block to synchronize the cells (Chen et al.,

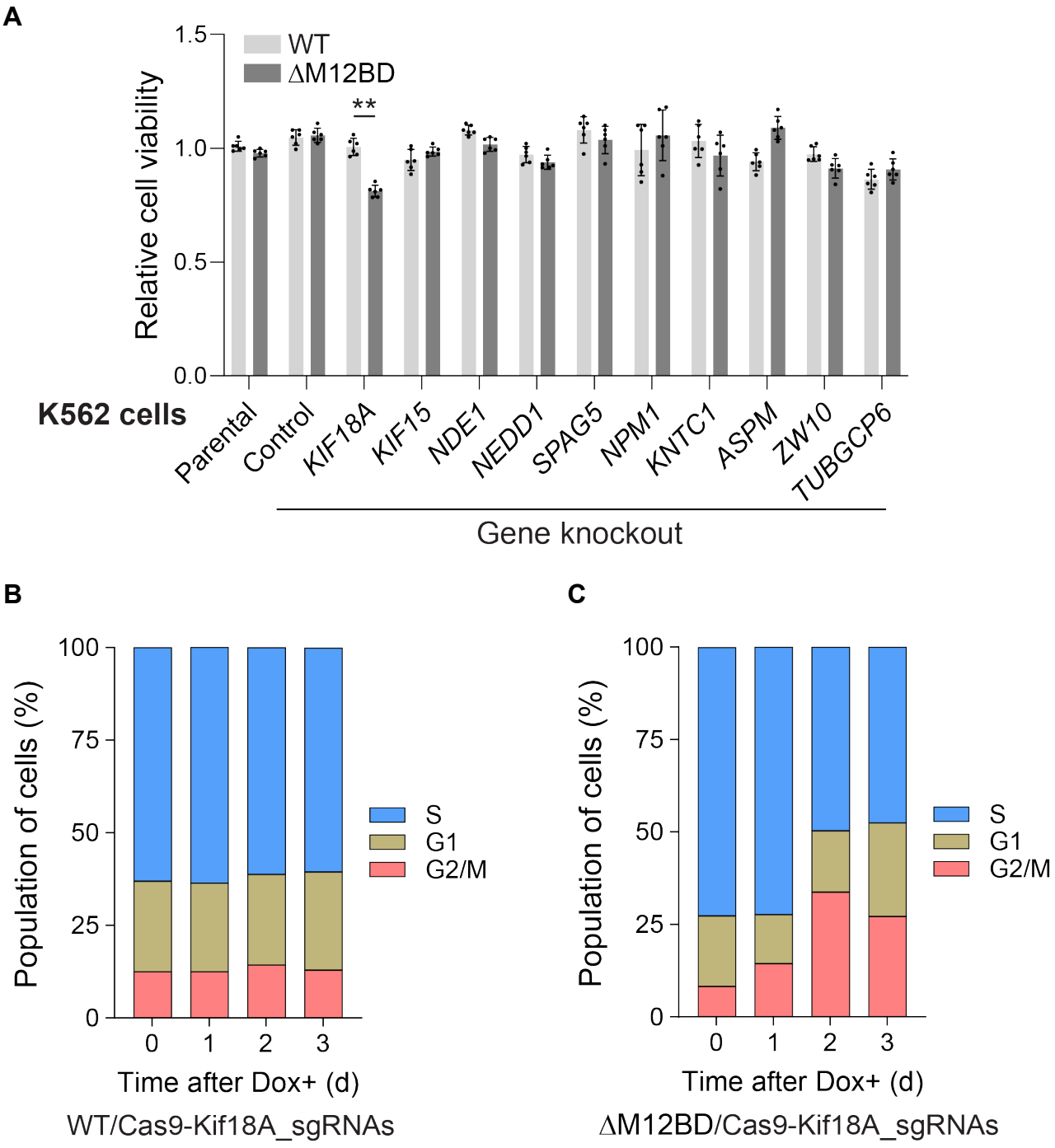
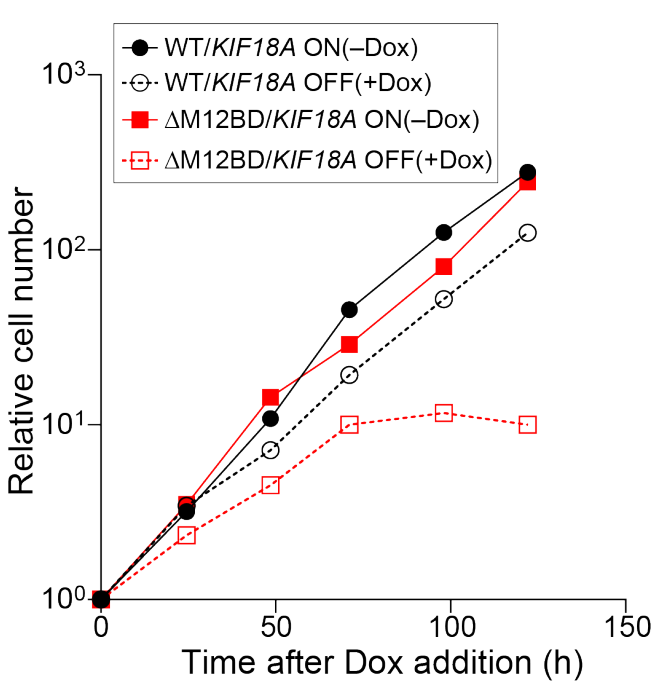


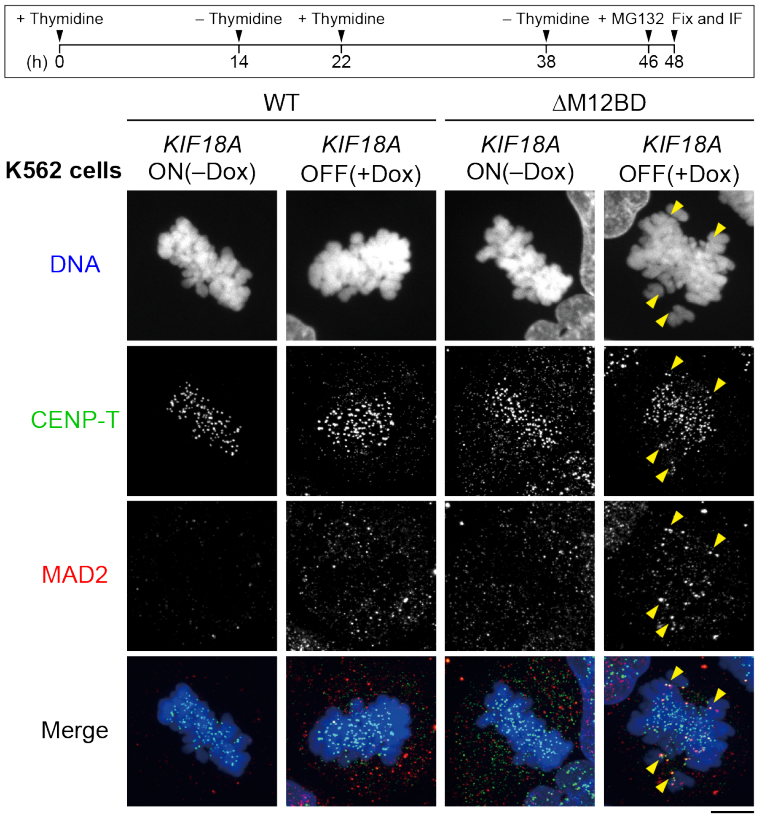
Figure 25. (A) Cell viability of K562 WT or CENP-C ΔM12BD cells after knockout of indicated genes at 2 days after Dox addition (Mean and SD, two-tailed Student's t-test, K562 WT cells: n = 6, K562 CENP-C ΔM12BD cells: n = 6; $^{**}p < 0.01$). (B) Cell-cycle distribution of conditional knockout of *KIF18A* in K562 WT cells at each day after Dox addition, based on FACS analysis. (C) Cell-cycle distribution of conditional knockout of *KIF18A* in K562 CENP-C ΔM12BD cells at each day after Dox addition, based on FACS analysis.

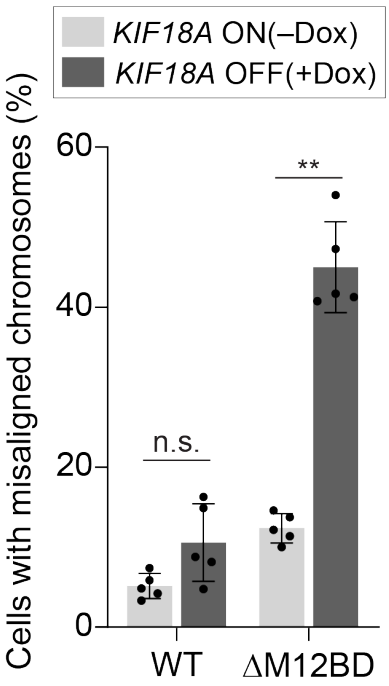
2018). Thymidine is an inhibitor of DNA synthesis thus arrest cell at G1/S boundary. I used double thymidine block to synchronize the cell for chromosome misalignment assay. After cell fixation, I stained the cells with anti-MAD2, a SAC (Spindle assembly

A



B





C

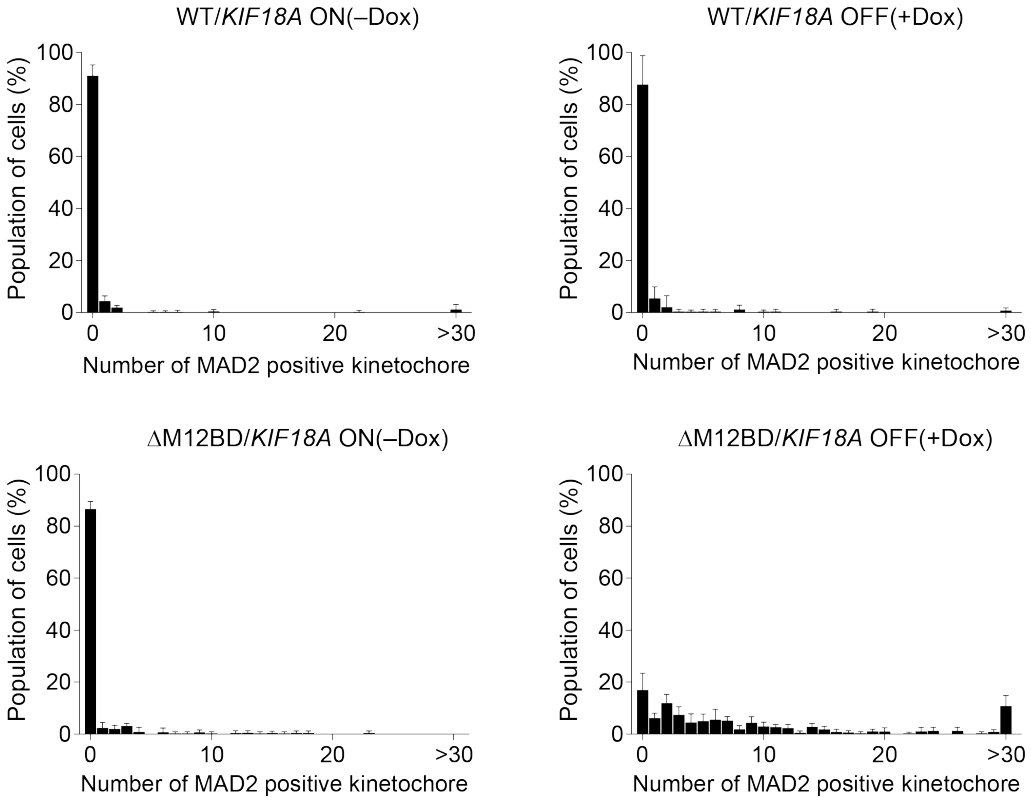


Figure 26. (A) The growth curve of K562 WT or CENP-C ΔM12BD cells with or without *KIF18A* knockout. K562 WT or CENP-C ΔM12BD cells were treated with or without Dox (*KIF18A* OFF or ON). The cell numbers were normalized to those at time 0 of each line. Dox was added at the time 0. (B) Quantification of cells with misaligned chromosomes in K562 WT or CENP-C ΔM12BD cells with or without *KIF18A* knockout. The cells were treated with thymidine for 14 h. Then, thymidine was washed out and incubated for 8 h. Thymidine was added again and cells were incubated for 16 h. After washing thymidine out and incubating for 8 h, MG132 was added and incubated for 2 h (–Dox, *KIF18A* ON). For *KIF18A* knockout, the cells were treated and cultured in the presence of Dox (+Dox, *KIF18A* OFF). The treated cells were fixed and stained with antibodies against MAD2 (red) to detect misaligned chromosomes and CENP-T (green) as a kinetochore marker. DNA was stained with DAPI (blue). Arrowheads show typical MAD2 positive unaligned chromosomes. Scale bar, 10 μm. The cells with MAD2 positive chromosomes were quantified. (Mean and SEM, two-tailed Student's t-test, n = 5 independent experiments; n.s., non-significant; $^{**}p < 0.01$). (C) Numbers of MAD2 positive kinetochores in each cell in each condition (WT *KIF18A* ON; WT *KIF18A* OFF; CENP-C ΔM12BD *KIF18A* ON; CENP-C ΔM12BD *KIF18A* OFF) (Mean and SEM, n = 5 independent experiments).

checkpoint) protein to examine misaligned chromosomes with defects of kinetochore-microtubule attachment. I observed significant increase of cells with misaligned chromosome (which has MAD2 positive signals) in CENP-C ΔM12BD K562 cells with *KIF18A* knockout (Figure 26B and 26C), suggesting that abnormal mitotic behavior might be the reason to cause subsequent cell death in CENP-C ΔM12BD K562 cells after *KIF18A* knockout.

2.4 CENP-C ΔM12BD cells are sensitive to the microtubule-destabilizing drug nocodazole

KIF18A is well studied and known as a plus-end directed kinesin that accumulates at the plus-end tips of microtubules and suppresses kinetochore-microtubule dynamics (Mayr et al., 2007; Stumpff et al., 2008). In the mitotic cells, knockout of *KIF18A* is expected to increase microtubule dynamics, and attachment between kinetochore and

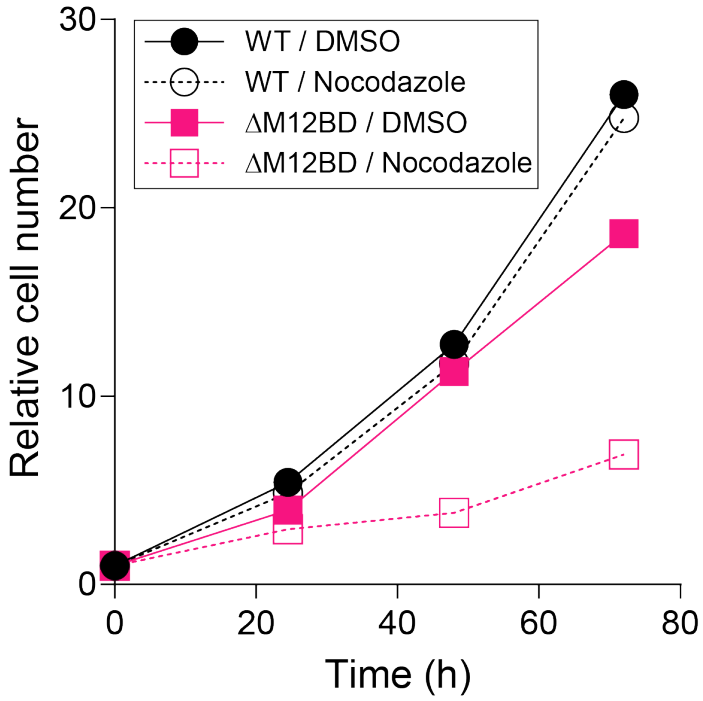


Figure 27. The growth curve of K562 WT or CENP-C ΔM12BD cells treat with or without 5 ng/mL nocodazole. The cell numbers were normalized to those at time 0 of each cell line. Nocodazole or DMSO was added at the time 0.

microtubule might become unstable. Therefore, I hypothesize that CENP-C ΔM12BD cells might be sensitive to unstable kinetochore-microtubule attachment. I treated CENP-C WT and CENP-C ΔM12BD cell with DMSO and 5 ng/mL nocodazole (Figure 27). Nocodazole is an inhibitor of microtubule polymerization while its treatment can cause unstable kinetochore-microtubule attachment. Under this 5 ng/mL sublethal level of nocodazole treatment, CENP-C ΔM12BD cells showed growth defects compared with those in CENP-C WT cells (Figure 27). This result suggests that the knockout of *KIF18A* leads to cell death in K562 CENP-C ΔM12BD cells, possibly due to impaired kinetochore-microtubule attachments and subsequent mitotic arrest.

As a summary of the CRISPR screening in K562 cells, I identified several candidate genes whose knockouts exhibit synthetic mitotic defects with CENP-C ΔM12BD mutant, then I established a doxycycline (Dox)-inducible Cas9 gene knockout system to verify these candidate genes. After checking the cell viability and mitotic cell phenotype among all of these knockout cell lines, I confirmed most of the candidate genes exhibit synthetic lethality in CENP-C ΔM12BD mutant (Figure 23). Among them, *KIF18A* is the most important and effective gene in CENP-C ΔM12BD cells. Knockout of *KIF18A* causes rapid and severe cell death in CENP-C ΔM12BD cells, possibly due to unstable kinetochore-microtubule attachments that lead to mitotic arrest and subsequent cell death. I will examine the detailed mechanisms in the following experiments.

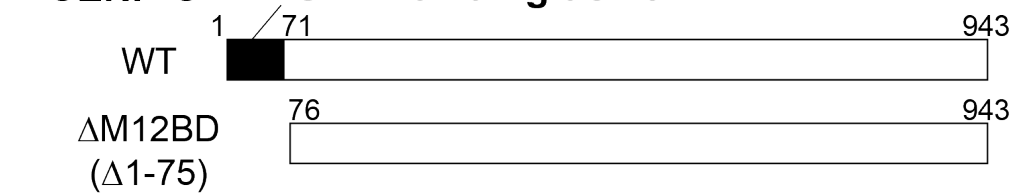
3. Investigation of *KIF18A* knockout in human CENP-C ΔM12BD RPE-1 cells

3.1 Generation of human CENP-C ΔM12BD RPE-1 cells

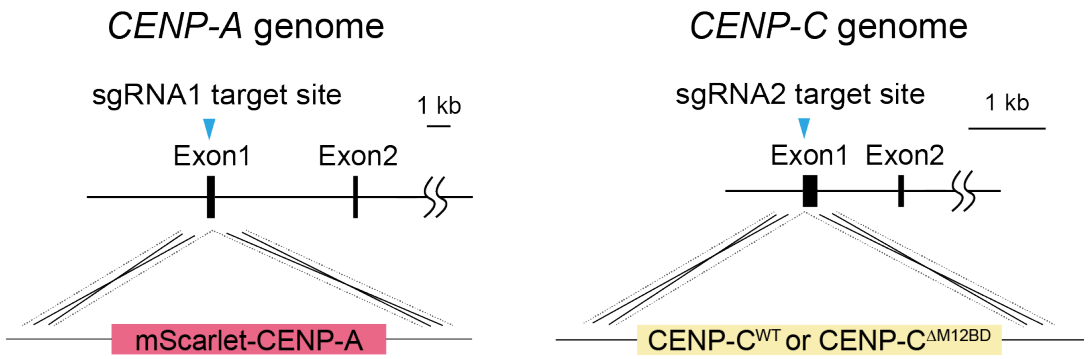
I demonstrated synthetic lethality of CENP-C ΔM12BD with *KIF18A* knockout in K562 cells. I also want to test the synthetic lethality in other normal cell types, because K562 cells are cancer cells. Then, I tested RPE-1 cells, which are near diploid non-cancer cells. In addition, previous studies demonstrated RPE-1 cells are insensitive to *KIF18A* knockdown (Gliech et al., 2024). Therefore, RPE-1 cells would be suitable for further depth cell biological analysis, because there are many already established experimental systems for RPE-1 cells, compared with K562 cells. I first generated CENP-C lacking Mis12C binding region in RPE-1 cells (CENP-C ΔM12BD cells) expressing mScarlet-CENP-A (Figure 28A and 28B). By using CRISPR Cas9 mediated genome editing, mScarlet-CENP-A sequence was inserted into the first exon of endogenous CENP-A locus in RPE-1 cells, under the control of the endogenous CENP-A promoter (RPE-1 mScarlet-CENP-A cells). To establish mScarlet-CENP-A RPE-1 expressing either CENP-C WT or CENP-C ΔM12BD under the control of the endogenous CENP-C promoter, cDNA of CENP-C WT or CENP-C ΔM12BD was inserted into the first exon of endogenous CENP-C locus in RPE-1 mScarlet-CENP-A cells independently (Figure 28B). Immunoblot analysis was performed to investigate expressions of CENP-C WT, CENP-C ΔM12BD and mScarlet-CENP-A in each cell line (Figure 28C).

Next, I examined the levels of CENP-C and KMN proteins on mitotic kinetochores in CENP-C WT and CENP-C ΔM12BD RPE-1 cells. CENP-C levels at mitotic kinetochores in CENP-C ΔM12BD RPE-1 cells were similar to those in CENP-C WT RPE-1 cells (Figure 29). By contrast, DSN1 (a subunit of Mis12 complex), KNL1 (a subunit of KNL1 complex), and Hec1 (a subunit of Ndc80 complex) levels at mitotic kinetochores in CENP-C ΔM12BD RPE-1 cells were significantly reduced, compared with those in CENP-C WT RPE-1 cells (Figure 29A-29D). As observed in K562 cells, these localization results in RPE-1 CENP-C ΔM12BD cells were expected.

A


RPE-1 cell
CENP-C
Mis12C-binding domain
1
71
943
WT
76
943
ΔM12BD
(Δ1-75)

B


CENP-A genome
sgRNA1 target site
1 kb
Exon1
Exon2
mScarlet-CENP-A
CENP-C genome
sgRNA2 target site
1 kb
Exon1
Exon2
CENP-CWT or CENP-CΔM12BD

C

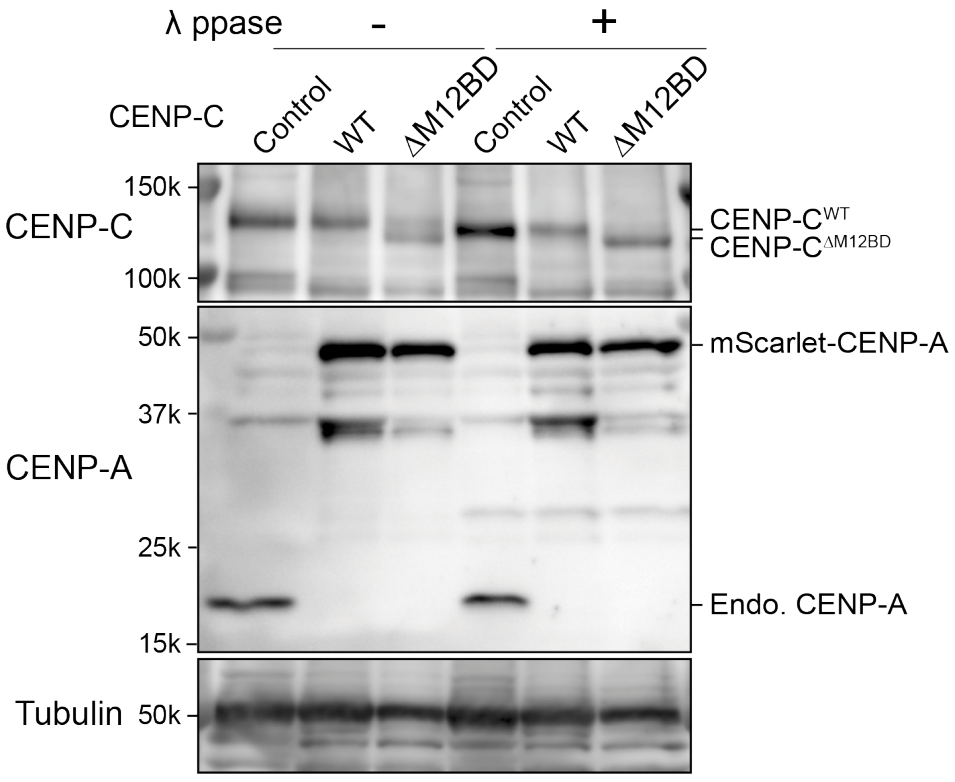

λ ppase
-
+
CENP-C
Control
WT
ΔM12BD
Control
WT
ΔM12BD
150k
CENP-C
100k
CENP-CWT
CENP-CΔM12BD
50k
37k
CENP-A
25k
15k
mScarlet-CENP-A
Endo. CENP-A
Tubulin
50k

Figure 28. (A) Schematic representation of human wild-type CENP-C (CENP-C WT) and CENP-C ΔM12BD mutant, which are expressed in RPE-1 cells. To generate RPE-1 CENP-C ΔM12BD cells, *CENP-C* cDNA encoding full length (WT: aa 1-943) or aa 76-943 (ΔM12BD: Δaa 1-75) was introduced into the endogenous *CENP-C* locus, respectively. (B) Strategy to generate RPE-1 CENP-C WT or CENP-C ΔM12BD RPE-1 cells. mScarlet fused CENP-A was introduced into the endogenous *CENP-A* gene locus in RPE-1 cells. Then, either CENP-C WT or CENP-C ΔM12BD cDNA containing construct was integrated into the endogenous *CENP-C* gene locus in RPE-1 cells expressing mScarlet fused CENP-A. (C) Immunoblot analysis to detect CENP-C WT, CENP-C ΔM12BD, and mScarlet-CENP-A in each cell line. a-tubulin was probed as a loading control. λPPase was used to detect clear signals of CENP-C proteins as previously shown in K562 cells (λPPase +, Figure 13D).

3.2 *KIF18A* is essential for cell viability in CENP-C ΔM12BD RPE-1 cells

I confirmed reduction of KMN but not CENP-C at kinetochores in CENP-C ΔM12BD RPE1 cells (Figure 29A-29D). Then, I treated these cells with siRNA for *KIF18A* (siKIF18A) and a control Non-Targeting siRNA (siNT). Immunoblot analysis demonstrated that KIF18A was undetectable after 24 h in the cells treated with siKIF18A, but not with a control siNT (Figure 30A). Next, I examined cell viability of CENP-C WT or CENP-C ΔM12BD RPE-1 cells after siNT or siKIF18A treatment. Although siKIF18A treatment did not cause growth defects in CENP-C WT RPE-1 cells, viability was significantly reduced in CENP-C ΔM12BD RPE-1 cells treated with siKIF18A (Figure 30B). This indicates that the deletion of the CENP-C Mis12 complex binding domain leads to *KIF18A* knockdown sensitivity (*KIF18A*-KD sensitivity) in RPE-1 cells. This result is consistent with the K562 cell experiments.

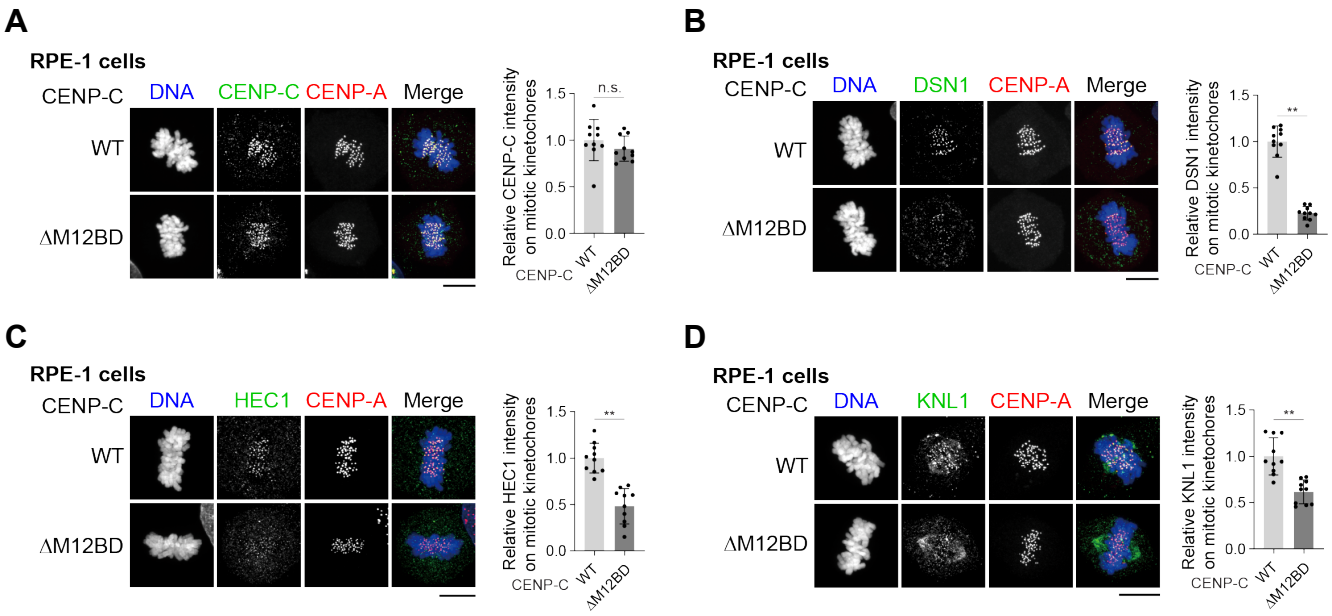


Figure 29. (A) CENP-C, (B) DSN1, (C) HEC1 and (D) KNL1 localization in RPE-1 CENP-C WT or CENP-C ΔM12BD cells. Each protein was stained with an antibody against each protein (green). mScarlet-CENP-A was used as a kinetochore marker (CENP-A, red). DNA was stained with DAPI (blue). Scale bar, 10 μm. Signal intensities of each protein at mitotic kinetochores were quantified (Mean and SD, two-tailed Student's t-test, CENP-C WT cells: n = 10 cells, CENP-C ΔM12BD cells: n = 10 cells; n.s., non-significant; $^{**}p < 0.01$).

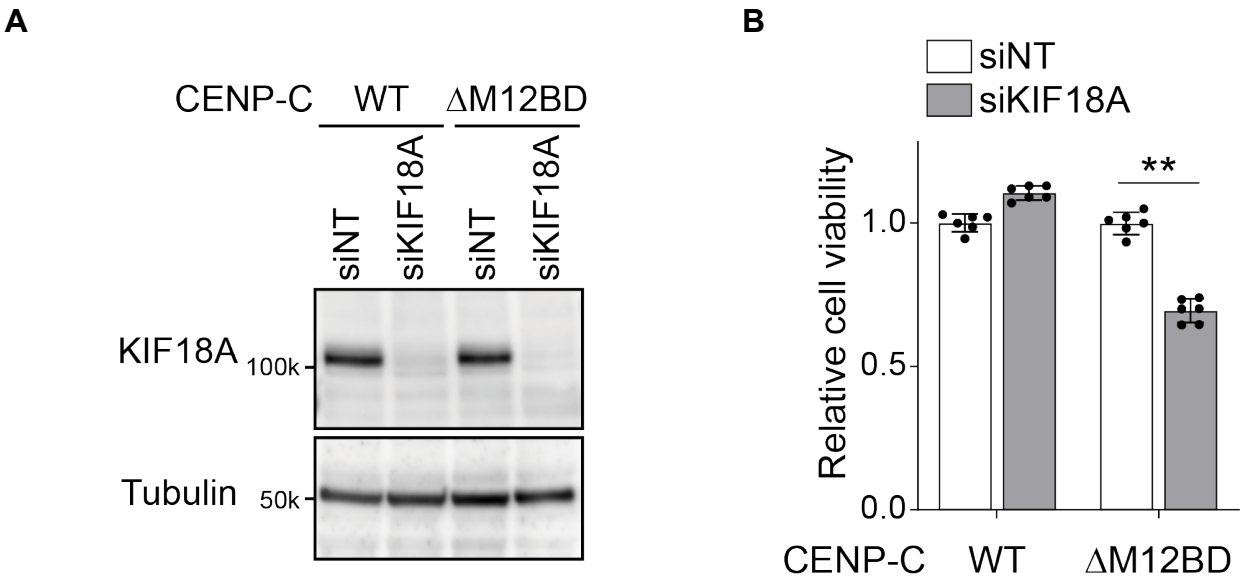
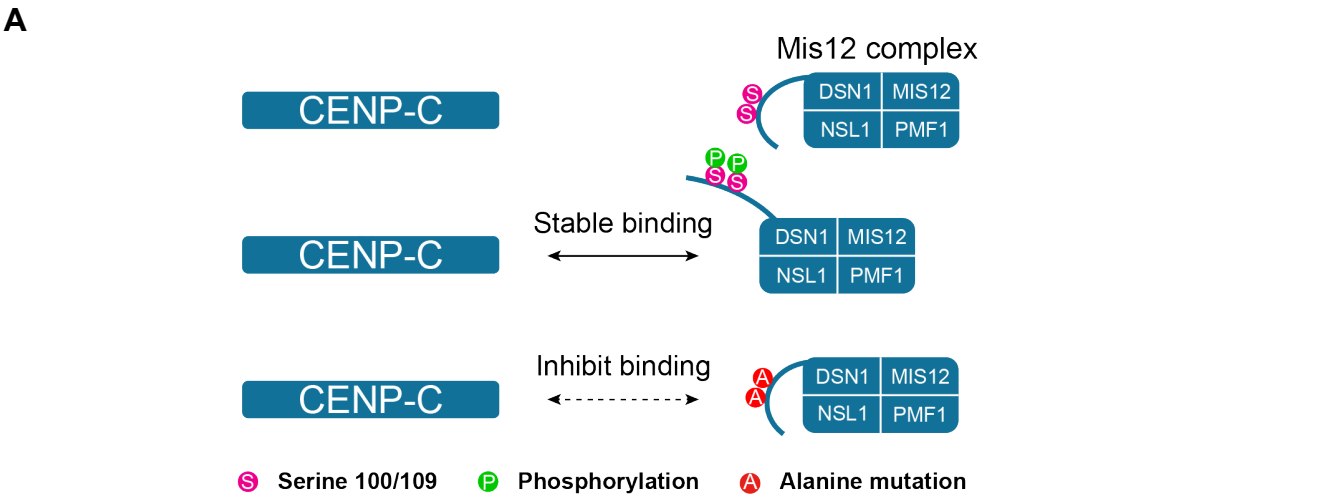


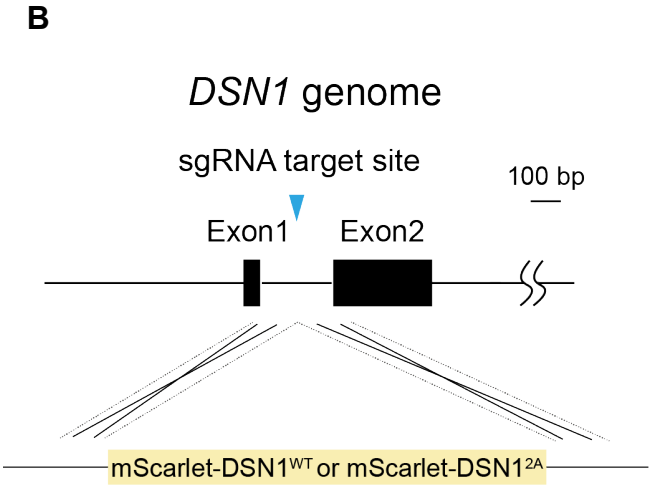
Figure 30. Immunoblot analysis to detect KIF18A in RPE-1 CENP-C WT or CENP-C ΔM12BD cells after treatment of control Non-Targeting siRNA (siNT) or KIF18A siRNA (siKIF18A). α-tubulin was probed as a loading control. (B) Cell viability assay of RPE-1 CENP-C WT or CENP-C ΔM12BD cells after treatment of siNT or siKIF18A. (Mean and SD, two-tailed Student's t-test, CENP-C WT cells with siNT: n = 6, CENP-C WT cells with siKIF18A: n = 6, CENPC ΔM12BD cells with siNT: n = 6, CENP-C ΔM12BD cells with siKIF18A: n = 6; $^{**}p < 0.01$).

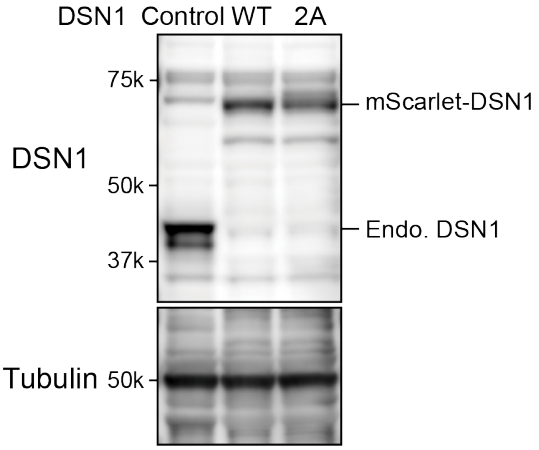
3.3 Perturbation of Mis12C-CENP-C interactions leads to increase of *KIF18A*-KD sensitivity

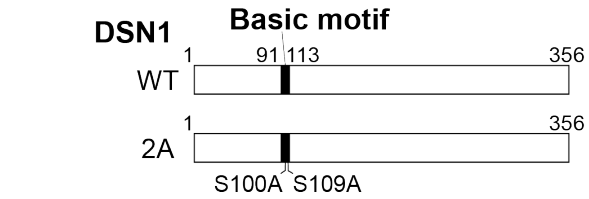
I next sought to determine whether the *KIF18A*-KD sensitivity in RPE-1 CENP-C ΔM12BD cells depends on altered Mis12C-CENP-C interactions or an alternative role of the M12BD in CENP-C. CENP-C-Mis12C binding is facilitated by Aurora B phosphorylation of DSN1, a Mis12C subunit, at Ser100 and Ser109 (Kim et al., 2015; Rago et al., 2015) (Figure 31A). I established DSN1 phospho-deficient mutants by replacing DSN1 Ser100 and Ser109 to alanine (DSN1 S100A/S109A, DSN1 2A). By using CRISPR Cas9 system, cDNA of mScarlet-fused DSN1 WT or DSN1 2A was knocked into the first exon of the endogenous *DSN1* gene locus, under the control of the endogenous *DSN1* promoter. Immunoblot analysis was performed to detect mScarlet-DSN1 WT or DSN1 2A in each cell line (Figure 31B-31D).

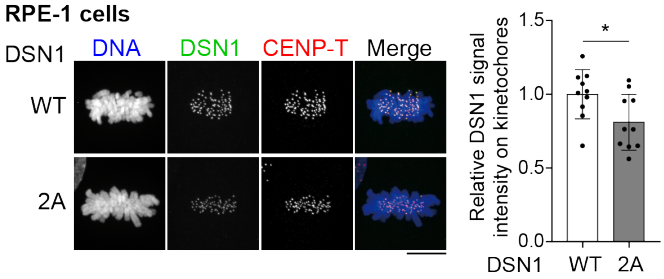
In the DSN1 phospho-deficient mutant DSN1 2A cells, the binding of Mis12C to CENP-C is reduced (Petrovic et al., 2016; Yatskevich et al., 2024; Takenoshita et al., 2024) (Figure 31E). As reported previously (Kim et al., 2015), I confirmed DSN1 2A reduced the centromeric localization of Mis12C (DSN1) as well as Ndc80C (HEC1) and KNL1C (KNL1) in RPE-1 cells (Figures 31E-31G). Most importantly, siKIF18A treatment significantly reduced the cell viability of RPE-1 DSN1 2A, but not DSN1 WT cells (Figure 32). However, the reduction of viability in RPE-1 DSN1 2A cells after *KIF18A* knockdown was milder than that in RPE-1 CENP-C ΔM12BD cells, possibly due to less reduction of Mis12C localization in RPE-1 DSN1 2A cells (Figures 29B and 31E). Nevertheless, results suggest that perturbating Mis12C-CENP-C interactions leads to increased *KIF18A*-KD sensitivity.

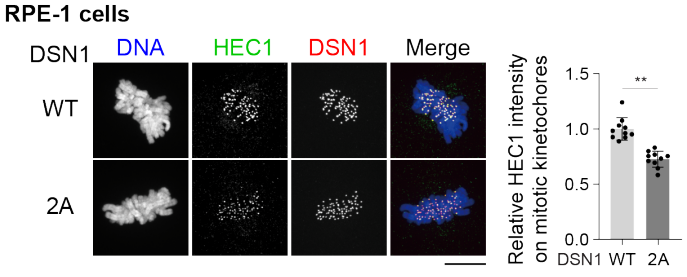

A
Mis12 complex
CENP-C
DSN1
MIS12
NSL1
PMF1
Stable binding
CENP-C
DSN1
MIS12
NSL1
PMF1
Inhibit binding
CENP-C
DSN1
MIS12
NSL1
PMF1
Serine 100/109
Phosphorylation
Alanine mutation


B
DSN1 genome
sgRNA target site
100 bp
Exon1
Exon2
mScarlet-DSN1WT or mScarlet-DSN1 2A


C
DSN1 Control WT 2A
75k
50k
37k
DSN1
mScarlet-DSN1
Endo. DSN1
Tubulin 50k


D
DSN1
Basic motif
1
91 113
356
WT
1
356
2A
S100A S109A


E
RPE-1 cells
DSN1
DNA
DSN1
CENP-T
Merge
WT
2A
Relative DSN1 signal intensity on kinetochores
1.5
1.0
0.5
0.0
*
DSN1 WT 2A


F
RPE-1 cells
DSN1
DNA
HEC1
DSN1
Merge
WT
2A
Relative HEC1 intensity on mitotic kinetochores
1.5
1.0
0.5
0.0
**
DSN1 WT 2A

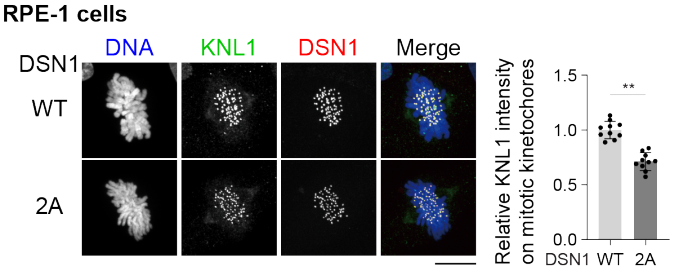

G
RPE-1 cells
DSN1
DNA
KNL1
DSN1
Merge
WT
2A
Relative KNL1 intensity on mitotic kinetochores
1.5
1.0
0.5
0.0
**
DSN1 WT 2A

Figure 31. (A) Schematic representation of the regulation of CENP-C-Mis12C interaction. The basic motif of DSN1, a subunit of Mis12C, masks the CENP-C binding surface of Mis12C, preventing the CENP-C-Mis12C interaction. Once Aurora B phosphorylates two residues (S100 and S109) on the basic motif, the mask is released, and the CENP-C-Mis12C interaction is facilitated. The alanine substitution of these sites reduces the CENP-C-Mis12C interaction. (B) Strategy to introduce mScarlet-fused DSN1 WT or DSN1 2A cDNA into endogenous *DSN1* gene locus. The position of sgRNA target site is shown. (C) Immunoblot analysis to detect DSN1 WT or DSN1 2A. α-tubulin was probed as a loading control. (D) Schematic representation of human wild-type DSN1 (DSN1 WT) and DSN1 2A (S100A/S109A) mutant, which are expressed in RPE-1 cells. (E) DSN1, (F) HEC1 and (G) KNL1 localization in RPE-1 DSN1 WT or DSN1 2A cells (green). mScarlet-DSN1 (either DSN1 WT or DSN1 2A) was used as a kinetochore marker (red). DNA was stained with DAPI (blue). Scale bar, 10 μm. Signal intensity of each protein at mitotic kinetochores were quantified (Mean and SD, two-tailed Student's t-test, DSN1 WT cells: n = 10 cells, DSN1 2A cells: n = 10 cells; $^{**}p < 0.01$).

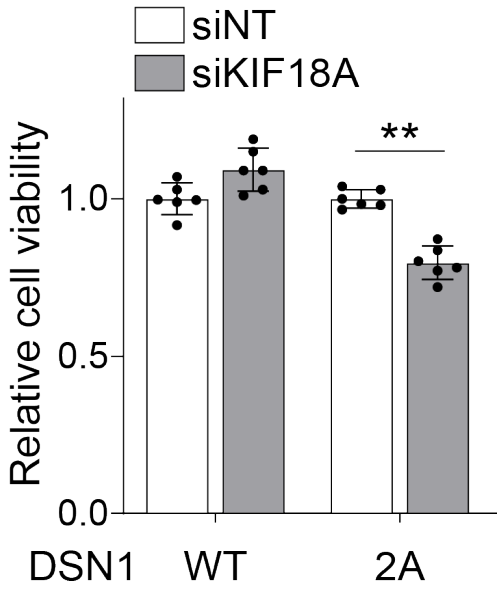


Figure 32. Cell viability of RPE-1 DSN1 WT or DSN1 2A cells after treatment of siNT or siKIF18A. (Mean and SD, two-tailed Student's t-test, DSN1 WT cells with siNT: n = 6, DSN1 WT cells with siKIF18A: n = 6, DSN1 2A cells with siNT: n = 6, DSN1 2A cells with siKIF18A: n = 6; $^{**}p < 0.01$).

3.4 *KIF18A* knockout disturbs mitotic progression in CENP-C ∆M12BD RPE-1 cells

As I observed abnormal mitotic behavior in CENP-C ∆M12BD K562 cells with *KIF18A* knockout, I examined detail mitotic behavior by time-lapse imaging in CENP-C WT or CENP-C ∆M12BD RPE-1 cells with siNT or siKIF18A (Figure 33). In my lab's previous study, we have established RPE-1 cells expressing mScarlet-CENP-A, GFP-H2A, and Flag-fused CENP-C WT or CENP-C ∆M12BD (Kong et al., 2024) for live cell imaging. Chromosomes can be visualized by GFP-H2A, kinetochore can be visualized by mScarlet-CENP-A, and spindle microtubule can be visualized by the treatment of SiR-Tubulin.

I performed live cell imaging to observe mitotic progression after siRNA treatment (Figure 33). CENP-C WT RPE-1 cells treated with siNT smoothly entered and exited mitosis. It took approximately 33 min from the nuclear envelope break down (NEBD) to completion of mitosis (Figure 33). CENP-C ∆M12BD RPE-1 cells with siNT showed a little mitotic delay and it took approximately 44 min for mitosis, which is consistent with our previous study (Kong et al., 2024). Whereas viability of wild-type RPE-1 cells treated with siKIF18A was comparable to that of wild-type with control siNT, mitotic duration of siKIF18A treated CENP-C WT cells was considerably prolonged (approximately 61 min) compare with CENP-C WT cells with siNT, suggesting that *KIF18A* knockdown causes mitotic defect, but some backup pathways may compensate those mitotic defects by *KIF18A* knockdown to overcome mitotic arrest. However, CENP-C ∆M12BD RPE-1 cells treated with siKIF18A showed severe mitotic arrest. Although I quantified the average mitotic duration of siKIF18A treated CENP-C ∆M12BD cells was 260 min, actually 63% of cells were arrested in mitosis and did not exit mitosis by the end of the imaging. These cells underwent server mitotic arrest and consequently died (Figure 33). These results indicate that the deletion of the CENP-C M12BD combined with *KIF18A* knockdown causes a synthetic mitotic defect in RPE-1 cells. Thus, RPE-1 CENP-C ∆M12BD cells require *KIF18A* for their mitotic progression and cell viability.

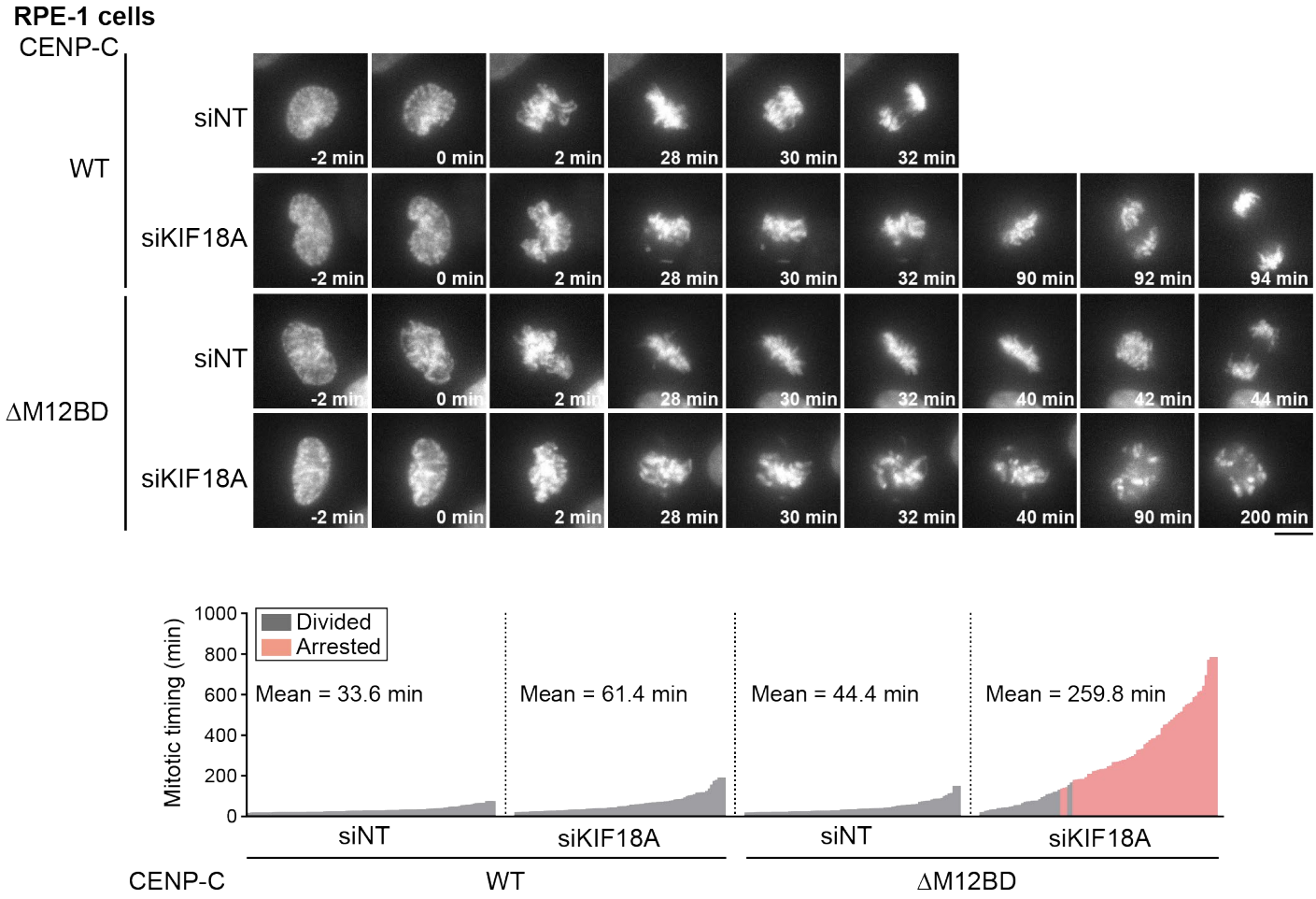


Figure 33. Representative time-lapse images of mitotic progression in RPE-1 CENP-C WT or CENP-C ΔM12BD cells after treatment of siNT or siKIF18A. DNA was visualized with GFP-H2A. Images were projected using maximum intensity projection. Time is relative to nuclear envelope breakdown (NEBD). Scale bar, 10 μm. The time-lapse images were analyzed to measure the mitotic timing from NEBD to anaphase onset (Mean and SD, two-tailed Student's t-test, CENP-C WT cells with siNT: n = 99 cells, CENP-C WT cells with siKIF18A: n = 84 cells, CENP-C ΔM12BD cells with siNT: n = 86 cells, CENP-C ΔM12BD cells with siKIF18A: n = 95 cells). The red bars show the cells that were arrested in mitosis and did not exit mitosis by the end of the imaging.

3.5 Inhibition of SAC rescues lethality of CENP-C ΔM12BD RPE-1 cells after *KIF18A* knockout

In my experiments, I demonstrated that *KIF18A* knockout or knockdown was not lethal in WT RPE-1 and K562 cells (Figure 23 and 30B). On the other hand, there were reports that *KIF18A* knockout or knockdown is lethal in some cancer cells such as HeLa cells (Quinton et al., 2021; Cohen-Sharir et al., 2021; Gliech et al., 2024), and the sensitivities of *KIF18A* knockdown to cell viability appear to be different among various cell lines (Gliech et al., 2024). The previous study also revealed that one of the determinants for sensitivity to *KIF18A* inhibition in cancer cells was prolonged mitosis but that SAC perturbation suppressed *KIF18A*-KD sensitivity in those cells (Gliech et al., 2024).

In line with this previous study, I confirmed that *KIF18A* knockdown reduced cell viability in HeLa cells and this reduced viability was suppressed by SAC inhibition using low doses of the Mps1 inhibitor Reversine (Figure 34A). Then, I demonstrated that Reversine treatment also suppressed the reduced viability observed after siKIF18A treatment in CENP-C ΔM12BD RPE-1 cells (Figure 34B), suggesting that a prolonged mitotic arrest is at least partially responsible for the *KIF18A*-KD sensitivity in CENP-C ΔM12BD RPE-1 cells.

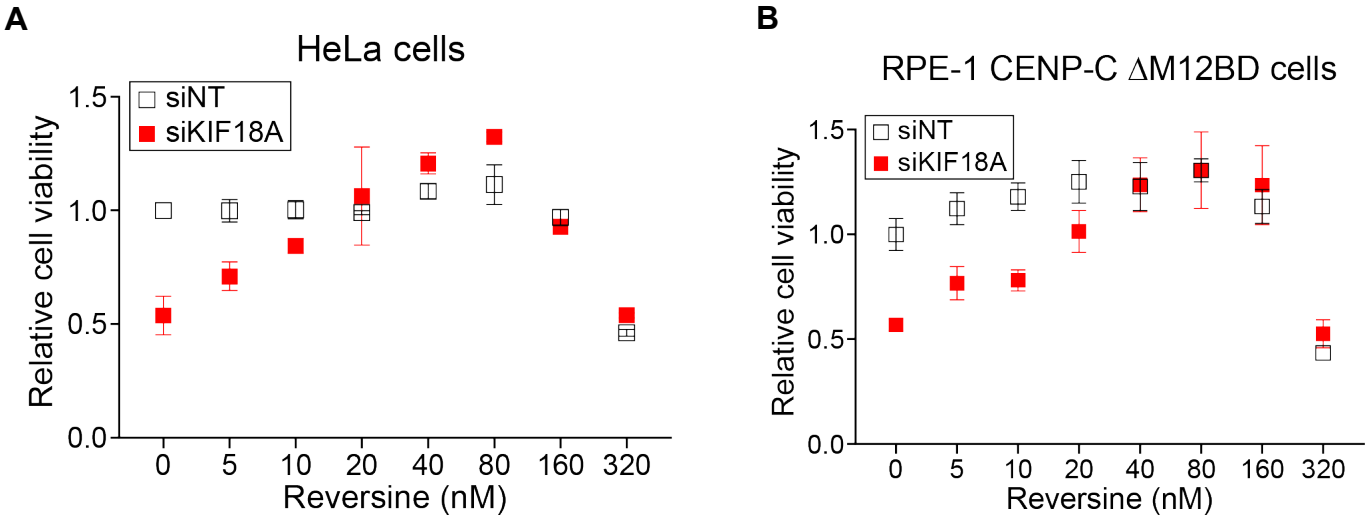


Figure 34. (A) Cell viability of HeLa cells in the presence of various concentrations of Reversine after treatment of siNT or siKIF18A (Mean and SD, two-tailed Student's t-test, each sample size: n = 3). (B) Cell viability of RPE-1 CENP-C ΔM12BD cells in the presence of various concentration of Reversine after treatment of siNT or siKIF18A (Mean and SD, two-tailed Student's t-test, n = 6).

3.6 KIF18A C-terminal domain is important for KIF18A function in CENP-C ΔM12BD RPE-1 cells

I examined the KIF18A functional domain using several KIF18A mutations in CENP-C ΔM12BD RPE-1 cells (Figure 35). KIF18A was identified to interact with microtubules through its N-terminal motor domain and C-terminal domain (Weaver et al., 2011; Stumpff et al., 2011). Therefore, I firstly established several KIF18A C-terminal deletion cell lines using siKIF18 resistant cDNA knock-in at *AAVS1* locus (Figure 36) and I investigated cell viability after siKIF18A treatment in these cell lines. In CENP-C WT RPE-1 cells, cell viability is not obviously affected in these KIF18A mutants. However, in CENP-C ΔM12BD RPE-1 cells, expression of all of these C-terminal deletion of KIF18A caused cell death after *KIF18A* knockdown (Figure 35B and 35C). This indicates that KIF18A C-terminal domain is important for KIF18A function RPE-1 CENP-C ΔM12BD RPE-1 cells. Next, detailed domain analysis of KIF18A was performed in CENP-C ΔM12BD RPE-1 cells.

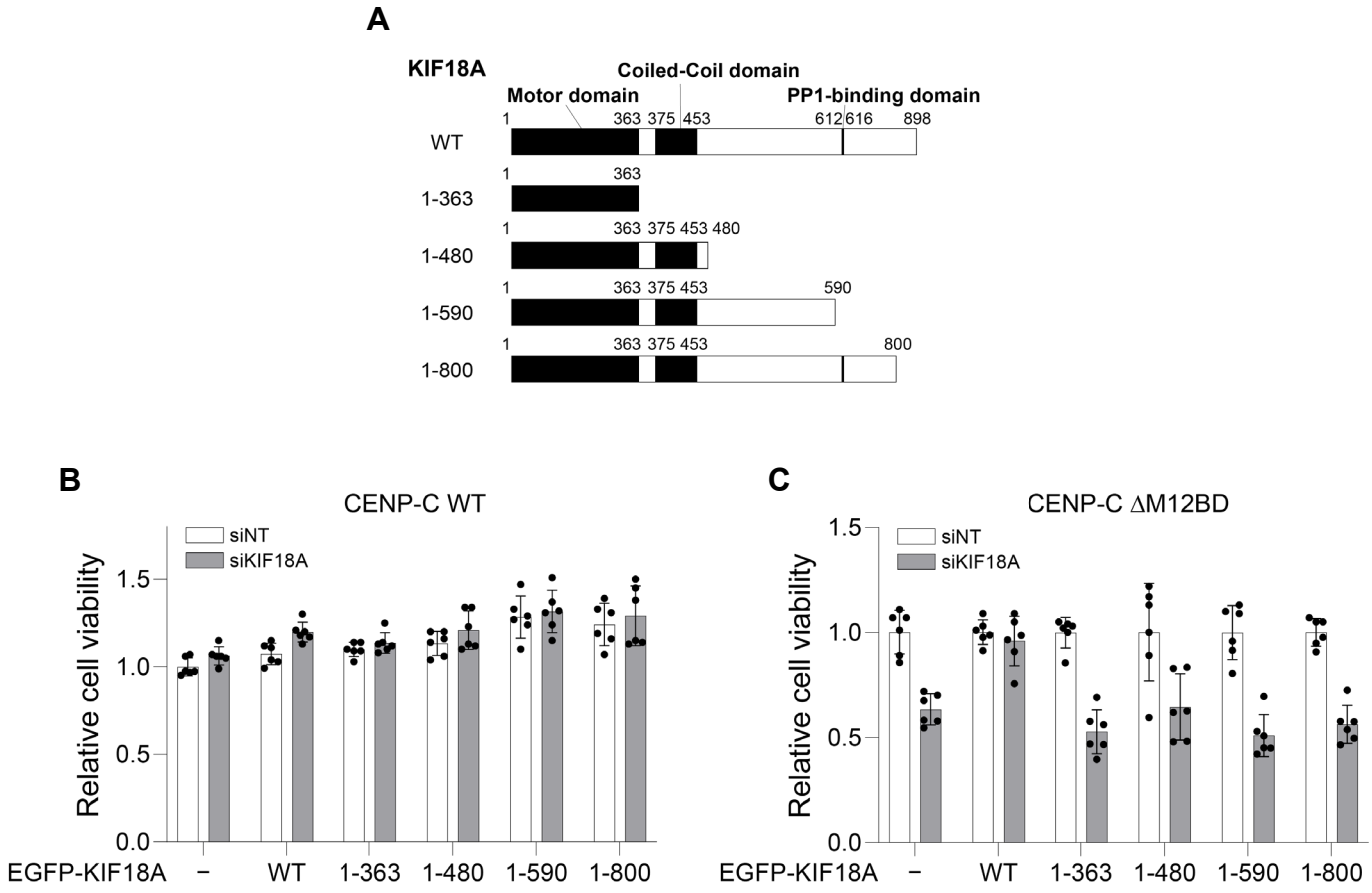


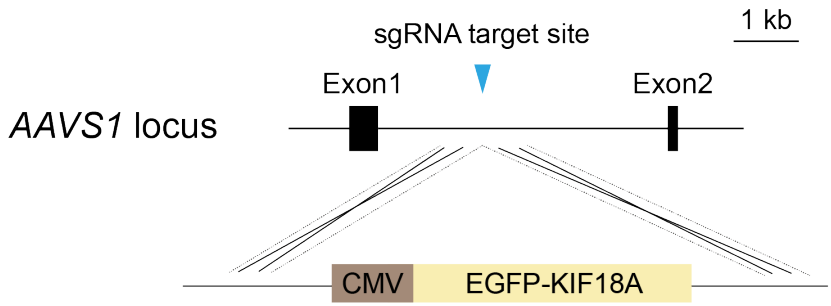
Figure 35. (A) Schematic representation of wild-type KIF18A and its functional domains, including the motor domain, coiled-coil domain, and PP1 binding domain. RPE-1 cells expressing KIF18A lacking the C-terminal domain KIF18A 1-363, 1-480, 1-590 or 1-800 were generated. (B and C) Cell viability assay of RPE-1 CENP-C WT (B) or CENP-C ΔM12BD (C) cells expressing WT or various KIF18A mutants with siNT or siKIF18A treatment (Mean and SD, each sample size: n = 6).

3.7 KIF18A microtubule plus-end localization is required for cell viability in CENP-C ΔM12BD RPE-1 cells

KIF18A is a plus-end directed kinesin that accumulates at the plus-end tips of microtubules and suppresses kinetochore-microtubule dynamics (Mayr et al., 2007; Stumpff et al., 2008). To understand which region of KIF18A is required for viability of CENP-C ΔM12BD RPE-1 cells, I dissected the functional domains in KIF18A. As I explained in the previous section, I integrated EGFP tagged and siRNA-resistant WT or mutants *KIF18A* cDNAs into the *AAVS1* locus (Figure 36A). Immunoblot analysis was performed to confirm the stable expression of EGFP-KIF18A WT or mutants in RPE-1 CENP-C WT and CENP-C ΔM12BD cells (Figure 36B). Endogenous *KIF18A* was knocked out in these cells after siKIF18A treatment (Figure 37B and 37C) and their viability was examined (Figures 37D and 37E). In control CENP-C RPE-1 WT cells, RNAi-based replacements with these *KIF18A* transgenes did not reduce cell viability (Figure 37D). Similarly, in CENP-C ΔM12BD RPE-1 cells, replacement with a KIF18A WT construct did not alter cell viability. In contrast, replacement with a KIF18A mutant lacking the motor domain, which is required for KIF18A localization to the plus-end tips of kinetochore microtubules (Mayr et al., 2007), resulted in reduced viability similar to *KIF18A*-depleted cell (Figures 37E and 37F).

KIF18A also has a domain that interacts with Protein phosphatase 1 (PP1) (PP1-binding domain, Figure 37A) (Hafner et al., 2014). KIF18A-PP1 interactions are required for KIF18A localization to the microtubule plus-end tips by dephosphorylating KIF18A at two CDK1 phosphorylation sites, Ser674 and Ser684 (Hafner et al., 2014). Deletion of the PP1-binding domain (ΔPP1) prevents KIF18A from localization to microtubule plus ends but the addition of alanine substitutions at Ser674/Ser684 (ΔPP1+2A) restores the localization of KIF18A lacking the PP1-binding domain (KIF18A ΔPP1 and KIF18A ΔPP1+2A, Figure 37F) (Hafner et al., 2014). Consistent with this localization, KIF18A ΔPP1+2A, but not KIF18A ΔPP1, rescued the reduction of cell viability caused by *KIF18A* knockdown in CENP-C ΔM12BD RPE-1 cells. These results demonstrate that the plus-end tip localization of KIF18A is required for cell viability in CENP-C ΔM12BD RPE-1 cells.

A



B

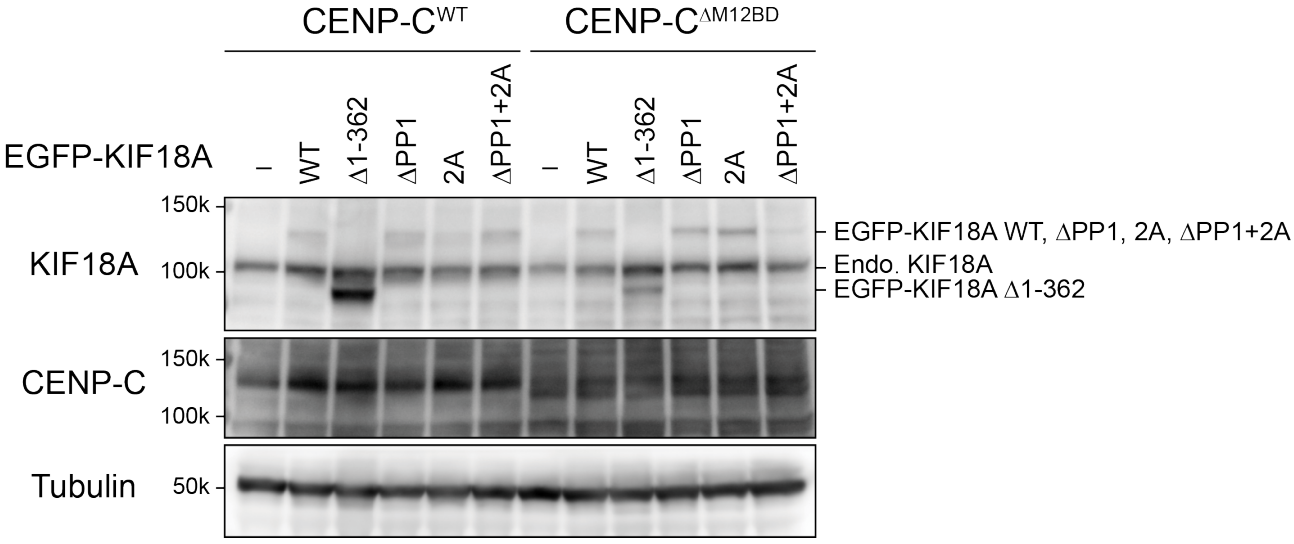


Figure 36. (A) Strategy to insert EGFP-fused various version of *KIF18A* cDNA into the *AAVS1* gene locus in RPE-1 CENP-C WT or CENP-C ΔM12BD cells. The position of the sgRNA target site is shown. (B) Immunoblot analysis to detect wild-type (WT) and various mutants of KIF18A in RPE-1 CENP-C WT or CENP-C ΔM12BD cells. α-tubulin was probed as a loading control.

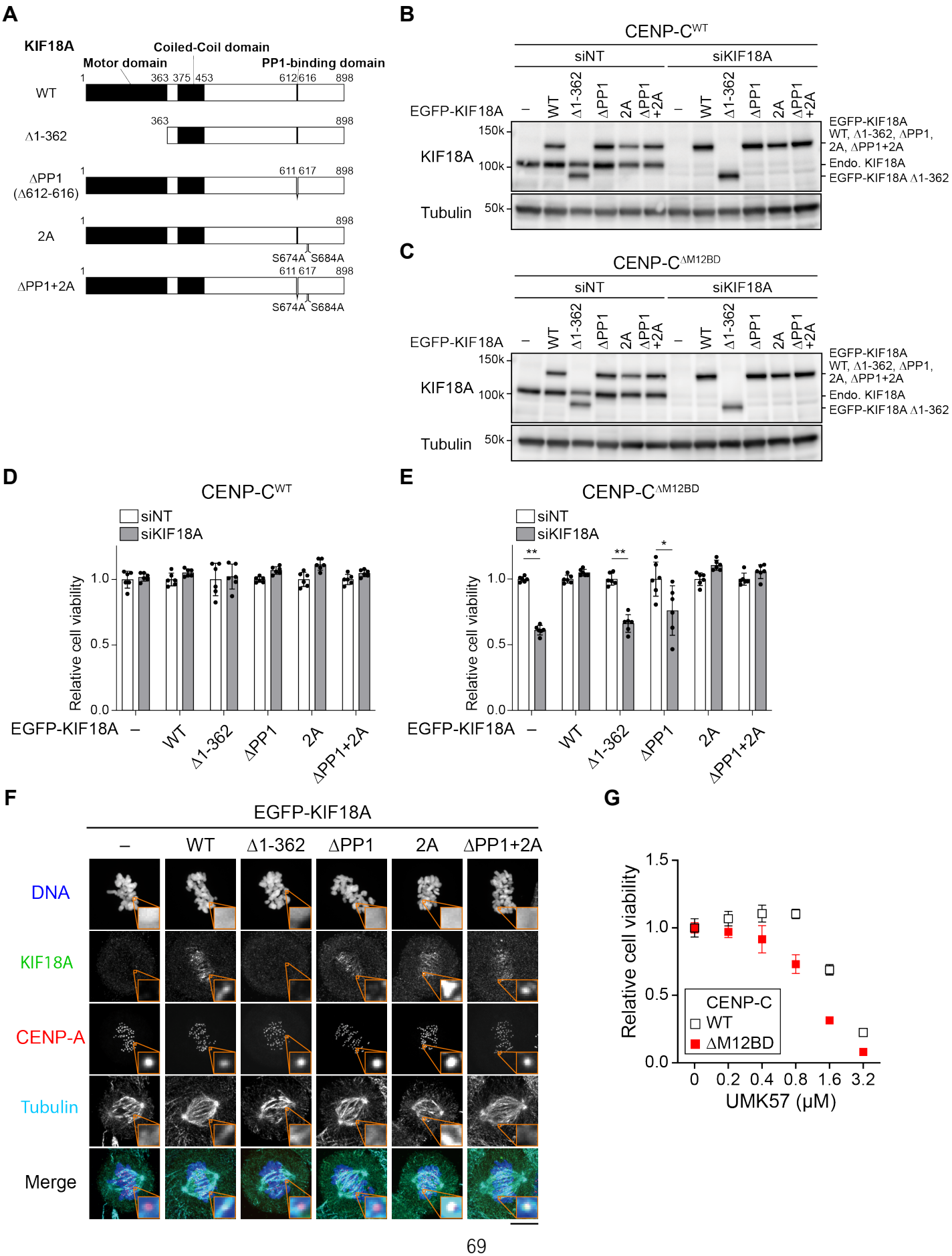

A
KIF18A
Coiled-Coil domain
Motor domain
PP1-binding domain
WT
Δ1-362
ΔPP1 (Δ612-616)
2A
ΔPP1+2A
S674A S684A
B
CENP-C^WT
siNT
siKIF18A
EGFP-KIF18A
KIF18A
Tubulin
EGFP-KIF18A WT, Δ1-362, ΔPP1, 2A, ΔPP1+2A
Endo. KIF18A
EGFP-KIF18A Δ1-362
C
CENP-C^ΔM12BD
D
CENP-C^WT
Relative cell viability
E
CENP-C^ΔM12BD
F
EGFP-KIF18A
DNA
KIF18A
CENP-A
Tubulin
Merge
G
Relative cell viability
CENP-C
WT
ΔM12BD
UMK57 (μM)

Figure 37. Microtubule plus-end localization of KIF18A is required for cell viability in RPE-1 CENP-C ΔM12BD cells.

(A) Schematic representation of wild-type KIF18A and its functional domains, including the motor domain, coiled-coil domain, and PP1 binding domain. RPE-1 cells expressing KIF18A lacking the motor domain (KIF18A Δ1-362) or PP1 binding domain (KIF18A ΔPP1) were generated. KIF18A is phosphorylated by CDK1 at S674 and S684. These phosphorylation sites are dephosphorylated by PP1 bound to KIF18A. RPE-1 cells expressing a KIF18A mutant in which S674 and S684 were replaced with Ala (KIF18A 2A) or KIF18A 2A lacking PP1 binding domain (KIF18A ΔPP1+2A) were also generated (also see Figure 35).

(B and C) Immunoblot analysis to detect WT or mutant KIF18A protein in RPE-1 CENP-C WT (B) or CENP-C ΔM12BD (C) cells with siNT or siKIF18A treatment. α-tubulin was probed as a loading control.

(D and E) Cell viability assay of RPE-1 CENP-C WT (D) or CENP-C ΔM12BD (E) cells expressing WT or various KIF18A mutants with siNT or siKIF18A treatment (Mean and SD, two-tailed Student's t-test, each sample size: n = 6; *$p < 0.1$; **$p < 0.01$).

(F) Localization of KIF18A WT and its mutants (green) at plus end of microtubules. The cells were treated with siKIF18A for 2 days before fixation. KIF18A was stained with an antibody against human KIF18A. mScarlet-CENP-A was used as a kinetochore marker (red) and microtubules were stained with an anti-α-tubulin antibody (cyan). DNA was stained with DAPI (blue). Scale bar, 10 μm.

(G) Cell viability assay of RPE-1 CENP-C WT or CENP-C ΔM12BD cells with UMK57 at various concentrations. (Mean and SD, two-tailed Student's t-test, each sample size: n = 6).

KIF18A suppresses kinetochore-microtubule dynamics, stabilizing kinetochore-microtubule attachments (Du et al., 2010). To test whether the regulation of kinetochore-microtubule dynamics is critical for the viability of CENP-C ΔM12BD RPE-1 cells, I treated the cells with the KIF2C/MCAK agonist UMK57, which destabilizes kinetochore-microtubules (Orr et al., 2016). Sublethal doses of UMK57 reduced the cell viability of CENP-C ΔM12BD RPE-1 cells (0.4-0.8 μM; Figure 37G), suggesting that CENP-C ΔM12BD RPE-1 cells require stable kinetochore-microtubules. Consistent with this result, my functional genetic screen reveals that knockout of the MCAK suppressor GTSE1 (Bendre et al., 2016) also display synthetic lethality with CENP-C ΔM12BD mutation (Figures 19B and 19D-19F).

3.8 Ndc80C or Aurora B reduction in CENP-C ΔM12BD RPE-1 cells does not cause mitotic defects after *KIF18A* knockdown

Next, I investigated what brought the *KIF18A* dependency in CENP-C ΔM12BD RPE-1 cells. The deletion of the M12BD in CENP-C reduced the kinetochore-localization of Mis12C as well as KNL1C and Ndc80C in K562 and RPE-1 cells (Figure 15B, 15D, 15E, 29B-29D). Since Ndc80C is a major microtubule-binding protein complex, to examine whether the reduction of Ndc80C sensitizes RPE-1 cells to *KIF18A* knockdown, I decreased the Ndc80C levels at kinetochore by using CENP-T mutants, which lacked a Ndc80C-binding domain (Figure 38A and 38B) (Takenoshita et al., 2022; Kong et al., 2024). Importantly, in these cells, neither Mis12C nor KNL1C levels at kinetochores were changed (Kong et al., 2024). The cell viability of the CENP-T mutants lacking each Ndc80C-binding domain was unaffected by siKIF18A treatment (Figure 38C), suggesting that the Ndc80C reduction was not the cause for *KIF18A*-KD sensitivity in CENP-C ΔM12BD RPE-1 cells.

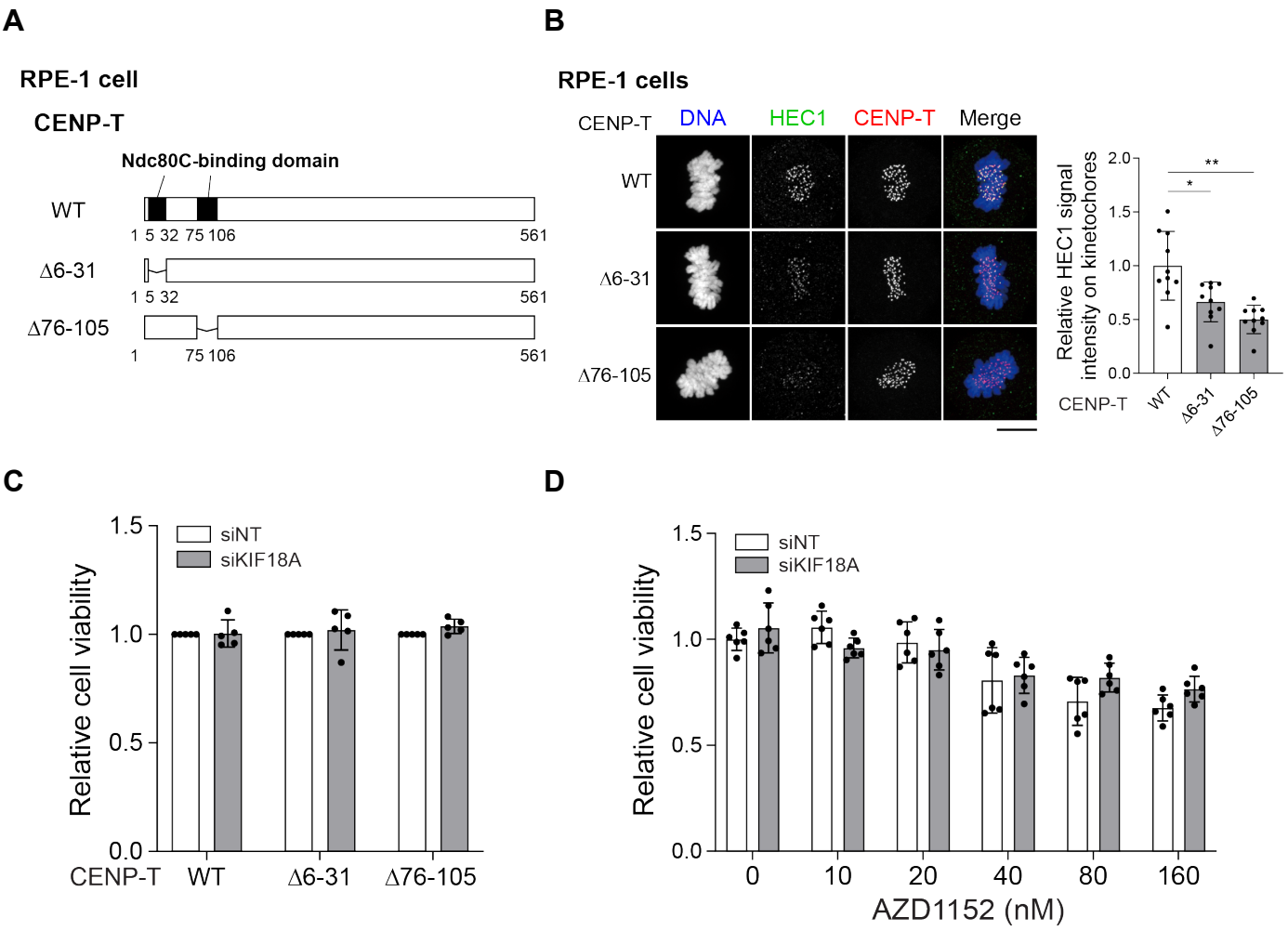


Figure 38. (A) Schematic representation of human CENP-T. Human wild-type CENP-T (WT) has two Ndc80C binding regions (amino acids 6-31 and 76-105). Each Ndc80C binding region was deleted in RPE-1 CENP-T Δ6-31 or CENP-T Δ76-105 cells, respectively. (B) HEC1 localization in RPE-1 CENP-T Δ6-31 or CENP-T Δ76-105 cells (green). CENP-T was used as a kinetochore marker (red). DNA was stained with DAPI (blue). Scale bar, 10 μm. Signal intensities of HEC1 at mitotic kinetochores in each cell line were quantified (Mean and SD, two-tailed Student's t-test, CENP-T WT cells: n = 10 cells, CENP-T Δ6-31 cells: n = 10 cells, CENP-T Δ76-105 cells: n = 10 cells; *$p < 0.1$; **$p < 0.01$). (C) Cell viability of RPE-1 CENP-T WT, CENP-T Δ6-31, or CENP-T Δ6-31 cells after treatment of siNT or siKIF18A. (Mean and SEM, two-tailed Student's t-test, n = 5 independent experiments). (D) Cell viability of RPE-1 cells in the presence of various concentration of AZD1152, an Aurora B inhibitor, with the treatment of siNT or siKIF18A. (Mean and SD, two-tailed Student's t-test, each sample size: n = 6).

Our previous study demonstrated that CENP-C ΔM12BD RPE-1 cells slightly but significantly reduced centromere localization of Aurora B, which contributes to establishment of the bipolar kinetochore-microtubule attachment (Kong et al., 2024). To test the synthetic effects of Aurora B inhibition and *KIF18A* knockdown in RPE-1 cells, I treated RPE-1 cells with the Aurora B inhibitor AZD1152 in combination with siKIF18A. As a result, siKIF18A treatment did not cause obvious changes in the cell viability of RPE-1 cells treated with sublethal levels of AZD1152 (Figure 38D). These results suggest that neither Ndc80C nor Aurora B reduction in CENP-C ΔM12BD RPE-1 cells is directly responsible for mitotic defects with *KIF18A* knockdown, indicating that there must be an alternate cause of the *KIF18A*-KD sensitivity in RPE-1 CENP-C ΔM12BD cells.

3.9 Reduction of CENP-E at the kinetochore is a major cause for the *KIF18A*-KD sensitivity of CENP-C ΔM12BD RPE-1 cells

To seek the cause of the *KIF18A*-KD sensitivity in CENP-C ΔM12BD RPE-1 cells, I closely inspected the time-lapse images for mitotic progression (Figure 33). More than 90% of control siNT-treated CENP-C WT RPE-1 cells aligned their chromosomes at the spindle equator within 25 min after NEBD (Figure 39A and 39B). In contrast, approximately 50% of siKIF18A-treated RPE-1 CENP-C WT cells still showed unaligned chromosomes at this time point, and it took more than 70 min after NEBD for 90% of cells to fully align their chromosomes (Figure 39B). CENP-C ΔM12BD RPE-1 cells treated with control siNT showed delayed chromosome congression, compared with CENP-C WT RPE-1 cells (Figure 39B). In siKIF18A-treated CENP-C ΔM12BD RPE-1 cells, the unaligned chromosomes that emerged after NEBD were sustained during observation (Figure 39B), suggesting that *KIF18A* was involved in the chromosome congression during early prometaphase and it is possible that the delayed chromosome congression in CENP-C ΔM12BD RPE-1 cells contributes to the *KIF18A*-KD sensitivity.

To examine this possibility, I closely evaluated the dynamics of unaligned chromosomes, I performed a high-resolution time-lapse imaging (Figures 39C and 39D). After NEBD, peripheral chromosomes (Figure 39C), which reside near one of

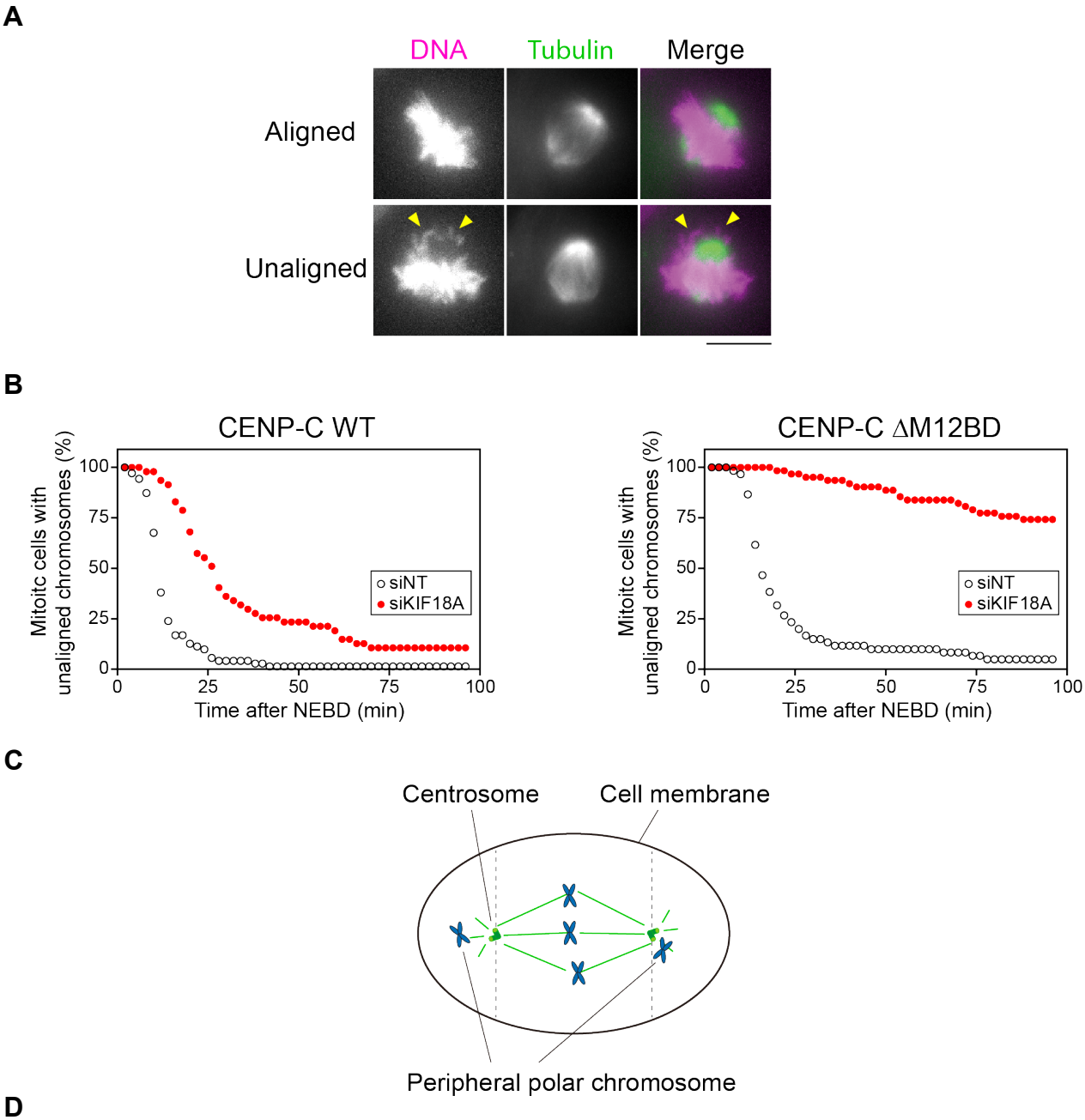

A
DNA
Tubulin
Merge
Aligned
Unaligned
B
CENP-C WT
CENP-C ΔM12BD
Mitoitc cells with unaligned chromosomes (%)
siNT
siKIF18A
Time after NEBD (min)
C
Centrosome
Cell membrane
Peripheral polar chromosome
D
RPE-1 cells
CENP-C
WT
ΔM12BD
siNT
siKIF18A
0 min
1 min
10 min
25 min
30 min
50 min
55 min
75 min
DNA
Tubulin
CENP-C^WT
CENP-C^ΔM12BD
Mitotic cells with polar chromosomes (%)

Figure 39. (A) The representative time-lapse images of unaligned or aligned chromosomes in RPE-1 cells are shown. Scale bar, 10 μm. (B) The time-lapse images in Figure 33 were inspected to assess chromosome alignment. The cells with unaligned chromosomes in RPE-1 CENP-C WT or CENP-C ΔM12BD cells treated with siNT or siKIF18A were quantified. (C) Schematic representation of peripheral chromosomes, which are located in the outside zone of two spindle poles (centrosomes). (D) Representative high-resolution time-lapse images to observe peripheral chromosome congression in RPE-1 CENP-C WT or CENP-C ΔM12BD cells treated with siNT or siKIF18A. Arrow heads indicate polar chromosomes. Scale bar, 10 μm. Population of cells with polar chromosomes in RPE-1 CENP-C WT or CENP-C ΔM12BD cells treated with siNT or siKIF18A were quantified (CENP-C WT cells with siNT: n = 25 cells, CENP-C WT cells with siKIF18A: n = 24 cells, CENP-C ΔM12BD cells with siNT: n = 25 cells, CENP-C ΔM12BD cells with siKIF18A: n = 25 cells).

the spindle poles, appeared and were aligned to the metaphase plate during mitotic progression in CENP-C WT RPE-1 cells treated with siNT (Figure 39D). The siKIF18A treatment delayed peripheral chromosome congression in RPE-1 CENP-C WT cells, suggesting that KIF18A is involved in the prevention of peripheral chromosome formation and/or peripheral chromosome congression (Figure 39D). The peripheral chromosome congression in RPE-1 CENP-C ΔM12BD cells treated with siNT occurred with a slight delay, compared with that in RPE-1 CENP-C WT cells treated with siNT (Figure 39D). In contrast, the peripheral chromosomes failed to congress to the spindle equator in RPE-1 CENP-C ΔM12BD cells treated with siKIF18A (Figure 39D). The sustained unaligned peripheral chromosomes would cause prolonged mitotic arrest, leading to severe mitotic defects, such as cohesion fatigue (Figure 33). These observations suggest that the M12BD of CENP-C is required for efficient peripheral chromosome congression and impaired chromosome congression may be a cause of *KIF18A*-KD sensitivity in RPE-1 CENP-C ΔM12BD cells.

Multiple motor proteins regulate microtubule dynamics and chromosome movements to promote chromosome congression during early prometaphase

(Risteski et al., 2021; Vukusic et al., 2022). Among them, CENP-E is an important plus-end-directed kinesin that directly contributes to the conversion of lateral to end-on kinetochore-microtubule attachments, chromosome congression, and the maintenance of alignment at the spindle equator (Kapoor et al., 2006; Kim et al., 2010; Barisic et al., 2014; Shrestha et al., 2013). I hypothesized that KIF18A is involved in chromosome congression at early prometaphase, but defects of chromosome congression in *KIF18A* knockdown might be compensated by CENP-E. However, weakened CENP-E function cause strong defects after *KIF18A* knockdown, leading to the *KIF18A*-KD sensitivity in CENP-C ΔM12BD RPE-1 cells. In support of this hypothesis 1) chromosome congression was delayed in CENP-C ΔM12BD RPE-1 cells (Figure 39B), similar to CENP-E depleted cells (Kapoor et al., 2006; Kim et al., 2010; Barisic et al., 2014); 2) a pool of CENP-E is recruited to kinetochores via BubR1, which binds to KNL1 (Ciossani et al., 2018; Legal et al., 2020), and KNL1 was reduced localization in CENP-C ΔM12BD RPE-1 cells (Figure 29D) (Kong et al., 2024); 3) CENP-E localization to kinetochores additionally relies on the RZZ complex (Cmentowski et al., 2023), and I confirmed that ZW10, which is one of the essential components for the RZZ complex, was also reduced in CENP-C ΔM12BD RPE-1 cells (Figure 40A); 4) chromosome congression mediated by CENP-E depends on stabilized microtubules (Iemura et al., 2015), which are diminished in *KIF18A* depleted cells (Mayr et al., 2007; Stumpff et al., 2008; Du et al., 2010).

To test this hypothesis, I investigated CENP-E levels at prometaphase kinetochores in CENP-C WT and CENP-C ΔM12BD RPE-1 cells. As previous reports demonstrated, CENP-E is a motor protein which is recruited to kinetochore during early prometaphase to contribute to conversion from lateral to end-on kinetochore-microtubule attachment. After kinetochore-microtubule gets stable end-on attachment, kinetochore localized CENP-E gradually decreases as dynein will strip the fibrous corona complex, including CENP-E (Itoh et al., 2018; Kim et al., 2010; Weber et al., 2024). Immunostaining for CENP-E revealed that CENP-E levels at prometaphase kinetochores were significantly reduced in CENP-C ΔM12BD RPE-1 cells (Figure 40B). In addition, CENP-E levels at kinetochores were also reduced in DSN1 2A RPE-1 cells (Figure 40C), which were also sensitive to *KIF18A* knockdown (Figure 32). Since BubR1 and ZW10 level both reduced in DSN1 2A RPE-1 cells (Figure 41), the reduced CENP-E in DSN1 2A RPE-1 cells can be expected. Taken together, these results are

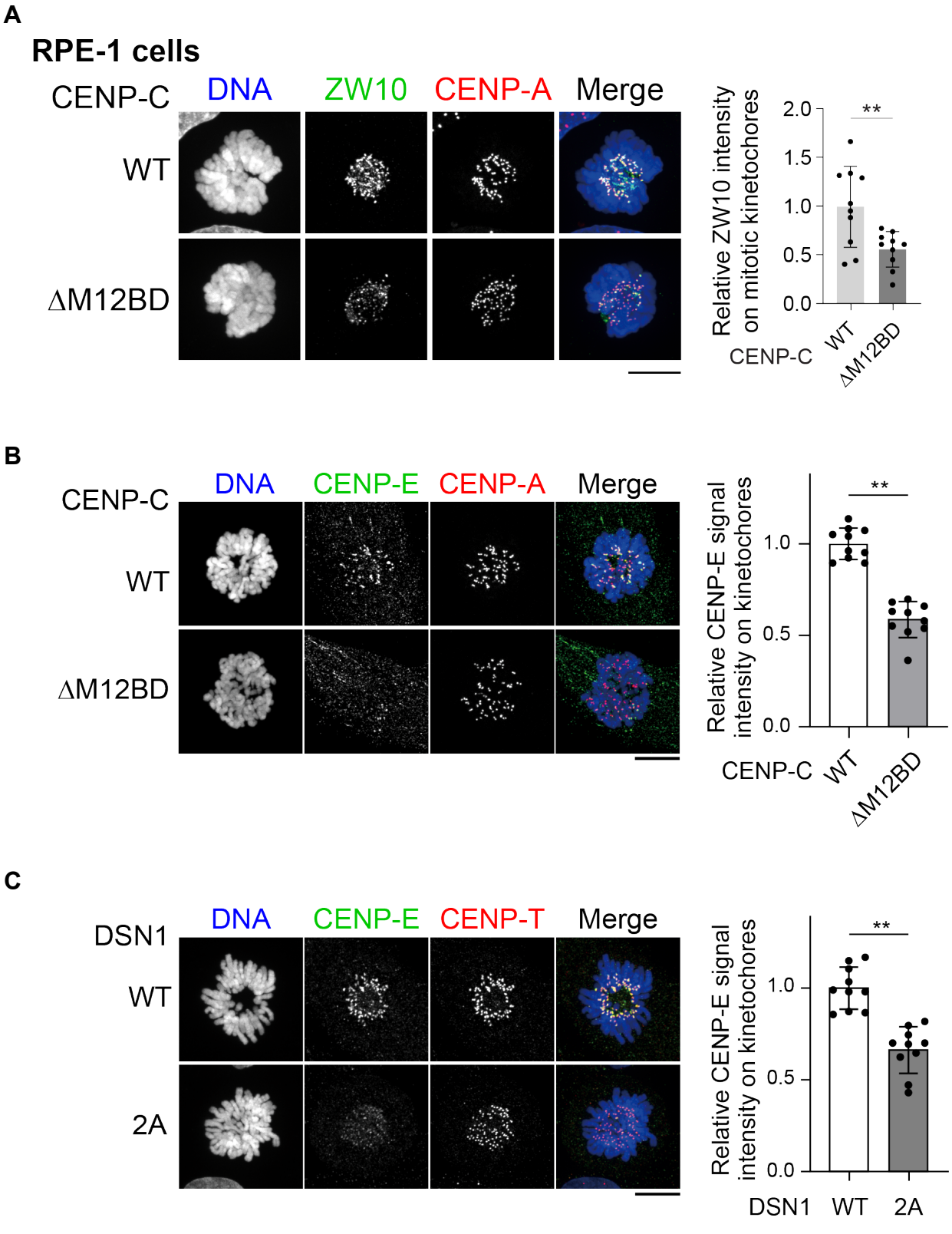

A
RPE-1 cells
CENP-C
DNA
ZW10
CENP-A
Merge
WT
ΔM12BD
Relative ZW10 intensity on mitotic kinetochores
2.0
1.5
1.0
0.5
0.0
**
CENP-C
WT
ΔM12BD
B
CENP-C
DNA
CENP-E
CENP-A
Merge
WT
ΔM12BD
Relative CENP-E signal intensity on kinetochores
1.0
0.5
0.0
**
CENP-C
WT
ΔM12BD
C
DSN1
DNA
CENP-E
CENP-T
Merge
WT
2A
Relative CENP-E signal intensity on kinetochores
1.0
0.5
0.0
**
DSN1
WT
2A

Figure 40. (A) ZW10 localization in RPE-1 CENP-C WT or CENP-C ΔM12BD cells. ZW10 was stained with an anti-ZW10 antibody (green). mScarlet-CENP-A was used as a kinetochore marker (CENP-A, red). DNA was stained with DAPI (blue). Scale bar, 10 μm. Signal intensities of ZW10 at mitotic kinetochores were quantified (Mean and SD, two-tailed Student's t-test, CENP-C WT cells: n = 10 cells, CENP-C ΔM12BD cells: n = 10 cells; n.s., non-significant; $^{**}p < 0.01$). (B) CENP-E localization in RPE-1 CENP-C WT or CENP-C ΔM12BD cells. CENP-E was stained with an anti-CENP-E antibody (green). mScarlet-CENP-A was used as a kinetochore marker (CENP-A, red). DNA was stained with DAPI (blue). Scale bar, 10 μm. Signal intensity of CENP-E at mitotic kinetochores was quantified (Mean and SD, two-tailed Student's t-test, CENP-C WT cells: n = 10 cells, CENP-C ΔM12BD cells: n = 10 cells; $^{**}p < 0.01$). (C) CENP-E localization in DSN1 WT or DSN1 2A RPE-1 cells. CENP-T was used as a kinetochore marker (CENP-T, red). CENP-E (green) and DNA (blue) were stained as in (B). Scale bar, 10 μm. Signal intensity of CENP-E at mitotic kinetochores was quantified (Mean and SD, two-tailed Student's t-test, DSN1 WT cells: n = 10 cells, DSN1 2A cells: n = 10 cells; $^{**}p < 0.01$).

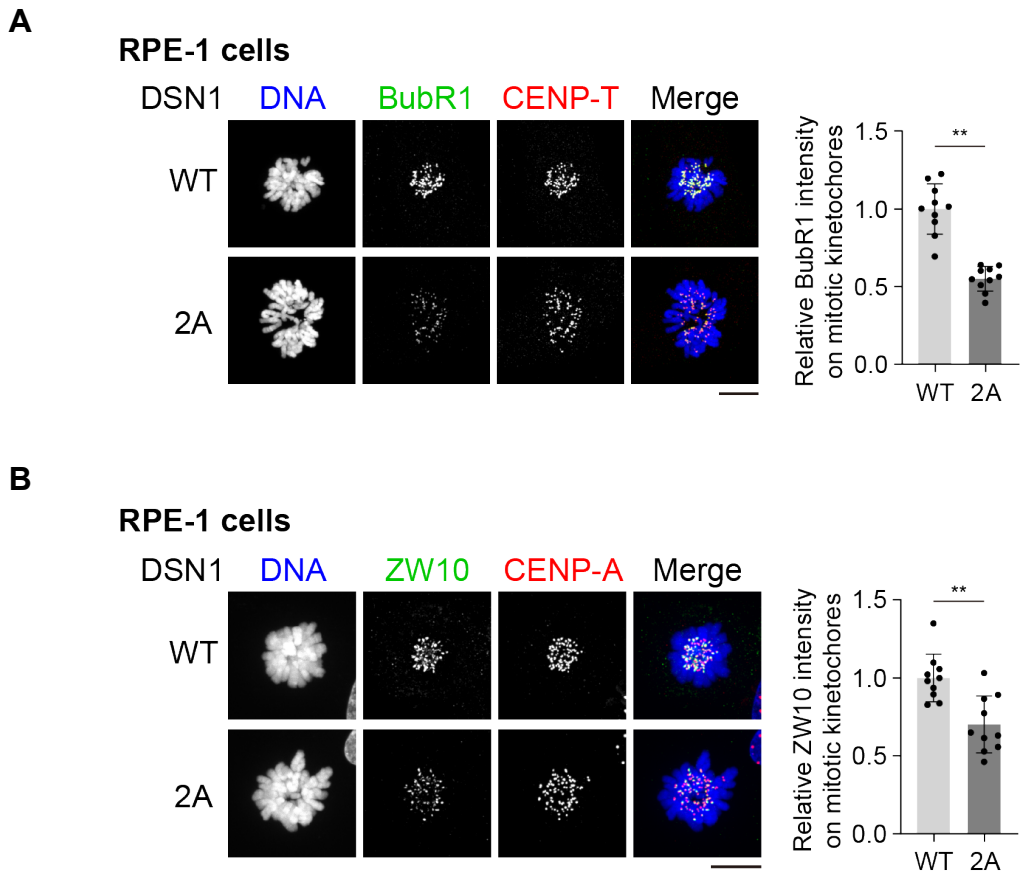


Figure 41. BubR1 (A) and ZW10 (B) localization in RPE-1 DSN1 WT or DSN1 2A cells (green). CENP-T or CENP-A was used as a kinetochore marker (red) for BubR1 and ZW10 staining, respectively. DNA was stained with DAPI (blue). Scale bar, 10 μm. Signal intensity of each protein at mitotic kinetochores was quantified (Mean and SD, two-tailed Student's t-test, DSN1 WT cells: n = 10 cells, DSN1 2A cells: n = 10 cells; $^{**}p < 0.01$).

consistent with the idea that the CENP-E reduction at kinetochores causes the *KIF18A*-KD sensitivity in CENP-C ΔM12BD RPE-1 cells.

If the CENP-E reduction at kinetochores is the cause of the *KIF18A*-KD sensitivity in CENP-C ΔM12BD RPE-1 cells, suppression of CENP-E function alone should also lead to *KIF18A*-KD sensitivity. To test this, I treated CENP-C WT RPE-1 cells with GSK923295, an inhibitor of CENP-E motor activity. Treatment with sublethal doses of GSK923295 reduced cell viability after siKIF18A treatment in RPE-1 CENP-C WT cells (Figure 42A). Thus, CENP-E inhibition results in *KIF18A*-KD sensitivity in RPE-1 cells, suggesting a functional relationship between CENP-E and KIF18A. This idea was further confirmed by UMK57 treatment, which increased microtubule dynamics. Sublethal-doses of either GSK923295 or UMK57 alone did not reduce cell viability (Figure 42B). However, their simultaneous treatment resulted in a significant reduction in cell viability (Figure 42B).

I also analyzed chromosome dynamics after NEBD in RPE-1 CENP-C WT cells treated with a sublethal dose of GSK923295, using high-resolution time-lapse imaging (Figure 42C). Although the dose of GSK923295 treatment delayed peripheral chromosome congression, eventually the chromosomes aligned to the equator (Figure 42C). By contrast, both siKIF18A and GSK923295 treatment sustained peripheral chromosomes in RPE-1 CENP-C WT cells during the observation (Figure 42C). Overall, my results suggest that CENP-E and KIF18A work together to facilitate chromosome congression during early prometaphase for proper mitotic progression. Based on these results, I concluded that the impaired CENP-E localization at kinetochores is a cause of the *KIF18A*-KD sensitivity in RPE-1 CENP-C ΔM12BD cells.

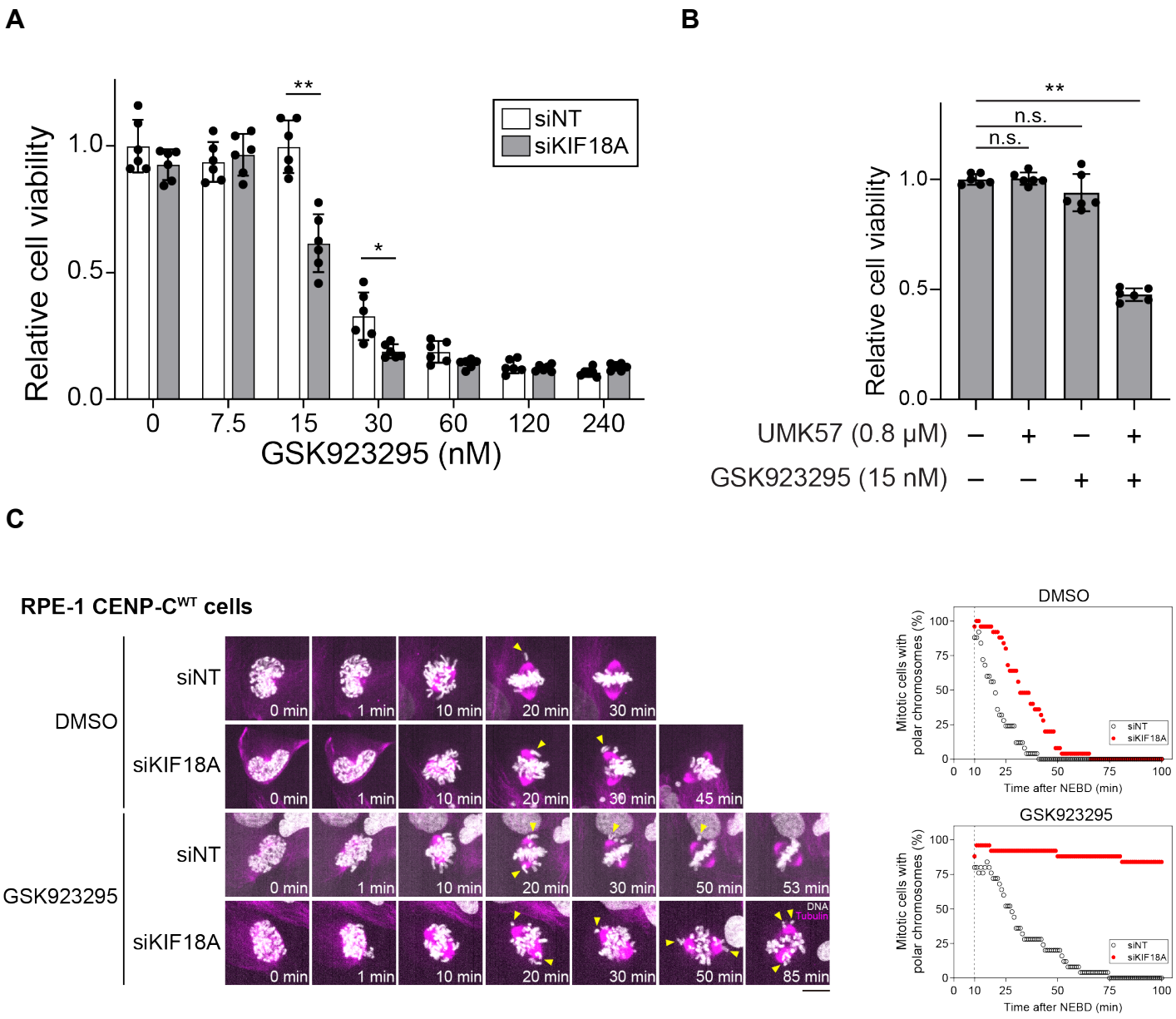
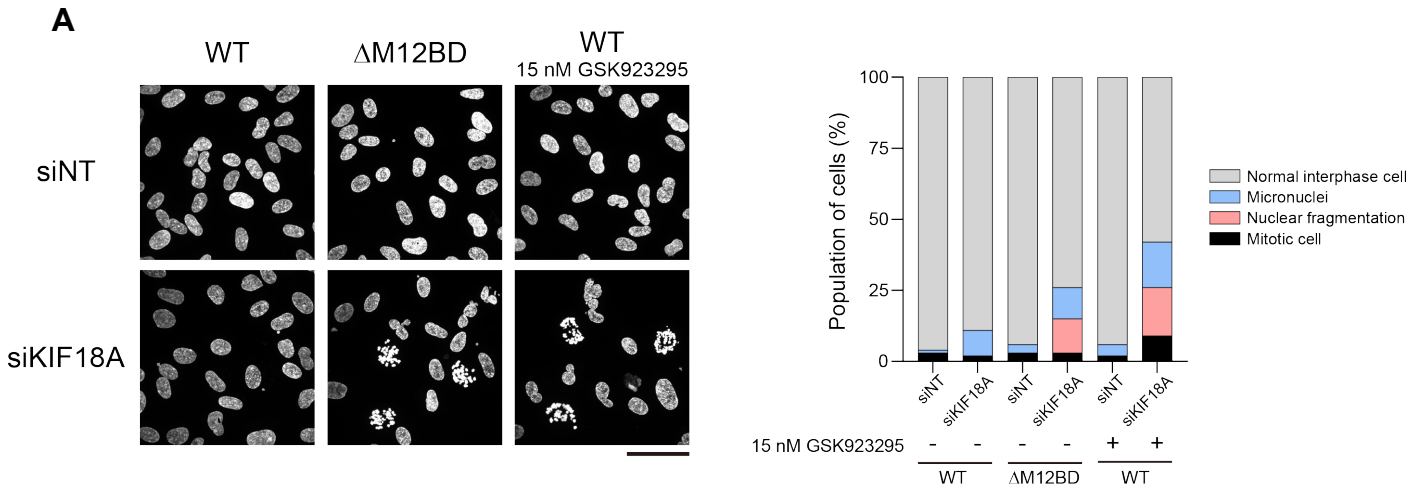

A
Relative cell viability
1.0
0.5
0.0
**
*
siNT
siKIF18A
0
7.5
15
30
60
120
240
GSK923295 (nM)
B
Relative cell viability
1.0
0.5
0.0
**
n.s.
n.s.
UMK57 (0.8 μM) – + – +
GSK923295 (15 nM) – – + +
C
RPE-1 CENP-C^WT cells
DMSO
siNT
siKIF18A
GSK923295
siNT
siKIF18A
0 min
1 min
10 min
20 min
30 min
45 min
50 min
53 min
85 min
DNA
Tubulin
DMSO
GSK923295
Mitotic cells with polar chromosomes (%)
Time after NEBD (min)
siNT
siKIF18A

Figure 42. (A) Cell viability of RPE-1 CENP-C WT cells in the presence of a CENP-E inhibitor GSK923295 at various concentrations after treatment of siNT or siKIF18A (Mean and SD, two-tailed Student's t-test, each sample size: n = 6; *p < 0.1; **p < 0.01). (B) Cell viability assay of RPE-1 CENP-C WT cells with treatment of 0.8 μM UMK57 and 15 nM GSK923295 (Mean and SD, two-tailed Student's t-test, RPE-1 cells neither UMK57 nor GSK923295: n = 6, RPE-1 cells with UMK57 but without GSK923295: n = 6, RPE-1 cells without UMK57 but with GSK923295: n = 6, RPE-1 cells with both UMK57 and GSK923295: n = 6; n.s., non-significant; **p < 0.01). (C) Representative high-resolution time-lapse images to observe peripheral chromosome congression in RPE-1 CENP-C WT cells treated with siNT or siKIF18A in the presence or absence of a CENP-E inhibitor GSK923295. Arrow heads indicate peripheral chromosomes. Scale bar, 10 μm. The population of cells with polar chromosomes in the indicated experimental samples was quantified (DMSO CENP-C WT cells with siNT: n = 25 cells, DMSO CENP-C WT cells with siKIF18A: n = 25 cells, GSK923295 CENP-C WT cells with siNT: n = 25 cells, GSK923295 CENP-C WT cells with siKIF18A: n = 25 cells).

3.10 CENP-E inhibition causes mitotic defect after *KIF18A* knockdown

I demonstrated that *KIF18A* knockdown caused cell death and mitotic defect in CENP-C ΔM12BD RPE-1 cells. Under the microscope observation, CENP-C ΔM12BD RPE-1 cells were arrested in mitosis after treatment of siKIF18A (Figure 43A), quantification results indicate that the cells with micronuclei and nuclear fragmentation were increased. A similar phenotype was observed after the simultaneous treatment of 15 nM GSK923295 and siKIF18A in CENP-C WT RPE-1 cells (Figure 43A). 15 nM GSK923295 is a sublethal level for CENP-C WT RPE-1 cells. Single treatment of either GSK923295 or siKIF18A alone did not cause obvious defects in CENP-C WT RPE-1 cells, however their simultaneous treatment resulted in a significant increasement of cells with micronuclei or nuclear fragmentation (Figure 43A). These phenotypes are terminal phenotypes of mitotic arrest, which indicate the consequence of long-time mitotic arrested cells.

As I previously confirmed that treatment of 0.8 μM UMK57 and 15 nM GSK923295 together caused cell death in CENP-C WT RPE-1 cells, I tested whether their treatment would also cause mitotic defects or not. I observed the cells under the microscope to examine the phenotype after treatment of UMK57 and GSK923295. Sublethal-doses of either GSK923295 or UMK57 alone did not cause obvious mitotic defects in CENP-C WT RPE-1 cells. However, their simultaneous treatment resulted in a significant increase of cells with mitotic defects (Figure 43B and 43C), the population of cells with micronuclei and nuclear fragmentation was increased. This suggests that the subsequent cell death observed following simultaneous treatment of UMK57 and GSK923295 is due to mitotic defects.



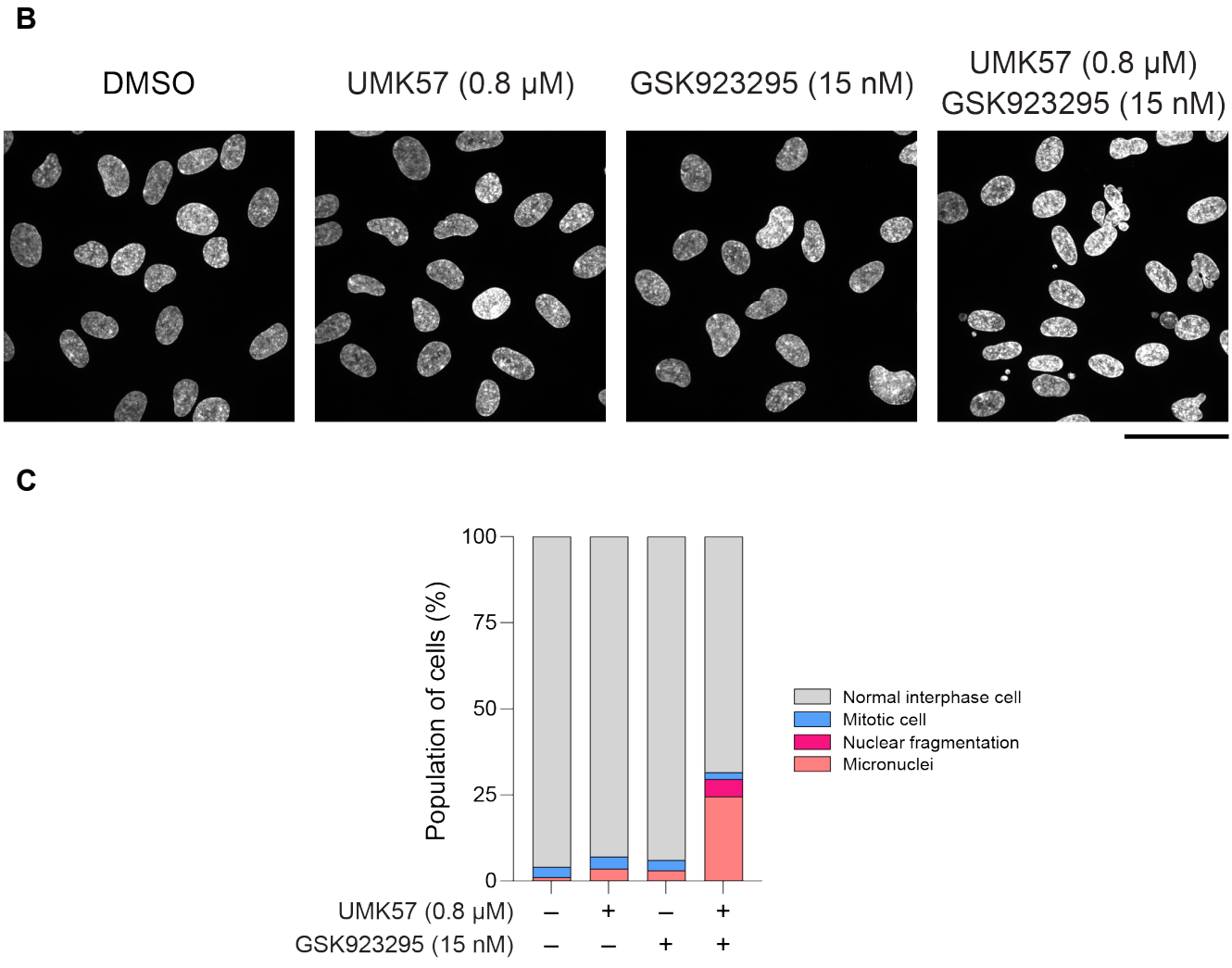


Figure 43. (A) *KIF18A* knockout cause micronuclei or nuclear fragmentation in GSK923235 treated CENP-C WT cells. Scale bar, 50 μm. Single treatment of either 15 nM GSK923295 or siKIF18A alone did not cause obvious defection in RPE-1 CENP-C WT cells, however their simultaneous treatment resulted in a significant increasement of cells with micronuclei or nuclear fragmentation. (B) Sublethal-doses of either GSK923295 or UMK57 alone did not cause obvious mitotic defects in RPE-1 CENP-C WT cells. However, their simultaneous treatment resulted in a substantial increase of cells with mitotic defects. (C) Quantification of mitotic defect of cells from (B).

3.11 CENP-E levels were significantly reduced in cancer cell lines showing sensitivity to *KIF18A* knockdown

The sensitivity to *KIF18A* knockdown or inactivation is observed in multiple cancer cell lines (Gliech et al., 2024; Cohen-Sharir et al., 2021; Marquis et al., 2021). Previous studies found that aneuploidy and weakened anaphase-promoting complex/cyclosome activity were the causes of the vulnerability to *KIF18A* inactivation in some cancer cell lines (Gliech et al., 2024; Cohen-Sharir et al., 2021; Marquis et al., 2021). Furthermore, my experiments revealed that *KIF18A* knockdown decreases the cell viability in CENP-C ΔM12BD RPE-1 cells (Figure 30B). Importantly, I demonstrated that the reduced kinetochore localization of CENP-E is the critical determinant of *KIF18A*-KD sensitivity in RPE-1 cells. This finding prompted me to examine *KIF18A*-KD sensitivity and CENP-E kinetochore localization across different cancer or non-cancer cell lines. I tested RPE-1, K562, U2OS, A549, TIG-3, HeLa, HT1080, OVCAR-3, HT29 and HCC1806 (Figures 44A and 44B). To precisely quantify CENP-E levels among different cell types, cells were treated with 50 μM monastrol for 2 h, then each tested cell line was collected and mixed with RPE-1 mScarlet-CENP-A cells as an internal control. CENP-E signal intensities at prometaphase kinetochores in RPE-1, K562, U2OS, A549, TIG-3, HeLa, HT1080, OVCAR-3, HT29 or HCC1806 cells were quantified and normalized with those signal intensities in mScarlet-CENP-A RPE-1 cells in each sample. As shown in Figure 44A, in addition to RPE-1 and K562 cells, U2OS, A549 and TIG-3 cells were insensitive to *KIF18A* knockdown. By contrast, HeLa, HT1080, OVCAR-3, HT29 and HCC1806 were sensitive to *KIF18A* knockdown (Figure 44A). The CENP-E levels at kinetochores were significantly lower in the *KIF18A*-KD sensitive cell lines, but not in the *KIF18A*-KD insensitive cells, compared to those in RPE-1 cells (Figure 44B). I also measured CENP-C and CENP-T levels at kinetochores in these cell lines (Figure 44C and 44D). CENP-C and CENP-T were reduced in HT29 and HCC1806, but not in HeLa, HT1080 and OVCAR-3 cells, suggesting that there were various ways to reduce CENP-E localization at kinetochores among cancer cell lines. In any case, my results demonstrated a correlation between the reduction in kinetochore-localized CENP-E and *KIF18A*-KD sensitivity in all tested cell lines. Thus, reduction of CENP-E levels or activity at kinetochores could serve as potential markers for vulnerability to KIF18A inactivation in cancer cell lines.

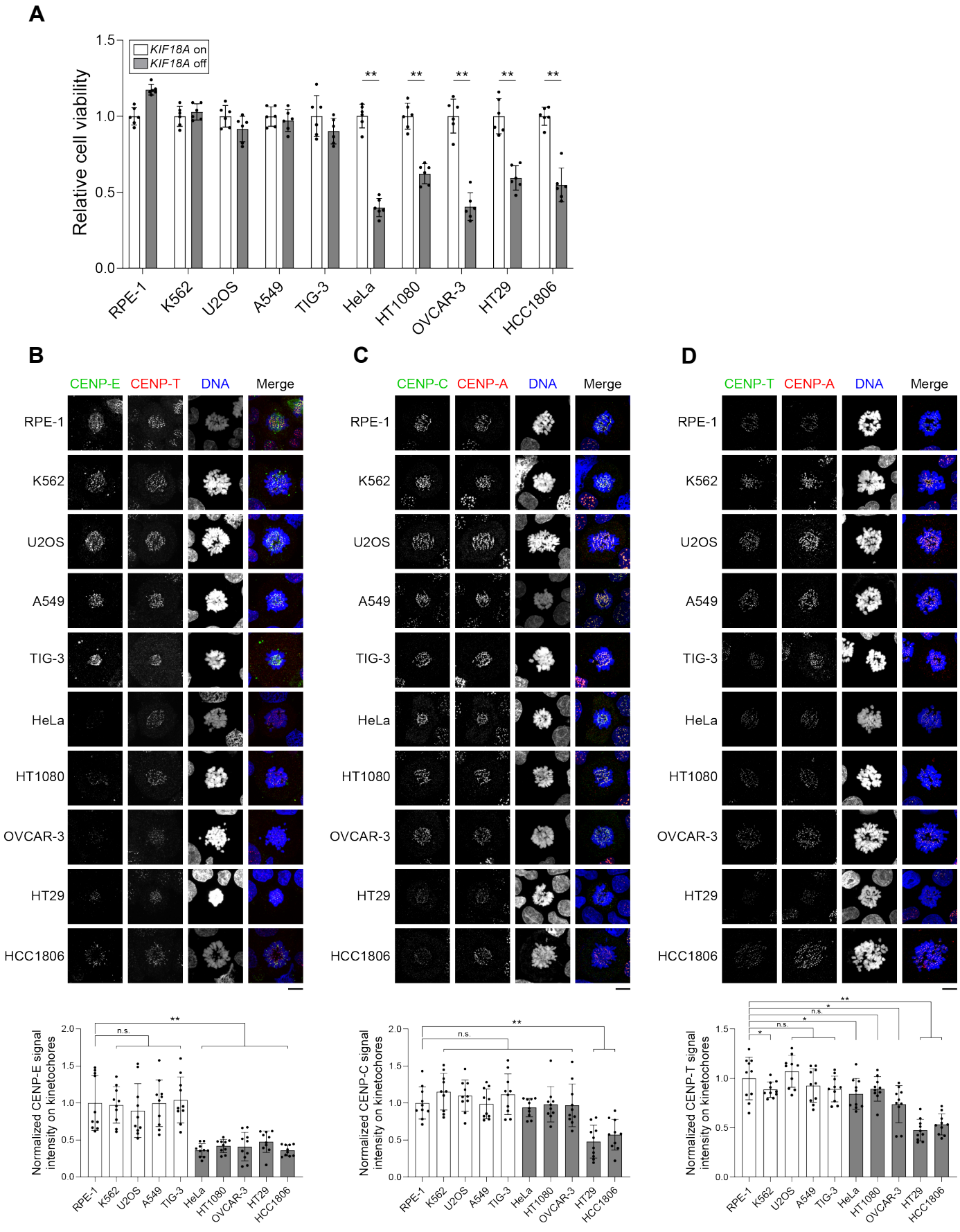

A
Relative cell viability
KIF18A on
KIF18A off
RPE-1
K562
U2OS
A549
TIG-3
HeLa
HT1080
OVCAR-3
HT29
HCC1806
B
CENP-E
CENP-T
DNA
Merge
C
CENP-C
CENP-A
D
Normalized CENP-E signal intensity on kinetochores
Normalized CENP-C signal intensity on kinetochores
Normalized CENP-T signal intensity on kinetochores
n.s.

Figure 44. CENP-E levels are reduced in cancer cell lines sensitive to *KIF18A* knockdown. (A) Cell viability of RPE-1, K562, U2OS, A549, TIG-3, HeLa, HT1080, OVCAR-3, HT29 and HCC1806 cells with or without *KIF18A* knockdown. (Mean and SD, two-tailed Student's t-test, each sample size: n = 6; $^{**}p < 0.01$). (B-D) CENP-E (B), CENP-C (C), and CENP-T (D) localization in RPE-1, K562, U2OS, A549, TIG-3, HeLa, HT1080, OVCAR-3, HT29 and HCC1806 cells. The cell lines were treated with 50 μM Monastrol for 2 h to enrich prometaphase cells. Each cell line was cytospan together with Monastrol-treated RPE-1 cells expressing mScarlet-CENP-A as an internal control for immunostaining. CENP-E was stained with an anti-CENP-E antibody (green) (B). CENP-C was stained with an anti-CENP-C antibody (green) (C). CENP-T was stained with an anti-CENP-T antibody (green) (D). DNA was stained with DAPI (blue). CENP-T or CENP-A was stained as a kinetochore marker (red). Scale bar, 10 μm. CENP-E, CENP-C or CENP-T signal intensities at mitotic kinetochores were quantified and normalized with those from the internal control mScarlet-CENP-A RPE-1 in each sample (Mean and SD, two-tailed Student's t-test, each cell line: n = 10 cells; n.s., non-significant; $^{*}p < 0.1$; $^{**}p < 0.01$).

4. A proposed model to demonstrate the correlation between KIF18A and CENP-E during mitosis

After the cells complete chromosome replication, they enter mitosis. During mitosis, nuclear envelope breakdown (NEBD) firstly occurs to release the chromosomes into the cytoplasm. In early prometaphase, CENP-E is recruited to the kinetochore to facilitate its attachment to the lateral sides of microtubules, a process known as lateral attachment. The kinetochore then moves along the lateral sides of microtubules toward the plus end of the microtubules. Meanwhile, KIF18A accumulates at the microtubule plus end to suppress microtubule dynamics, which is important for the stable binding of the kinetochore to the microtubule tip.

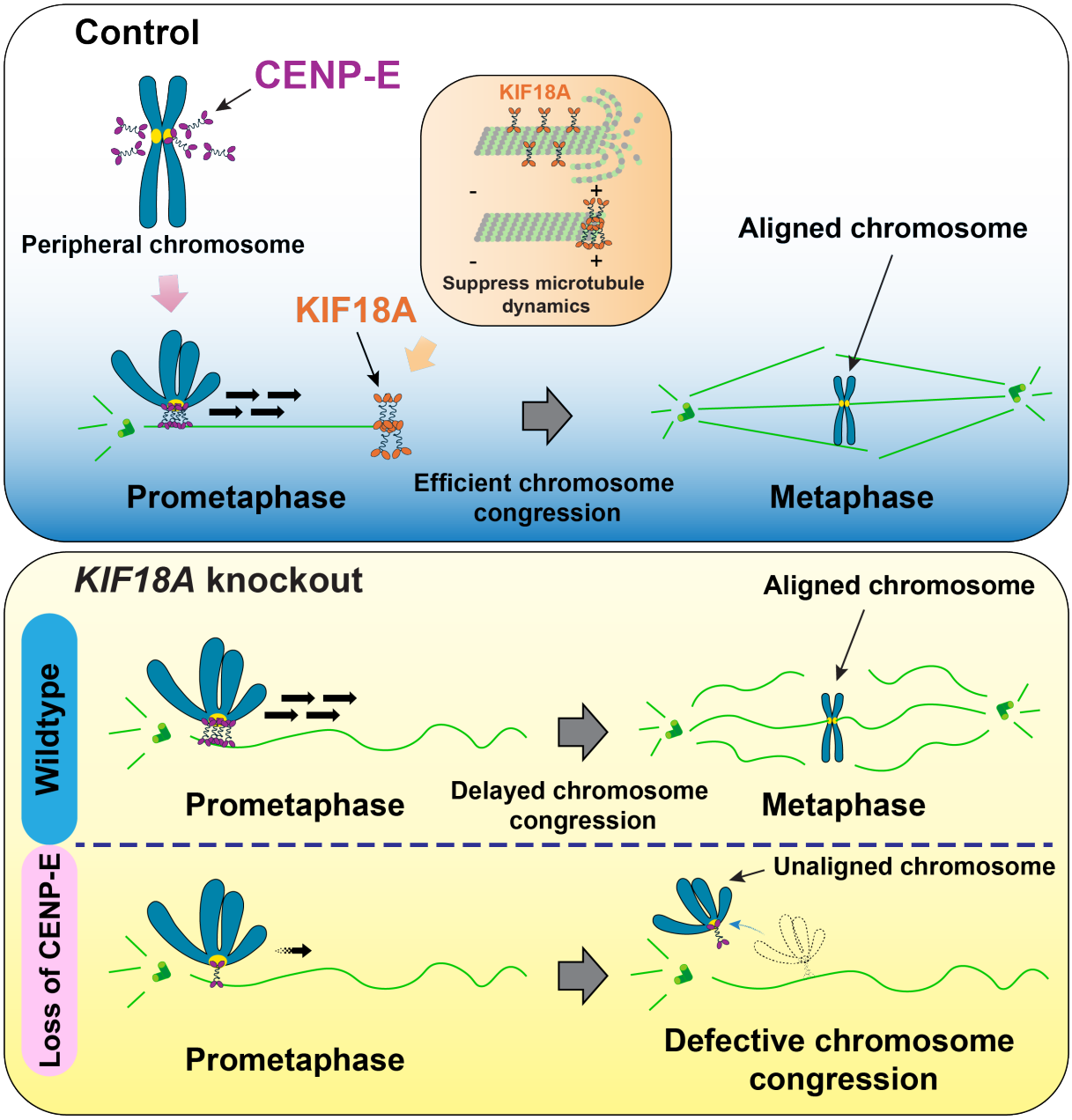
In normal cells, peripheral chromosomes efficiently move along microtubules due to the sufficient amount of CENP-E localized at kinetochores. At the same time, the microtubule tips remain stable because the accumulation of KIF18A suppresses microtubule dynamics. As a result, chromosomes achieve efficient congression and alignment in metaphase. Subsequently, the cell undergoes faithful chromosome segregation and was divided without any problems (Figure 45A).

When *KIF18A* is knocked down, microtubule dynamics become highly activated, leading to bent and excessively long microtubules. Misaligned chromosomes are significantly increased at early prometaphase, suggesting that KIF18A has a certain role for chromosome congression. However, as the chromosomes in these cells still maintain sufficient levels of CENP-E at kinetochores, misaligned chromosomes are easily fixed and move along the microtubules to their plus ends, and form end-on kinetochore-microtubule attachments. Although the chromosome congression process is prolonged, the cell can still undergo chromosome segregation and complete cell division. Nevertheless, this prolonged congression often leads to subtle mitotic defects, such as lagging chromosomes or chromosome missegregation (Figure 45A).

In CENP-E deficient cells such as CENP-C ΔM12BD cells or certain cancer cell lines like HeLa cells, *KIF18A* knockdown results in highly activated microtubule dynamics and elongated microtubules, meanwhile level of kinetochore-localized CENP-E is low. As a consequence, kinetochores are unable to achieve stable attachment to the lateral side of microtubules and making the long-distance lateral to

end-on transition defectively. Therefore, chromosome congression does not successfully proceed. During this impaired chromosome congression process, chromosomes are prone to detaching from microtubules, resulting in unaligned chromosomes. Consequently, the cells will be arrested in prometaphase and eventually undergo cell death (Figure 45B).

A



B

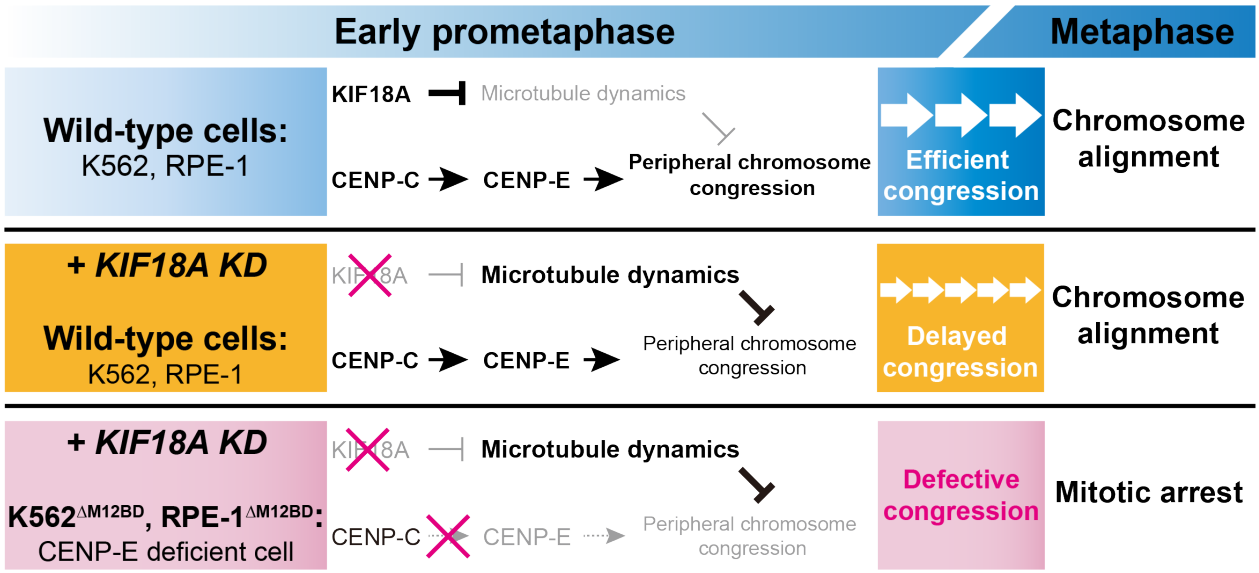


Figure 45. KIF18A and CENP-E cooperatively function for the congression of peripheral chromosomes at early prometaphase.

(A and B) In wild-type K562 and RPE-1 cells, although *KIF18A* depletion enhances microtubule dynamics and increases peripheral chromosomes, CENP-E downstream of CENP-C compensates for *KIF18A* depletion, supporting chromosome congression and alignment, albeit with a delay in the congression. By contrast, in CENP-E deficient cells (for example K562 CENP-C ΔM12BD and RPE-1 CENP-C ΔM12BD cells), *KIF18A* depletion disrupts chromosome congression due to weakened CENP-E activity downstream of CENP-C at kinetochores, leading to mitotic arrest and subsequent cell death. Based on these observations, I propose that the CENP-C pathway plays a role in chromosome congression, with KIF18A and CENP-E acting cooperatively to promote the congression of peripheral chromosomes during early prometaphase in wild-type K562 and RPE-1 cells. KIF18A suppresses microtubule dynamics to facilitate congression and/or prevent the formation of peripheral chromosomes. CENP-E also plays a key role in efficient chromosome congression by gliding kinetochores along microtubules.

5. Discussion

In the previous section, I proposed a model which explains why *KIF18A* knockout results in lethality in CENP-C ΔM12BD cells. The key mechanism is the significant reduction of CENP-E at the kinetochores in CENP-C ΔM12BD cells. Proper localization of CENP-E to kinetochores is highly dependent on the intrinsic condition of the kinetochore itself. When the structural integrity or the amount of kinetochore components is compromised, the formation of the fibrous corona is readily impaired, consequently leading to a dramatic reduction of outer kinetochore-associated CENP-E. Although reduced CENP-E alone does not immediately compromise cell viability, it significantly slows down chromosome congression. Under this circumstance, cells could still manage to complete mitosis and survive, because KIF18A can remain functional and is able to regulate microtubule dynamics, maintaining the necessary spindle microtubule stability. However, once KIF18A is inactivated in cells with less CENP-E, microtubule dynamics become excessively active and microtubules grow abnormally long, these concurrent changes severely disrupt chromosome congression. Given that CENP-E levels are already low and initial kinetochore–microtubule wall attachments are weakened, the combined effects render chromosome congression exceptionally difficult, ultimately causing cells to be arrested in prometaphase and fail to complete mitosis. This phenomenon reveals a remarkable backup mechanism for chromosome congression, where CENP-E or KIF18A can compensate for chromosome congression in either KIF18A- or CENP-E-deficient cells, respectively. When one factor is compromised, the presence of the other allows chromosome congression to happen. It was hard to identify such a redundant pathway in previous studies. While it has long been hypothesized that cells employ multiple pathways to ensure accurate mitotic progression, experimental evidence has been limited. In my study, I approached the problem using a hypomorphic CENP-C mutant combined with a genome-wide CRISPR screening, through which I can identify KIF18A and propose that KIF18A function chromosome congression in cooperation with CENP-E. This ultimately led to the discovery of a previously unrecognized dual-insurance mechanism for mitotic fidelity.

In addition to the above-mentioned experiments, I performed some further experiments to clarify KIF18A functions. While it is difficult to interpret some of the

findings, but I will propose my hypotheses based on current results. I firmly believe that these remaining questions will be answered with continued efforts in the future research.

5.1 *KIF18A*-KD reduced kinetochore localized CENP-E level

A previous study demonstrated that *KIF18A*-KD could reduce stability of CENP-E in HeLa cells (Huang et al., 2009). In this report, *KIF18A*-KD reduced total protein level of CENP-E. I examined levels of CENP-E at kinetochores after siKIF18A treatment in RPE-1 cells (Figure 46A). I found that *KIF18A*-KD reduced CENP-E level in both CENP-C WT and CENP-C ΔM12BD RPE-1 cells (Figure 46A). This is consistent with the previous report. Although it is still unknown why *KIF18A*-KD caused reduction of CENP-E level at kinetochores, CENP-E might be directly associated with KIF18A. As a possibility, microtubule dynamics might regulate CENP-E levels at kinetochores, because *KIF18A*-KD increases microtubule dynamics. In the previous section I demonstrated that the treatment of UMK57 showed similar phenotype of *KIF18A*-KD (Figure 37G, 42B, 43B and 43C). Interestingly, sublethal level of UMK57 treatment did not alter levels of CENP-E at kinetochores in RPE-1 cells (Figure 46B). These concentration of UMK57 (0.4 μM – 0.8 μM) is sufficient to cause growth defect in CENP-C RPE-1 ΔM12BD cells (Figure 37G). This result indicates that the microtubule dynamic is not directly related with the localization of CENP-E during prometaphase.

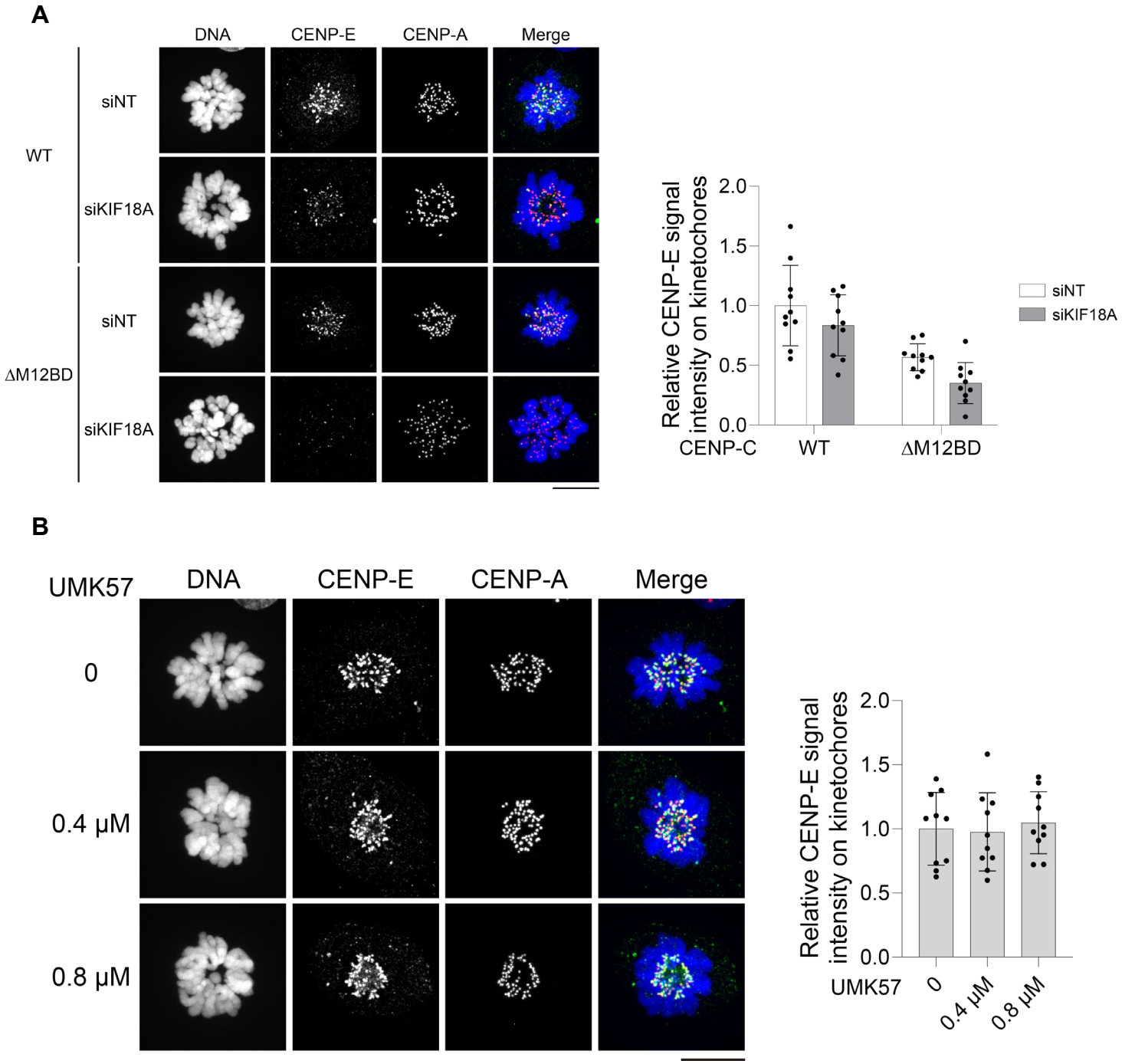


Figure 46. (A) CENP-E localization after *KIF18A* knockout. CENP-E was stained with an anti-CENP-E antibody (green). mScarlet-CENP-A was used as a kinetochore marker (CENP-A, red). DNA was stained with DAPI (blue). Scale bar, 10 μm. Signal intensity of CENP-E at mitotic kinetochores was quantified (Mean and SD, CENP-C WT cells: n = 10 cells, CENP-C ΔM12BD cells: n = 10 cells). (B) CENP-E localization after UMK57 treatment. CENP-E was stained as in (A), scale bar, 10 μm, Signal intensity of CENP-E at mitotic kinetochores was quantified (Mean and SD, CENP-C WT cells: n = 10 cells, CENP-C ΔM12BD cells: n = 10 cells).

5.2 Reduced CENP-E level in CENP-C ΔM12BD cells is not primarily due to CENP-E removal

My lab's previous study has shown that CENP-C ΔM12BD RPE-1 cells were significantly reduced levels of kinetochore/centromere-localized Aurora B kinase (Kong et al., 2024). Then in my study, I proposed the reduced CENP-E activity as the main cause of the synthetic lethality between CENP-C ΔM12BD and KIF18A. In the previous section I examined the impact of Aurora B inhibition in *KIF18A*-depleted RPE-1 cells and found no obvious changes in the cell viability of *KIF18A*-depleted RPE-1 cells treated with low dose of the Aurora B inhibitor AZD1152 (Figure 38D). Because of this result, I proposed that Aurora B reduction in RPE-1 CENP-C ΔM12BD cells cannot be directly responsible for mitotic defects induced by *KIF18A* knockdown. However, it is evident that 40 – 160 nM concentration of AZD1152 is toxic both for the siNT and siKIF18A cells, which may mask eventual contribution of the reduced kinetochore/centromere-localized Aurora B to the cell survival of *KIF18A*-depleted CENP-C ΔM12BD cells. Moreover, reduced Aurora B activity was shown to reduce the activity of CENP-E and induce its removal from kinetochores (Eibes et al., 2023). Following this point, it is possible that the reduced CENP-E level observed in CENP-C ΔM12BD cells is attributable to the decreased level of kinetochore/centromere-localized Aurora B, which subsequently facilitates CENP-E removal from kinetochores. To test whether the CENP-E kinetochore levels are reduced in CENP-C ΔM12BD cells (Figure 40B) due to the CENP-E loading or removal, the control prometaphase cells are compared to high-dose nocodazole-treated cells in both RPE-1 WT and CENP-C ΔM12BD cells (Figure 47). I found that CENP-E levels are increased in nocodazole-treated cells compared with those in untreated cells. Nevertheless, CENP-E levels were reduced in CENP-C ΔM12BD cells even after nocodazole treatment (Figure 47). Since I confirmed that both ZW10- and BubR1-mediated CENP-E loading pathways are reduced in CENP-C ΔM12BD cells (Figure 40A) (Kong et al., 2024), I conclude that the decreased CENP-E level in CENP-C ΔM12BD cells is primarily due to weakened CENP-E loading activity.

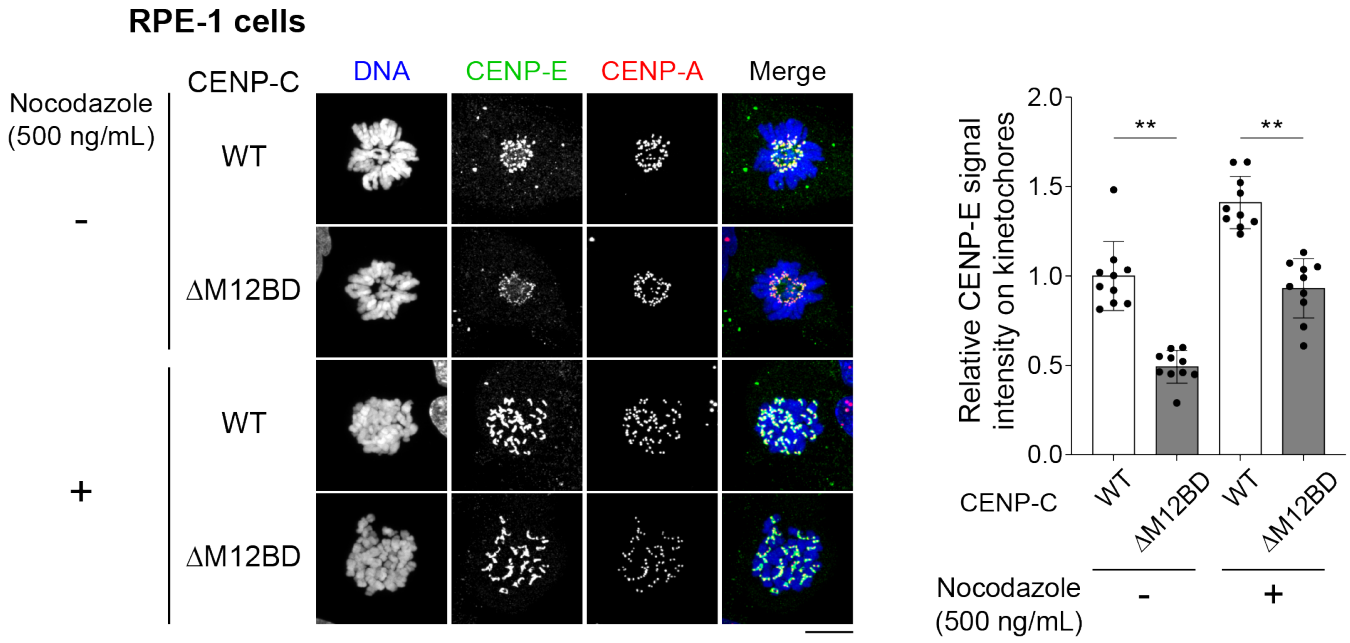


Figure 47. CENP-E localization in RPE-1 CENP-C WT or CENP-C ΔM12BD cells in the presence or absence of 500 ng/mL nocodazole treatment for 6 h. CENP-E was stained with an anti-CENP-E antibody (green). mScarlet-CENP-A was used as a kinetochore marker (CENP-A, red). DNA was stained with DAPI (blue). Scale bar, 10 μm. Signal intensity of CENP-E at mitotic kinetochores was quantified (Mean and SD, two-tailed Student's t-test, CENP-C WT cells: n = 10 cells, CENP-C ΔM12BD cells: n = 10 cells; $^{**}p < 0.01$).

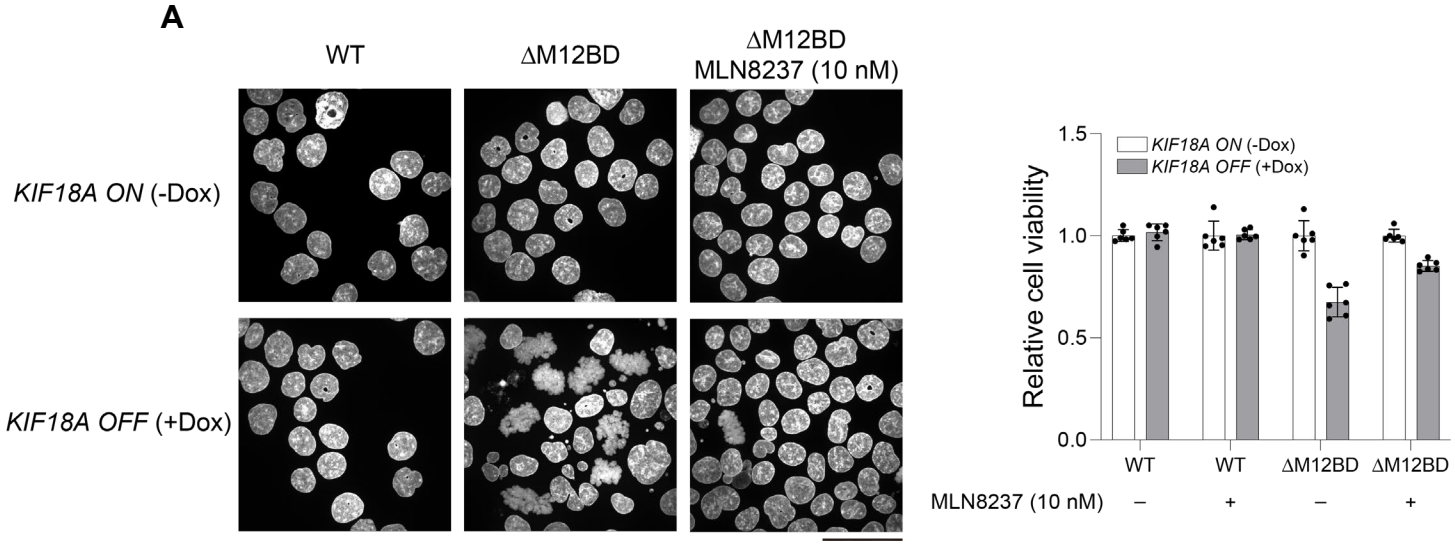
5.3 Aurora A inhibition rescued *KIF18A*-KD sensitivity in CENP-C ΔM12BD K562 and RPE-1 cells and HeLa cells

In Aurora B inhibition experiments, I proposed that reduced Aurora B might not be directly related with *KIF18A*-KD sensitivity in CENP-C ΔM12BD cells. However, a recent report suggests that Aurora A and Aurora B facilitate for the maintenance of CENP-E at the kinetochore (Eibes et al., 2023). Therefore, I tested Aurora A inhibition to examine the viability and phenotype in CENP-C ΔM12BD cells after *KIF18A*-KD. Surprisingly, Aurora A inhibition rescued *KIF18A*-KD sensitivity in CENP-C ΔM12BD K562 and RPE-1 cells. 10 nM treatment of Aurora A inhibitor MLN8237 rescued cell viability in CENP-C ΔM12BD K562 cells after *KIF18A*-KD (Figure 48A). I found that *KIF18A*-KD caused mitotic arrest in K562 CENP-C ΔM12BD cells, but this mitotic arrest could be rescued by 10 nM MLN8237 treatment, indicating that Aurora A inhibition rescued the cell division defect (Figure 48A). Then I investigated cell viability of MLN8237 treated HeLa and CENP-C ΔM12BD RPE-1 cells after *KIF18A*-KD. As I mentioned in previous section, wild-type HeLa cells show *KIF18A*-KD sensitivity like CENP-C ΔM12BD RPE-1 cells (Figure 44A). In HeLa cells, 2.5 nM – 5 nM MLN8237 treatment is sufficient to rescue *KIF18A*-KD sensitivity and in CENP-C ΔM12BD RPE-1 cells, 5 nM – 10 nM MLN8237 treatment is sufficient to rescue *KIF18A*-KD sensitivity (Figure 48B and 48C). These results indicate that Aurora A inhibition rescued *KIF18A*-KD sensitivity in CENP-C ΔM12BD K562 cells, CENP-C ΔM12BD RPE-1 cells and HeLa cells.

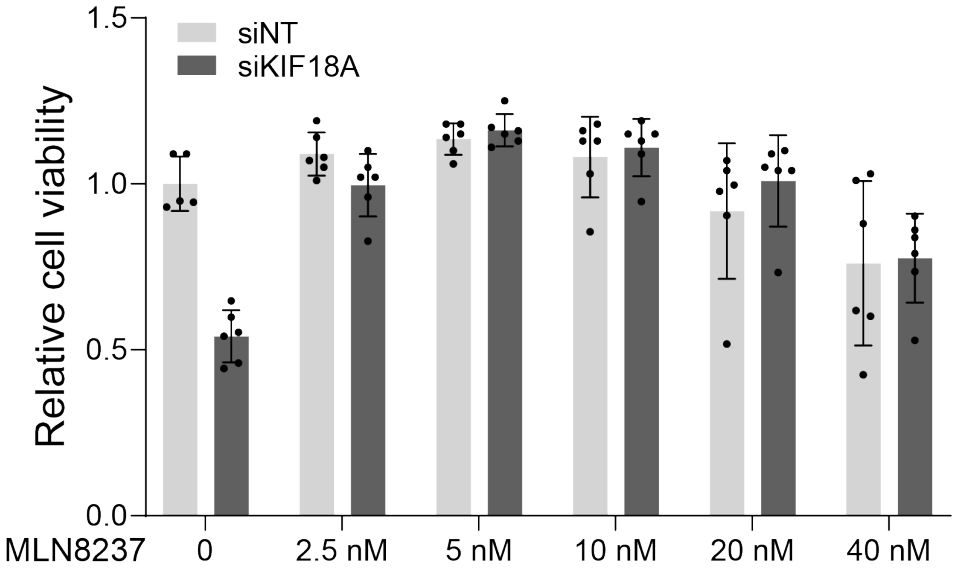
Since the substrates of Aurora A and Aurora B are common, it may be possible that Aurora B inhibition could also rescue *KIF18A*-KD sensitivity. However, Aurora B inhibition did not rescue *KIF18A*-KD sensitivity in CENP-C ΔM12BD RPE-1 cells (Figure 49A). This indicates that Aurora A inhibition specifically rescues *KIF18A*-KD sensitivity.

How is Aurora A involved in the *KIF18A*-KD sensitivity? To get a clue, I compared Aurora A levels of RPE-1 CENP-C WT with those of CENP-C ΔM12BD RPE-1 cells. Aurora A accumulates near the spindle pole during mitosis, and I found that Aurora A level is not changed between CENP-C WT and CENP-C ΔM12BD RPE-1 cells (Figure 49B), suggesting that CENP-C pathway might not be involved in Aurora A recruitment. The reason why Aurora A inhibition rescued the *KIF18A*-KD sensitivity

is still unclear. But I can give some hypothesis: *KIF18A*-KD impairs the congression of polar chromosomes, leading to their prolonged retention near the spindle poles, however these polar chromosomes can be efficiently congressed with the help of CENP-E in WT cells. On the other hand, if polar chromosomes cannot proceed efficient congression due to reduced CENP-E, the cell will be arrested in mitosis. This is what exactly happened in CENP-C ΔM12BD after *KIF18A*-KD. A recent report suggests that Aurora kinase is involved in chromosome congression by facilitating an end-on attachment (Vukušić et al, 2024). During this process, Aurora A regulation is quite critical. When Aurora A activity is low, Hec1 phosphorylation at kinetochores on the polar chromosomes will be reduced (DeLuca et al., 2018; Iemura et al., 2021), then unphosphorylated Hec1 facilitates end-on kinetochore-microtubule attachment, and subsequently the polar chromosomes can be aligned. In addition, another study reported that Aurora A can regulate CENP-E localization and Aurora A inhibition will cause accumulation of CENP-E at the spindle pole (Eibes et al., 2023). As a result, such sustained polar chromosomes might have more chance to recruit CENP-E for efficient chromosome congression. While this may represent a possible explanation, further experiments are required to address this issue.



B



C

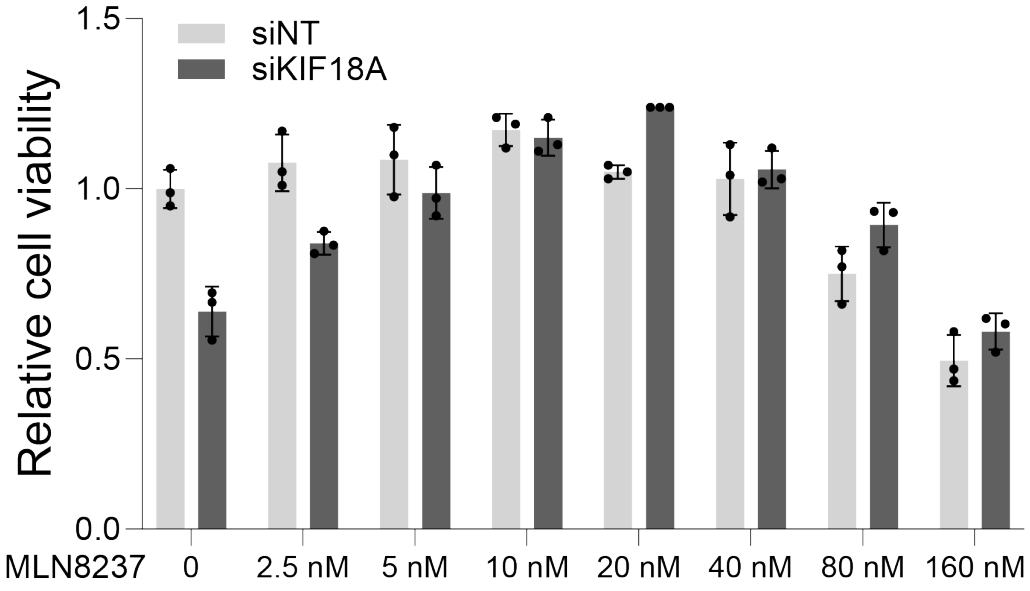


Figure 48. (A) Microscope observation and cell viability assay of K562 cell with or without MLN8237 after *KIF18A* knockout. (Mean and SD, two-tailed Student's t-test, each sample size: n = 6). Scale bar, 50 μm. (B) Cell viability of HeLa cell with or without MLN8237 after *KIF18A* knockout. (Mean and SD, two-tailed Student's t-test, each sample size: n = 6). (C) Cell viability of RPE-1 CENP-C ΔM12BD cell with or without MLN8237 after *KIF18A* knockout. (Mean and SD, two-tailed Student's t-test, each sample size: n = 3).

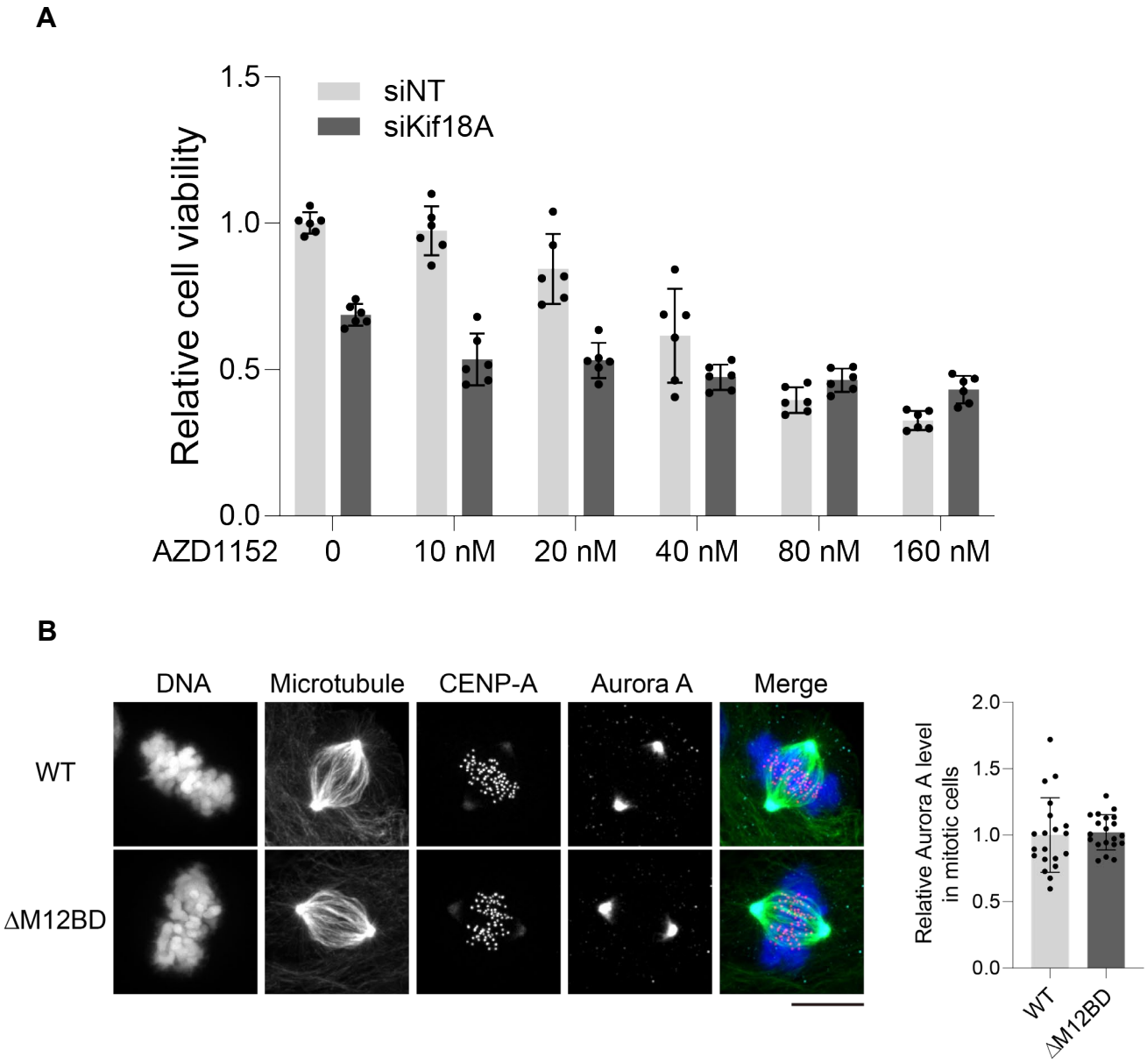
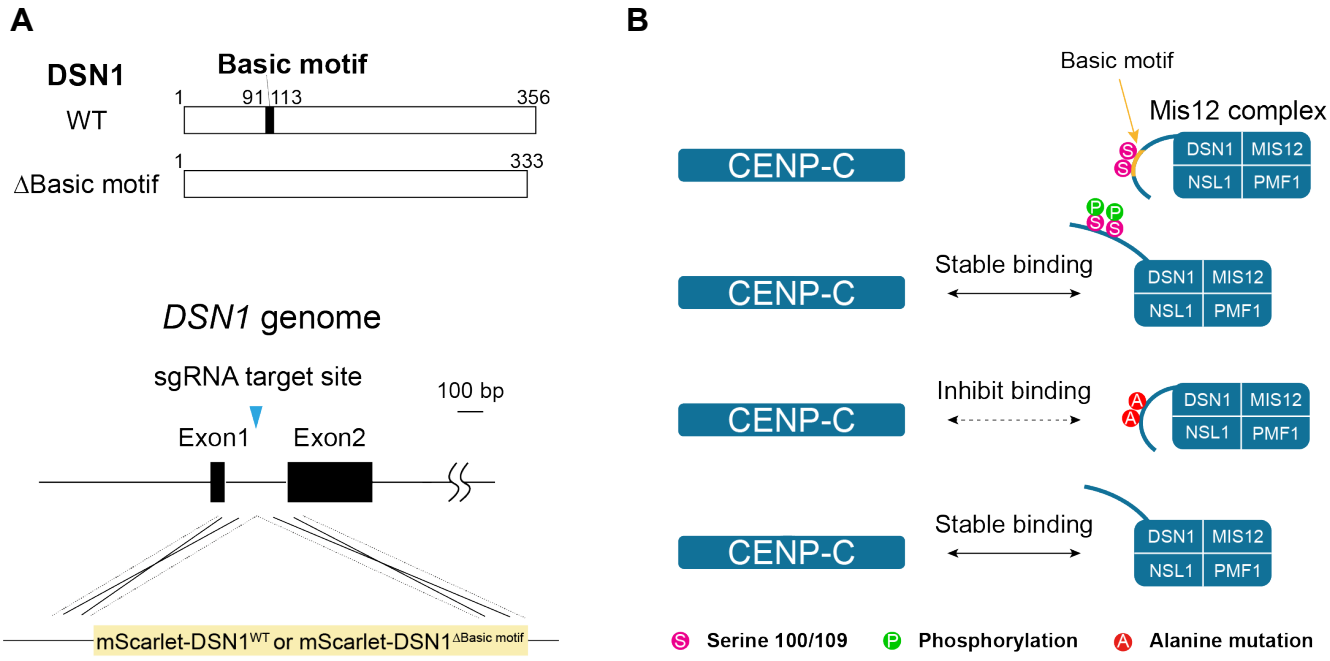
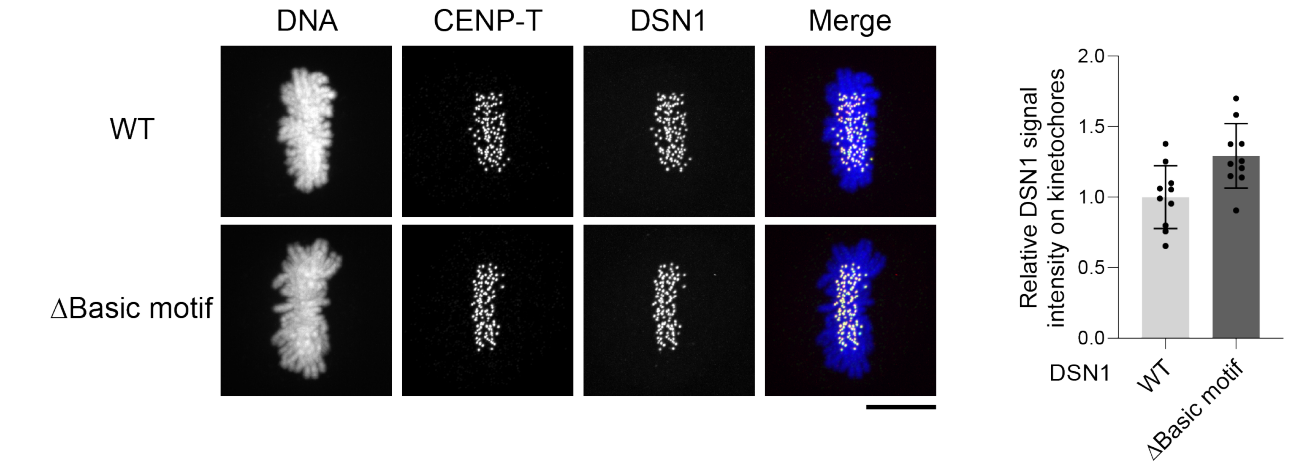


Figure 49. (A) Cell viability of RPE-1 CENP-C ΔM12BD cell with or without AZD1152 after *KIF18A* knockout. (Mean and SD, two-tailed Student's t-test, each sample size: n = 6). (B) Aurora A localization in RPE-1 CENP-C WT and CENP-C ΔM12BD cell. Aurora A was stained with an anti-Aurora A antibody (cyan). Microtubule was stained with an anti-α-tubulin antibody (green). DNA was stained with DAPI (blue). mScarlet-CENP-A was used as a kinetochore marker (red). Scale bar, 10 μm. Aurora A signal intensities at mitotic spindle pole were quantified (Mean and SD, RPE-1 CENP-C WT cells: n = 20, CENP-C ΔM12BD cells: n = 20).

5.4 Enhanced binding of Mis12C to CENP-C did not rescue *KIF18A*-KD sensitivity in HeLa cells

I also mentioned Aurora B activity, which was low in some cancer cell lines such as HeLa cells (Abe et al., 2016). Aurora B phosphorylates DSN1 at S100/S109 in basic motif and facilitates the interaction between Mis12C and CENP-C (Kim et al., 2015). It can be predicted that HeLa cell might have weak Mis12C-CENP-C interaction since Aurora B activity is low. As mentioned in previous section, HeLa cells show *KIF18A*-KD sensitivity. Therefore, it is possible that reduced Mis12 localization due to low Aurora B activity may cause *KIF18A*-KD sensitivity in HeLa cells. Therefore, if the interaction between Mis12C and CENP-C in HeLa cell was enhanced, *KIF18A*-KD might be rescued. To test this idea, I deleted basic motif (aa 91-113) from DSN1 (Figure 50A), and inserted mScarlet-tagged DSN1 WT or DSN1 ΔBasic motif cDNA into *AAVS1* locus in HeLa Kyoto cells. When basic motif was deleted, DSN1 no longer masks the bind surface between Mis12C and CENP-C, and the interaction between Mis12C and CENP-C would be enhanced (Kim et al., 2015; Petrovic et al., 2016) (Figure 50B). Indeed, I confirmed that mitotic DSN1 level was increased in DSN1 ΔBasic motif HeLa cells (Figure 50C). Then, I examined cell viability in DSN1 ΔBasic motif HeLa after *KIF18A*-KD. Surprisingly, DSN1 ΔBasic motif HeLa cells died after siKIF18A treatment (Figure 50D). There are several possibilities to explain this result. First, this enhanced Mis12C–CENP-C interaction may not be able to recruit enough high level of Mis12C at kinetochores to rescue *KIF18A*-KD sensitivity. Second, DSN1 ΔBasic motif HeLa cells died after *KIF18A*-KD may have different reason with CENP-C ΔM12BD RPE-1 cells. Although I cannot rule out this possibility, but in HeLa cell, CENP-E level is low, this is the main reason to cause *KIF18A*-KD sensitivity, so the second possibility may not be the case. Taken together, I hypothesize that this experimental design may not have resulted in sufficient levels of CENP-E to rescue *KIF18A*-KD in HeLa cells.


A
DSN1
Basic motif
1
91
113
356
WT
1
333
ΔBasic motif
DSN1 genome
sgRNA target site
100 bp
Exon1
Exon2
mScarlet-DSN1WT or mScarlet-DSN1ΔBasic motif
B
Basic motif
Mis12 complex
CENP-C
DSN1
MIS12
NSL1
PMF1
Stable binding
CENP-C
Inhibit binding
CENP-C
Stable binding
CENP-C
Serine 100/109
Phosphorylation
Alanine mutation


C
DNA
CENP-T
DSN1
Merge
WT
ΔBasic motif
Relative DSN1 signal intensity on kinetochores
2.0
1.5
1.0
0.5
0.0
DSN1
WT
ΔBasic motif

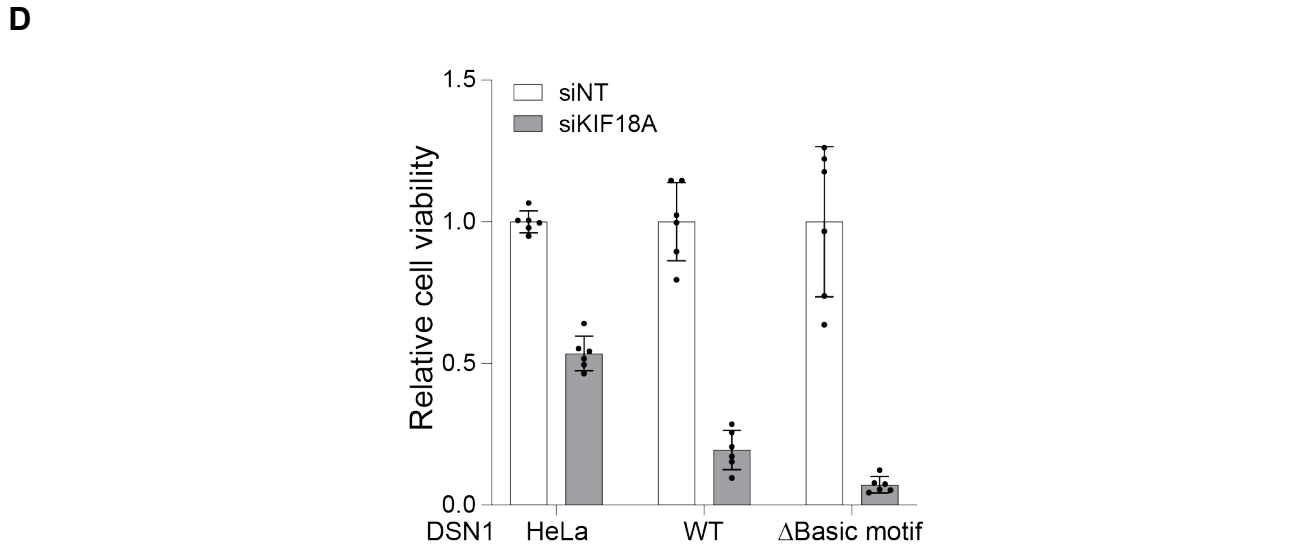

D
siNT
siKIF18A
Relative cell viability
1.5
1.0
0.5
0.0
DSN1
HeLa
WT
ΔBasic motif

Figure 50. (A) Schematic representation of human wild-type DSN1 (DSN1 WT) and DSN1 ΔBasic motif mutant, which are expressed in HeLa cells. To generate HeLa DSN1 WT or DSN1 ΔBasic motif cells, mScarlet-fused DSN1 cDNA encoding DSN1 WT or DSN1 ΔBasic motif was introduced into the endogenous *DSN1* locus, respectively. (B) Schematic representation of the regulation of CENP-C–Mis12C interaction. The basic motif of DSN1, a subunit of Mis12C, masks the CENP-C binding surface of Mis12C, preventing the CENP-C–Mis12C interaction. Once Aurora B phosphorylates two residues (S100 and S109) on the basic motif, or delete this basic motif, the mask is released, and the CENP-C–Mis12C interaction is facilitated. (C) DSN1 localization in HeLa DSN1 WT or DSN1 ΔBasic motif cells (Red). CENP-T was used as a kinetochore marker (green). DNA was stained with DAPI (blue). Scale bar, 10 μm. Signal intensity of each protein at mitotic kinetochores were quantified (Mean and SD, DSN1 WT cells: n = 10 cells, DSN1 ΔBasic motif cells: n = 10 cells). (D) Cell viability of HeLa DSN1 WT or DSN1 ΔBasic motif cells after treatment of siNT or siKIF18A. (Mean and SD, DSN1 WT cells with siNT: n = 6, DSN1 WT cells with siKIF18A: n = 6, DSN1 ΔBasic motif cells with siNT: n = 6, DSN1 ΔBasic motif cells with siKIF18A: n = 6).

5.5 KIF15 inhibition causes mitotic defects in CENP-C ΔM12BD K562 cells

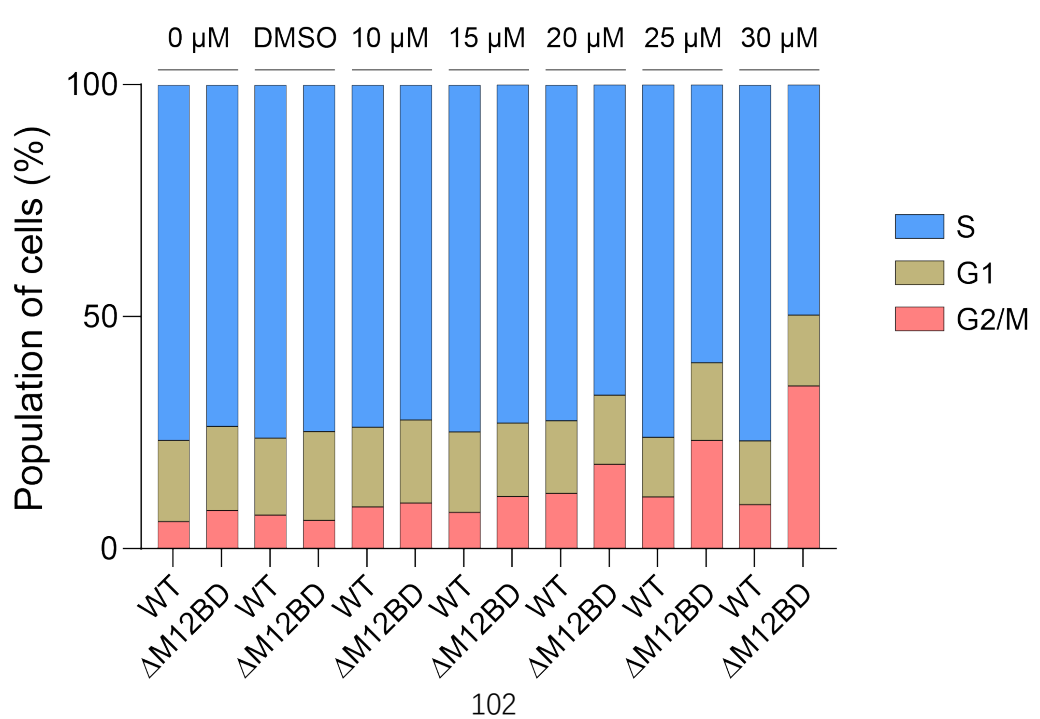
In my CRISPR screening I identified several candidate genes whose knockout exhibit synthetic lethality with CENP-C ΔM12BD mutant. As a main project in my Ph.D. study, I focused on KIF18A. However, it would be also important to characterize each candidate. I will introduce some of these results. Firstly, I characterized KIF15 in CENP-C ΔM12BD K562 cells. KIF15 is a kinesin to drive centrosome separation to maintain bipolar microtubule spindle formation (Tanenbaum et al., 2009). To inhibit KIF15 function, I used a well-studied KIF15 inhibitor KIF15-IN-1. KIF15-IN-1 is a potent inhibitor of KIF15 motility (Milic et al., 2018). I treated KIF15-IN-1 with WT and CENP-C ΔM12BD K562 cells for 20 h and then quantified the population of mitotic cell by a flow cytometry analysis (FACS). I found that treatment of 20 μM, 25 μM and 30 μM KIF15-IN-1 with CENP-C ΔM12BD K562 cells clearly increased mitotic cell population, indicating that KIF15 inhibition caused mitotic arrest in CENP-C ΔM12BD K562 cells

(Figure 51A). Therefore, I expect that growth for CENP-C ΔM12BD K562 cells would be reduced after treatment of KIF15-IN-1. This result is consistent with the individual *KIF15* knockdown in CENP-C ΔM12BD K562 cells (Figure 23).

I stained CENP-C ΔM12BD K562 cells to observe the mitotic phenotype after treatment of KIF15-IN-1. 30 μM KIF15-IN-1 treatment in WT K562 cell did not cause obvious mitotic defect. Since KIF15 and Eg5 are functionally redundant, KIF15 is not essential for spindle assembly in the presence of full Eg5 activity. However, CENP-C ΔM12BD K562 cells treated with 30 μM KIF15-IN-1 were arrested in mitosis (Figure 51B). Although bipolar spindles are formed in these M phase arrested cells, the mitotic behavior was abnormal. I suspect that the microtubule kinetochore attachment becomes unstable, because I could observe some unattached chromosomes in the CENP-C ΔM12BD K562 cells treated with KIF15-IN-1. Based on the cell viability assay and KIF15 inhibitor experiments, I propose that KIF15 is another important factor related with the CENP-C downstream pathway during cell division.

Since I demonstrated that sublethal level of UMK57 caused cell death in CENP-C ΔM12BD RPE-1 cells, I also tested whether CENP-C ΔM12BD K562 cells is also sensitive to UMK57 or not. 500 nM UMK57 treatment did not cause obvious defection in WT K562 cells. However, CENP-C ΔM12BD K562 cells treated with 500 nM UMK57 exhibited a pronounced mitotic arrest (Figure 51B), indicating microtubule dynamics caused cell death in CENP-C ΔM12BD K562 cells.

A



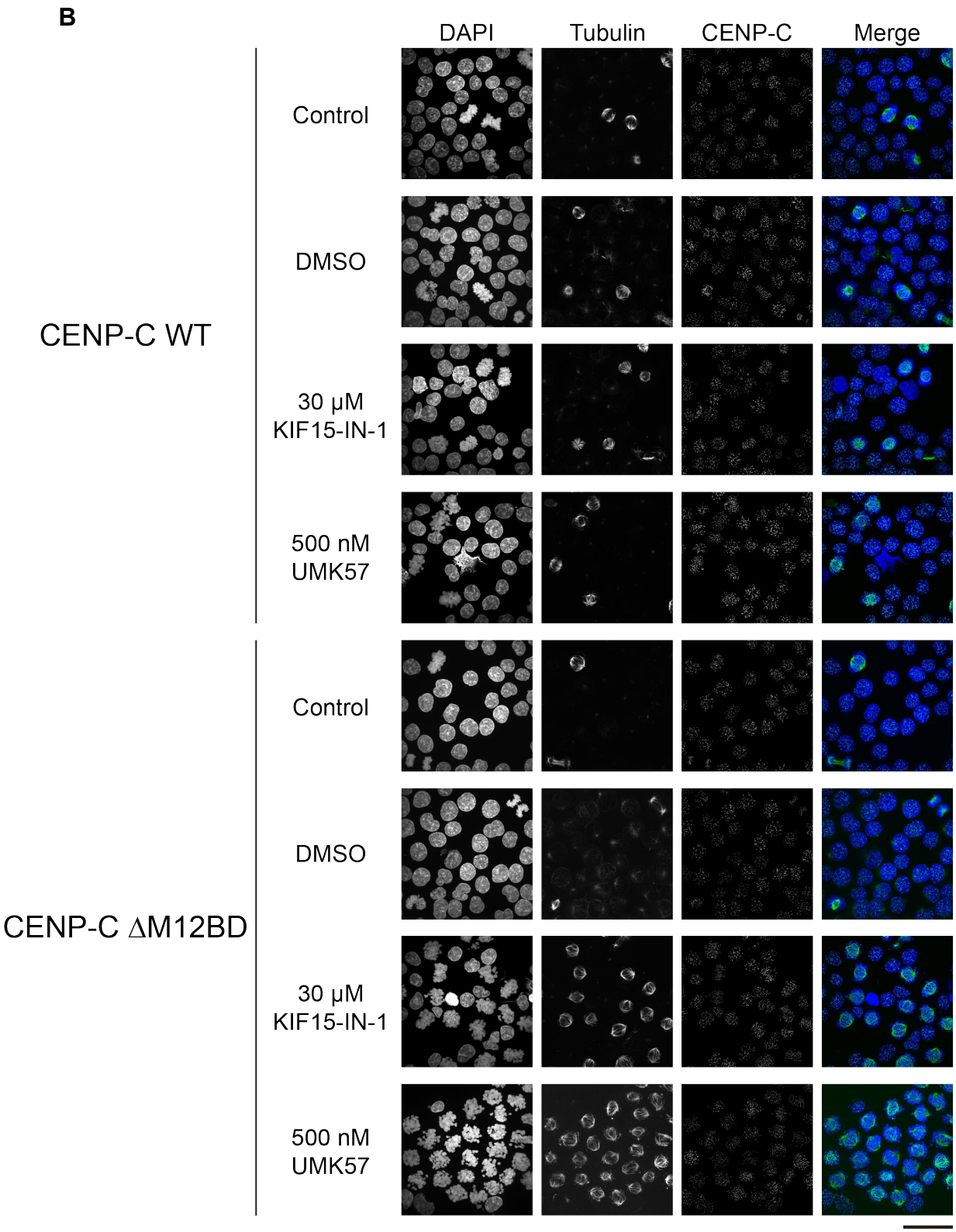


Figure 51. (A) Cell-cycle distribution after treatment of KIF15-IN-1 in K562 WT or CENP-C ΔM12BD cells for 20 h, based on FACS analysis. (B) Representative images of DAPI-stained K562 WT or CENP-C ΔM12BD cells after treatment of DMSO, 30 μm KIF15-IN-1 or 500 nM UMK57. Scale bar, 50 μm.

5.6 *SPAG5* knockdown dramatically increases micronuclei formation in CENP-C ∆M12BD K562 cells

SPAG5 is one of candidate genes from my CRISPR screening experiment in CENP-C ∆M12BD K562 cells. SPAG5 is a spindle associated protein, which plays a key role in maintaining stable kinetochore microtubule attachment (Thein et al., 2007; Ying et al., 2020). In the cell viability assay, *SPAG5* knockdown did not cause severe growth defect in WT K562 cells, but lead to cell death in CENP-C ∆M12BD K562 cells (Figure 23). In WT K562 cells, *SPAG5* knockdown caused an increasement of micronuclei cells and micronuclei formation dramatically enhanced in CENP-C ∆M12BD K562 cells after *SPAG5* knockdown (Figure 52). My quantification results clearly indicate that *SPAG5* knockdown induced more micronuclei cells in CENP-C ∆M12BD K562 cells compared to that in WT K562 cells (Figure 52A and 52B). When chromosomes form micronuclei, it will usually cause loss of genetic information, and cells finally die. The growth defect in CENP-C ∆M12BD K562 cells after *SPAG5* knockdown could be due to this high population of cells with micronuclei. Further study is required to address the question that why *SPAG5* knockdown induce more micronuclei cells in CENP-C ∆M12BD background.

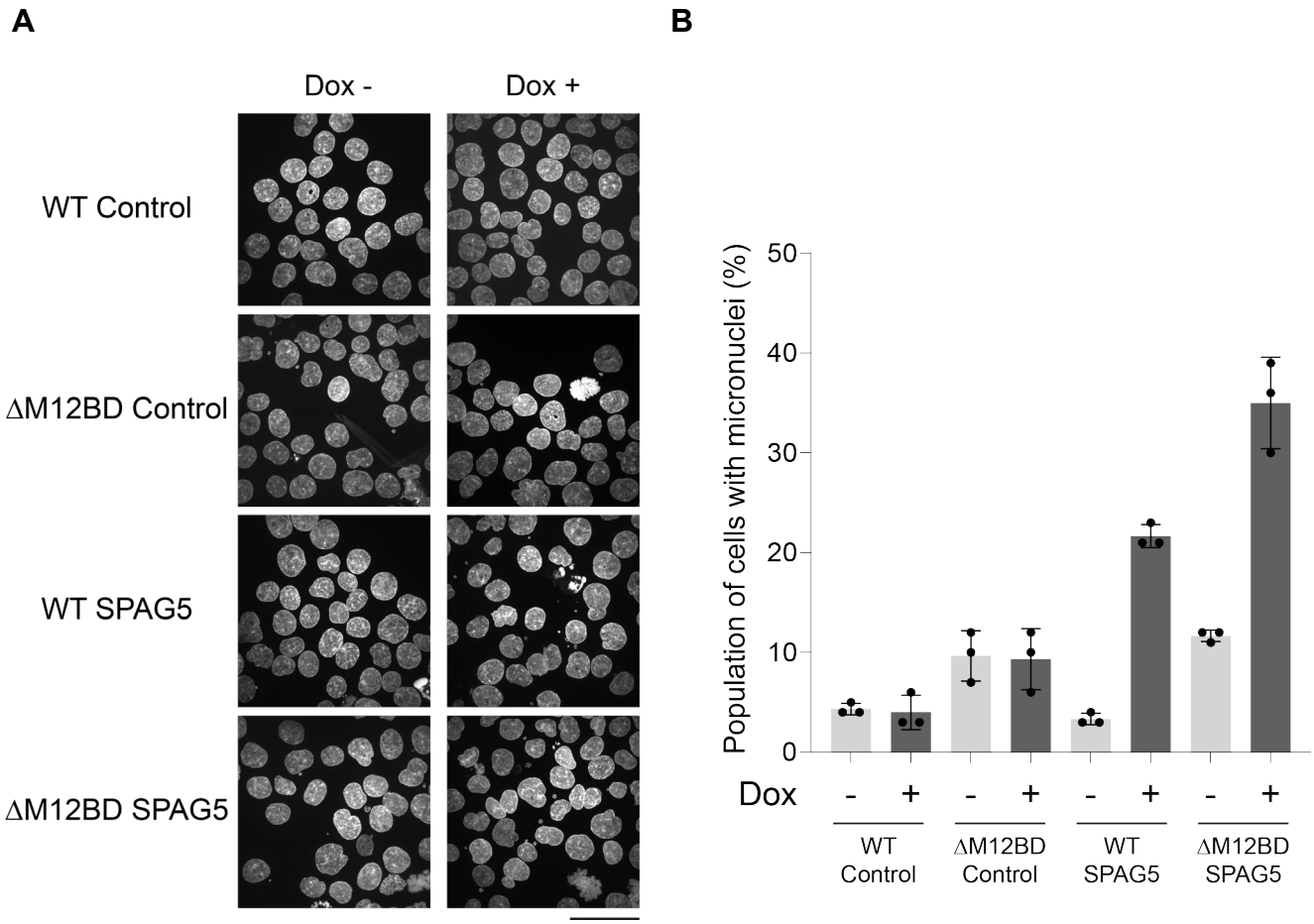


Figure 52. (A) Representative images of DAPI-stained K562 WT or CENP-C ΔM12BD cells after knockout of *SPAG5*, Scale bar, 50 μm. (B) Population of cells with micronuclei in K562 WT or CENP-C ΔM12BD cells after knockout of *SPAG5* at 2 days. Error bars indicated SEM. n = 3 independent experiments; 200 cells from each cell line were quantified in each experiment.

Chapter 2

Functional genetic screening reveals genes whose knockouts exhibit synthetic lethality with CENP-C ∆CC-motif mutation

1. Generation of CENP-C ∆CC-motif K562 cell line

In addition to the Mis12C, other kinetochore components also bind to CENP-C. The C-terminal domain of CENP-C directly binds to the CENP-A nucleosome through the CENP-C motif domain (CC-motif) (Figure 11A and 53) (Kato et al., 2013; Ariyoshi et al., 2021). Although this interaction is predicted to be essential for kinetochore formation, previous work in my lab found that the CC-motif is dispensable for cell proliferation and kinetochore assembly in chicken DT40 cells and human RPE-1 cells (Watanabe et al., 2019).

In the Chapter 1, I identified genes whose knockout exhibit synthetic lethality with CENP-C mutant lacking the Mis12C binding domain, and I revealed unexpected relationship of KIF18A with CENP-C downstream factor CENP-E. Then in this Chapter 2, I will talk about CENP-C mutant which disrupt CENP-A–CENP-C interaction (∆CC-motif mutant), since this CENP-A–CENP-C interaction was also predicted to be essential, but CENP-C ∆CC-motif mutant cell is still viable. I hypothesis that some compensation pathways function in CENP-C ∆CC-motif mutant. In this chapter, I will identify genes that exhibit synthetic lethality with the CENP-C ∆CC-motif mutation by a genome-wide CRISPR screening. I took similar CRISPR screening strategy which I used for CENP-C ∆M12BD K562 cells in the Chapter 1. I generated mutant K562 cells deleting CENP-C CC-motif domain (∆729-763) (Figure 53 and 54) and applied the similar experimental design which I used in the Chapter 1.

Using the CRISPR/Cas9 based genome editing, I designed 2 gRNAs which target genomic sequence upstream and downstream of exon 14 in human *CENP-C* gene locus to delete the entire exon 14 from endogenous human *CENP-C* gene locus. *CENP-C* exon14 encodes aa 729-763 (Figure 54A), their deletion removed the most part of the CC motif (CENP-C ∆CC-motif; Figure 53 and 54) (Kato et al., 2013; Ariyoshi et al., 2021; Watanabe et al., 2019). I confirmed that CENP-C CC-motif deletion was

successfully established in human K562 cell by a genomic PCR, Southern blot analysis, RT-PCR and immunoblot analyses (CENP-C ΔCC-motif K562 cells; Figure 54).

For genomic PCR, I designed 2 primers (F5 and R5). When I use the primer set (F5+R5), the PCR product size for CENP-C WT and that for CENP-C ΔCC-motif were 1690 bp and 441 bp, respectively. These bands can be clearly distinguished on the agarose gel (Figure 54A).

For Southern blot analysis, PstI was used to digest genomic DNA. I designed an 834 bp size probe to hybridize with digested DNA fragments and the hybridized band can be detected by chemiluminescence. In CENP-C WT, the hybridized band size are 4.3 kb and 3.1 kb for CENP-C WT and CENP-C ΔCC-motif, respectively (Figure 54B).

For RT-PCR analysis, total RNA from CENP-C WT and CENP-C ΔCC-motif cells were extracted by TRIzol Reagent. Using the isolated total RNA, CENP-C cDNA was reverse transcribed using SuperScript IV Reverse Transcriptase (Thermo Fisher Scientific). Transcribed cDNA was applied for PCR to detect the exon 14 deletion. The PCR product size for CENP-C WT and for CENP-C ΔCC-motif are 424 bp and 319 bp, respectively (Figure 54C).

For immunoblot analysis, proteins in cell lysates were dephosphorylated with Lambda Protein Phosphatase to detect clear CENP-C signals as mentioned in the Chapter 1. A smaller size of CENP-C protein band can be detected for CENP-C ΔCC-motif by the immunoblot analysis (Figure 54D).

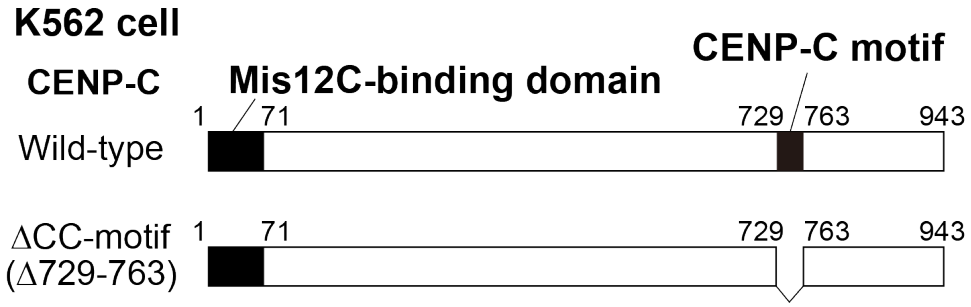
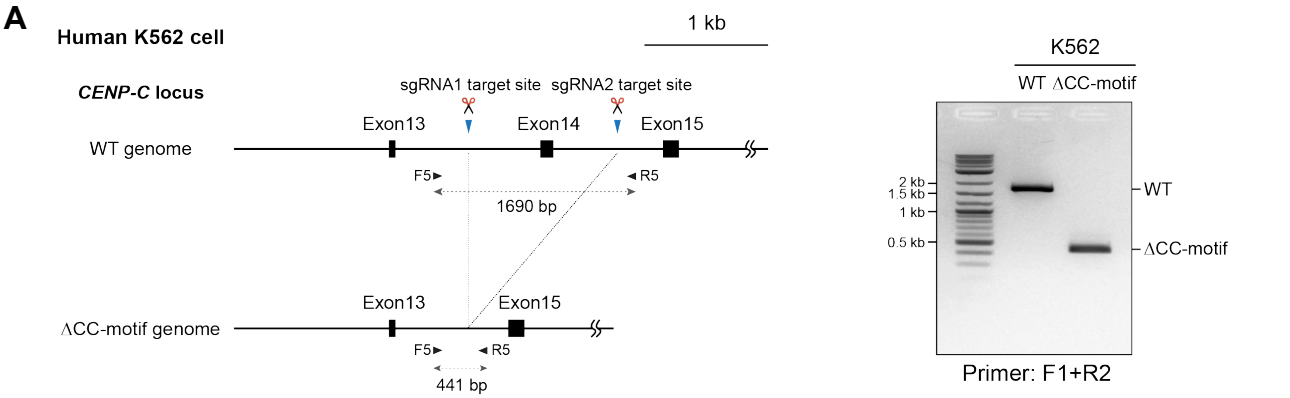
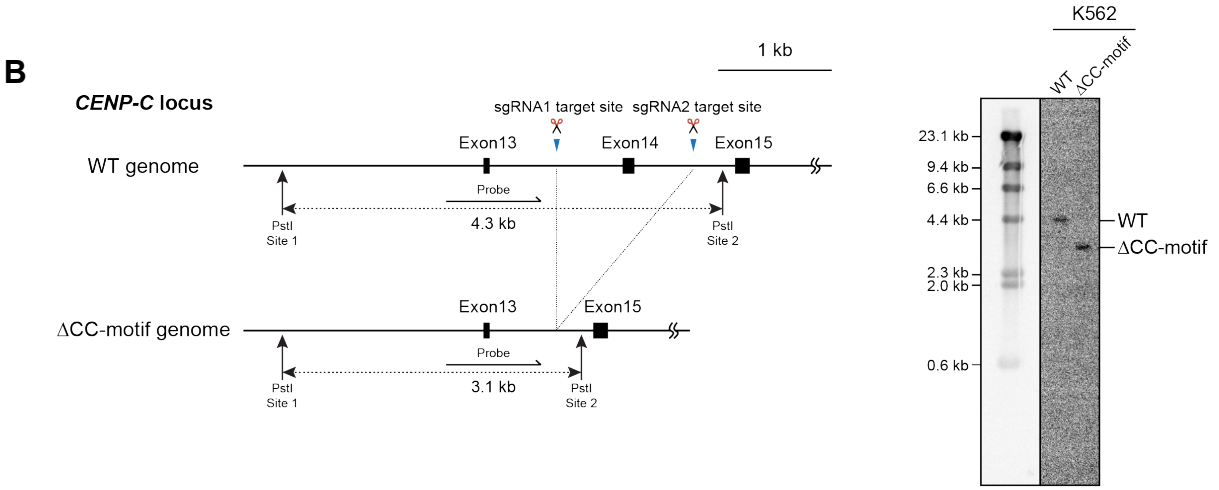
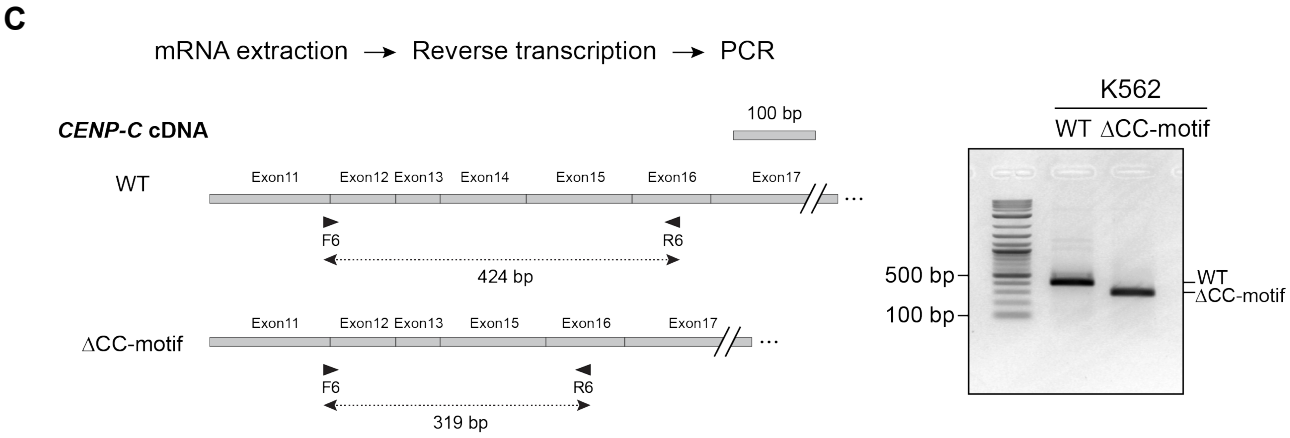


Figure 53. Schematic model of human CENP-C WT and ΔCC-motif.


A
Human K562 cell
1 kb
CENP-C locus
sgRNA1 target site
sgRNA2 target site
Exon13
Exon14
Exon15
WT genome
F5
R5
1690 bp
ΔCC-motif genome
441 bp
K562
WT ΔCC-motif
2 kb
1.5 kb
1 kb
0.5 kb
WT
ΔCC-motif
Primer: F1+R2


B
1 kb
CENP-C locus
sgRNA1 target site
sgRNA2 target site
WT genome
Probe
4.3 kb
PstI Site 1
PstI Site 2
ΔCC-motif genome
3.1 kb
K562
23.1 kb
9.4 kb
6.6 kb
4.4 kb
2.3 kb
2.0 kb
0.6 kb


C
mRNA extraction → Reverse transcription → PCR
CENP-C cDNA
100 bp
WT
Exon11
Exon12
Exon13
Exon14
Exon15
Exon16
Exon17
F6
R6
424 bp
ΔCC-motif
319 bp
K562
WT ΔCC-motif
500 bp
100 bp

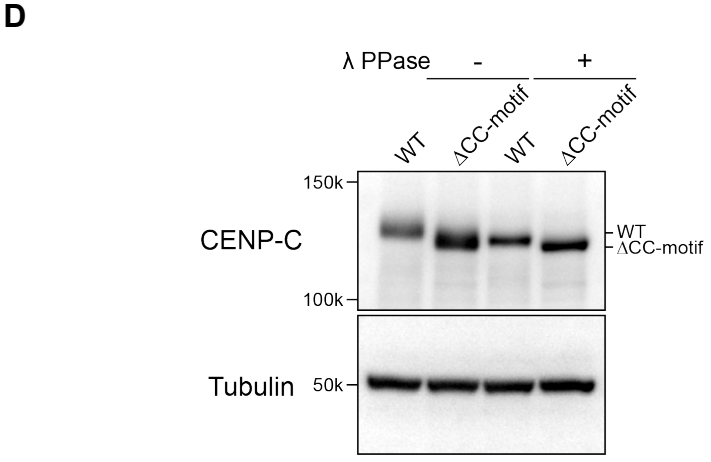

D
λ PPase
-
+
WT
ΔCC-motif
150k
100k
CENP-C
Tubulin
50k

Figure 54. Generation of K562 CENP-C ΔCC-motif cells.

(A) Schematic representation of the exon 14 deletion from human *CENP-C* gene locus in K562 cells. Using the CRISPR-Cas9 system with two sgRNAs, the exon 14 is deleted to generate K562 CENP-C ΔCC-motif cells. The position of sgRNAs and PCR primers for genotyping PCR are shown. The amplicon sizes are 1690 bp (F5+R5) in K562 WT cells, 441 bp (F5+R5) in K562 CENP-C ΔCC-motif cells. Results of genotyping PCR with K562 WT and CENP-C ΔCC-motif cells are shown.

(B) Design for Southern blot analysis to detect a deletion of the exon 14 at the *CENP-C* gene locus in K562 CENP-C ΔCC-motif cells. PstI sites and the probe are shown. Purified genomic DNA from K562 WT or CENP-C ΔCC-motif cells was digested with PstI and run on an agarose gel. The DNA fragments on the gel were transferred to the nylon membrane and hybridized with the indicated probe.

(C) RT-PCR to examine the expression and exon 14 deletion of mRNA for wildtype (WT) CENP-C and CENP-C ΔCC-motif in K562 cells.

(D) Immunoblot analysis to detect WT CENP-C and CENP-C ΔCC-motif in each cell line. α-tubulin was probed as a loading control. As CENP-C is highly phosphorylated, CENP-C band was smeared. To detect the CENP-C protein band, λPPase was used to dephosphorylate proteins.

2. CENP-C motif domain of CENP-C is dispensable for cell growth in human K562 cells

Consistent with the results of human CENP-C ΔCC-motif RPE-1 cells (Watanabe et al., 2019), CENP-C ΔCC-motif K562 cells comparably grew to wild-type (WT) K562 cells (Figure 55), indicating that CENP-C motif domain is dispensable for cell growth in human K562 cells.

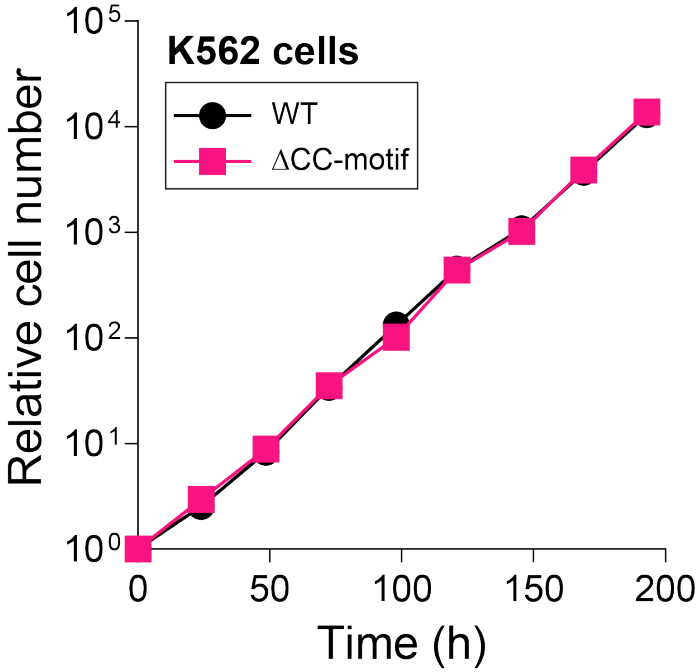
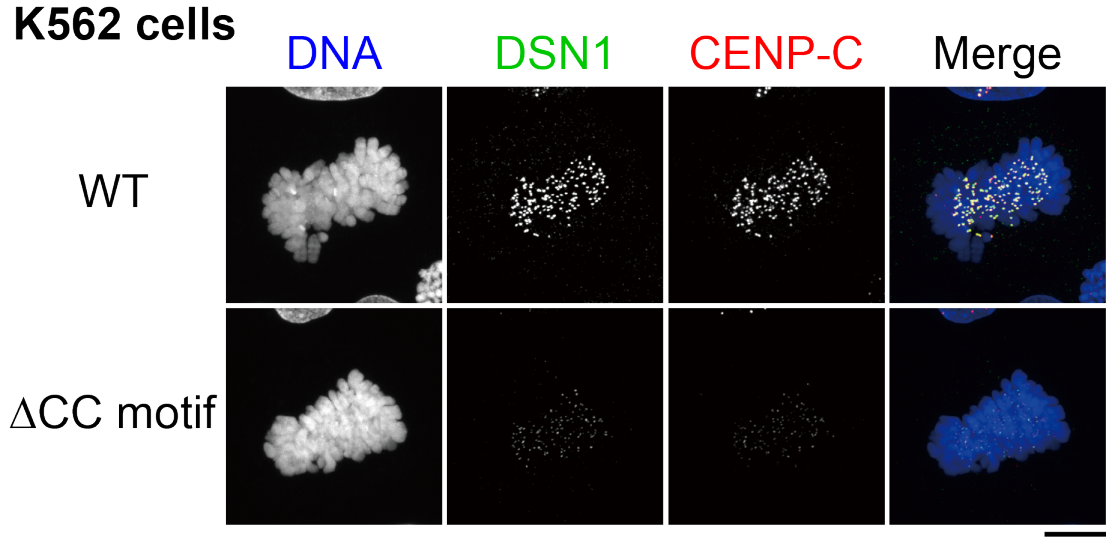


Figure 55. The growth curve of K562 WT or CENP-C ΔCC-motif cells. The cell numbers were normalized to those at time 0 of each cell line.

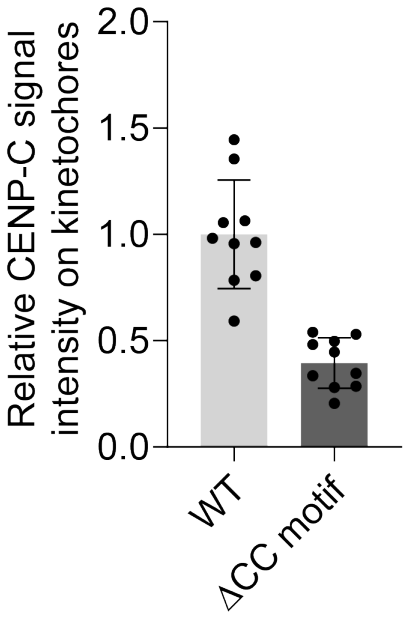
3. CENP-C ΔCC-motif reduces recruitment of CENP-C and DSN1 during mitosis

I examined the levels of CENP-C and DSN1 protein on mitotic kinetochores in CENP-C ΔCC-motif and CENP-C WT K562 cells. CENP-C and DSN1 levels at kinetochores in CENP-C ΔCC-motif K562 cells were significantly reduced in mitotic cells, compared with those in CENP-C WT K562 mitotic cells (Figure 56). As observed in RPE-1 cells, these localization results in K562 cells were expected (Watanabe et al., 2019).

A



B



C

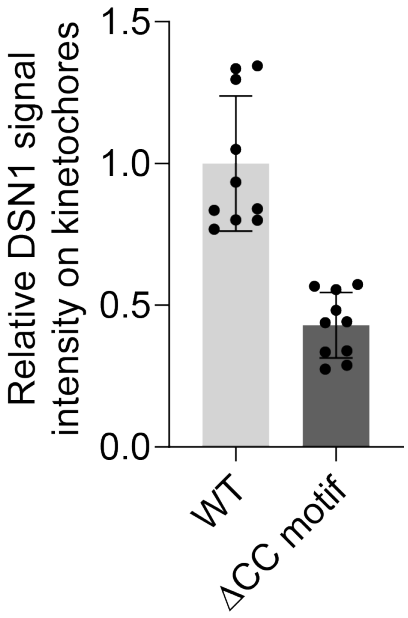


Figure 56. (A) CENP-C and DSN1 localization in K562 WT or CENP-C ΔCC-motif cells. Each protein was stained with an antibody against the target protein. DNA was stained with DAPI. Scale bar, 10 μm. (B and C) Signal intensities of CENP-C (B) and DSN1 (C) on mitotic kinetochores were quantified (Mean and SD, K562 WT cells: n = 10 cells, K562 CENP-C ΔCC-motif cells: n = 10 cells).

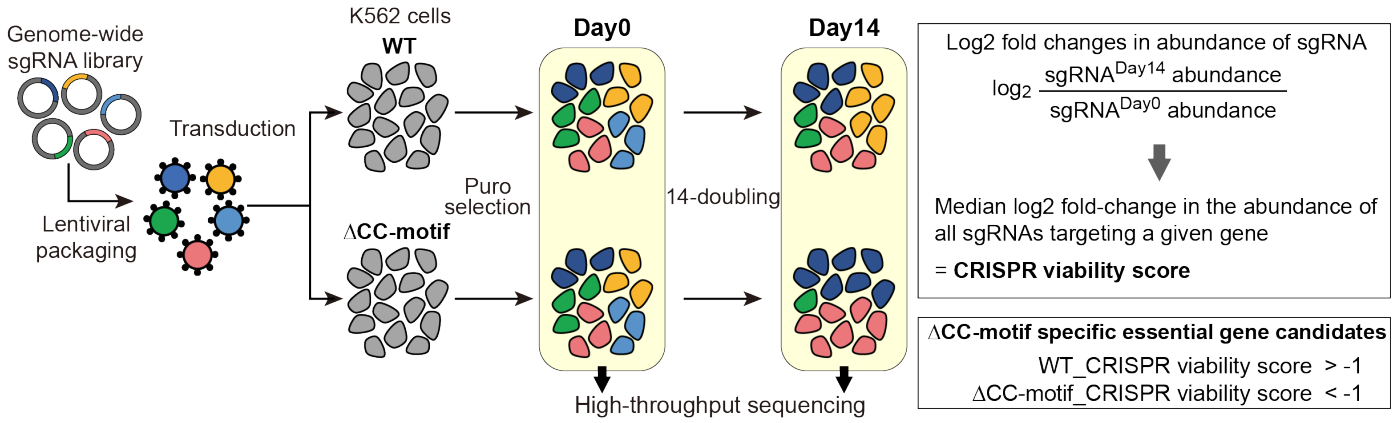
4. A genome-wide CRISPR/Cas9 screening identified genes that exhibit synthetic lethality with the CENP-C ΔCC-motif mutation

To identify hidden relationships within the CENP-C motif associated kinetochore network, I performed pooled genome-wide CRISPR/Cas9 screening in wild-type and CENP-C ΔCC-motif K562 cells (Figure 57A), following previously described methods and steps which I described in the first chapter (Wang et al., 2014; Su et al., 2025). CENP-C WT or CENP-C ΔCC-motif K562 cells were transduced with lentivirus single guide RNA (sgRNA) knockout library targeting 18,663 genes and cultured for 14 population doublings (Figure 57A). Deep sequencing of the sgRNA representation allowed me to calculate a CRISPR viability score reflecting cell viability and proliferation change after sgRNA targeting for each gene (Figures 57B and 57C). The CRISPR viability score was calculated by the log2 fold change in sgRNA abundance between Day 14 and Day 0. The negative viability score indicates that the knockout of the corresponding gene results in reduced cell viability, and the genes with scores less than –1 were defined as essential genes under a given growth condition.

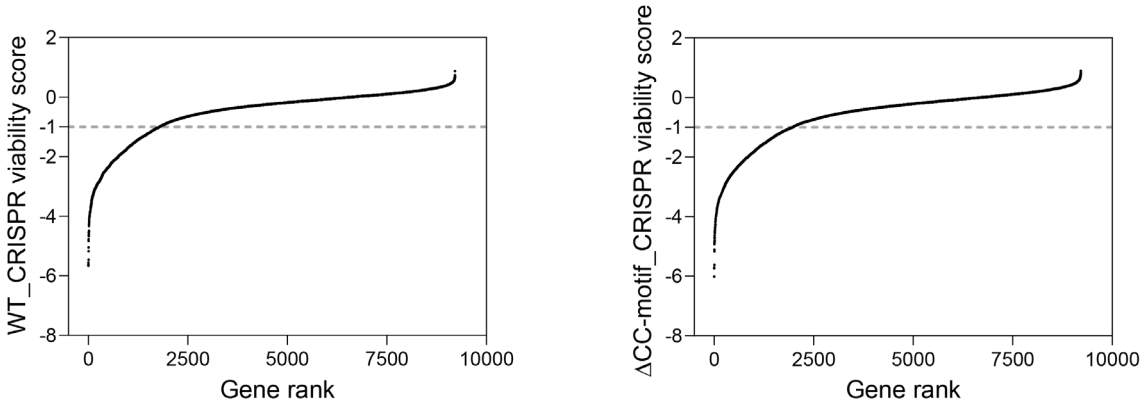
Targeting of most genes resulted in similar overall fitness effects in wild-type or CENP-C ΔCC-motif K562 cells (Figure 57B and 57C), with R^2 of 0.79 for K562 WT versus K562 CENP-C ΔCC-motif cells (Figure 57C). However, a subset of gene knockouts displayed reduced viability scores in K562 CENP-C ΔCC-motif cells compared to those in K562 WT cells (Figure 57C). This includes a total of 385 genes (Figure 57C; red dots). These 385 candidate genes were clarified as non-essential

genes in K562 WT cells (Log2 fold change > –1) but essential in CENP-C ΔCC-motif K562 cells (Log2 fold change < –1). Then these 385 candidate genes were preranked based on the magnitude of differences of log2 fold changes between WT and CENP-C ΔCC-motif K562 cells, in descending order. Thereafter the preranked genes were analyzed with GSEA (Gene set enrichment analysis) version 4.2.3 (Broad Institute). Gene set enrichment analysis found that abnormal enzyme concentration or activity, cell adhesion, anatomical structure formation involved in morphogenesis, ATP dependent activity, protein domain specific binding, adenyl nucleotide binding gene sets were enriched amongst the candidate genes (Figure 57D). But unlike the GSEA result for CENP-C ΔM12BD cells, I didn't find many overlapped genes among these top 6 enriched gene sets (Figures 58A-58F). The only overlapped gene which I can conclude is *MYH9*, this gene can be found in all top 6 enriched gene sets. *MYH9* is also called non-muscle myosin heavy chain IIA (NMHC IIA) and it encodes a protein of 1960 amino acids. *MYH9* is a housekeeping gene which expresses in all eukaryotic cells, its main function is assembly to form myosin filament. Why and how knockout of *MYH9* can cause synthetic lethality with CENP-C ΔCC-motif is still unknown. Further experiments are needed to validate and clarify the hidden relationship between *MYH9* and CENP-C ΔCC-motif mutation.

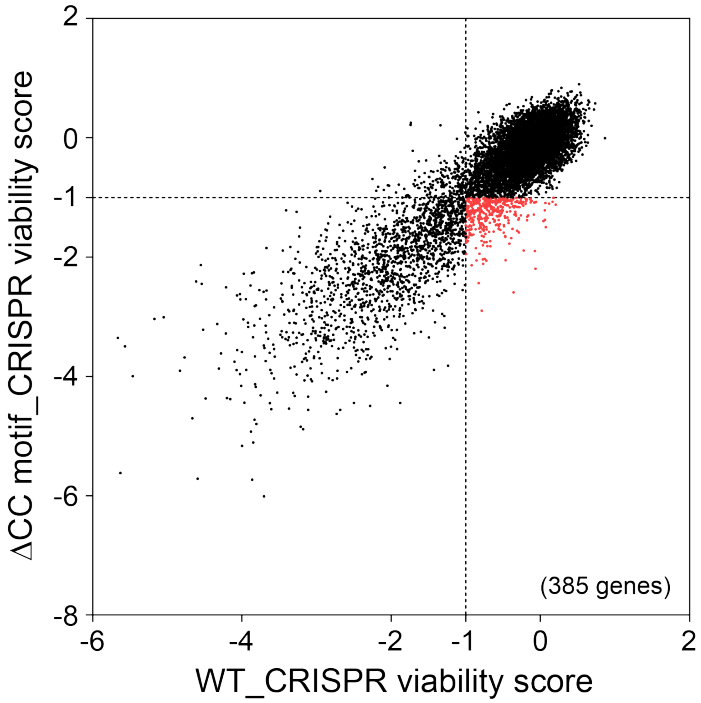
A



B


WT_CRISPR viability score
2
0
-1
-2
-4
-6
-8
0
2500
5000
7500
10000
Gene rank
ΔCC-motif_CRISPR viability score
2
0
-1
-2
-4
-6
-8
0
2500
5000
7500
10000
Gene rank

C


ΔCC motif_CRISPR viability score
2
0
-1
-2
-4
-6
-8
-6
-4
-2
-1
0
2
(385 genes)
WT_CRISPR viability score

D

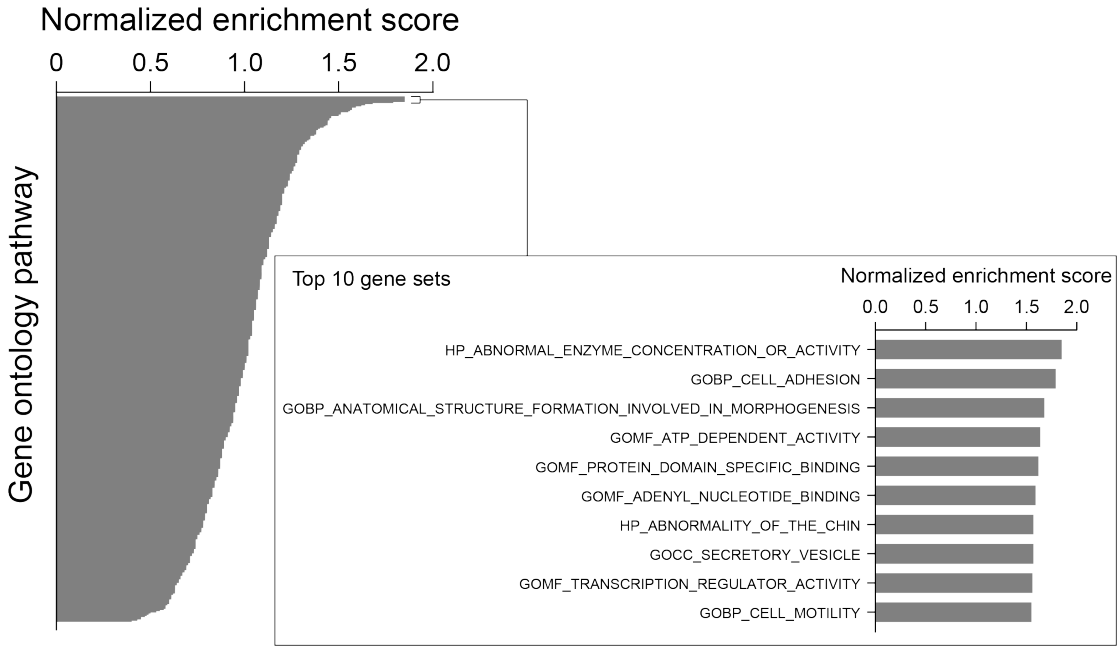

Normalized enrichment score
0
0.5
1.0
1.5
2.0
Gene ontology pathway
Top 10 gene sets
Normalized enrichment score
0.0
0.5
1.0
1.5
2.0
HP_ABNORMAL_ENZYME_CONCENTRATION_OR_ACTIVITY
GOBP_CELL_ADHESION
GOBP_ANATOMICAL_STRUCTURE_FORMATION_INVOLVED_IN_MORPHOGENESIS
GOMF_ATP_DEPENDENT_ACTIVITY
GOMF_PROTEIN_DOMAIN_SPECIFIC_BINDING
GOMF_ADENYL_NUCLEOTIDE_BINDING
HP_ABNORMALITY_OF_THE_CHIN
GOCC_SECRETORY_VESICLE
GOMF_TRANSCRIPTION_REGULATOR_ACTIVITY
GOBP_CELL_MOTILITY

Figure 57. (A) Schematic representation of the pooled CRISPR screening in K562 WT or CENP-C ΔCC-motif cells. Using CRISPR viability scores, genes which are essential for cell growth in K562 CENP-C ΔCC-motif cells but not in K562 WT cells were selected as candidates whose knockout showed synthetic lethality with CENP-C ΔCC-motif.

(B) Distribution of CRISPR viability score of each gene in K562 WT or CENP-C ΔCC-motif cells. Gene with a median fold change (log2) > -1 was identified as a nonessential gene in K562 WT cells and gene with a median fold change (log2) < -1 was identified as an essential gene in K562 CENP-C ΔCC-motif cells.

(C) Scatter plots showing the CRISPR viability score in K562 WT versus CENP-C ΔCC-motif cell pools. Red dots are essential genes in K562 CENP-C ΔCC-motif cells but not in K562 WT cells.

(D) Gene set enrichment analysis (GSEA) for 385 candidate genes. The candidate genes were ranked by the magnitude of differences in CRISPR viability score between K562 WT and CENP-C ΔCC-motif cells in descending order and applied to GSEA. The top 10 enriched gene sets were highlighted.

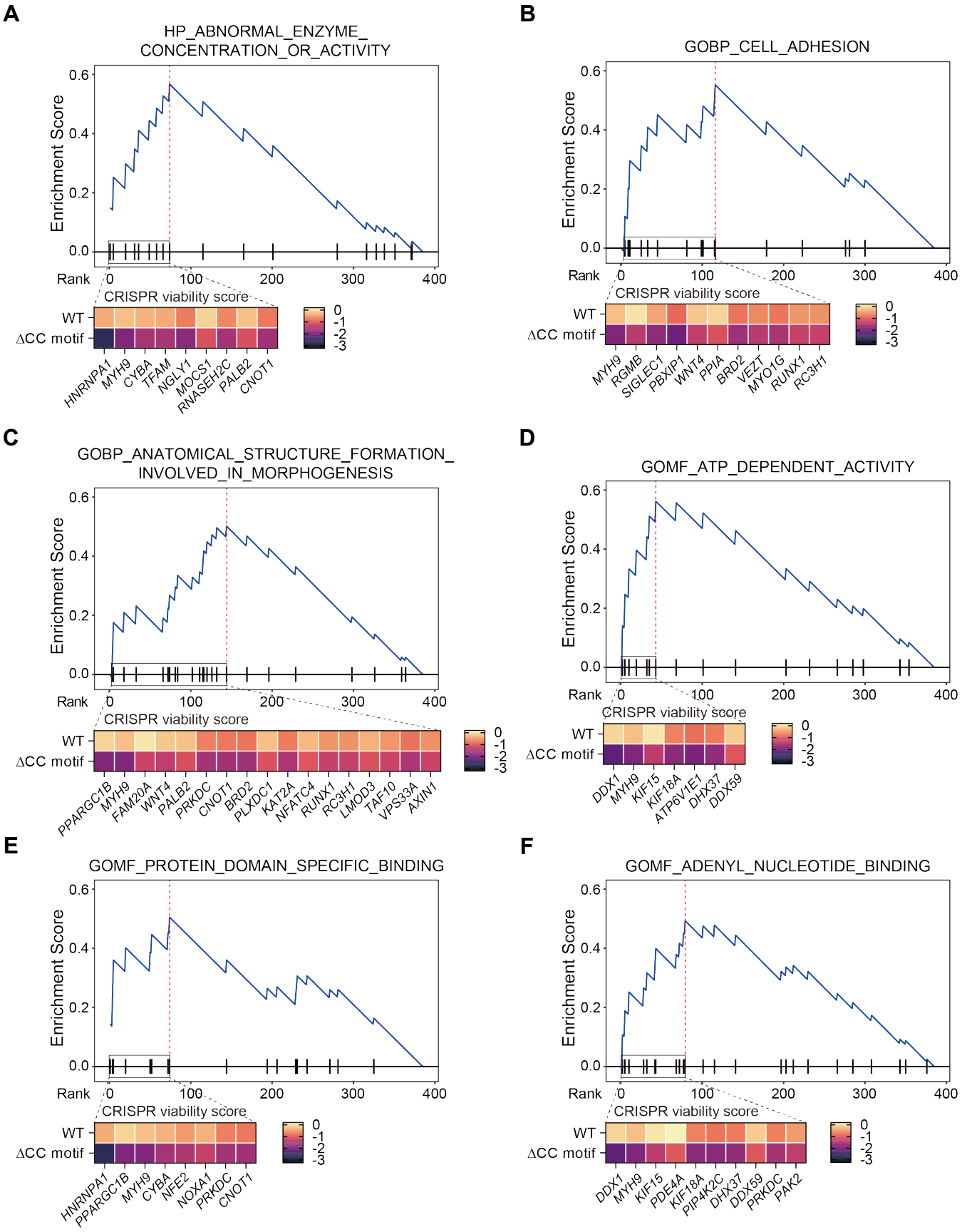

A
HP_ABNORMAL_ENZYME_
CONCENTRATION_OR_ACTIVITY
Enrichment Score
Rank
CRISPR viability score
WT
ΔCC motif
HNRNPA1
MYH9
CYBA
TFAM
NGLY1
MOCS1
RNASEH2C
PALB2
CNOT1
B
GOBP_CELL_ADHESION
MYH9
RGMB
SIGLEC1
PBXIP1
WNT4
PPIA
BRD2
VEZT
MYO1G
RUNX1
RC3H1
C
GOBP_ANATOMICAL_STRUCTURE_FORMATION_
INVOLVED_IN_MORPHOGENESIS
PPARGC1B
MYH9
FAM20A
WNT4
PALB2
PRKDC
CNOT1
BRD2
PLXDC1
KAT2A
NFATC4
RUNX1
RC3H1
LMOD3
TAF10
VPS33A
AXIN1
D
GOMF_ATP_DEPENDENT_ACTIVITY
DDX1
MYH9
KIF15
KIF18A
ATP6V1E1
DHX37
DDX59
E
GOMF_PROTEIN_DOMAIN_SPECIFIC_BINDING
HNRNPA1
PPARGC1B
MYH9
CYBA
NFE2
NOXA1
PRKDC
CNOT1
F
GOMF_ADENYL_NUCLEOTIDE_BINDING
DDX1
MYH9
KIF15
PDE4A
KIF18A
PIP4K2C
DHX37
DDX59
PRKDC
PAK2

Figure 58. (A) GSEA result of HP_ABNORMAL_ENZYME_CONCENTRATION_OR_ACTIVITY gene set. The heat map indicates the CRISPR viability score of the leading edge genes of the preranking based on the magnitude of differences in CRISPR viability score between K562 WT and CENP-C ΔCC-motif cells, in descending order.

(B) GSEA result of GOBP_CELL_ADHESION gene set. The heat map indicates the CRISPR viability score of the leading edge genes as in (A).

(C) GSEA result of GOBP_ANATOMICAL_STRUCTURE_FORMATION_INVOLVED_IN_MORPHOGENESIS gene set. The heat map indicates the CRISPR viability score of the leading edge genes as in (A).

(D) GSEA result of GOMF_ATP_DEPENDENT_ACTIVITY gene set. The heat map indicates the CRISPR viability score of the leading edge genes as in (A).

(E) GSEA result of GOMF_PROTEIN_DOMAIN_SPECIFIC_BINDING gene set. The heat map indicates the CRISPR viability score of the leading edge genes as in (A).

(F) GSEA result of GOMF_ADENYL_NUCLEOTIDE_BINDING gene set. The heat map indicates the CRISPR viability score of the leading edge genes as in (A).

5. Discussion

Even though I conducted the same CRISPR screening and performed identical GSEA analyses on both the CENP-C ΔM12BD and CENP-C ΔCC-motif cell lines, the results obtained from the CENP-C ΔCC-motif analysis were a little hard to interpret.

MYH9 is a top hit in my screening. However, as an essential gene involved in the formation of actin filaments, *MYH9* is closely associated with cytoskeletal organization and is widely recognized as a fundamental structural component of the cytoskeleton. It was difficult to envision a direct connection between *MYH9* and CENP-C ΔCC-motif.

However, a recent study revealed that actin filaments play a regulatory role in spindle assembly during mitosis in early mouse embryos (Hernandez et al., 2025). In that study, actin filaments were shown to stabilize spindle microtubules and to enclose the metaphase spindle, acting as a physical barrier that restricts excessive microtubule elongation. Besides, reports of actin filament involvement in cell division are not rare, for instance, actin filaments have been implicated in facilitating the even distribution of organelles by enclosing them during cytokinesis, thereby ensuring their proper inheritance to each daughter cell.

These findings prompted me to reconsider the potential relationship between *MYH9* and CENP-C ΔCC-motif. It could be possible that *MYH9* may function in a manner analogous to the interplay observed between CENP-E and KIF18A—namely, in a complementary function with CENP-C to support proper mitotic progression.

To evaluate this hypothesis, further experiments are required. For example, *MYH9* knockout will be generated in the CENP-C ΔCC-motif cells and the cellular phenotypes can be characterized.

Materials and Methods

Cell culture

Human K562 cells were maintained in a culture medium containing RPMI-1640 (Nacalai Tesque) supplemented with 10% fetal bovine serum (Sigma-Aldrich) and Penicillin (100 unit/ml)-Streptomycin (100 μg/ml) (Thermo Fisher Scientific) and cultured at 37°C with 5% CO_2. Human hTERT-RPE-1, Lenti-X 293T (Takara Bio), HeLa Kyoto, HT1080, U2OS, TIG-3 and A549 cell lines were maintained in a culture medium containing DMEM (Nacalai Tesque) supplemented with 10% fetal bovine serum (Sigma-Aldrich) and Penicillin (100 unit/ml)-Streptomycin (100 μg/ml) (Thermo Fisher Scientific) and cultured at 37°C with 5% CO_2. For the large-scale lentiviral preparation, Lenti-X 293T cells were maintained in a culture medium containing IMDM (Thermo Fisher Scientific) supplemented with 20% fetal bovine serum (Sigma-Aldrich), and cultured at 37°C with 5% CO_2. Human OVCAR-3, HT29 and HCC1806 cell lines were maintained in a culture medium containing RPMI1640 (Nacalai Tesque) supplemented with 10% fetal bovine serum, and cultured at 37°C with 5% CO_2.

Plasmid constructions for cell transfection

To establish K562 cells expressing CENP-C ΔM12BD, CRISPR/Cas9-mediated gene editing was utilized by employing two independent pX330 (a gift from Feng Zhang, Addgene plasmid, #42230), one pX330 containing single-guide RNA (sgRNA) targeting a genomic sequence in the *CENP-C* exon2 (pX330_sgCCExon2), another pX330 containing sgRNA targeting a genomic sequence in the *CENP-C* exon 4 (pX330_sgCCExon4). sgRNA for *CENP-C* genome editing was designed using CRISPOR.

To establish an inducible Cas9 mediated gene knockout system in K562 cell, a Doxycycline-inducible Cas9 cassette and a landing pad with *attB* sequences for integration of sgRNA sequences were cloned into the human *AAVS1* backbone plasmid using In-Fusion HD Cloning Kit (Takara Bio). The Doxycycline-inducible Cas9 cassette contains *Cas9* with the Tet-responsible (Tet-On) promoter followed by *rtTA*-

T2A-neomycin resistance genes (*NeoR*) with the *EF1a* promoter. The cassette was amplified from HP138-neo (Addgene plasmid, #134247) by PCR. The landing pad contains *HSV TK* with CMV promoter flanked with two *attB* sequences. The Doxycycline-inducible Cas9 cassette and landing pad were cloned into the human *AAVS1* backbone plasmid which was derived from digested pAAVS1-NDi-CRISPRi (Gen1) (a gift from Bruce Conklin, Addgene plasmid, #73497) by the restriction enzyme EcoRV and HindIII by using In-Fusion HD Cloning Kit (Takara Bio) (pAAVS1_Tet-Cas9). This construct was integrated into the *AAVS1* locus by CRISPR/Cas9-mediated homologous recombination, employing pX330 containing sgRNA targeting a sequence around the *AAVS1* exon1 (pX330_sgAAVS1).

To generate a donor plasmid containing *attP* and three sgRNA sequences targeting a gene, each sgRNA was cloned into pX330 (a gift from Feng Zhang, Addgene plasmid, #42230) independently. Three sgRNAs were designed for a gene at different exons using CRISPOR. Using each pX330 with sgRNA as a template, the sequence with the U6 promoter and sgRNA was amplified with PCR. The amplified sequences (three for each gene target) were fused and flanked with two *attP* sequences by using In-Fusion HD Cloning Kit (Takara Bio) (pattP_tri-gRNA).

To express mScarlet-fused human full-length CENP-A under the control of the endogenous *CENP-A* promoter in human RPE-1 cells, the sequence of *mScarlet-fused CENP-A* cDNA followed by puromycin resistance gene (*PuroR*) or *NeoR* expression cassette driven by the *beta-actin* promoter (*ACTB*) was flanked with 5' and 3' *CENP-A* homology arm fragments (approximately 1 kb each) which were surrounding the *CENP-A* start codon was cloned into the pBluescript II SK (pBSK) by using In-Fusion HD Cloning Kit (Takara Bio) (pBSK_mScarlet-CENP-A). The construct was integrated into the endogenous *CENP-A* genome locus by CRISPR/Cas9-mediated homologous recombination with pX330 containing sgRNA targeting a sequence around the *CENP-A* start codon (pX330_sgCENP-A).

To express mScarlet-fused human full-length DSN1 (DSN1 WT) or S100A/S109A (DSN1 2A) mutant under the control of the endogenous *DSN1* promoter in RPE-1 cells, the cDNA of *mScarlet-fused DSN1 WT* or *2A* mutant followed by *PuroR* or *NeoR* expression cassette driven by the *ACTB* promoter was flanked with 5' and 3' homology arm fragments (approximately 1 kb each) which is surrounding the *DSN1*

start codon was cloned into the pBSK (pBSK_mScarlet-DSN1 WT or pBSK_mScarlet-DSN1 2A) by using In-Fusion HD Cloning Kit (Takara Bio). The constructs were integrated into the endogenous *DSN1* gene locus by CRISPR/Cas9-mediated homologous recombination with pX330 containing sgRNA targeting a sequence around the *DSN1* start codon (pX330_sgDSN1).

For KIF18A analysis with siRNA knockdown, siRNA targeting sequences of *EGFP-fused full-length KIF18A* cDNA were modified with synonymous mutations to make siRNA-resistant KIF18A construct (KIF18A WT). The synonymous mutations were designed by Synonymous Mutation Generator. To express EGFP-fused KIF18A WT under the control of *CMV* promoter in RPE1 cells, the *EGFP-fused KIF18A WT* cDNA followed by the Blasticidin S resistance gene (*BsR*) expression cassette driven by the *ACTB* promoter flanked with 5' and 3' homology arm fragments of *AAVS1* locus (approximately 1 kb each) was cloned into the pBSK by using In-Fusion HD Cloning Kit (Takara Bio) (pBSK_CMV-KIF18A WT-BsR). To express EGFP-fused human KIF18A ∆1-362 (KIF18A ∆1-362), ∆PP1 (KIF18A ∆PP1), S674A/S684A (KIF18A 2A) or ∆PP1 + S674A/S684A (KIF18A ∆PP1+2A) mutant, each siRNA-resistant mutant construct was cloned as EGFP-fused KIF18A WT. (pBSK_CMV-KIF18A ∆1-362-BsR, pBSK_CMV-KIF18A ∆PP1-BsR, pBSK_CMV-KIF18A 2A-BsR and pBSK_CMV-KIF18A ∆PP1+2A-BsR). Each construct was integrated into the endogenous *AAVS1* gene locus by CRISPR/Cas9-mediated homologous recombination with (pX330_sgAAVS1).

To clone an sgRNA sequence to pX330 (a gift from Feng Zhang, Addgene plasmid, #42230), forward and reverse oligos including sgRNA sequence and flanking sequences were incubated with T4 Polynucleotide Kinase (TOYOBO) at 37°C for 30 min, then annealed under the following sequential protocol: 95°C for 5 min, 75°C for 5 min, 55°C for 5 min, finally 35°C for 5 min. Annealed DNAs were ligated with pX330 (a gift from Feng Zhang, Addgene plasmid, #42230), which is digested by BpiI (Thermo Fisher Scientific). All sgRNA sequences and oligo sequences used in this study are listed in the Table.

Generation of cell lines

To establish K562 cells expressing CENP-C ΔM12BD, wild-type K562 cells (K562 WT cells) were co-transfected with pX330_sgExon2 and pX330_sgExon4 using Neon Transfection System (Thermo Fisher Scientific) with 1 pulse (1000 V, 50 msec). Single-cell clones were isolated from transfected cells (K562 CENP-C ΔM12BD cells).

To establish a Doxycycline-inducible Cas9-mediated gene knockout system in K562 cells, K562 WT or K562 CENP-C ΔM12BD cells were co-transfected with pX330_sgAAVS1 and pAAVS1_Tet-Cas9 using Neon Transfection System (Thermo Fisher Scientific) with 1 pulse (1000 V, 50 msec). Transfected cells were selected in a medium containing 1 mg/ml G418 (Santa Cruz Biotechnology) to isolate single-cell clones (K562 WT/Cas9 cells, K562 CENP-C ΔM12BD/Cas9 cells). To integrate sgRNA sequences to the *attB* landing pad in K562 WT/Cas9 or CENP-C ΔM12BD/Cas9 cells, cells were co-transfected with pattP_tri-gRNA for each target gene and Bxb1 expression plasmid pCAG-NLS-HA-Bxb1 (a gift from Pawel Pelczar, Addgene plasmid, #51271) using Neon Transfection System (Thermo Fisher Scientific) with 1 pulse (1000 V, 50 msec). Transfected cells were selected in a medium containing 500 nM FIAU (Sigma-Aldrich) to isolate single-cell clones.

To establish RPE-1 cell lines expressing mScarlet-fused CENP-A under the control of the endogenous *CENP-A* promoter, the RPE-1 cells were co-transfected with pX330_sgCENP-A and two pBSK_mScarlet-CENP-A plasmids, each containing *PuroR* or *NeoR*, using Neon Transfection System (Thermo Fisher Scientific) with 6 pulses (1400 V, 5 msec). Transfected cells were then selected in a medium containing 2 μg/ml puromycin (Takara Bio) and 500 μg/ml G418 (Santa Cruz Biotechnology) to isolate single-cell clones (RPE-1 mScarlet-CENP-A cells).

To establish RPE-1 expressing either CENP-C WT or CENP-C ΔM12BD under the control of the endogenous *CENP-C* promoter, and also expressing mScarlet-CENP-A, RPE-1 cells expressing mScarlet-CENP-A under the control of the endogenous *CENP-A* promoter (RPE-1 mScarlet-CENP-A cells) were co-transfected with pX330_sgCENP-C and two pBSK_CENP-C WT plasmids, each containing *ZeoR* or *HisD,* or two pBSK_CENP-C ΔM12BD plasmids, each containing *ZeoR* or *HisD,* using Neon Transfection System (Thermo Fisher Scientific) with 6 pulses (1400 V, 5 msec). Transfected cells were selected in a medium containing 10 ng/ml zeocin

(Thermo Fisher Scientific) and 1.5 mg/ml L-Histidinol dihydrochloride (Sigma-Aldrich) to isolate single-cell clones (RPE1 mScarlet-CENP-A_CENP-C WT or mScarlet-CENP-A_CENP-C ΔM12BD cells).

To establish RPE-1 cells expressing mScarlet-fused DSN1 WT or DSN1 2A under the control of the endogenous *DSN1* promoter, RPE-1 cells were co-transfected with pX330_sgDSN1 and two pBSK_mScarlet-DSN1 WT plasmids, each containing *PuroR* or *NeoR*, or two pBSK_mScarlet-DSN1 2A plasmids, each containing *PuroR* or *NeoR*, using Neon Transfection System (Thermo Fisher Scientific) with 6 pulses (1400 V, 5 msec). Transfected cells were selected in a medium containing 5 μg/ml puromycin (Takara Bio) and 2 mg/ml G418 (Santa Cruz Biotechnology) to isolate single-cell clones (RPE-1 mScarlet-DSN1 WT or mScarlet-DSN1 2A cells).

To establish RPE-1 cells expressing EGFP-fused KIF18A WT, KIF18A Δ1-362, KIF18A ΔPP1, KIF18A 2A or KIF18A ΔPP1+2A, RPE-1 cells were co-transfected with pX330_sgAAVS1 and pBSK_CMV-KIF18A WT-BsR, pBSK_CMV-KIF18A Δ1-362-BsR, pBSK_CMV-KIF18A ΔPP1-BsR, pBSK_CMV-KIF18A 2A-BsR, or pBSK_CMV-KIF18A ΔPP1+2A-BsR using Neon Transfection System (Thermo Fisher Scientific) with 6 pulses (1400 V, 5 msec). Transfected cells were selected in a medium containing 20 μg/ml Blasticidin S hydrochloride (Wako) to isolate single-cell clones (RPE-1 EGFP-KIF18A WT, EGFP-KIF18A Δ1-362, EGFP-KIF18A ΔPP1, EGFP-KIF18A 2A and EGFP-KIF18A ΔPP1+2A cells).

Genotyping

To isolate genomic DNA from K562 or RPE-1 cells, cells were collected and washed with cold PBS. Then cells were centrifuged. The cell pellet was resuspended in 50 mM NaOH and incubated for 10 min at 95°C followed by mixing with a 10% sample volume of 1 M Tris-HCl pH8.0. After centrifugation, supernatant was applied for genome PCR using primers listed in the Table.

Southern blot

1×10^7 K562 cells were collected and washed with cold PBS, then suspended with lysis buffer (100 mM NaCl, 10 mM Tris-HCl pH 8.0, 25 mM EDTA, 0.5% SDS, 0.1 mg/ml, proteinase K (Sigma-Aldrich)). The lysate was incubated overnight at 50°C with shaking. An equal volume of phenol/chloroform/isoamyl alcohol (25:24:1) (NIPPON GENE) was added and mixed well. The sample was centrifuged for 10 min at 1700*g* at RT. Then, the aqueous phase was isolated and mixed with 1/10 volume of 3 M sodium acetate and twice the volume of 100% ethanol. Centrifugation at 1700*g* for 2 min was applied to precipitate genomic DNA. The DNA pellet was rinsed with 70% ethanol twice and suspended in TE buffer (10 mM Tris-HCl, 1 mM EDTA, pH 8.0). Dissolved genomic DNA was digested by EcoRI overnight at 37°C. Then, digested DNA was run on 0.8% agarose gel and transferred to nylon membranes (Biodyne B, Cytiva). The membrane was incubated with the DNA probe, which was labeled with alkaline phosphatase with AlkPhos Direct Labeling kit (Cytiva, RPN3680). To detect DNA fragments hybridized with the probe, the membrane was incubated with CDP-Star detection reagent (Cytiva), and signals were visualized using a ChemiDoc Touch imaging system (Bio-Rad). Images were processed using Image Lab (Bio-Rad) and Fiji (v1.53).

Cell counting

To count the number of K562 cells, living K562 cells were collected and mixed with an equal volume of 0.4% (w/v) Trypan Blue Solution (Wako). The cell numbers were counted using the Countess II (Thermo Fisher Scientific). Relative cell numbers were calculated based on the cell numbers at time 0 h in each experiment.

Immunoblotting

5×10^5 K562 or RPE-1 cells were collected, washed with cold PBS, and then suspended in 1 x Laemmli Sample Buffer (LSB: 62.5 mM Tris-HCl pH6.8, 10% glycerol, 2% SDS, 5% 2-mercaptoethanol, bromophenol blue) at a final concentration of $1x10^4$ cells/μl. The lysate was sonicated and heated for 5 min at 96°C. The samples were

separated by SDS-PAGE using 5-20% gradient polyacrylamide gels (SuperSepAce 5-20%, Wako) and transferred onto a PVDF membrane (Immobilon-P, Merck). After washing the membrane in TBST (50 mM Tris-HCl pH7.5, 150 mM NaCl, 0.1% Tween 20) for 15 min, the membrane was incubated with a primary antibody overnight at 4°C. Following a 15-min wash with TBST, the membrane was incubated with a secondary antibody for 1 h at RT. With a 15-min wash with TBST, the membrane was incubated with ECL Prime Western Blotting Detection Reagent (Cytiva) for 5 min. The signal was detected and visualized using a ChemiDoc Touch imaging system (Bio-Rad) and the image was processed using Image Lab (Bio-Rad) and Fiji (v1.53).

As CENP-C is highly phosphorylated, the CENP-C signals were smeared and unclear on immunoblots. To detect clear CENP-C signals, proteins in cell lysates were dephosphorylated with Lambda Protein Phosphatase (New England Biolabs). Collected cells were suspended in lysis buffer (50 mM NaH_2PO_4, 50 mM Na_2HPO_4, 300 mM NaCl, 0.1% NP-40, 5 mM 2-mercaptoethanol, 1 x cOmplete EDTA-free proteinase inhibitor (Roche)) at a final concentration of $1x10^5$ cells/μl. The lysate was sonicated, and the supernatant was recovered after centrifugation. 3 μl of the supernatant sample was mixed with 20 μl H_2O, then 3 μl of 10 x NEBuffer and 3 μl of 10 mM $MnCl_2$ were added. Then, 1 μl of Lambda Protein Phosphatase was added to the premixed supernatant sample and incubated for 10 min at 30°C according to the manufacturer's instructions. After mixing with LSB, and heated for 5 min at 96°C. The proteins were detected as described above.

The primary antibodies used in this study were, Guinea pig anti-human CENP-C (1:10,000), rabbit anti-Cas9 (1:2,000) (Takara Bio), mouse anti-human CENP-A (1:1,000), rabbit anti-human DSN1 (1:5,000), rabbit anti-human KIF18A (1:2000) (Bethyl), rabbit anti-human KIF15 (1:2000) (Proteintech), rabbit anti-human NDE1 (1:2000) (Proteintech), rabbit anti-human NEDD1 (1:2000) (Proteintech), rabbit anti-human SPAG5 (1:2000) (Proteintech), rabbit anti-human KNTC1 (1:2000) (Proteintech), rabbit anti-human ASPM (1:2000) (Proteintech), rabbit anti-human TUBGCP6 (1:2000) (Novus biologicals), mouse anti-human NPM1 (1:2000) (Proteintech) and mouse anti-α-tubulin (1:5,000) (Sigma-Aldrich). The secondary antibodies were horseradish peroxidase (HRP) -conjugated goat anti-rabbit IgG (1:5,000) (Jackson ImmunoResearch), HRP-conjugated anti-guinea pig IgG (1:5,000)

(Jackson ImmunoResearch) and HRP-conjugated anti-mouse IgG (1:5,000) (Jackson ImmunoResearch). All antibodies were diluted in Signal Enhancer Hikari (Nacalai Tesque) to enhance signal sensitivity and specificity.

Immunofluorescence and image acquisition

To localize CENP-C, CENP-T, CENP-A, DSN1, KNL1, HEC1, and MAD2 in K562 cells, K562 cells were cytospan onto slide glasses (MATSUNAMI, S2111) or coverslips (MATSUNAMI, C024361) and then fixed with 3% paraformaldehyde (PFA; Nacalai Tesque) for 10 min at RT, and rinsed with PBS. The cells were permeabilized with 0.5% NP-40/PBS for 10 min at RT, and rinsed with PBS. After blocking with 0.5% BSA/PBS for 5 min at RT, the cells were incubated with primary antibodies diluted in 0.5% BSA/PBS for 1 h at 37°C. The cells were washed three times with 0.5% BSA/PBS, incubated with secondary antibodies diluted in 0.5% BSA/PBS for 1 h at 37°C, and washed three times with 0.5% BSA/PBS. The cells were post-fixed in 3% PFA/PBS for 10 min. DNA was stained with 100 ng/ml DAPI/PBS for 20 min at RT. The stained cells were mounted with VECTASHIELD Mounting Medium (Vector Laboratories).

To localize CENP-C, CENP-T, BubR1, DSN1, KNL1, and HEC1 in RPE-1 cells, RPE-1 cells were seeded onto 35 mm glass-bottom culture dishes (MatTek) and incubated for 24 to 36 h. The cells were fixed with 4% PFA (Electron Microscopy Sciences) in PHEM buffer (60 mM PIPES, 25 mM HEPES, 10 mM EGTA, 2 mM $MgCl_2$, pH 6.8) for 10 min at RT. The cells were permeabilized with 0.5% Triton X-100/PBS for 10 min at RT, followed by blocking with blocking solution (3% BSA, 0.1% Triton X-100, 0.1% sodium azide in TBS (50 mM Tris-HCl pH 7.5, 150 mM NaCl)) for 5 to 10 min at RT. The samples were then incubated with primary antibodies in blocking solution overnight at 4°C. After washing the samples with PBST (0.1% Triton X-100/PBS) three times for 5 min each, they were incubated with secondary antibodies in blocking solution for 1 h at RT. Subsequently, the samples were washed in PBST three times for 5 min each, and DNA was stained with 100 ng/ml DAPI/PBS for 10 min at RT. After washing with PBS, cells were mounted with VECTASHIELD Mounting Medium (Vector Laboratories).

To localize ZW10 in RPE-1 cells, the cells were seeded onto 35 mm glass-

bottom culture dishes (MatTek) and incubated for 24 h. Then cells were permeabilized for 1 min with warm 0.2% Triton X-100/PHEM buffer, and fixed with 4% PFA/PBS for 10 min. After 3-time wash with PBS, the cells were blocked with 3% BSA/PBS for 1 h at RT. The cells were incubated with primary antibodies diluted in 3% BSA/PBS for 16 h at 4 °C. Subsequently, the cells were washed three times for 5 min each with PBST and incubated with secondary antibodies in 3% BSA/PBS for 1 h at RT. After washing with PBST three times for 5 min each, DNA was stained with 100 ng/ml DAPI/PBS for 10 min at RT. After washing with PBS, cells were mounted with VECTASHIELD Mounting Medium (Vector Laboratories).

I used immunofluorescence to localize EGFP-fused KIF18A proteins in RPE-1 because their EGFP signals were weak. The cells were seeded onto 35 mm glass-bottom culture dishes (MatTek), treated with siKIF18A, and then incubated for 48 h. The cells were fixed in −20°C methanol with 1% PFA for 10 min on ice and washed three times for 5 min each in TBS. The cells were blocked with 20% goat serum (Jackson ImmunoResearch) in antibody-diluting buffer (1% BSA, 0.1% Triton X-100, and 0.1% sodium azide in TBS) for 1 h at RT and incubated with primary antibodies diluted in antibody-diluting buffer for 1 h at RT. Subsequently, the cells were washed with TBS twice for 5 min each and incubated with secondary antibodies for 1 h at RT. After three washs with TBS for 5 min each, DNA was stained with 100 ng/ml DAPI/PBS for 10 min at RT. After washing with PBS, cells were mounted with VECTASHIELD Mounting Medium (Vector Laboratories).

To localize CENP-E in RPE-1 cells, the cells were seeded onto 35 mm glass-bottom culture dishes (MatTek) for 24 h. Then cells were fixed with 4% PFA/PHEM buffer for 5 min at RT, then permeabilized with 0.1% Triton X-100/PHEM buffer for 2 min at RT and rinsed once with PHEM buffer. Cells were blocked for 30 min in antibody dilution solution (AbDil, 4% BSA, 0.1% Triton X-100, 0.1% sodium azide in PBS) and incubated with primary antibodies in AbDil overnight at 4°C. After washing for three times for 5 min each with PBST, cells were incubated with secondary antibodies in AbDil for 1 h at RT. The cells were washed three times for 5 min each with PBST, and DNA was stained with 100 ng/ml DAPI/PBS for 10 min at RT. After washing with PBS, cells were mounted with VECTASHIELD Mounting Medium (Vector Laboratories).

To localize CENP-E, CENP-C and CENP-T in RPE-1, K562, U2OS, A549, TIG-

3, HeLa Kyoto, HT1080, OVCAR-3, HT29 or HCC1806 cells in Figure 44, cells were treated with 50 μM monastrol (Selleckchem) for 2 h, then each cell line was collected and mixed with RPE-1 mScarlet-CENP-A cells as an internal control. Each mixed cell sample was cytospan onto coverslips (MATSUNAMI), and the cells were fixed and stained as described above. The CENP-E, CENP-C and CENP-T signal intensities at mitotic kinetochores in RPE-1, K562, U2OS, A549, TIG-3, HeLa Kyoto, HT1080, OVCAR-3, HT29 or HCC1806 cells were normalized with those signal intensities in mScarlet-CENP-A RPE-1 cells, which were in each sample.

Immunofluorescence images were captured by Nikon Eclipse Ti inverted microscope (Nikon) with a spinning disk confocal unit CSU-W1 (Yokogawa) controlled with NIS-elements (v5.42.01, Nikon) with an objective lens (Nikon; PlanApo VC 60×/1.40 or Lambda 100×/1.45 NA) and an Orca-Fusion BT (Hamamatsu Photonics) sCMOS camera. The images were acquired with Z-stacks at intervals of 0.2 or 0.3-μm. Maximum intensity projections (MIPs) of the Z-stack were generated using Fiji (v1.53) for display and analysis. All antibodies used in this study were listed in the Key resource table.

Lentivirus preparation

For large-scale lentiviral preparation, Lenti-X 293T cells (Takara Bio) were transfected with a transfection mix containing X-tremeGENE 9 DNA Transfection Reagent (Roche), pCMV-VSV-G (a gift from Robert Weinberg, Addgene plasmid, #8454), psPAX2 (a gift from Didier Trono, Addgene plasmid, #12260), and pooled sgRNA library plasmids in Opti-MEM I Reduced Serum Medium (Gibco). The culture medium was changed to a fresh medium at 16 h after the transfection. At 48 h after the transfection, the supernatant of the cell culture medium containing viruses was collected, filtered through a 0.45μm filter (Pall Corporation), and stored at −80°C until use.

Genome-Wide CRISPR Screening

The lentivirus pool containing the genome-wide sgRNA library was used to transduce 6×10^8 K562 WT or CENP-C ΔM12BD cells with 10 μg/ml polybrene (Merck) to

maintain 1,000-fold coverage of the sgRNA library, as previously described. Three days after lentiviral transduction, the cells were passaged into fresh media supplemented with 3 μg/ml puromycin (Takara Bio) and selected for another 3 days. Collected 8×10^7 cells were frozen at the endpoint of puromycin selection to assess initial sgRNA library representation ($sgRNA^{Day0}$ abundance). The cells were allowed to grow with 1.5 μg/ml puromycin for 2 days then passaged with non-puromycin fresh medium every 2 days until 14 population doublings. Collected 8×10^7 cells were frozen at the endpoint of the screen to assess the final sgRNA library representation ($sgRNA^{Day14}$ abundance). The genomic DNA of Day 0 and Day 14 cells were extracted using the QIAamp DNA Blood Maxiprep Kit (Qiagen) according to the manufacturer's instructions. For each extraction, the integrated sgRNAs were PCR-amplified for deep sequencing. Base calls were performed by the instrument control software and further processed using the Offline Base Caller (Illumina) v.1.9.4.

sgRNA sequences were counted and analyzed using MAGeCK v0.5.9.2, with a gene test false discovery rate (FDR) threshold of 0.05 and a list of control and intergenic sgRNAs for normalization and generation of the null distribution. The median of sgRNA scores was selected to represent the gene score. For comparison of gene knockout effect between K562 WT and CENP-C ΔM12BD cells, genes with FDR < 0.1 were picked for further analysis. A gene with a median fold change (log2) < -1 was identified as an essential gene, and a gene with a median fold change (log2) > -1 was identified as a nonessential gene. 375 candidate genes for non-essential in K562 WT cells but essential in K562 CENP-C ΔM12BD cells were preranked based on the magnitude of differences of fold changes between K562 WT and CENP-C ΔM12BD cells, in descending order. The preranked genes were analyzed with GSEA version 4.2.3 (Broad Institute) or R version 4.3.1 and all plots were generated in either base R, using the R corrplot package, or in Prism Version 10.1.2 (GraphPad).

RT-PCR

To isolate total RNA from K562 cells, 5×10^6 cells were collected by centrifugation and suspended in TRIzol Reagent (Thermo Fisher Scientific), according to the manufacturer's instructions. Using the isolated total RNA, CENP-C cDNA was reverse

transcribed using SuperScript IV Reverse Transcriptase (Thermo Fisher Scientific), according to the manufacturer's instructions. The cDNA was applied for PCR to examine the exon 2-4 deletion. The primes used are listed in the Table.

Real-Time PCR

Total RNA was extracted from K562 cells with TRIzol (Thermo Fisher Scientific) as above. Relative mRNA expression levels were examined using iTaq Universal SYBR Green One-Step Kit (Bio-Rad) with QuantStudio 3 (Thermo Fisher Scientific). The Ct values of each gene were normalized with *GAPDH* Ct values in each sample. Data was collected and analyzed by the QuantStudio Design & Analysis Software v1.5.1 (Thermo Fisher Scientific). Primers used for Real-Time PCR were listed in the Table.

Flow cytometry

5×10^6 K562 cells were cultured with 20 μM 5-bromo-2-deoxyuridine (BrdU, Sigma-Aldrich) for 20 min. The cells were collected, washed with ice-cold PBS, fixed with ice-cold 70% ethanol, and stored at -20°C until use. The fixed cells were washed with 1% BSA/PBS and incubated with 4 M HCl/0.5% Triton X-100 for 30 min at RT. Following washing 3 times with 1% BSA/PBS, the cells were incubated with an anti-BrdU antibody (BD Biosciences) for 1 h at RT. Following washing twice with 1% BSA/PBS, the cells were incubated with 1:20 anti-mouse IgG-FITC (Jackson ImmunoResearch) in 1% BSA/PBS for 30 min at RT. After a wash with 1% BSA/PBS, the cells were incubated with 10 μg/ml propidium iodide (Sigma-Aldrich) in 1% BSA/PBS overnight at 4°C. The stained cells were subjected to flow cytometry analysis using BD FACS Canto II Flow Cytometer (BD Biosciences), and BD FACSDiva 9.0 Software (BD Biosciences).

Cell viability assay

Cell viability was assessed using RealTime-Glo MT Cell Viability Assay (Promega). K562 cells were transferred to 96-well Flat Clear Bottom White Polystyrene TC-treated

Microplates (Corning) at the indicated time points. The cells were treated with RealTime-Glo reagents (Promega) and incubated for 1 h at 37°C. Luminescence was measured using GloMax Discover Microplate Reader (Promega) and GloMax Navigator (Promega). RPE-1, U2OS, A549, TIG-3, HeLa Kyoto, HT1080, OVCAR-3, HT29 or HCC1806 cells were seeded into 96-well Flat Clear Bottom White Polystyrene TC-treated Microplates (Corning) at the concentration of 1250 cells/well. Following culture for 3 days, the cells were treated with RealTime-Glo reagents (Promega) and incubated for 1 h at 37°C. Luminescence was measured using GloMax Discover Microplate Reader (Promega) and GloMax Navigator (Promega).

siRNA treatment

3 µl Lipofectamine RNAiMAX Reagent (Thermo Fisher Scientific) and 10 pmol siRNA were diluted in 125 µl Opti-MEM I Reduced Serum Medium (Gibco) separately. Diluted siRNA and diluted Lipofectamine RNAiMAX Reagent were mixed at 1:1 ratio and were incubated for 5 min at RT. The 250 µl siRNA-lipid complex was added into a 6-well plate (IWAKI) or 35 mm glass-bottom culture dishes (MatTek), then 5 – 7.5×10^4 cells were added into the plate or 35 mm dish. Cells were incubated for 1-3 days at 37°C before analyzing. For the cell viability assay, 20 µl siRNA-lipid complex was added into 96-well Flat Clear Bottom White Polystyrene TC-treated Microplates (Corning), then 1250 cells/80 µl were added into the plate. Cells were incubated for 3 days at 37°C before analyzing. The sequences of siRNA used in this study are listed in the Table.

Live-cell imaging

For live-cell imaging, I used RPE-1 cells expressing mScarlet-CENP-A, GFP-H2A, and Flag-fused CENP-C WT or CENP-C ΔM12BD (RPE-1 mScarlet-CENP-A GFP-H2A Flag-CENP-C WT, RPE-1 mScarlet-CENP-A GFP-H2A Flag-CENP-C ΔM12BD) (Kong et al., 2025). 1×10^5 cells were treated with siRNA as described in the above section and plated onto 35 mm glass-bottom culture dishes (MatTek). After incubation at 37°C for 24 h, cells were switched to phenol red-free culture medium (phenol red-free DMEM (Nakalai Tesque), supplemented with 20% fetal bovine serum (Sigma-Aldrich),

25 mM HEPES (HEPES Buffer Solution, Nacalai Tesque), 2 mM L-glutamine (Sigma-Aldrich) and treated with SiR-Tubulin (1:5,000) (CYTOSKELETON) for 4 h. Then, samples were sealed with mineral oil (Sigma-Aldrich) before the start of imaging. To quantify mitotic timing in Figure 33, the images were captured every 2 min by Olympus IX71 microscope (Olympus) with DeltaVision Elite imaging system (GE healthcare) equipped with a PlanApo N OSC 60×/1.40 NA oil immersion objective lens (Olympus) and a CoolSNAP HQ2 CCD camera (Photometrics) controlled with built-in SoftWoRx software (version 5.5) in a temperature-controlled room at 37°C. A Z-series of 7 sections with 2 μm increments was acquired. The Z-series was then projected using MIP for analysis by SoftWoRx. To quantify peripheral chromosome congression in Figure 39D and 41C, the images were captured every 1 min by Nikon Eclipse Ti inverted microscope (Nikon) with a spinning disk confocal unit CSU-W1 (Yokogawa) controlled with NIS-elements (v5.42.01, Nikon) with an objective lens (Nikon; PlanApo VC 60×/1.40) and an Orca-Fusion BT (Hamamatsu Photonics) sCMOS camera. The images were acquired with Z-stacks at intervals of 2 μm. MIP of the Z-stack were generated using NIS-elements Imaging Software (v5.42.01, Nikon). Acquired time-lapse images were processed by using Fiji software (v1.53).

Quantification and Statistical Analysis

The fluorescence signal intensities of CENP-C, CENP-T, BubR1, DSN1, KNL1, HEC1, CENP-E, ZW10 and mScarlet-DSN1 on kinetochores were quantified using Imaris v9.0.2. (Bitplane). Data processing was carried out using Microsoft Excel and GraphPad Prism 10.1.2 (GraphPad), and *p*-values were calculated using two-tailed Student's t-test. Cell viability was measured by luminescence using GloMax Discover Microplate Reader (Promega) and GloMax Navigator (Promega). Data processing was carried out using Microsoft Excel and GraphPad Prism 10.1.2 (GraphPad), and *p*-values were calculated using two-tailed Student's t-test. Each experiment was repeated at least three times when not mentioned in figure legends, and representative data of replicates were presented.

Key resources table

REAGENT or RESOURCE	SOURCE	IDENTIFIER
Antibodies		
Rabbit anti-human DSN1	Kline et al., 2006	N/A
Rabbit anti-human KNL1	Cheeseman et al., 2008	N/A
Rabbit anti-human HEC1	Abcam	Cat#Ab3613; RRID: AB_303949
Mouse monoclonal anti-α-tubulin	Sigma-Aldrich	Cat#T9026; RRID: AB_477593
Rabbit anti-Cas9	Takara Bio	Cat#632607; RRID: AB_3251495
Rabbit anti-human KIF18A	Bethyl	Cat#A301-080A; RRID: AB_2296551
Mouse anti-human CENP-E	Abcam	Cat#ab5093; RRID: AB_304747
Mouse anti-human MAD2	Santa Cruz Biotechnology	Cat#sc-65492; RRID: AB_831526
Rabbit anti-human KIF15	Proteintech	Cat#55407-1-AP; RRID: AB_11182836
Rabbit anti-human NDE1	Proteintech	Cat#10233-1-AP; RRID: AB_2149877
Rabbit anti-human NEDD1	Proteintech	Cat#13993-1-AP; RRID: AB_2149202
Rabbit anti-human SPAG5	Proteintech	Cat#14726-1-AP; RRID: AB_2194787
Rabbit anti-human KNTC1	Proteintech	Cat#24694-1-AP; RRID: AB_3669445

Rabbit anti-human ASPM	Proteintech	Cat#26223-1-AP; RRID: AB_2880431
Rabbit anti-human TUBGCP6	Novus Biologicals	Cat#NBP2-94428
Mouse anti-human NPM1	Proteintech	Cat#60096-1-Ig; RRID: AB_2155162
Mouse anti-human BubR1	Sigma-Aldrich	Cat#MAB3612; RRID: AB_2066086
Rabbit polyclonal anti-human ZW10	Abcam	Cat#ab21582; RRID: AB_779030
Guinea pig anti-human CENP-C	Ando et al., 2002	N/A
Mouse anti-human CENP-A	Ando et al., 2002	N/A
Rat anti-human CENP-T	A gift from Kinya Yoda, Nagoya University, Nagoya, Japan	N/A
Mouse anti-BrdU	BD Biosciences	Cat#347580; RRID: AB_400326
FITC-conjugated rabbit anti-mouse IgG	Jackson ImmunoResearch	Cat#315-095-003; RRID: AB_2340106
FITC-conjugated goat anti-mouse IgG	Jackson ImmunoResearch	Cat#115-095-003; RRID: AB_2338589
FITC-conjugated goat anti-rat IgG	Jackson ImmunoResearch	Cat#112-095-003; RRID: AB_2338189
FITC-conjugated goat anti-guinea pig IgG	Jackson ImmunoResearch	Cat#106-095-003; RRID: AB_2337415
Cy3-conjugated mouse anti-rabbit IgG	Jackson ImmunoResearch	Cat#211-165-109; RRID: AB_2339158
Cy3-conjugated goat anti-mouse IgG	Jackson ImmunoResearch	Cat#115-165-003; RRID: AB_2338680
Alexa647-conjugated goat anti-mouse IgG	Jackson ImmunoResearch	Cat#115-605-003; RRID: AB_2338902

HRP-conjugated anti-rabbit IgG	Jackson ImmunoResearch	Cat#111-035-144; RRID: AB_2307391
HRP-conjugated anti-guinea pig IgG	Jackson ImmunoResearch	Cat#106-035-003; RRID: AB_2337402
HRP-conjugated anti-mouse IgG	Jackson ImmunoResearch	Cat#115-035-003; RRID: AB_10015289
Bacterial and virus strains		
E.coli. DH5α	TOYOBO	Cat#DNA-903
Chemicals, peptides, and recombinant proteins		
Penicillin-Streptomycin	Thermo Fisher	Cat#15140-122
T4 Polynucleotide Kinase	TOYOBO	Cat#PNK-111
BpiI	Thermo Fisher	Cat#ER1011
EcoRV	NIPPON GENE	Cat#317-00462
HindIII	NIPPON GENE	Cat#311-01163
EcoRI	NIPPON GENE	Cat#314-00112
In-Fusion® HD Cloning Kit	Takara Bio	Cat#639648
FIAU	Sigma-Aldrich	Cat#SML0632
Puromycin	Takara Bio	Cat#Z1305N
G418	Santa Cruz Biotechnology	Cat#SC-29065B
Blasticidin S hydrochloride	Wako	Cat#029-18701
L-Histidinol dihydrochloride	Sigma-Aldrich	Cat#H6647-10MG
Zeocin	Thermo Fisher	Cat#R25001
Trypan Blue Solution	Wako	Cat#207-17081
Proteinase K	Sigma-Aldrich	Cat#P2308
ECL Prime Western Blotting Detection Reagent	Cytiva	Cat#RPN2232
TRIzol™ Reagent	Thermo Fisher	Cat#15596026
SuperScript IV Reverse Transcriptase	Thermo Fisher	Cat#18090010
Phenol/chloroform/isoamyl alcohol (25:24:1)	NIPPON GENE	Cat#311-90151
AlkPhos Direct Labeling	GE Healthcare	Cat#RPN3680
CDP-Star	GE Healthcare	Cat#RPN3682
5-20% SDS-PAGE	Wako	Cat#194-15021
Lambda Protein Phosphatase	New England Biolabs	Cat#P0753S
1xcOmplete EDTA-free proteinase inhibitor	Roche	Cat#11873580001
X-tremeGENE™ 9 DNA Transfection Reagent	Roche	Cat#06365779001
Opti-MEM	Gibco	Cat#31985-062
Polybrene	Merck	Cat#TR-1003-G
16% PFA	Electron Microscopy Sciences	Cat#15710
Phenol red-free DMEM	Nacalai Tesque	Cat#08489-45

HEPES	Nacalai Tesque	Cat#17557-94
L-Glutamine solution	Sigma-Aldrich	Cat#G7513-20ML
SiR-Tubulin	Spirochrome	Cat#SC002
Monastrol	Selleckchem	Cat#S8439
MG132	Sigma-Aldrich	Cat#C2211
Mineral oil	Sigma-Aldrich	Cat#M5310-1L
BrdU	Sigma-Aldrich	Cat#10280879001
Propidium iodide	Sigma-Aldrich	Cat#P4170
Signal Enhancer Hikari	Nacalai Tesque	Cat#02270-81
DAPI	Roche	Cat#10236276001
Lipofectamine RNAiMAX Reagent	Thermo Fisher	Cat#13778075
Goat serum	Jackson ImmunoResearch	Cat#005-000-121
VECTASHIELD Mounting Medium	Vector Laboratories	Cat#H-1000
Critical commercial assays		
RealTime-Glo MT Cell Viability Assay	Promega	Cat#G9711
iTaq Universal SYBR Green One-Step Kit	Bio-Rad	Cat#1725151
Experimental models: Cell lines		
K562	ATCC	Cat#CCL-243
hTERT-RPE-1	ATCC	Cat#CRL-4000
Lenti-X™ 293T	Takara Bio	Cat#632180
U2OS	ATCC	Cat#HTB-96; RRID: CVCL_0042
TIG-3	JCRB Cell Bank	Cat#JCRB0510; RRID: CVCL_3209
A549	ATCC	Cat#CCL-185; RRID: CVCL_0023
HT29	JCRB Cell Bank	Cat#JCRB1962
HCC1806	ATCC	Cat#CRL-2335
HeLa Kyoto	Laboratory of Shu Narumiya, Kyoto University Graduate School of Medicine, Japan	N/A
HT1080	JCRB Cell Bank	Cat#JCRB9113; RRID: CVCL_0317
OVCAR-3	RIKEN Bioresource Center Cell Bank	Cat# RCB2135
K562 CENP-C$^{\Delta M12BD}$	This paper	N/A

K562 WT / Cas9	This paper	N/A
K562 WT / Cas9-KIF18A_sgRNAs	This paper	N/A
K562 WT / Cas9-KIF15_sgRNAs	This paper	N/A
K562 WT / Cas9-NDE1_sgRNAs	This paper	N/A
K562 WT / Cas9-NEDD1_sgRNAs	This paper	N/A
K562 WT / Cas9-SPAG5_sgRNAs	This paper	N/A
K562 WT / Cas9-NPM1_sgRNAs	This paper	N/A
K562 WT / Cas9-KNTC1_sgRNAs	This paper	N/A
K562 WT / Cas9-ASPM_sgRNAs	This paper	N/A
K562 WT / Cas9-ZW10_sgRNAs	This paper	N/A
K562 WT / Cas9-TUBGCP6_sgRNAs	This paper	N/A
K562 CENP-C$^{\Delta M12BD}$ / Cas9	This paper	N/A
K562 CENP-C$^{\Delta M12BD}$ / Cas9-KIF18A_sgRNAs	This paper	N/A
K562 CENP-C$^{\Delta M12BD}$ / Cas9-KIF15_sgRNAs	This paper	N/A
K562 CENP-C$^{\Delta M12BD}$ / Cas9-NDE1_sgRNAs	This paper	N/A
K562 CENP-C$^{\Delta M12BD}$ / Cas9-NEDD1_sgRNAs	This paper	N/A
K562 CENP-C$^{\Delta M12BD}$ / Cas9-SPAG5_sgRNAs	This paper	N/A
K562 CENP-C$^{\Delta M12BD}$ / Cas9-NPM1_sgRNAs	This paper	N/A
K562 CENP-C$^{\Delta M12BD}$ / Cas9-KNTC1_sgRNAs	This paper	N/A
K562 CENP-C$^{\Delta M12BD}$ / Cas9-ASPM_sgRNAs	This paper	N/A
K562 CENP-C$^{\Delta M12BD}$ / Cas9-ZW10_sgRNAs	This paper	N/A
K562 CENP-C$^{\Delta M12BD}$ / Cas9-TUBGCP6_sgRNAs	This paper	N/A
RPE-1 mScarlet-CENP-A	Kong et al., 2025	N/A
RPE-1 mScarlet-CENP-A_CENP-C^{WT}	This paper	N/A
RPE-1 mScarlet-CENP-A_CENP-C$^{\Delta M12BD}$	This paper	N/A
RPE-1 mScarlet-DSN1^{WT}	This paper	N/A
RPE-1 mScarlet-DSN1^{2A}	This paper	N/A
RPE-1 mScarlet-CENP-A GFP-H2A Flag-CENP-C^{WT}	Kong et al., 2025	N/A
RPE-1 mScarlet-CENP-A GFP-H2A Flag-CENP-C$^{\Delta M12BD}$	Kong et al., 2025	N/A
RPE-1 mScarlet-CENP-A_CENP-C^{WT} EGFP-KIF18A^{WT}	This paper	N/A
RPE-1 mScarlet-CENP-A_CENP-C^{WT} EGFP-KIF18A$^{\Delta 1-362}$	This paper	N/A
RPE-1 mScarlet-CENP-A_CENP-C^{WT} EGFP-KIF18A$^{\Delta PP1}$	This paper	N/A
RPE-1 mScarlet-CENP-A_CENP-C^{WT} EGFP-KIF18A^{2A}	This paper	N/A
RPE-1 mScarlet-CENP-A_CENP-C^{WT} EGFP-KIF18A$^{\Delta PP1+2A}$	This paper	N/A
RPE-1 mScarlet-CENP-A_CENP-C$^{\Delta M12BD}$ EGFP-KIF18A^{WT}	This paper	N/A

RPE-1 mScarlet-CENP-A_CENP-C$^{\Delta M12BD}$ EGFP-KIF18A $^{\Delta 1\text{-}362}$	This paper	N/A
RPE-1 mScarlet-CENP-A_CENP-C$^{\Delta M12BD}$ EGFP-KIF18A $^{\Delta PP1}$	This paper	N/A
RPE-1 mScarlet-CENP-A_CENP-C$^{\Delta M12BD}$ EGFP-KIF18A ^{2A}	This paper	N/A
RPE-1 mScarlet-CENP-A_CENP-C$^{\Delta M12BD}$ EGFP-KIF18A $^{\Delta PP1+2A}$	This paper	N/A
RPE-1 cKO-hCENP-T mScarlet-CENP-T^{WT}	Kong et al., 2025	N/A
RPE-1 cKO-hCENP-T mScarlet-CENP-T$^{\Delta 6\text{-}31}$	Kong et al., 2025	N/A
RPE-1 cKO-hCENP-T mScarlet-CENP-T$^{\Delta 76\text{-}105}$	Kong et al., 2025	N/A
Oligonucleotides		
sgRNA sequences and corresponding oligonucleotide sequences	This paper	Table
Primers for genotyping	This paper	Table
Primers for RT-qPCR	This paper	Table
ON-TARGETplus Non-targeting Pool	Horizon Discovery	Table
ON-TARGETplus Human KIF18A (81930) siRNA – SMARTpool	Horizon Discovery	Table
Recombinant DNA		
pX330	Cong et al., 2013	Addgene plasmid, #42230
pX330_sgCCExon2	This paper	N/A
pX330_sgCCExon4	This paper	N/A
pX330_sgAAVS1	Kong et al., 2025	N/A
pAAVS1-NDi-CRISPRi (Gen1)	Mandegar et al., 2016	Addgene plasmid, #73497
HP138-neo	McKinley et al., 2015	Addgene plasmid, #134247
pAAVS1_Tet-Cas9	This paper	N/A
pCAG-NLS-HA-Bxb1	Hermann et al., 2014	Addgene plasmid, #51271
pCMV-VSV-G	Stewart et al., 2003	Addgene plasmid, #8454
psPAX2	A gift from Didier Trono	Addgene plasmid, #12260
pattP_tri-gRNA_KIF18A	This paper	N/A
pattP_tri-gRNA_KIF15	This paper	N/A
pattP_tri-gRNA_NDE1	This paper	N/A
pattP_tri-gRNA_NEDD1	This paper	N/A
pattP_tri-gRNA_SPAG5	This paper	N/A
pattP_tri-gRNA_NPM1	This paper	N/A
pattP_tri-gRNA_KNTC1	This paper	N/A
pattP_tri-gRNA_ASPM	This paper	N/A

pattP_tri-gRNA_ZW10	This paper	N/A
pattP_tri-gRNA_TUBGCP6	This paper	N/A
pBSK_mScarlet-CENP-A_PuroR	Kong et al., 2025	N/A
pBSK_mScarlet-CENP-A_NeoR	Kong et al., 2025	N/A
pX330_sgCENP-A	Kong et al., 2025	N/A
pBSK_CENP-C^{WT}_ZeoR	Kong et al., 2025	N/A
pBSK_CENP-C^{WT}_HisD	Kong et al., 2025	N/A
pBSK_CENP-C$^{\Delta M12BD}$_ZeoR	Kong et al., 2025	N/A
pBSK_CENP-C$^{\Delta M12BD}$_HisD	Kong et al., 2025	N/A
pX330_sgCENP-C	Kong et al., 2025	N/A
pBSK_mScarlet-DSN1^{WT}_PuroR	Kong et al., 2025	N/A
pBSK_mScarlet-DSN1^{WT}_NeoR	Kong et al., 2025	N/A
pBSK_mScarlet-DSN1^{2A}_PuroR	This paper	N/A
pBSK_mScarlet-DSN1^{2A}_NeoR	This paper	N/A
pX330_sgDSN1	Kong et al., 2025	N/A
pBSK_CMV-KIF18A^{WT}-BsR	This paper	N/A
pBSK_CMV-KIF18A$^{\Delta 1-362}$-BsR	This paper	N/A
pBSK_CMV-KIF18A$^{\Delta PP1}$-BsR	This paper	N/A
pBSK_CMV-KIF18A^{2A}-BsR	This paper	N/A
pBSK_CMV-KIF18A$^{\Delta PP1+2A}$-BsR	This paper	N/A
sgRNA library plasmids	Wang T et al., 2015	Addgene plasmid, #1000000100
Software and algorithms		
GraphPad Prism 10.1.2	GraphPad	https://www.graphpad.com/
QuantStudio Design & Analysis Software v1.5.1	Thermo Fisher	N/A
Fiji software (v1.53)	Schindelin et al., 2012	https://imagej.net/software/fiji/
MAGeCK-RRA 0.5.9.2	Li et al., 2014	https://sourceforge.net/p/mageck/wiki/Home/
Image Lab 6.1.0	Bio-Rad	https://www.bio-rad.com/en-jp/product/image-lab-software?ID=KRE6P5E8Z
R 4.3.1		https://www.r-project.org/
GSEA version 4.2.3	Subramanian et al., 2005	https://www.gsea-msigdb.org/gsea/index.jsp
Imaris 9.0.2	Bitplane	N/A
BD FACSDiva 9.0 Software	BD Biosciences	N/A
SoftWoRx software 5.5	GE healthcare	N/A

NIS-Elements v5.42.01	Nikon	https://www.microscope.healthcare.nikon.com/products/software/nis-elements

Tables

Figure Position	Primer name	Primer sequence
Fig.13A	F1	Cttcgatgatctcccattatgtgacg
	R1	acgtaaatcacCTGGAAGGTCGAC
	F2	AAAGACACTTGTATTCAGTCACCAAGC
	R2	cattgcttggaaccaaaaggctac
Fig.13B	Probe primer 5'	AGTCTAGCTCCAGTTCCTAGGCCTC
	Probe primer 3'	CTGCAGGCATCTGGTAAGCTTTATTCC
Fig.13C	F3	CTGAGACTTAAGGTTATTGCTTGGCCG
	R3	GATGAACTTCATGGGCCTGAACTGA
Fig.20A	F4	gtttacgggctgcttgccaatacg
	R4	agtgcccttgctgtgccgccggaac
Fig.54A	F5	gcatgatcctcccttagctatgaagctag
	R5	tgctcccctgaaatcaacagtcatcag
Fig.54B	Probe primer 5'	ggacaaacttgCAATGTATTCATTGTAGC
	Probe primer 3'	AGTGAAAGAGCACTCACAGCCTC
Fig.54C	F6	GAAAGTGGACCTTCCAGGCTCAAT
	R6	GCTGCAAAGGATCTCCAAGAGGTA

Primer used in RT-qPCR (Fig.21)

Target gene	Primer name	Primer sequence
GAPDH	5' primer	GAGAACGGGAAGCTTGTCATCAATGG
	3' primer	AAATGAGCCCCAGCCTTCTCCATGG
KIF18A	5' primer	AAGAATGTGGACAGGAGGACTTGG
	3' primer	CCATGCTTGGTACAGGCATAGAATGC
KIF15	5' primer	TTGGAAGCAACAAAAGCCTGCAAGC
	3' primer	GAATGAAGTTGGTAGGCCTTGGTTGG
SPAG5	5' primer	GAAATATCCTAGAGGAGAACCTTCG
	3' primer	CCAGCAATCCCTGTAGTTCTTTGC
NPM1	5' primer	CTTGCTGCTGATGAAGATGATGACG
	3' primer	GTGCATTTTTGGCTGGAGTATCTCG
KNTC1	5' primer	CCAGTTAGAACTTCCGGCTTTTGC
	3' primer	AATAACCTGAGGGTCACAGGAACC
ZW10	5' primer	GTGCCAAAATGGATGCCATTCAAGG
	3' primer	TTACTTCACTGGAAGAGAACGCAGC
NDE1	5' primer	AGGCCATCGAAAGAAATGCCTTCC
	3' primer	TGCCGCAAATCTCTGGCTTCATCC
NEDD1	5' primer	GTTCTCACCTATCAGAGATGATGC
	3' primer	GGAGGAAACACTGAGTTCAACTGC
ASPM	5' primer	GGCTGTGAAGAATGCTAACAAGCAGG
	3' primer	TTACTGATGCAGCCCTATTTCGCTGG

TUBGCP6	5' primer	ACTCATGCAGCAGTCCTACAACACC
	3' primer	TGAAGTTGATGCGCAGCAGAAAGTCC

siRNA sequences

Name	Catalog#	Target sequences
ON-TARGETplus Non-targeting Pool	D-001810-10-05	UGGUUUACAUGUCGACUAA
		UGGUUUACAUGUUGUGUGA
		UGGUUUACAUGUUUUCUGA
		UGGUUUACAUGUUUUCCUA

ON-TARGETplus Human KIF18A (81930) siRNA - SMARTpool	J-006849-05	UAAAUUACCCGAACAAGAA
	J-006849-06	GAAAGUAGUAGUUCGUGUA
	J-006849-07	CAAAAUCCGUCUACAGUAA
	J-006849-08	GGAUAUAAUUGCACAGUAC

References

Abe Y, Sako K, Takagaki K, et al. HP1-assisted Aurora B kinase activity prevents chromosome segregation errors. Developmental cell, 2016, 36(5): 487-497.

Anna A Y, Deretic J, Hoel C M, et al. Aurora A kinase contributes to a pole-based error correction pathway. Current Biology, 2015, 25(14): 1842-1851.

Ariyoshi M, Makino F, Watanabe R, et al. Cryo-EM structure of the CENP-A nucleosome in complex with phosphorylated CENP-C. The EMBO journal, 2021, 40(5): e105671.

Barbosa J, Sunkel C E, Conde C. The role of mitotic kinases and the RZZ complex in kinetochore-microtubule attachments: doing the right link. Frontiers in Cell and Developmental Biology, 2022, 10: 787294.

Barisic M, Aguiar P, Geley S, et al. Kinetochore motors drive congression of peripheral polar chromosomes by overcoming random arm-ejection forces. Nature cell biology, 2014, 16(12): 1249-1256.

Bendre S, Rondelet A, Hall C, et al. GTSE1 tunes microtubule stability for chromosome alignment and segregation by inhibiting the microtubule depolymerase MCAK. Journal of Cell Biology, 2016, 215(5): 631-647.

Black B E, Bassett E A. The histone variant CENP-A and centromere specification. Current opinion in cell biology, 2008, 20(1): 91-100.

Bloom K, Yeh E. Tension management in the kinetochore. Current Biology, 2010, 20(23): R1040-R1048.

Burbank K S, Mitchison T J. Microtubule dynamic instability. Current Biology, 2006, 16(14): R516-R517.

Cheeseman I M. The kinetochore. Cold Spring Harbor perspectives in biology, 2014, 6(7): a015826.

Cheeseman I M, Desai A. Molecular architecture of the kinetochore–microtubule interface. Nature reviews Molecular cell biology, 2008, 9(1): 33-46.

Chen G, Deng X. Cell Synchronization by Double Thymidine Block. Bio-Protocol 8, e2994. (2018)

Ciferri C, Pasqualato S, Screpanti E, et al. Implications for kinetochore-microtubule attachment from the structure of an engineered Ndc80 complex. Cell, 2008, 133(3): 427-439.

Ciossani G, Overlack K, Petrovic A, et al. The kinetochore proteins CENP-E and CENP-F directly and specifically interact with distinct BUB mitotic checkpoint Ser/Thr kinases. Journal of Biological Chemistry, 2018, 293(26): 10084-10101.

Cleveland D W, Mao Y, Sullivan K F. Centromeres and kinetochores: from epigenetics to mitotic checkpoint signaling. Cell, 2003, 112(4): 407-421.

Cmentowski V, Ciossani G, d'Amico E, et al. RZZ-Spindly and CENP-E form an integrated platform to recruit dynein to the kinetochore corona. The EMBO Journal, 2023, 42(24): e114838.

Cohen-Sharir Y, McFarland J M, Abdusamad M, et al. Aneuploidy renders cancer cells vulnerable to mitotic checkpoint inhibition. Nature, 2021, 590(7846): 486-491.

Craske B, Welburn J P I. Leaving no-one behind: how CENP-E facilitates chromosome alignment. Essays in biochemistry, 2020, 64(2): 313-324.

Dawkins R. The selfish gene. 1976.

DeLuca J G, Gall W E, Ciferri C, et al. Kinetochore microtubule dynamics and attachment stability are regulated by Hec1. Cell, 2006, 127(5): 969-982.

DeLuca K F, Meppelink A, Broad A J, et al. Aurora A kinase phosphorylates Hec1 to regulate metaphase kinetochore–microtubule dynamics. Journal of Cell Biology, 2018, 217(1): 163-177.

de Regt A K, Clark C J, Asbury C L, et al. Tension can directly suppress Aurora B kinase-triggered release of kinetochore-microtubule attachments. Nature Communications, 2022, 13(1): 2152.

Dimitrova Y N, Jenni S, Valverde R, et al. Structure of the MIND complex defines a regulatory focus for yeast kinetochore assembly. Cell, 2016, 167(4): 1014-1027. e12.

Du Y, English C A, Ohi R. The kinesin-8 Kif18A dampens microtubule plus-end

dynamics. Current Biology, 2010, 20(4): 374-380.

Earnshaw W C, Rothfield N. Identification of a family of human centromere proteins using autoimmune sera from patients with scleroderma. Chromosoma. 1985;91(3-4):313-21.

Earnshaw W C, Allshire R C, Black B E, et al. Esperanto for histones: CENP-A, not CenH3, is the centromeric histone H3 variant. Chromosome research, 2013, 21: 101-106.

Eibes S, Rajendraprasad G, Guasch-Boldu C, et al. CENP-E activation by Aurora A and B controls kinetochore fibrous corona disassembly. Nature Communications, 2023, 14(1): 5317.

Garcia M A, Koonrugsa N, Toda T. Two kinesin-like Kin I family proteins in fission yeast regulate the establishment of metaphase and the onset of anaphase A. Current biology, 2002, 12(8): 610-621.

Gascoigne K E, Cheeseman I M. Kinetochore assembly: if you build it, they will come. Current opinion in cell biology, 2011, 23(1): 102-108.

Gliech C R, Yeow Z Y, Tapias-Gomez D, et al. Weakened APC/C activity at mitotic exit drives cancer vulnerability to KIF18A inhibition. The EMBO Journal, 2024, 43(5): 666-694.

Grishchuk EL. Biophysics of Microtubule End Coupling at the Kinetochore. Prog Mol Subcell Biol. 2017;56:397-428.

Gupta Jr M L, Carvalho P, Roof D M, et al. Plus end-specific depolymerase activity of Kip3, a kinesin-8 protein, explains its role in positioning the yeast mitotic spindle. Nature cell biology, 2006, 8(9): 913-923.

Häfner J, Mayr M I, Möckel M M, et al. Pre-anaphase chromosome oscillations are regulated by the antagonistic activities of Cdk1 and PP1 on Kif18A. Nature communications, 2014, 5(1): 4397.

Hara M, Ariyoshi M, Okumura E, et al. Multiple phosphorylations control recruitment of the KMN network onto kinetochores. Nature cell biology, 2018, 20(12): 1378-1388.

Hara M, Ariyoshi M, Sano T, et al. Centromere/kinetochore is assembled through

CENP-C oligomerization. Molecular cell, 2023, 83(13): 2188-2205. e13.

Hara M, Fukagawa T. Critical foundation of the kinetochore: the constitutive centromere-associated network (CCAN). Centromeres and Kinetochores: Discovering the Molecular Mechanisms Underlying Chromosome Inheritance, 2017: 29-57.

Hara M, Fukagawa T. Kinetochore assembly and disassembly during mitotic entry and exit. Current opinion in cell biology, 2018, 52: 73-81.

Henikoff S, Ahmad K, Malik H S. The centromere paradox: stable inheritance with rapidly evolving DNA. Science, 2001, 293(5532): 1098-1102.

Hernandez B, Tetlak P, Domingo-Muelas A, et al. Actin organizes chromosomes and microtubules to ensure mitotic fidelity in the preimplantation embryo. Science, 2025, 388(6749): eads1234.

Hori T, Amano M, Suzuki A, et al. CCAN makes multiple contacts with centromeric DNA to provide distinct pathways to the outer kinetochore. Cell, 2008, 135(6): 1039-1052.

Hori T, Shang W H, Takeuchi K, et al. The CCAN recruits CENP-A to the centromere and forms the structural core for kinetochore assembly. Journal of Cell Biology, 2013, 200(1): 45-60.

Howman E V, Fowler K J, Newson A J, et al. Early disruption of centromeric chromatin organization in centromere protein A (Cenpa) null mice. Proceedings of the National Academy of Sciences, 2000, 97(3): 1148-1153.

Huang Y, Yao Y, Xu H Z, et al. Defects in chromosome congression and mitotic progression in KIF18A-deficient cells are partly mediated through impaired functions of CENP-E. Cell Cycle, 2009, 8(16): 2643-2649.

Huis in't Veld P J, Jeganathan S, Petrovic A, et al. Molecular basis of outer kinetochore assembly on CENP-T. Elife, 2016, 5: e21007.

Iemura K, Natsume T, Maehara K, et al. Chromosome oscillation promotes Aurora A–dependent Hec1 phosphorylation and mitotic fidelity. Journal of Cell Biology, 2021, 220(7): e202006116.

Iemura K, Tanaka K. Chromokinesin Kid and kinetochore kinesin CENP-E differentially

support chromosome congression without end-on attachment to microtubules. Nature communications, 2015, 6(1): 6447.

Ishikawa Y, Fukue H, Iwakami R, et al. Fibrous corona is reduced in cancer cell lines that attenuate microtubule nucleation from kinetochores. Cancer Science, 2025.

Itoh G, Ikeda M, Iemura K, et al. Lateral attachment of kinetochores to microtubules is enriched in prometaphase rosette and facilitates chromosome alignment and bi-orientation establishment. Scientific reports, 2018, 8(1): 3888.

Joglekar A P, Bloom K S, Salmon E D. Mechanisms of force generation by end-on kinetochore-microtubule attachments. Current opinion in cell biology, 2010, 22(1): 57-67.

Kapoor T M, Lampson M A, Hergert P, et al. Chromosomes can congress to the metaphase plate before biorientation. Science, 2006, 311(5759): 388-391.

Kapoor T M, Mayer T U, Coughlin M L, et al. Probing spindle assembly mechanisms with monastrol, a small molecule inhibitor of the mitotic kinesin, Eg5. Journal of Cell Biology, 2000, 150(5): 975-988.

Kato H, Jiang J, Zhou B R, et al. A conserved mechanism for centromeric nucleosome recognition by centromere protein CENP-C. Science, 2013, 340(6136): 1110-1113.

Kim S, Yu H. Multiple assembly mechanisms anchor the KMN spindle checkpoint platform at human mitotic kinetochores. Journal of Cell Biology, 2015, 208(2): 181-196.

Kim Y, Holland A J, Lan W, et al. Aurora kinases and protein phosphatase 1 mediate chromosome congression through regulation of CENP-E. Cell, 2010, 142(3): 444-455.

Kisselev A F, Goldberg A L. Proteasome inhibitors: from research tools to drug candidates. Chemistry & biology, 2001, 8(8): 739-758.

Kiyomitsu T, Murakami H, Yanagida M. Protein interaction domain mapping of human kinetochore protein Blinkin reveals a consensus motif for binding of spindle assembly checkpoint proteins Bub1 and BubR1. Molecular and cellular biology, 2011, 31(5): 998-1011.

Klaasen S J, Truong M A, van Jaarsveld R H, et al. Nuclear chromosome locations dictate segregation error frequencies. Nature, 2022, 607(7919): 604-609.

Kline S L, Cheeseman I M, Hori T, et al. The human Mis12 complex is required for kinetochore assembly and proper chromosome segregation. Journal of Cell Biology, 2006, 173(1): 9-17.

Kong W, Hara M, Tokunaga Y, et al. CENP-C-Mis12 complex establishes a regulatory loop through Aurora B for chromosome segregation. Life Science Alliance, 2025, 8(1).

Legal T, Hayward D, Gluszek-Kustusz A, et al. The C-terminal helix of BubR1 is essential for CENP-E-dependent chromosome alignment. Journal of cell science, 2020, 133(16): jcs246025.

Maiato H, Gomes A M, Sousa F, et al. Mechanisms of chromosome congression during mitosis. Biology, 2017, 6(1): 13.

Marquis C, Fonseca C L, Queen K A, et al. Chromosomally unstable tumor cells specifically require KIF18A for proliferation. Nature Communications, 2021, 12(1): 1213.

Maure J F, Komoto S, Oku Y, et al. The Ndc80 loop region facilitates formation of kinetochore attachment to the dynamic microtubule plus end. Current biology, 2011, 21(3): 207-213.

Mayr M I, Hümmer S, Bormann J, et al. The human kinesin Kif18A is a motile microtubule depolymerase essential for chromosome congression. Current Biology, 2007, 17(6): 488-498.

McKinley K L, Cheeseman I M. The molecular basis for centromere identity and function. Nature reviews Molecular cell biology, 2016, 17(1): 16-29.

McKinley K L, Sekulic N, Guo L Y, et al. The CENP-LN complex forms a critical node in an integrated meshwork of interactions at the centromere-kinetochore interface. Molecular cell, 2015, 60(6): 886-898.

Milic B, Chakraborty A, Han K, et al. KIF15 nanomechanics and kinesin inhibitors, with implications for cancer chemotherapeutics. Proceedings of the National Academy of Sciences, 2018, 115(20): E4613-E4622.

Monda J K, Cheeseman I M. The kinetochore–microtubule interface at a glance. Journal of cell science, 2018, 131(16): jcs214577.

Moroi Y, Peebles C, Fritzler M J, et al. Autoantibody to centromere (kinetochore) in scleroderma sera. Proceedings of the National Academy of Sciences, 1980, 77(3): 1627-1631.

Muir K W, Batters C, Dendooven T, et al. Structural mechanism of outer kinetochore Dam1-Ndc80 complex assembly on microtubules. Science, 2023, 382(6675): 1184-1190.

Musacchio A, Desai A. A molecular view of kinetochore assembly and function. Biology, 2017, 6(1): 5.

Musacchio A. The molecular biology of spindle assembly checkpoint signaling dynamics. Current biology, 2015, 25(20): R1002-R1018.

Nagpal H, Fukagawa T. Kinetochore assembly and function through the cell cycle. Chromosoma, 2016, 125(4): 645-659.

Navarro A P, Cheeseman I M. Kinetochore assembly throughout the cell cycle. Seminars in cell & developmental biology. Academic Press, 2021, 117: 62-74.

Nishino T, Rago F, Hori T, et al. CENP-T provides a structural platform for outer kinetochore assembly. The EMBO journal, 2013, 32(3): 424-436.

N. McNeil and T. Ried. Expert Reviews in Molecular Medicine. 2000, 2:1–14.

O'Connor C. Cell division: Stages of mitosis. Nature Education, 2008, 1(1): 188.

Okada M, Cheeseman I M, Hori T, et al. The CENP-H–I complex is required for the efficient incorporation of newly synthesized CENP-A into centromeres. Nature cell biology, 2006, 8(5): 446-457.

Orr B, Talje L, Liu Z, et al. Adaptive resistance to an inhibitor of chromosomal instability in human cancer cells. Cell reports, 2016, 17(7): 1755-1763.

Panchenko T, Sorensen T C, Woodcock C L, et al. Replacement of histone H3 with CENP-A directs global nucleosome array condensation and loosening of nucleosome superhelical termini. Proceedings of the National Academy of Sciences, 2011, 108(40): 16588-16593.

Pentakota S, Zhou K, Smith C, et al. Decoding the centromeric nucleosome through CENP-N. Elife, 2017, 6: e33442.

Pereira C, Reis R M, Gama J B, et al. Self-assembly of the RZZ complex into filaments drives kinetochore expansion in the absence of microtubule attachment. Current Biology, 2018, 28(21): 3408-3421. e8.

Pesenti M E, Raisch T, Conti D, et al. Structure of the human inner kinetochore CCAN complex and its significance for human centromere organization. Molecular cell, 2022, 82(11): 2113-2131. e8.

Petrovic A, Keller J, Liu Y, et al. Structure of the MIS12 complex and molecular basis of its interaction with CENP-C at human kinetochores. Cell, 2016, 167(4): 1028-1040. e15.

Petrovic A, Mosalaganti S, Keller J, et al. Modular assembly of RWD domains on the Mis12 complex underlies outer kinetochore organization. Molecular cell, 2014, 53(4): 591-605.

Petrovic A, Pasqualato S, Dube P, et al. The MIS12 complex is a protein interaction hub for outer kinetochore assembly. Journal of Cell Biology, 2010, 190(5): 835-852.

Polley S, Müschenborn H, Terbeck M, et al. Stable kinetochore-microtubule attachment requires loop-dependent Ndc80-Ndc80 binding. The EMBO journal, 2023, 42(13): e112504.

Powers A F, Franck A D, Gestaut D R, et al. The Ndc80 kinetochore complex forms load-bearing attachments to dynamic microtubule tips via biased diffusion. Cell, 2009, 136(5): 865-875.

Przewloka M R, Venkei Z, Bolanos-Garcia V M, et al. CENP-C is a structural platform for kinetochore assembly. Current Biology, 2011, 21(5): 399-405.

Quinton R J, DiDomizio A, Vittoria M A, et al. Whole-genome doubling confers unique genetic vulnerabilities on tumour cells. Nature, 2021, 590(7846): 492-497.

Rago F, Gascoigne K E, Cheeseman I M. Distinct organization and regulation of the outer kinetochore KMN network downstream of CENP-C and CENP-T. Current Biology, 2015, 25(5): 671-677.

Raisch T, Ciossani G, d'Amico E, et al. Structure of the RZZ complex and molecular basis of Spindly-driven corona assembly at human kinetochores. The EMBO journal,

2022, 41(9): e110411.

Régnier V, Vagnarelli P, Fukagawa T, et al. CENP-A is required for accurate chromosome segregation and sustained kinetochore association of BubR1. Molecular and cellular biology, 2005, 25(10): 3967-3981.

Risteski P, Jagrić M, Pavin N, et al. Biomechanics of chromosome alignment at the spindle midplane. Current Biology, 2021, 31(10): R574-R585.

Roscioli E, Germanova T E, Smith C A, et al. Ensemble-level organization of human kinetochores and evidence for distinct tension and attachment sensors. Cell reports, 2020, 31(4).

Sacristan C, Kops G J P L. Joined at the hip: kinetochores, microtubules, and spindle assembly checkpoint signaling. Trends in cell biology, 2015, 25(1): 21-28.

Schrodinger E. What is life?: the physical aspect of the living cell. 1946.

Schutt K L, Queen K A, Fisher K, et al. Identification of the KIF18A alpha-4 helix as a therapeutic target for chromosomally unstable tumor cells. Frontiers in Molecular Biosciences, 2024, 11: 1328077.

Screpanti E, De Antoni A, Alushin G M, et al. Direct binding of Cenp-C to the Mis12 complex joins the inner and outer kinetochore. Current Biology, 2011, 21(5): 391-398.

Shepperd L A, Meadows J C, Sochaj A M, et al. Phosphodependent recruitment of Bub1 and Bub3 to Spc7/KNL1 by Mph1 kinase maintains the spindle checkpoint. Current Biology, 2012, 22(10): 891-899.

Shrestha R L, Ahn G S, Staples M I, et al. Mislocalization of centromeric histone H3 variant CENP-A contributes to chromosomal instability (CIN) in human cells. Oncotarget, 2017, 8(29): 46781.

Shrestha R L, Conti D, Tamura N, et al. Aurora-B kinase pathway controls the lateral to end-on conversion of kinetochore-microtubule attachments in human cells. Nature Communications, 2017, 8(1): 150.

Shrestha R L, Draviam V M. Lateral to end-on conversion of chromosome-microtubule attachment requires kinesins CENP-E and MCAK. Current biology, 2013, 23(16): 1514-1526.

Shrestha R L, Rossi A, Wangsa D, et al. CENP-A overexpression promotes aneuploidy with karyotypic heterogeneity. Journal of Cell Biology, 2021, 220(4): e202007195.

Sissoko G B, Tarasovetc E V, Marescal O, et al. Higher-order protein assembly controls kinetochore formation. Nature cell biology, 2024, 26(1): 45-56.

Skoufias D A, Indorato R L, Lacroix F, et al. Mitosis persists in the absence of Cdk1 activity when proteolysis or protein phosphatase activity is suppressed. The Journal of cell biology, 2007, 179(4): 671-685.

Sridhar S, Fukagawa T. Kinetochore architecture employs diverse linker strategies across evolution. Frontiers in Cell and Developmental Biology, 2022, 10: 862637.

Stumpff J, Du Y, English C A, et al. A tethering mechanism controls the processivity and kinetochore-microtubule plus-end enrichment of the kinesin-8 Kif18A. Molecular cell, 2011, 43(5): 764-775.

Stumpff J, Von Dassow G, Wagenbach M, et al. The kinesin-8 motor Kif18A suppresses kinetochore movements to control mitotic chromosome alignment. Developmental cell, 2008, 14(2): 252-262.

Su K C, Radul E, Maier N K, et al. Functional genetics reveals modulators of antimicrotubule drug sensitivity. Journal of Cell Biology, 2024, 224(2): e202403065.

Sullivan K F, Hechenberger M, Masri K. Human CENP-A contains a histone H3 related histone fold domain that is required for targeting to the centromere. The Journal of cell biology, 1994, 127(3): 581-592.

Takenoshita Y, Hara M, Fukagawa T. Recruitment of two Ndc80 complexes via the CENP-T pathway is sufficient for kinetochore functions. Nat. Commun. 13, 851. (2022)

Takenoshita Y, Hara M, Nakagawa R, et al. Molecular details and phosphoregulation of the CENP-T-Mis12 complex interaction during mitosis in DT40 cells. iScience, 2024, 27(12).

Tanaka T U, Zhang T. SWAP, SWITCH, and STABILIZE: Mechanisms of kinetochore–microtubule error correction. Cells, 2022, 11(9): 1462.

Tanenbaum M E, Macůrek L, Janssen A, et al. Kif15 cooperates with eg5 to promote bipolar spindle assembly. Current biology, 2009, 19(20): 1703-1711.

Thein K H, Kleylein-Sohn J, Nigg E A, et al. Astrin is required for the maintenance of sister chromatid cohesion and centrosome integrity. Journal of Cell Biology, 2007, 178(3): 345-354.

Uhlmann F, Lottspeich F, Nasmyth K. Sister-chromatid separation at anaphase onset is promoted by cleavage of the cohesin subunit Scc1. Nature, 1999, 400(6739): 37-42.

Valverde R, Ingram J, Harrison S C. Conserved tetramer junction in the kinetochore Ndc80 complex. Cell reports, 2016, 17(8): 1915-1922.

Varga V, Helenius J, Tanaka K, et al. Yeast kinesin-8 depolymerizes microtubules in a length-dependent manner. Nature cell biology, 2006, 8(9): 957-962.

Verma V, Maresca T J. A celebration of the 25th anniversary of chromatin-mediated spindle assembly. Molecular Biology of the Cell, 2022, 33(2): rt1.

Vicente J J, Wordeman L. The quantification and regulation of microtubule dynamics in the mitotic spindle. Current opinion in cell biology, 2019, 60: 36-43.

Vukušić K, Tolić I M. Polar chromosomes—challenges of a risky path. Cells, 2022, 11(9): 1531.

Waizenegger I C, Giménez-Abián J F, Wernic D, et al. Regulation of human separase by securin binding and autocleavage. Current biology, 2002, 12(16): 1368-1378.

Wang T, Wei J J, Sabatini D M, et al. Genetic screens in human cells using the CRISPR-Cas9 system. Science, 2014, 343(6166): 80-84.

Warburton P E, Cooke C A, Bourassa S, et al. Immunolocalization of CENP-A suggests a distinct nucleosome structure at the inner kinetochore plate of active centromeres. Current Biology, 1997, 7(11): 901-904.

Watanabe R, Hara M, Okumura E, et al. CDK1-mediated CENP-C phosphorylation modulates CENP-A binding and mitotic kinetochore localization. Journal of Cell Biology, 2019, 218(12): 4042-4062.

Watson J D, Crick F H C. Molecular structure of nucleic acids: a structure for deoxyribose nucleic acid. Nature, 1953, 171(4356): 737-738.

Weaver L N, Ems-McClung S C, Stout J R, et al. Kif18A uses a microtubule binding

site in the tail for plus-end localization and spindle length regulation. Current Biology, 2011, 21(17): 1500-1506.

Weber J, Legal T, Lezcano A P, et al. A conserved CENP-E region mediates BubR1-independent recruitment to the outer corona at mitotic onset. Current Biology, 2024, 34(5): 1133-1141. e4.

West R R, Malmstrom T, Troxell C L, et al. Two related kinesins, klp5+ and klp6+, foster microtubule disassembly and are required for meiosis in fission yeast. Molecular biology of the cell, 2001, 12(12): 3919-3932.

Wu J, Larreategui-Aparicio A, Lambers M L A, et al. Microtubule nucleation from the fibrous corona by LIC1-pericentrin promotes chromosome congression. Current Biology, 2023, 33(5): 912-925. e6.

Yan K, Yang J, Zhang Z, et al. Structure of the inner kinetochore CCAN complex assembled onto a centromeric nucleosome. Nature, 2019, 574(7777): 278-282.

Yatskevich S, Muir K W, Bellini D, et al. Structure of the human inner kinetochore bound to a centromeric CENP-A nucleosome. Science, 2022, 376(6595): 844-852.

Yatskevich S, Yang J, Bellini D, et al. Structure of the human outer kinetochore KMN network complex. Nature structural & molecular biology, 2024, 31(6): 874-883.

Ying Z, Yang J, Li W, et al. Astrin: a key player in mitosis and cancer. Frontiers in Cell and Developmental Biology, 2020, 8: 866.

Zahm J A, Harrison S C. A communication hub for phosphoregulation of kinetochore-microtubule attachment. Current Biology, 2024, 34(11): 2308-2318. e6.

Acknowledgements

First and foremost, I would like to express my deepest gratitude to Professor Fukagawa for accepting me as a PhD student in his laboratory. I am truly fortunate to have had the opportunity to study under his guidance. His profound knowledge, insightful advice, and continuous support have been indispensable throughout my graduate research.

I am especially grateful to Hara-san, who has been a consistent source of guidance over the past five years. His thoughtful advice, experimental expertise, and dedication have shaped the way I approach science and have greatly contributed to the progress of my work.

I also sincerely thank all the members of the Fukagawa laboratory for their kind support and helpful suggestions. Their feedback and collaboration have been instrumental in overcoming various challenges in my research.

I would like to express special thanks to Professor Hiroshi Sasaki for his valuable support at the initial stage of my CRISPR screening experiments. His guidance on how to handle lentivirus was crucial for establishing the foundation of this work. I am also deeply thankful to Dr. Heather R. Keys for her support and advice throughout the CRISPR screening project.

I would like to acknowledge Dr. Iain M. Cheeseman and Dr. Kuan-Chung Su from the Cheeseman laboratory for their generous support and for providing essential plasmids and technical advice that greatly benefited my research.

I am grateful to the administrative staff of the Graduate School of Frontier Biosciences for their assistance and support during my PhD studies. Their help ensured that I could focus fully on my research.

Finally, I would like to thank my parents for their financial support during my doctoral studies, and my friends for their constant encouragement. It is thanks to their belief in me that I was able to make it this far.

Achievements

Publication

Jiahang Miao, Masatoshi Hara, Kuan-Chung Su, Heather R. Keys, Weixia Kong, Yusuke Takenoshita, Iain M. Cheeseman and Tatsuo Fukagawa. KIF18A promotes chromosome congression in cooperation with CENP-E downstream of CENP-C. (*Cell Reports*, 2025: 116515)

Jiahang Miao, Masatoshi Hara, Kuan-Chung Su, Heather R. Keys, Weixia Kong, Yusuke Takenoshita, Iain M. Cheeseman and Tatsuo Fukagawa. Functional genetics with a hypomorphic CENP-C mutant reveals a regulatory system for chromosome congression. (*bioRxiv*, 2025: 2025.08. 06.668996.)

Weixia Kong, Masatoshi Hara, Yurika Tokunaga, Kazuhiro Okumura, Yasuhiro Hirano, **Jiahang Miao**, Yusuke Takenoshita, Masakazu Hashimoto, Hiroshi Sasaki, Toshihiko Fujimori, Yuichi Wakabayashi, and Tatsuo Fukagawa. CENP-C-Mis12 complex establishes a regulatory loop through Aurora B for chromosome segregation. (*Life Science Alliance*, 2025, 8(1))

Dongyang Xu, **Jiahang Miao**, Emi Yumoto, Takao Yokota, Masashi Asahina, Masaaki Watahiki. *YUCCA9*-Mediated Auxin Biosynthesis and Polar Auxin Transport Synergistically Regulate Regeneration of Root Systems Following Root Cutting. (*Plant and Cell Physiology*, 2017, 58(10): 1710-1723)

Presentation

1. 2021/12/01 – 2021/12/03 Poster presentation in the 44th Annual Meeting of the Molecular Biology Society of Japan (MBSJ).

2. 2022/11/30 – 2022/12/02 Poster presentation in the 45th Annual Meeting of the Molecular Biology Society of Japan (MBSJ).

3. 2023/12/06 – 2023/12/08 Poster presentation in the 46th Annual Meeting of the Molecular Biology Society of Japan (MBSJ).

4. 2024/11/27 – 2024/11/29 Poster presentation in the 47th Annual Meeting of the Molecular Biology Society of Japan (MBSJ).